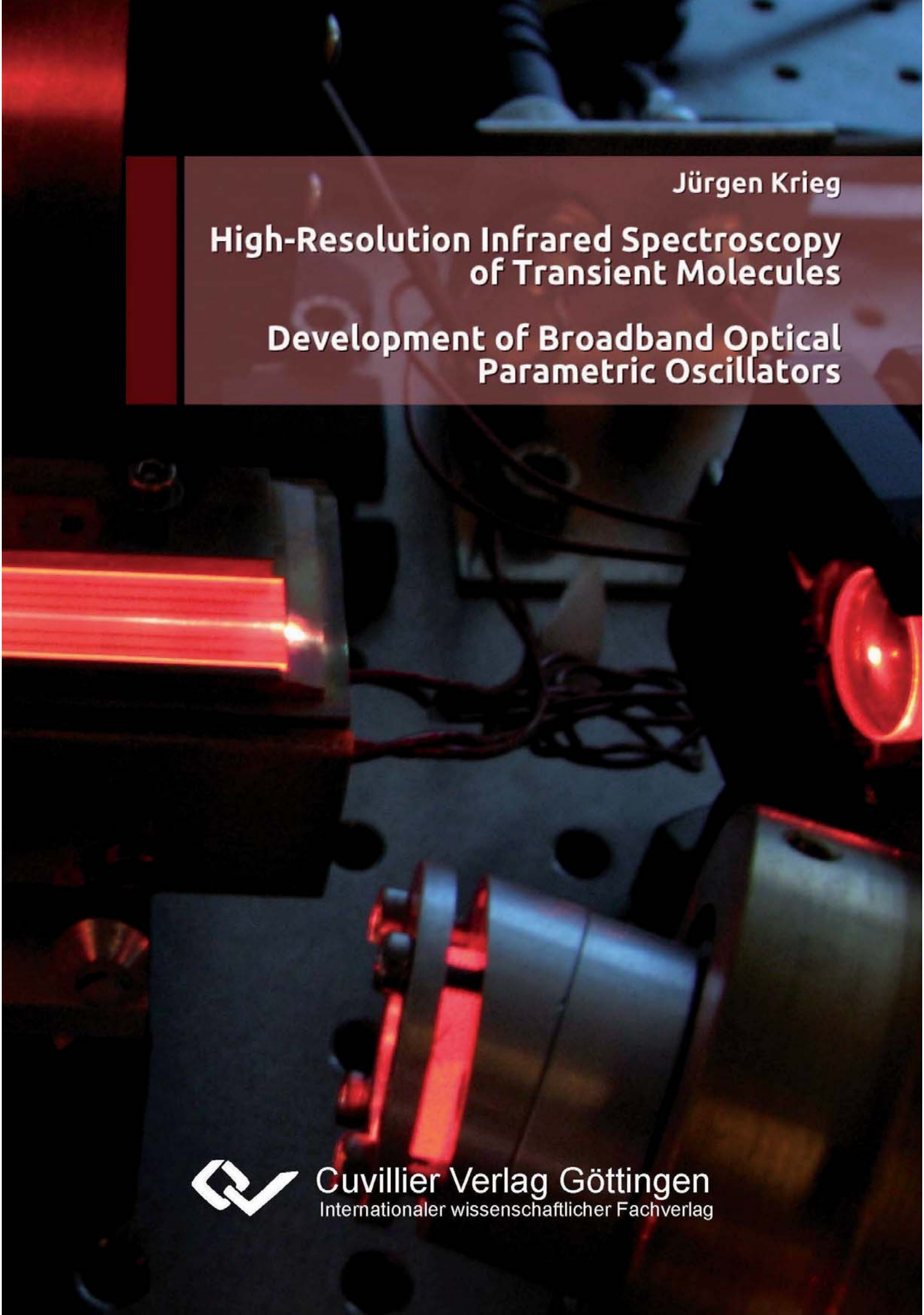

Jürgen Krieg

High-Resolution Infrared Spectroscopy of Transient Molecules

Development of Broadband Optical Parametric Oscillators

Cuvillier Verlag Göttingen
Internationaler wissenschaftlicher Fachverlag

Dieses Werk ist copyrightgeschützt und darf in keiner Form vervielfältigt werden noch an Dritte weitergegeben werden.
Es gilt nur für den persönlichen Gebrauch.

Dieses Werk ist copyrightgeschützt und darf in keiner Form vervielfältigt werden noch an Dritte weitergegeben werden.
Es gilt nur für den persönlichen Gebrauch.

High-Resolution Infrared Spectroscopy of Transient Molecules

–

Development of Broadband Optical Parametric Oscillators

Inaugural-Dissertation

zur

Erlangung des Doktorgrades

der Mathematisch-Naturwissenschftlichen Fakultät

der Universität zu Köln

vorgelegt von

Jürgen Krieg

aus Köln

Köln 2011

Dieses Werk ist copyrightgeschützt und darf in keiner Form vervielfältigt werden noch an Dritte weitergegeben werden.
Es gilt nur für den persönlichen Gebrauch.

Bibliografische Information der Deutschen Nationalbibliothek
Die Deutsche Nationalbibliothek verzeichnet diese Publikation in der Deutschen Nationalbibliografie; detaillierte bibliografische Daten sind im Internet über http://dnb.d-nb.deiabrufbar.
1. Aufl. - Göttingen: Cuvillier, 2012
Zugl.: Köln, Univ., Diss., 2011

978-3-95404-012-4

Cover photo: infrared optical parametric oscillator generating small amounts of visible red light

Berichterstatter:	Professor Dr. Stephan Schlemmer
(Gutachter)	Privatdozent Dr. Joachim Hemberger
	Professor Dr. Friedrich Huisken

Tag der mündlichen Prüfung: 08.11.2011

© CUVILLIER VERLAG, Göttingen 2012
Nonnenstieg 8, 37075 Göttingen
Telefon: 0551-54724-0
Telefax: 0551-54724-21
www.cuvillier.de

Alle Rechte vorbehalten. Ohne ausdrückliche Genehmigung des Verlages ist es nicht gestattet, das Buch oder Teile daraus auf fotomechanischem Weg (Fotokopie, Mikrokopie) zu vervielfältigen.
1. Auflage, 2012
Gedruckt auf säurefreiem Papier

978-3-95404-012-4

Dieses Werk ist copyrightgeschützt und darf in keiner Form vervielfältigt werden noch an Dritte weitergegeben werden.
Es gilt nur für den persönlichen Gebrauch.

"In the beginning the Universe was created. This has made a lot of people very angry and has been widely regarded as a bad move."

Douglas Adams, "The Restaurant at the End of the Universe"

Для Лены, Сашки и Анюты

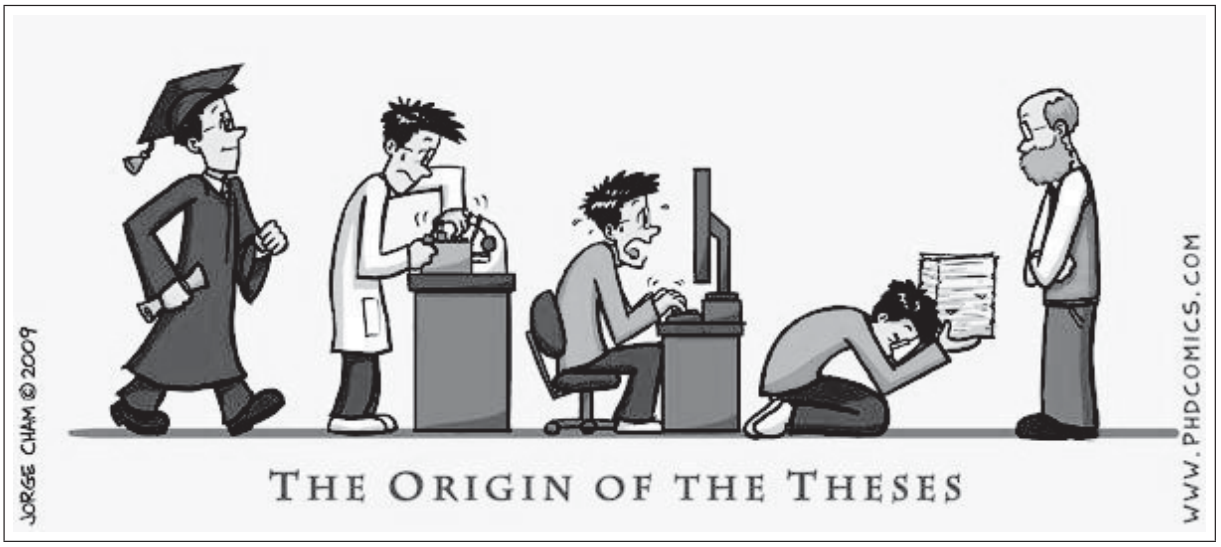

"Piled Higher And Deeper" by Jorge Cham, printed with permission

Dieses Werk ist copyrightgeschützt und darf in keiner Form vervielfältigt werden noch an Dritte weitergegeben werden.
Es gilt nur für den persönlichen Gebrauch.

Dieses Werk ist copyrightgeschützt und darf in keiner Form vervielfältigt werden noch an Dritte weitergegeben werden.
Es gilt nur für den persönlichen Gebrauch.

Abstract

The infrared spectral region between wavelengths of 2 and 6 μm is of great importance in molecular physics. Molecules with an X-H bond (X being carbon, nitrogen or oxygen) exhibit strong vibrational transitions there, but also linear carbon clusters C_n ($n = 2, 3, \ldots$). Many combination bands and overtones of low-energy vibrational modes also occur in this spectral range. Analyses of these spectral features allow – if highly resolved – for example the prediction of pure rotational transitions in the sub-mm wavelength regime, or help understanding the internal dynamics of the molecule.

To provide radiation sources with extremely large frequency coverage, two optical parametric oscillator (OPO) systems in the wavelength regions from 2.5 to 4.1 μm and from 4.7 to 5.4 μm have been set up and characterized in this thesis. The OPO system around 5 μm wavelength is the only one in this spectral region used in high-resolution spectroscopy up to now. Both of the OPO systems have been shown to be ideal tools for spectroscopic studies delivering highly accurate transition frequencies of transient molecules, using the following example cases:

The rovibrational spectrum of the fundamental cation CH_2D^+ around 3.2 μm wavelength has been measured with unprecedented spectral resolution and frequency accuracy. The combination of the OPO as radiation source with a cold ion trap to produce and store the ions has been proven to have a high predictive power for pure rotational transition frequencies of CH_2D^+. Located at around 100 to 200 GHz, these are of great importance in astrophysics.

The ν_3 fundamental vibration of Si_2C_3 around 5.1 μm wavelength has been measured using the OPO and a newly built jet spectrometer for the production of transient molecules. Molecular parameters have been determined with high precision. An associated hot band originating from the ν_7 vibrational bending mode has been resolved and analyzed for the first time.

The pure carbon clusters C_3 and C_7 have also been examined. For the first time, a combination band of C_3 and an associated hot band were detected around 3.0 μm wavelength in the gas phase. Their analyses yield valuable information about the potential energy surface of C_3. Analysis of the ν_5 mode of C_7 delivered further proof of its rigidity, which was put into question by earlier works. Last but not least, a previously unknown associated hot band of C_7 has been detected and analyzed.

Dieses Werk ist copyrightgeschützt und darf in keiner Form vervielfältigt werden noch an Dritte weitergegeben werden.
Es gilt nur für den persönlichen Gebrauch.

Dieses Werk ist copyrightgeschützt und darf in keiner Form vervielfältigt werden noch an Dritte weitergegeben werden.
Es gilt nur für den persönlichen Gebrauch.

Kurzzusammenfassung

Der infrarote Spektralbereich mit Wellenlängen zwischen 2 und 6 μm ist von sehr großer Bedeutung in der Molekülphysik, weil dort Rotations-Vibrationsübergänge vieler Moleküle stattfinden, z.B. die Streckschwingungen der funktionellen Gruppen C-H, O-H und N-H, und Schwingungen der C-C Bindung von linearen Kohlenstoffketten. Auch viele höher angeregte Schwingungen, sogenannte Obertöne oder Kombinationsbanden von Schwingungen niedriger Energie, liegen in diesem Bereich. Die Analyse solch hochauflösender Spektren erlaubt z.B. die Vorhersage reiner Rotationsübergänge und kann zum Verständnis der internen Moleküldynamik beitragen.

Um extrem große Frequenzabdeckungen zu erreichen, wurden in dieser Arbeit zwei optisch-parametrische Oszillatoren (OPO) in den Wellenlängenbereichen von 2,5 bis 4,1 μm und von 4,7 bis 5,4 μm aufgebaut und charakterisiert. Der OPO im Bereich um 5 μm ist bisher der einzige, der für hochauflösende Spektroskopie verwendet wird. Es konnte gezeigt werden, dass beide OPO Systeme ideale Werkzeuge für die Spektroskopie sind, indem Messungen an folgenden kurzlebigen Moleküle vorgenommen wurden:

Das Rotations-Vibrations-Spektrum des fundamentalen Kations CH_2D^+ im Bereich um 3,2 μm Wellenlänge wurde mit bisher unerreichter Genauigkeit und Auflösung gemessen. Die Kombination aus OPO als Strahlungsquelle und einer kalten Ionenfalle zur Erzeugung und Speicherung der Ionen hat hochgenaue Vorhersagen von reinen Rotationsübergängen ermöglicht, welche in der Astrophysik von enormer Bedeutung sind.

Um die antisymmetrische Streckschwingung ν_3 des Cluster-Moleküls Si_2C_3 zu untersuchen, wurde ein neu aufgebautes Infrarotspektrometer in Kombination mit dem OPO im Wellenlängenbereich um 5,1 μm benutzt. Es konnte zum ersten Mal eine sogenannte heiße Bande von Si_2C_3 mit hoher Genauigkeit nachgewiesen und analysiert werden.

Bei Untersuchungen von C_3 bei Wellenlängen um 3,1 μm konnten zwei Schwingungsbanden zum ersten Mal in der Gasphase hochgenau gemessen werden. Die Kombinationsbande aus zwei Streckschwingungen und die zugehörige sogenannte heiße Bande aus der angeregten Biegeschwingung heraus wurden vermessen und analysiert. Die Messungen haben wertvolle Informationen über das Potential und die interne Dynamik des C_3-Moleküls geliefert.

Die Untersuchung der ν_5-Bande von C_7 lieferte weitere Beweise für die Starrheit des Moleküls, welche in früheren Arbeiten angezweifelt wurde. Eine zugehörige heiße Bande wurde nachgewiesen und analysiert.

Dieses Werk ist copyrightgeschützt und darf in keiner Form vervielfältigt werden noch an Dritte weitergegeben werden.
Es gilt nur für den persönlichen Gebrauch.

Dieses Werk ist copyrightgeschützt und darf in keiner Form vervielfältigt werden noch an Dritte weitergegeben werden.
Es gilt nur für den persönlichen Gebrauch.

Zusammenfassung

Der infrarote Spektralbereich mit Wellenlängen zwischen 2 und 6 μm ist von sehr großer Bedeutung in der Molekülphysik, weil dort Rotations-Vibrationsübergänge vieler Moleküle stattfinden, z.B. die Streckschwingungen der funktionellen Gruppen C-H, O-H und N-H, und Schwingungen der C-C Bindung von linearen Kohlenstoffketten. Auch viele höher angeregte Schwingungen, sogenannte Obertöne oder Kombinationsbanden von Schwingungen niedriger Energie, liegen in diesem Bereich.

Die Analyse dieser Übergänge mit hoher spektraler Auflösung ermöglicht den Gewinn einer Vielzahl an Informationen über das jeweilige Molekül, die sich zu einer Modellbeschreibung der Spezies nutzen lassen. Mit diesen an Messungen angepassten Modellen lassen sich bisher nicht gemessene Übergänge in anderen Frequenzbereichen vorhersagen. Auch das Potential und damit die interne Dynamik von Molekülen kann mit solchen Messungen verstanden werden. Eine Voraussetzung für die Durchführung genauer spektroskopischer Untersuchungen ist jedoch die Verfügbarkeit von Strahlungsquellen mit geringer Linienbreite und breiter Abstimmbarkeit.

Laserquellen, die in der Spektroskopie von Molekülen wichtige und verbreitete Werkzeuge sind, decken jeweils nur einen Bruchteil des gewünschten Spektrums ab. Ein optisch parametrischer Oszillator (OPO) nutzt nichtlineare optische Effekte zur Frequenzkonversion von Laserstrahlung mit dem Resultat einer extrem breiten Frequenzabdeckung. Kapitel 1 beschäftigt sich mit den Grundlagen von OPOs, die für das weitere Verständnis wichtig sind.

Im nahen Infrarotbereich zwischen 1 und 4 μm Wellenlänge haben OPOs in wissenschaftlichen Laboren bereits eine gewisse Verbreitung gefunden (siehe z.B. [30, 86, 116]). Bei diesen Wellenlängen gibt es kommerziell erhältliche Kristalle aus Lithiumniobat, $LiNbO_3$, mit denen die Frequenzkonversion einfach umgesetzt werden kann. Bei Wellenlängen größer als 4,5 μm setzt starke Absorption in $LiNbO_3$ ein und begrenzt die Konversion erheblich. In diesem langwelligen Bereich gab es deshalb bisher keine OPOs, die für hochauflösende Spektroskopie geeignet waren.

Im Rahmen dieser Arbeit wurden zwei OPO-Systeme in den Wellenlängenbereichen von 2,5 bis 4,1 μm (im folgenden System 1 genannt) und von 4,7 bis 5,4 μm (System 2) für die hochauflösende Spektroskopie aufgebaut und charakterisiert. Beide Systeme basieren auf $LiNbO_3$-Kristallen, weshalb das System 2 im Bereich um 5 μm Wellenlänge wegen der o.g. Absorption deutlich niedrigere Ausgangsleistungen als System 1 erreicht. Es

Dieses Werk ist copyrightgeschützt und darf in keiner Form vervielfältigt werden noch an Dritte weitergegeben werden.
Es gilt nur für den persönlichen Gebrauch.

konnte jedoch gezeigt werden, dass die Leistung für die üblichen Methoden der Spektroskopie mehr als ausreicht. In Kapitel 2 wird im Detail auf die unterschiedlichen Anforderungen an den Aufbau und auf die Eigenschaften der OPO-Systeme eingegangen. Mit den aufgebauten OPO Systemen wurden astrophysikalisch relevante kurzlebige Moleküle untersucht, was im folgenden kurz dargestellt wird.

Das OPO System 1 im Bereich um 3 μm Wellenlänge wurde benutzt, um Rotation-Vibrationsübergänge des Kations CH_2D^+ mit hoher Genauigkeit zu vermessen. Dazu wurde die Reaktion von kalten CH_2D^+-Ionen mit H_2 Molekülen in einer Multipol-Ionenfalle untersucht. Die Reaktion zu CH_3^+ ist endotherm und die Energiedifferenz für die gekühlten Ionen zu gross, um die Reaktion ablaufen zu lassen. Daher findet die Reaktion nur bei solchen Frequenzen des einstrahlenden OPOs statt, die eine resonante Anregung des Moleküls bewirken. Aus dem mit dieser Methode vermessenen Spektrum resultieren Vorhersagen reiner Rotationsübergänge von CH_2D^+ im sub-mm Bereich mit bisher unerreichter Genauigkeit. Dies ist für astrophysikalische Anwendungen interessant, weil CH_2D^+ eine interessante Rolle bei der Messung der Isotopenanreicherung (H/D) im All spielt. Kapitel 3 erläutert die hier gemachten Untersuchungen zu CH_2D^+.

Der zweite große Schwerpunkt dieser Arbeit sind lineare Kohlenstoff- und Kohlenstoff-Silizium-Cluster, von denen C_3, C_7 und Si_2C_3 genau untersucht worden sind. Diese Moleküle sind von großem Interesse in der Astrophysik, aber auch in der theoretischen Strukturchemie. Lineare Strukturen mit Kohlenstoffketten als Gerüst besitzen ihre starken fundamentalen Streckschwingungen im Bereich um 5 μm Wellenlänge. In diesem Bereich konnte im Laufe der Arbeit erstmalig ein breitbandiger OPO (System 2 um 5 μm Wellenlänge) für hochauflösende Spektroskopie eingesetzt werden. Für diesen Zweck wurde ein neues Infrarot-Spektrometer zur Erzeugung dieser kurzlebigen Moleküle aufgebaut, dessen Prinzip aus anderen Experimenten (siehe z.B. [75]) bekannt ist. Wesentliche Verbesserungen im Vergleich zu ähnlichen Spektrometern konnten bei der Frequenzgenauigkeit und bei der Datenaufnahme erzielt werden.

Um das neue Cluster-Spektrometer zu charakterisieren, wurde der Silizium-Kohlenstoffcluster Si_2C_3 im Bereich um 5,1 μm Wellenlänge untersucht. Si_2C_3 ist bisher das einzige lineare, symmetrische Clustermolekül vom Typ SiC_nSi (n=2,3,4,...), das in hoher spektraler Auflösung untersucht wurde [117]. Die hier vorgestellte Messung der stärksten antisymmetrischen Streckschwingungsbande von Si_2C_3 zeigt die Stärken des neuen Experiments. Neben der kompletten Frequenzabdeckung des OPOs über die Bande hinweg, die mit Infrarot-Diodenlasern wie in der Originalarbeit [117] nicht möglich war, erwies sich auch eine höhere Empfindlichkeit des neuen Spektrometers

Dieses Werk ist copyrightgeschützt und darf in keiner Form vervielfältigt werden noch an Dritte weitergegeben werden.
Es gilt nur für den persönlichen Gebrauch.

als großer Fortschritt. Es konnte zum ersten Mal eine sogenannte heiße Bande von Si_2C_3 nachgewiesen und analysiert werden. Dabei vollzieht das Molekül einen Schwingungsübergang von einer bereits angeregten Biegeschwingung in eine Schwingungskombination. Die Messungen und die Analyse sind detailliert in Kapitel 4 beschrieben.

Der Kohlenstoffcluster C_3 spielt eine wichtige Rolle in der Astrophysik [71], ist aber aufgrund seiner komplexen internen Dynamik auch von fundamentalem Interesse für den theoretischen Chemiker [122]. Bei Untersuchungen dieses Kohlenstoffclusters bei Wellenlängen um 3,1 μm konnten zwei Schwingungsbanden zum ersten Mal in der Gasphase hochgenau gemessen werden. Die Kombinationsbande aus der symmetrischen Streckschwingung und der antisymmetrischen Streckschwingung und die zugehörige sogenannte heiße Bande aus der angeregten Biegeschwingung heraus wurden vermessen und analysiert. Die Messungen geben wertvolle Informationen über das Potential und die interne Dynamik des C_3-Moleküls und finden sich in Abschnitt 5.2 von Kapitel 5.

Über den Kohlenstoffcluster C_7 gab es in der Vergangenheit eine Diskussion bezüglich seines Potentials. Messungen von zwei antisymmetrischen Streckschwingungen und von zugehörigen heißen Banden ließen den Schluss zu, das Molekül habe ein sehr flaches Potential für die Biegeschwingung [38, 40]. Spätere quantenchemische Rechnungen standen im Widerspruch zu diesem Ergebnis [14]. Eine zweite experimentelle Arbeit an einer antisymmetrischen Streckschwingung mit zugehörigen heißen Banden ergab dann eine Stützung der quantenchemischen Rechnungen [76]. Im Rahmen der vorliegenden Arbeit wurde die zweite antisymmetrische Streckschwingung im Wellenlängenbereich um 5,2 μm unter Verwendung eines neuartigen Quantenkaskaden-Lasersystems untersucht und ebenfalls eine gute Übereinstimmung mit den Berechnungen [14] gefunden. Zum ersten Mal konnte eine heiße Bande zu dieser schwächeren Streckschwingung nachgewiesen und analysiert werden. Dieser Teil der Arbeit findet sich in Abschnitt 5.3 von Kapitel 5 wieder.

Im Zuge dieser Arbeit ist es gelungen, eine neue Technologie breitbandiger Infrarot-Strahlungsquellen mit teilweise vorhandenen und teilweise neu aufgebauten Spektrometern zu verbinden. Die Spektrometer sind bei der Frequenzgenauigkeit und der Datenaufnahme signifikant verbessert worden. Die nun vorhandene große Frequenzabdeckung ermöglicht es — wie die Beispiele der hier untersuchten Spezies CH_2D^+, Si_2C_3, C_3 und C_7 eindrucksvoll zeigen — eine Vielzahl an unterschiedlichen kurzlebigen Molekülen im Infraroten hochpräzise und empfindlich zu vermessen.

Dieses Werk ist copyrightgeschützt und darf in keiner Form vervielfältigt werden noch an Dritte weitergegeben werden.
Es gilt nur für den persönlichen Gebrauch.

Dieses Werk ist copyrightgeschützt und darf in keiner Form vervielfältigt werden noch an Dritte weitergegeben werden.
Es gilt nur für den persönlichen Gebrauch.

Contents

Abstract **i**

Kurzzusammenfassung **iii**

Zusammenfassung **v**

1 Fundamentals of Optical Parametric Oscillators **1**
1.1 The Nonlinear Optical Susceptibility 2
1.2 Electromagnetic Waves in Optically Nonlinear Media 3
1.2.1 Coupled Wave Equations 4
1.3 Optical Parametric Amplification 5
1.3.1 Coupled Wave Equations for Parametric Processes 5
1.3.2 Solution of the Coupled Wave Equations 6
1.3.3 Parametric Gain 8
1.4 Optical Parametric Oscillation 10
1.4.1 Threshold 10
1.4.2 Oscillation Conditions 12
1.4.3 Steady-State Efficiency and Idler Power 16
1.5 Phase Matching 18
1.5.1 Quasi Phase Matching 18
1.5.2 Parametric Bandwidth 23
1.6 Summary of OPO Fundamentals 25

2 Setup and Characterization of Optical Parametric Oscillators **27**
2.1 Experimental Setup of OPOs 27
2.1.1 Pump Laser 28
2.1.2 Nonlinear Crystals and Crystal Oven 29
2.1.3 Signal Cavity 30

Dieses Werk ist copyrightgeschützt und darf in keiner Form vervielfältigt werden noch an Dritte weitergegeben werden.
Es gilt nur für den persönlichen Gebrauch.

2.1.4 System Setup 36
2.2 OPO Performances 42
2.2.1 Idler Coverage and Tuning 43
2.2.2 Threshold 46
2.2.3 Idler Power 48
2.2.4 Linewidth and Frequency Stability 51
2.2.5 Beam Profile 53
2.3 Outlook 54

3 Action Spectroscopy of CH_2D^+ using Laser Induced Reactions 57
3.1 Introduction 57
3.2 Laser Induced Reactions of CH_2D^+ 59
3.3 Experimental Setup 60
3.3.1 22-pole ion trap 60
3.3.2 CW OPO 61
3.3.3 Calibration procedure 61
3.4 Measurement and Analysis 62
3.5 Conclusion and Outlook 66

4 Rovibrational Spectroscopy of the Silicon-Carbon Cluster Si_2C_3 69
4.1 Introduction 69
4.2 Spectrometer for transient molecules 71
4.2.1 CW OPO and Frequency Calibration 71
4.2.2 Production of Species 73
4.2.3 Detection Technique 73
4.3 Measurement and Analysis: Si_2C_3 75
4.3.1 The ν_3 fundamental band 75
4.3.2 The $\nu_3 + \nu_7 - \nu_7$ hot band 79
4.4 Conclusion and Outlook 84

5 High-Resolution Spectroscopy of Small Carbon Clusters 87
5.1 Introduction 88
5.2 Experiments on linear C_3 88
5.2.1 Experimental Setup 90
5.2.2 Measurements and Results: C_3 90
5.2.3 Conclusion and Outlook 96
5.3 Experiments on linear C_7 98
5.3.1 Spectrometer Setup 99
5.3.2 Measurements and Results: C_7 100
5.3.3 Conclusion and Outlook 108

Dieses Werk ist copyrightgeschützt und darf in keiner Form vervielfältigt werden noch an Dritte weitergegeben werden.
Es gilt nur für den persönlichen Gebrauch.

A Rovibrational transitions of CH_2D^+ **111**

B Temperature Controller Electronics **115**

Bibliography **117**

Acknowledgement **131**

Dieses Werk ist copyrightgeschützt und darf in keiner Form vervielfältigt werden noch an Dritte weitergegeben werden.
Es gilt nur für den persönlichen Gebrauch.

Dieses Werk ist copyrightgeschützt und darf in keiner Form vervielfältigt werden noch an Dritte weitergegeben werden.
Es gilt nur für den persönlichen Gebrauch.

List of Tables

1.1 Sellmeier coefficients for Lithium Niobate 22

2.1 Specifications of the OPO pump laser 29
2.2 specifications of the PPLN crystals 31
2.3 Specifications of the OPO resonator mirrors 32

3.1 Comparison of ground-state combination differences of CH_2D^+ . 63
3.2 Molecular parameters of CH_2D^+ 66
3.3 Predicted and observed pure rotational transitions of CH_2D^+ . . . 68

4.1 Molecular parameters for Si_2C_3 78
4.2 Line positions of the ν_3 fundamental band of Si_2C_3 78
4.3 Line positions of the $\nu_3 + \nu_7 - \nu_7$ hot band of Si_2C_3 83
4.4 Molecular parameters for Si_2C_3 hot band 84

5.1 Line positions of the (101)←(000) combination band of C_3 . . . 92
5.2 Line positions of the (11^11)←(01^10) hot band of C_3 94
5.3 Molecular parameters of C_3 96
5.4 Measured transition frequencies of the ν_5 fundamental of C_7 . . . 103
5.5 Molecular parameters for the ground, ν_4 and ν_5 states of C_7 . . . 104
5.6 Measured transitions of the $\nu_5 + \nu_{11} - \nu_{11}$ hot band of C_7 105
5.7 Molecular parameters for the ν_{11}, $\nu_4 + \nu_{11}$ and $\nu_5 + \nu_{11}$ states of C_7 107

A.1 Transition frequencies of the ν_1 band of CH_2D^+ 111
A.2 Transition frequencies of the ν_4 band of CH_2D^+ 112

Dieses Werk ist copyrightgeschützt und darf in keiner Form vervielfältigt werden noch an Dritte weitergegeben werden.
Es gilt nur für den persönlichen Gebrauch.

Dieses Werk ist copyrightgeschützt und darf in keiner Form vervielfältigt werden noch an Dritte weitergegeben werden.
Es gilt nur für den persönlichen Gebrauch.

List of Figures

1.1 Signal gain curves for different idler absorptions 9
1.2 Signal gain dependency on crystal length 10
1.3 Influence of idler absorption on the signal gain 11
1.4 Influence of signal absorption on the signal gain 12
1.5 OPO rise time simulation 14
1.6 OPO rise time simulation including absorption 15
1.7 Quantum efficiency of a steady state OPO 17
1.8 Idler powers of a steady state OPO 18
1.9 Index of refraction in Lithium Niobate 19
1.10 Spatial modulation of the nonlinear coefficient 20
1.11 Periodically Poled Lithium Niobate crystal 20
1.12 Quasi phase matching 21
1.13 Temperature tuning curve example of PPLN 23
1.14 Gain curves for different idler wavelengths 24
1.15 Bandwidth of the Parametric Process 24

2.1 Pump laser tuning curve 28
2.2 OPO cavity mirror transmission graph 32
2.3 Labeling of the OPO cavity parameters 33
2.4 Signal waist size in the crystal, dependent on cavity geometry . . 35
2.5 Signal beam radius along the cavity 36
2.6 Schematic setup of the OPO system 1 38
2.7 Photo of running OPO system 1 39
2.8 Absorption in $LiNbO_3$ 41
2.9 Photo of OPO system 2 41
2.10 Schematic setup of OPO system 2 42
2.11 Frequency coverage of OPO system 1 43
2.12 Frequency coverage of OPO system 2 44

Dieses Werk ist copyrightgeschützt und darf in keiner Form vervielfältigt werden noch an Dritte weitergegeben werden.
Es gilt nur für den persönlichen Gebrauch.

2.13 Cavity round-trip loss of signal radiation due to water vapor . . . 45
2.14 Slow frequency scan 46
2.15 Threshold of the OPO system 1 47
2.16 Zoom of the OPO cavity mirror transmission 47
2.17 Threshold of the OPO system 2 48
2.18 Idler Power as function of Pump Power 49
2.19 Idler Power as function of wavelength for OPO 1 50
2.20 Idler Power as function of wavelength for OPO 2 50
2.21 OPO linewidth estimation 51
2.22 Beam profile of the OPO signal beam 53
2.23 Difference-Frequency Coverage between idler and signal 55

3.1 Graphical representation of the CH_3^+ molecule 58
3.2 LIR principle 59
3.3 LIRTRAP scheme 60
3.4 OPO setup for measuring CH_2D^+ 62
3.5 Sample LIR Frequency Scan of CH_2D^+ 63
3.6 Residuals of the fit for CH_2D^+ 67

4.1 Silicon containing molecules detected in space 70
4.2 Graphical representation of the Si_2C_3 molecule 71
4.3 Schematic Setup of the OPO - Jet Spectrometer 72
4.4 Timing in the Supersonic Jet Expansion 74
4.5 Spectrum of the ν_3 stretching vibration of Si_2C_3 76
4.6 Spectrum of the $\nu_3 + \nu_7 - \nu_7$ hot band of Si_2C_3 80

5.1 Graphical Representation of the C_3 molecule 88
5.2 Bending Potential of Carbon Clusters 89
5.3 Overview spectrum of the measured combination band of C_3 . . . 91
5.4 Q-branch of the $(11^11)\leftarrow(01^10)$ hot band of C_3 95
5.5 Graphical representation of the C_7molecule 98
5.6 $R(24)$ transition of the ν_5 band of C_7 100
5.7 Etalon fringes of an internally coupled Fabry-Pérot Interferometer 101
5.8 The ν_5 fundamental band of linear C_7 at 1898.4cm^{-1} 102
5.9 Schematic energy level diagram for vibrational states of C_7 106
5.10 Selected hotband transitions of C_7 at 1897 cm^{-1} 107

B.1 Output Stage of Temperature Controller 115
B.2 Temperature Controlling Electronics 116

Dieses Werk ist copyrightgeschützt und darf in keiner Form vervielfältigt werden noch an Dritte weitergegeben werden.
Es gilt nur für den persönlichen Gebrauch.

1

Fundamentals of Optical Parametric Oscillators

"Reality is frequently inaccurate."
Douglas Adams, "The Restaurant at the End of the Universe"

An Optical Parametric Oscillator (OPO) transfers energy of an intense electromagnetic wave called the pump wave at frequency ν_p to two other waves of different frequency. These are called the signal (frequency ν_s) and idler wave (frequency ν_i). This effect opens up new spectral regimes for coherent radiation where it is difficult to provide suitable lasers. In the scope of this work, optical parametric oscillators have been built for spectroscopic applications. A simple theoretical treatment necessary to understand the effects will be given in this chapter*.

The interaction of waves is a consequence of the nonlinear response of the polarization to the electric field, which will be introduced in the first section. The following sections describe the propagation of electromagnetic waves in a nonlinear medium. The effect of parametric amplification is presented quantitatively with the help of the so-called coupled wave equations. A section about optical parametric oscillation is followed by considerations about matching the phase velocities of the relevant waves, which is important to achieve efficient frequency conversion. The derivation of the cou-

*Parts of this chapter have been published in:

- A continuous-wave optical parametric oscillator around 5 μm wavelength for high-resolution spectroscopy. J. Krieg, A. Klemann, I. Gottbehüt, S. Thorwirth, T. F. Giesen, S. Schlemmer, *Review of Scientific Instruments* **82** 063195 (2011)

Dieses Werk ist copyrightgeschützt und darf in keiner Form vervielfältigt werden noch an Dritte weitergegeben werden.
Es gilt nur für den persönlichen Gebrauch.

pled wave equations mainly follows Ref. [66], and solutions to those can be found with different ansatzes in Refs. [66, 100]. When absorption can be neglected, a comprehensive theoretical introduction to OPOs can also be found in Ref. [16].

1.1 The Nonlinear Optical Susceptibility

The superposition principle of electromagnetic waves is an implication of the linearity of Maxwell's equations. As a result, waves of different frequency interfere and do not interact with each other. If the waves travel in a dielectric medium, the polarization of the medium has to be taken into account. Usually, the relation between the polarization $\mathbf{P}$ and the electric field $\mathbf{E}$ is also linear:

$$P_i = \varepsilon_0 \sum_j \chi_{ij} E_j$$

with the electric susceptibility χ, which is a tensor of rank 2. In this context, Maxwell's equations are still linear and electric fields just superimpose and energy transfer between different waves is impossible.

The linear relation for the polarization does not hold in the case of strong electric fields, as for example in a focused laser beam. Then the polarization of the medium deviates from the linear expression above and has to be expanded in terms of the electric field:

$$P_i = \varepsilon_0 \left(\sum_j \chi_{ij}^{(1)} E_j + \sum_j \sum_k \chi_{ijk}^{(2)} E_j E_k + \mathcal{O}(\mathbf{E}^3) \right) , \tag{1.1}$$

where $\chi^{(2)}$ is a tensor of rank 3 and is referred to as the second-order susceptibility. The quadratic terms in the above expression including $\chi^{(2)}$ explain all nonlinear optical effects relevant for this work. Because of the nonlinearity of the polarization, waves of different frequency can now interact with each other.

$\chi^{(2)}$ as a tensor of rank 3 should have 27 elements, but symmetry considerations (see, e.g. Ref. [66, 104]) lead to a reduction of the elements. Often the tensor $d_{ijk} = \frac{1}{2}\chi_{ijk}$ is given instead of χ_{ijk} and can be written in a reduced notation, where the last two indices (j, k) form a new index l. d_{il} is in this notation a 3×6 matrix with the translation

l :	1	2	3	4	5	6
jk :	11	22	33	23, 32	31, 13	12, 21

The quantity of independent elements can be further reduced in a given material depending on its symmetry. For example, the crystal used in the scope

Dieses Werk ist copyrightgeschützt und darf in keiner Form vervielfältigt werden noch an Dritte weitergegeben werden.
Es gilt nur für den persönlichen Gebrauch.

of this work is Lithium-Niobate ($LiNbO_3$), and its nonlinear susceptibility in reduced notation is

$$d = \begin{pmatrix} 0 & 0 & 0 & 0 & -4.6 & -2.6 \\ -2.6 & 2.6 & 0 & -4.6 & 0 & 0 \\ -4.6 & -4.6 & -25.0 & 0 & 0 & 0 \end{pmatrix} \cdot 10^{-12}\ \frac{\mathrm{m}}{\mathrm{V}} \tag{1.2}$$

and has only three independent elements, of which d_{33} is the largest.

1.2 Electromagnetic Waves in Optically Nonlinear Media

In a nonlinear dielectric, where there are no free charges ($\rho = 0$), no electric current ($\mathbf{j} = 0$) and no magnetization ($\mathbf{M} = 0$), Maxwell's equations in matter take the form

$$\nabla \times \mathbf{E} = -\frac{\partial \mathbf{B}}{\partial t} \qquad \nabla \cdot \mathbf{D} = 0 \tag{1.3}$$

$$\nabla \times \mathbf{B} = \mu_0 \frac{\partial \mathbf{D}}{\partial t} \qquad \nabla \cdot \mathbf{B} = 0. \tag{1.4}$$

Here, $\mathbf{B}$ is the magnetic induction, and $\mathbf{D}$ is the electric displacement which can be related to $\mathbf{E}$:

$$\mathbf{D} = \varepsilon\varepsilon_0 \mathbf{E} = \varepsilon_0 \mathbf{E} + \mathbf{P}.$$

When we apply the operator $(\nabla\times)$ to the first of Maxwell's equations and substitute the third equation in there, we obtain

$$\begin{aligned} \nabla \times \nabla \times \mathbf{E} &= -\nabla \times \frac{\partial \mathbf{B}}{\partial t} \\ &= -\frac{\partial}{\partial t}(\nabla \times \mathbf{B}) \\ &= -\mu_0 \frac{\partial^2}{\partial t^2}\mathbf{D} \\ &= -\varepsilon_0\mu_0 \frac{\partial^2}{\partial t^2}\mathbf{E} - \mu_0 \frac{\partial^2}{\partial t^2}\mathbf{P}. \end{aligned}$$

The vector calculus identity $\nabla \times \nabla \times \mathbf{E} = \nabla(\nabla \cdot \mathbf{E}) - \nabla^2 \mathbf{E}$ can be simplified by arguing that $\nabla(\nabla \cdot \mathbf{E})$ vanishes in the case of plane waves (Ref. [66]), which is why we find

$$\left(\nabla^2 - \frac{1}{c^2}\frac{\partial^2}{\partial t^2}\right)\mathbf{E} = \frac{1}{\varepsilon_0 c^2}\frac{\partial^2}{\partial t^2}\mathbf{P}.$$

Dieses Werk ist copyrightgeschützt und darf in keiner Form vervielfältigt werden noch an Dritte weitergegeben werden.
Es gilt nur für den persönlichen Gebrauch.

The linear term of the polarization can be split off using $\mathbf{P} = \mathbf{P}^{(1)} + \mathbf{P}^{(\mathrm{NL})} = \varepsilon_0(n^2-1)\mathbf{E} + \mathbf{P}^{(\mathrm{NL})}$, where $\mathbf{P}^{(\mathrm{NL})}$ is the nonlinear part of the polarization. It results in the wave equation in a nonlinear dielectric:

$$\left(\nabla^2 - \frac{n^2}{c^2}\frac{\partial^2}{\partial t^2}\right)\mathbf{E} = \frac{1}{\varepsilon_0 c^2}\frac{\partial^2}{\partial t^2}\mathbf{P}^{(\mathrm{NL})}.$$

This equation forms the basis to describe nonlinear optical effects. Wave equations for different frequency components couple through the nonlinear polarization, which can be seen in the next section. The electric field can be written as a superposition of plane waves with a frequency ω_l and a wave-vector $\mathbf{k}$.

$$\mathbf{E}(\mathbf{r},t) = \frac{1}{2}\sum_l \left[\boldsymbol{\mathcal{E}}_l(\mathbf{r})e^{-i(\omega_l t - \mathbf{k_l r})} + c.c.\right]. \tag{1.5}$$

c.c. means the complex conjugate. Analogously, the polarization is expressed using the same frequency components:

$$\mathbf{P}^{(\mathrm{NL})} = \frac{1}{2}\sum_l \left[\boldsymbol{\mathcal{P}}(\omega_l,\mathbf{r})e^{-i\omega_l t} + c.c.\right]. \tag{1.6}$$

In this context, the wave equation takes the form

$$\left(\nabla^2 + \frac{n_l^2\omega_l^2}{c^2}\right)\boldsymbol{\mathcal{E}}_l(\mathbf{r})e^{i\mathbf{k_l r}} = -\frac{\omega_l^2}{\varepsilon_0 c^2}\boldsymbol{\mathcal{P}}(\omega_l,\mathbf{r}). \tag{1.7}$$

1.2.1 Coupled Wave Equations

We assume plane waves traveling in forward z-direction and the electric field oscillating in x-direction, which gives $\mathbf{k_l} = k_l\hat{\mathbf{e}}_z$ and $\boldsymbol{\mathcal{E}}_l(\mathbf{r}) = \mathcal{E}_l(z)\hat{\mathbf{e}}_x$:

$$\nabla^2\boldsymbol{\mathcal{E}}_l(\mathbf{r})e^{i\mathbf{k_l r}} = \hat{\mathbf{e}}_x\frac{\partial^2}{\partial z^2}\left[\mathcal{E}_l(z)e^{ik_l z}\right] \tag{1.8}$$

$$= \hat{\mathbf{e}}_x e^{ik_l z}\left[\underbrace{\frac{\partial^2}{\partial z^2}\mathcal{E}_l(z)}_{\approx 0} + 2ik_l\frac{\partial}{\partial z}\mathcal{E}_l(z) - k_l^2\mathcal{E}_l(z)\right]. \tag{1.9}$$

In the last equation, the term $\frac{\partial^2}{\partial z^2}\mathcal{E}_l(z)$ is neglected, because the amplitude is supposed to vary slowly with distance z. With $k_l^2 = n_l^2\omega_l^2/c^2$, the x-component of equation (1.7) reduces to

$$\frac{\partial}{\partial z}\mathcal{E}_l(z) = i\frac{\omega_l}{2\varepsilon_0 n_l c}\mathcal{P}_x(\omega_l,z)e^{-ik_l z}. \tag{1.10}$$

This equation has to be solved for every frequency component ω_l of the electric field relevant in the given nonlinear process.

Dieses Werk ist copyrightgeschützt und darf in keiner Form vervielfältigt werden noch an Dritte weitergegeben werden.
Es gilt nur für den persönlichen Gebrauch.

1.3 Optical Parametric Amplification

The effect of optical parametric amplification (OPA) describes the enhancement of an optical wave at frequency ν_s ("signal") at the cost of the attenuation of an intense wave called "pump" at frequency $\nu_p > \nu_s$. For reasons of energy conservation, a third wave is generated at frequency ν_i, so that the following condition is fulfilled:

$$\nu_p = \nu_s + \nu_i. \tag{1.11}$$

In this process, the electric field can be expressed using three frequency components. Assuming plane waves which are all linearly polarized in x-direction and traveling in $+z$-direction ($\mathbf{k_l} = k_l \hat{\mathbf{e}}_z$), we have:

$$\mathbf{E} = \frac{\hat{\mathbf{e}}_x}{2} \left[\mathcal{E}_p e^{-i(\omega_p t - k_p z)} + \mathcal{E}_s e^{-i(\omega_s t - k_s z)} + \mathcal{E}_i e^{-i(\omega_i t - k_i z)} + c.c. \right]. \tag{1.12}$$

The three waves do not necessarily have to have the same polarization axis to couple via the nonlinear polarization, because the tensor $\chi^{(2)}$ is in general not diagonal. However, the assumption of one single polarization direction for all involved waves is more illustrative and also holds for the parametric process used in this work.

In the following sections, the coupled wave equations (1.10) are derived for this explicit case and solved to get a quantitative understanding.

1.3.1 Coupled Wave Equations for Parametric Processes

The x-component of the nonlinear polarization $P_x^{(\mathrm{NL})} = 2\varepsilon_0 d E_x^2$ contains many linear combinations of the frequencies $\omega_p, \omega_s, \omega_i$. Due to interference, only waves which have a fixed phase relationship to their driving polarization build up to a macroscopic scale. This issue will be addressed in section 1.5. Now it is assumed that only the following polarization components are relevant as in a parametric process:

$$\mathcal{P}_x(\omega_p = \omega_s + \omega_i, z) = 2\varepsilon_0 d\, \mathcal{E}_s \mathcal{E}_i \quad e^{(k_i + k_s)z} \tag{1.13}$$

$$\mathcal{P}_x(\omega_s = \omega_p - \omega_i, z) = 2\varepsilon_0 d\, \mathcal{E}_p \mathcal{E}_i^* \quad e^{(k_p - k_i)z} \tag{1.14}$$

$$\mathcal{P}_x(\omega_i = \omega_p - \omega_s, z) = 2\varepsilon_0 d\, \mathcal{E}_p \mathcal{E}_s^* \, e^{(k_p - k_s)z}. \tag{1.15}$$

Dieses Werk ist copyrightgeschützt und darf in keiner Form vervielfältigt werden noch an Dritte weitergegeben werden.
Es gilt nur für den persönlichen Gebrauch.

By substituting these polarizations into equation (1.10), one obtains the coupled wave equations for three-wave-mixing:

$$\frac{\partial}{\partial z}\mathcal{E}_p(z) = i\gamma_p\,\mathcal{E}_s(z)\mathcal{E}_i(z)\,e^{-i\Delta kz} - \frac{\alpha_p}{2}\mathcal{E}_p(z) \tag{1.16}$$

$$\frac{\partial}{\partial z}\mathcal{E}_s(z) = i\gamma_s\,\mathcal{E}_p(z)\mathcal{E}_i^*(z)\,e^{+i\Delta kz} - \frac{\alpha_s}{2}\mathcal{E}_s(z) \tag{1.17}$$

$$\frac{\partial}{\partial z}\mathcal{E}_i(z) = i\gamma_i\,\mathcal{E}_p(z)\mathcal{E}_s^*(z)\,e^{+i\Delta kz} - \frac{\alpha_i}{2}\mathcal{E}_i(z). \tag{1.18}$$

Here, γ_l ($l = p,s,i$) is the nonlinear coupling factor $\gamma_l = (2\pi\nu_l d)/(n_l c)$ and $\Delta k = k_p - k_s - k_i$ is called the phase mismatch of the process. Absorption of the waves in the crystal was added using a term $-\frac{\alpha_l}{2}\mathcal{E}_l$ in the coupled wave equations, because in this work the absorption cannot be neglected. α_l is then the absorption coefficient from the Lambert-Beer law for the intensity of a wave $I_l(z) = I_l(0)e^{-\alpha_l z}$, where I_l can be expressed as $I_l = c\varepsilon_0 n_l|\mathcal{E}_l|^2/2$. The intensity of the plane wave is connected to its power P by the beam area A: $I_l = P_l/A$.

By comparing $\frac{\partial}{\partial z}|\mathcal{E}_l|^2 = \mathcal{E}_l^*\frac{\partial}{\partial z}\mathcal{E}_l + \mathcal{E}_l\frac{\partial}{\partial z}\mathcal{E}_l^*$ of every of the above equation, one obtains the Manley-Rowe relations including correction terms for the absorption in the nonlinear medium:

$$-\frac{1}{\nu_p}\left(\frac{\partial}{\partial z} - \alpha_p\right)I_p = \frac{1}{\nu_s}\left(\frac{\partial}{\partial z} - \alpha_s\right)I_s = \frac{1}{\nu_i}\left(\frac{\partial}{\partial z} - \alpha_i\right)I_i. \tag{1.19}$$

1.3.2 Solution of the Coupled Wave Equations for a Parametric Process

To solve the coupled wave equations including absorption, we assume that the incident pump wave has a constant amplitude over the length of the nonlinear medium: $\mathcal{E}_p(z) = \mathcal{E}_p(0) = \mathcal{E}_p$. This approximation holds when the pump wave is much stronger than the other waves and the absorption of the pump in the crystal can also be neglected. Because of $\frac{\partial}{\partial z}\mathcal{E}_p(z) = 0$, the problem reduces to two coupled equations:

$$\frac{\partial}{\partial z}\mathcal{E}_s(z) = i\gamma_s\,\mathcal{E}_p\mathcal{E}_i^*(z)\,e^{+i\Delta kz} - \frac{\alpha_s}{2}\mathcal{E}_s(z) \tag{1.20}$$

$$\frac{\partial}{\partial z}\mathcal{E}_i(z) = i\gamma_i\,\mathcal{E}_p\mathcal{E}_s^*(z)\,e^{+i\Delta kz} - \frac{\alpha_i}{2}\mathcal{E}_i(z). \tag{1.21}$$

With the ansatz $\mathcal{E}_l(z) = \tilde{\mathcal{E}}_l e^{(\Gamma + i\frac{\Delta k}{2})z}$, where $\tilde{\mathcal{E}}_l$ are constant amplitudes independent of z, we find a characteristic equation for Γ:

$$\left[\left(\Gamma + i\frac{\Delta k}{2} + \frac{\alpha_s}{2}\right)\left(\Gamma - i\frac{\Delta k}{2} + \frac{\alpha_i}{2}\right) - \gamma_s\gamma_i|\mathcal{E}_p|^2\right]\tilde{\mathcal{E}}_s = 0. \tag{1.22}$$

Dieses Werk ist copyrightgeschützt und darf in keiner Form vervielfältigt werden noch an Dritte weitergegeben werden.
Es gilt nur für den persönlichen Gebrauch.

For the non-trivial case $\tilde{\mathcal{E}}_s \neq 0$, the term in the square brackets vanishes, which results in a quadratic equation for Γ with two independent results $\Gamma_\pm$:

$$\Gamma_\pm = -\underbrace{\frac{1}{4}(\alpha_i + \alpha_s)}_{=\alpha} \pm \underbrace{\sqrt{\gamma_s \gamma_i |\mathcal{E}_p|^2 + \delta^2}}_{=g}, \tag{1.23}$$

where the parameter $\delta = (\alpha_i - \alpha_s - 2i\Delta k)/4$ has been introduced. Now the coupled wave equations take the shape

$$\mathcal{E}_s(z) = \left(\tilde{\mathcal{E}}_s^+ e^{+gz} + \tilde{\mathcal{E}}_s^- e^{-gz}\right) e^{-\alpha z} e^{i\frac{\Delta k}{2}z} \tag{1.24}$$

$$\mathcal{E}_i(z) = \left(\tilde{\mathcal{E}}_i^+ e^{+gz} + \tilde{\mathcal{E}}_i^- e^{-gz}\right) e^{-\alpha z} e^{i\frac{\Delta k}{2}z}, \tag{1.25}$$

with the abbreviations $\alpha = (\alpha_s + \alpha_i)/4$ as a mean value for signal and idler absorption coefficients, and $g^2 = \gamma_s \gamma_i |\mathcal{E}_p|^2 + \delta^2 = g_\star^2 + \delta^2$ as a driving term including pump intensity, nonlinear coupling factors, and also absorption coefficients and phase mismatch. For an OPO being pumped at 1064 nm wavelength, g is dominated by the absorption parameter δ for long idler wavelengths $\lambda_i > 4.5\ \mu$m, as an example may illustrate: Using a 1 W pump laser focused down to a beam radius of 100 μm producing perfectly phase matched 5 μm wavelength of idler radiation, $\gamma_s \gamma_i |\mathcal{E}_p|^2 \approx 40\ \mathrm{m}^{-1}$ and $\delta^2 \approx 625\ \mathrm{m}^{-1}$.

The amplitude coefficients $\tilde{\mathcal{E}}_{s,i}^\pm$ have to be determined by boundary conditions. Hence, we set the amplitudes of signal and idler at the front facet of the nonlinear medium $\mathcal{E}_i(0) = \mathcal{E}_{i0}$ and $\mathcal{E}_s(0) = \mathcal{E}_{s0}$, respectively. At position $z = 0$, equations (1.24) and (1.25) give the relations $\tilde{\mathcal{E}}_s^- = \mathcal{E}_{s0} - \tilde{\mathcal{E}}_s^+$ and $\tilde{\mathcal{E}}_i^- = \mathcal{E}_{i0} - \tilde{\mathcal{E}}_i^+$. By further comparison of $\frac{\partial}{\partial z}\mathcal{E}_s(z)\big|_{z=0}$ and $\frac{\partial}{\partial z}\mathcal{E}_i(z)\big|_{z=0}$ with the right sides of equations (1.20) and (1.21) at position $z = 0$, one finally obtains for the amplitude coefficients:

$$\tilde{\mathcal{E}}_s^\pm = \pm\frac{1}{2g}\left[i\gamma_s \mathcal{E}_p \mathcal{E}_{i0}^* - \left(\Gamma_\mp + i\frac{\Delta k}{2} + \frac{\alpha_s}{2}\right)\mathcal{E}_{s0}\right] \tag{1.26}$$

$$\tilde{\mathcal{E}}_i^\pm = \pm\frac{1}{2g}\left[i\gamma_i \mathcal{E}_p \mathcal{E}_{s0}^* - \left(\Gamma_\mp + i\frac{\Delta k}{2} + \frac{\alpha_i}{2}\right)\mathcal{E}_{i0}\right]. \tag{1.27}$$

The solutions can now be expressed as follows:

$$\mathcal{E}_s(z) = \left[\mathcal{E}_{s0}\cosh(gz) + \frac{1}{g}\left(i\gamma_s \mathcal{E}_p \mathcal{E}_{i0}^* + \delta\mathcal{E}_{s0}\right)\sinh(gz)\right] e^{-\alpha z} e^{i\frac{\Delta k}{2}z} \tag{1.28}$$

$$\mathcal{E}_i(z) = \left[\mathcal{E}_{i0}\cosh(gz) + \frac{1}{g}\left(i\gamma_i \mathcal{E}_p \mathcal{E}_{s0}^* + \delta\mathcal{E}_{i0}\right)\sinh(gz)\right] e^{-\alpha z} e^{i\frac{\Delta k}{2}z}. \tag{1.29}$$

In the parametric process of a singly resonant OPO, there is no idler wave incident at the front facet of the nonlinear crystal, which gives $\mathcal{E}_{i0} = \mathcal{E}_{i0}^* = 0$,

Dieses Werk ist copyrightgeschützt und darf in keiner Form vervielfältigt werden noch an Dritte weitergegeben werden.
Es gilt nur für den persönlichen Gebrauch.

while the signal wave amplitude is non-zero because of the constant feedback in the optical cavity: $\mathcal{E}_{s0}, \mathcal{E}_{s0}^* \neq 0$. These two conditions lead to:

$$\mathcal{E}_s(z) = \mathcal{E}_{s0}\left[\cosh(gz) + \frac{\delta}{g}\sinh(gz)\right] e^{-\alpha z} e^{i\frac{\Delta k}{2}z} \tag{1.30}$$

$$\mathcal{E}_i(z) = \mathcal{E}_{s0}^*\left[i\frac{\gamma_i \mathcal{E}_p}{g}\sinh(gz)\right] e^{-\alpha z} e^{i\frac{\Delta k}{2}z}. \tag{1.31}$$

Note that these relations have been derived using the approximation of a constant pump field over the entire nonlinear crystal, thus they are only valid in the low conversion efficiency regime. They can be used to derive the threshold condition (see section 1.4), because the signal field present in the cavity close to threshold is small.

Neglecting absorption by setting $\alpha_i = \alpha_s = 0$, we find for the intensity $I_l(z)$ of the waves:

$$I_s(z) = I_{s0}\left[1 + (g_\star z)^2 \frac{\sinh^2(gz)}{(gz)^2}\right] \tag{1.32}$$

$$I_i(z) = I_{s0}\frac{\nu_i}{\nu_s}(g_\star z)^2 \frac{\sinh^2(gz)}{(gz)^2}. \tag{1.33}$$

And for perfect phase matching $\Delta k = 0$, we find

$$I_s(z) = I_{s0}\left(\cosh(gz) + \frac{\delta}{g}\sinh(gz)\right)^2 e^{-2\alpha z} \approx I_{s0} e^{2(g-\alpha)z} \tag{1.34}$$

$$I_i(z) = I_{s0}\frac{\nu_i}{\nu_s}(g_\star z)^2 \frac{\sinh^2(gz)}{(gz)^2} e^{-2\alpha z}. \tag{1.35}$$

The approximation for the signal intensity is valid for strong idler absorption $\alpha^2 \gg \gamma_s \gamma_i |\mathcal{E}_p|^2$.

1.3.3 Parametric Gain

The gain G_s the signal wave experiences upon a single pass through the nonlinear medium of length L can be expressed as follows:

$$G_s = \frac{I_s(L) - I_s(0)}{I_s(0)} = \frac{I_s(L)}{I_s(0)} - 1 = \frac{|\mathcal{E}_s(L)|^2}{|\mathcal{E}_s(0)|^2} - 1. \tag{1.36}$$

Substituting the solutions found above results in the relation

$$G_s = \left(\cosh(gL) + \frac{\delta}{g}\sinh(gL)\right)^2 e^{-2\alpha L} - 1. \tag{1.37}$$

Dieses Werk ist copyrightgeschützt und darf in keiner Form vervielfältigt werden noch an Dritte weitergegeben werden.
Es gilt nur für den persönlichen Gebrauch.

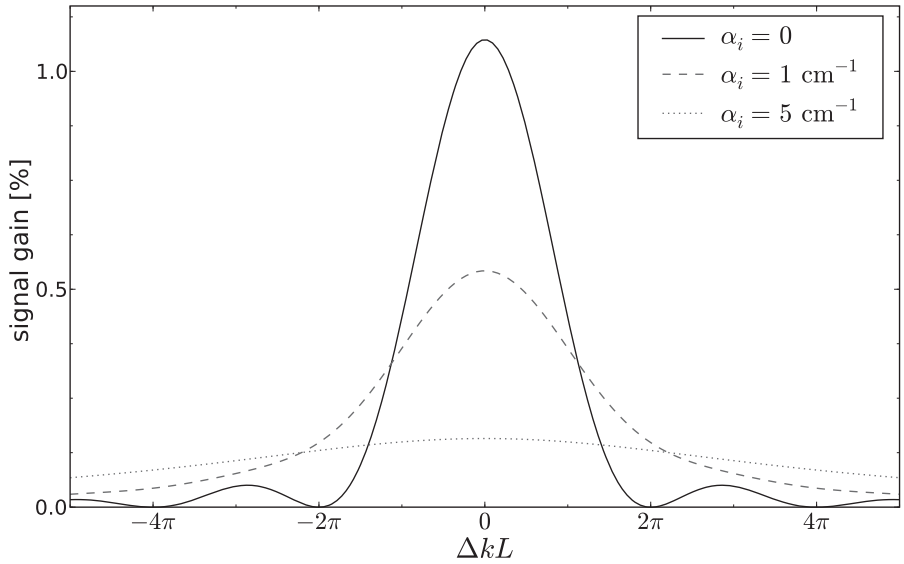

Figure 1.1: Signal gain profiles for different absorption coefficients of the idler wave. With increasing absorption, the maximum decreases and the profile gets broader. Side-lobes vanish. The pump laser has a wavelength of $\lambda_p = 1064$ nm, a power of 1 W and a beam radius of 100 μm. Idler wavelength is $\lambda_i = 5000$ nm, the nonlinear crystal has a length of 5 cm and an effective nonlinear coefficient $d = 17$ pm/V. Myers *et al.* reported an idler absorption coefficient of $\alpha_i \approx 1$ cm^{-1} for this idler frequency [74], corresponding to the dashed red line.

Figure 1.1 shows the gain curve $G_s(\Delta kL)$ calculated for different idler absorption coefficients. Note that the gain in the signal wave gets smaller, even though absorption is only present in the idler wave. Also the gain curve gets broader when the idler absorption increases.

When we neglect absorption ($\alpha_i = \alpha_s = 0$) and assume perfect phase matching ($\Delta k = 0$), the parameter δ equals zero and the signal gain reduces to

$$G_s = \sinh^2(g_\star L) \approx g_\star^2 L^2 + \mathcal{O}(g_\star^4 L^4) \tag{1.38}$$

with the abbreviation $g_\star^2 = g^2|_{(\alpha=\Delta k=0)} = (2\omega_s\omega_i d^2 I_p)/(\varepsilon_0 n_p n_s n_i c^3)$.

For perfect phase matching ($\Delta k = 0$) but strong idler absorption ($\alpha^2 \gg \gamma_s\gamma_i|\mathcal{E}_p|^2$), the gain can be approximated as

$$G_s \approx e^{2(g-\alpha)L} - 1 \tag{1.39}$$

$$\approx 2(g-\alpha)L. \tag{1.40}$$

In this case, the gain increases only linear with length instead of quadratically. Figure 1.2 illustrates this behavior.

Dieses Werk ist copyrightgeschützt und darf in keiner Form vervielfältigt werden noch an Dritte weitergegeben werden.
Es gilt nur für den persönlichen Gebrauch.

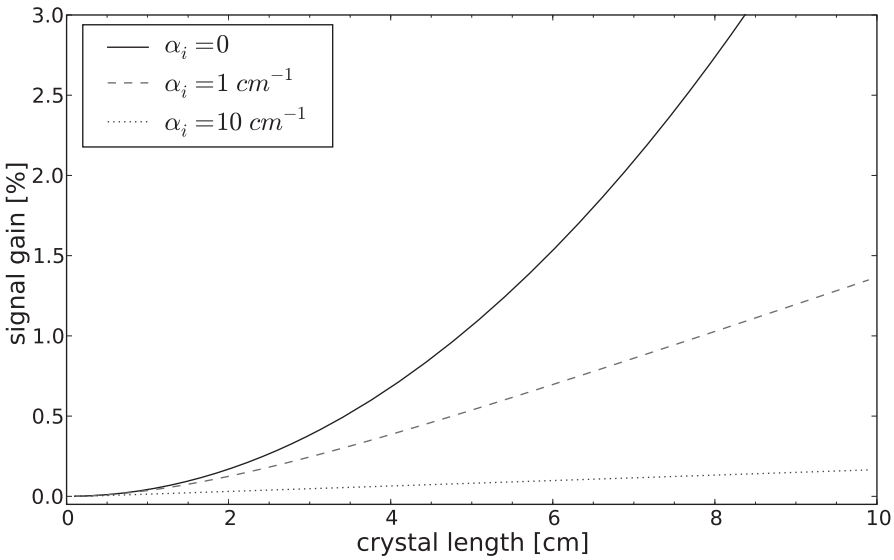

Figure 1.2: Signal gain dependency on crystal length for perfect phase matching and zero absorption of signal radiation for different idler absorptions. In the limit of zero absorption, gain grows quadratically with length. With increasing idler absorption, gain grows only linearly. The pump laser has a wavelength of $\lambda_p = 1064$ nm, a power of 1 W and a beam radius of 100 μm. Idler wavelength is $\lambda_i = 5000$ nm, the nonlinear crystal has an effective nonlinear coefficient $d = 17$ pm/V.

1.4 Optical Parametric Oscillation

An optical parametric oscillator (OPO) bases on the optical parametric amplification (OPA) as described above. Thus in an OPO, energy is converted from an intense field of radiation at frequency ν_p — called the pump wave — to two other waves of different frequency, which are called signal wave (frequency ν_s) and idler wave (frequency ν_i). The designation is made in a way so that $\nu_p > \nu_s > \nu_i$. In this process, the energy is conserved, which results in the frequency relation (1.11).

If the signal wave is amplified as shown in Sec. 1.3.3, it can also start to oscillate when the amplified signal is fed back to the front side of the nonlinear medium. Since the conversion efficiency depends on the intensity of all three waves in the parametric process, a feedback (and oscillation) can enhance the process by orders of magnitude. The following sections give an insight to effects in OPOs.

1.4.1 Threshold

With increasing pump power, the signal gain grows approximately linear according to equation (1.37). The feedback in the signal wave incorporates

Dieses Werk ist copyrightgeschützt und darf in keiner Form vervielfältigt werden noch an Dritte weitergegeben werden.
Es gilt nur für den persönlichen Gebrauch.

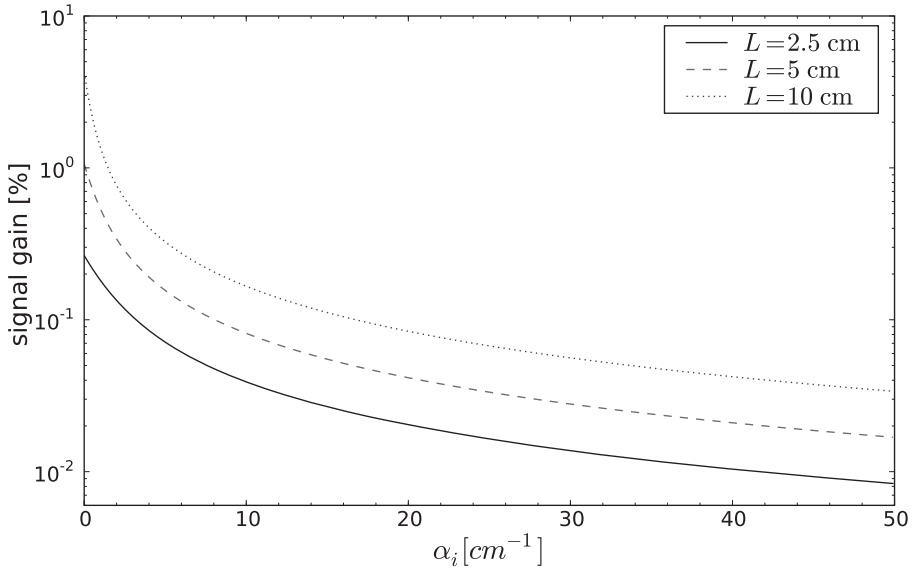

Figure 1.3: Signal gain as a function of idler absorption for perfect phase matching and vanishing signal absorption for different crystal lengths L. The pump laser has a wavelength of $\lambda_p = 1064$ nm, a power of 1 W and a beam radius of 100 μm. Idler wavelength is $\lambda_i = 5000$ nm and the nonlinear crystal has an effective nonlinear coefficient $d = 17$ pm/V. The gain drops very fast at small absorptions and more slowly at higher absorptions.

losses, which have to be overcome by the signal gain for the system to start oscillating. Given the signal intensity $I_s(0)$ at the front facet of the crystal, the wave gets amplified and leaves the crystal with an intensity $I_s(L)$. The signal cavity then provides feedback for a certain proportion $T = 1 - V$ of that intensity, which is again entering the crystal front facet after one cavity round trip. V means here the intensity loss per cavity round trip. Therefore one obtains for the threshold condition:

$$I_s(0) = I_s(L)(1 - V). \tag{1.41}$$

This equation can be transformed to include the signal gain G_s:

$$G_s(\mathcal{E}_p) = \frac{I_s(L)}{I_s(0)} - 1 = \frac{V}{1 - V} \quad . \tag{1.42}$$

Ideal conditions, namely zero absorption and perfect phase matching ($\alpha_i = \alpha_s = \Delta k = 0$) result in a threshold pump power P_{th} of

$$P_{\text{th}} = \frac{c\varepsilon_0 n_p n_s n_i \lambda_s \lambda_i}{8\pi^2} \frac{A}{d^2 L^2} \frac{V}{1 - V} \quad . \tag{1.43}$$

That means the threshold is approximately proportional to the losses per cavity round trip V. As a typical value for the systems relevant in this thesis

Dieses Werk ist copyrightgeschützt und darf in keiner Form vervielfältigt werden noch an Dritte weitergegeben werden.
Es gilt nur für den persönlichen Gebrauch.

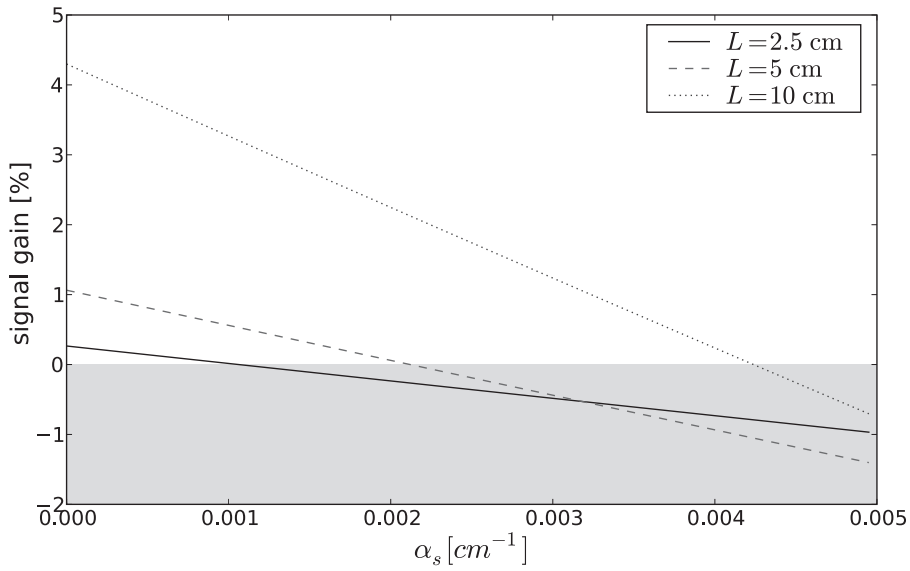

Figure 1.4: Signal gain for perfect phase matching and zero absorption of idler radiation for different crystal lengths L. The pump laser has a wavelength of $\lambda_p = 1064$ nm, a power of 1 W and a beam radius of 100 μm. Idler wavelength is $\lambda_i = 5000$ nm, and the crystal has an effective nonlinear coefficient $d = 17$ pm/V. The gain is extremely sensitive to absorption in the resonant signal frequency. Note the different scale on the x-axis compared to Figure 1.3.

($\lambda_p = 1064\,\mathrm{nm}$, $\lambda_i = 3000\,\mathrm{nm}$, a 5 cm long Lithium Niobate crystal and a beam area of $A = \pi(100\,\mu\mathrm{m})^2$), the threshold is roughly $P_{\mathrm{th}} = 0.7\,\mathrm{W}$ for a total cavity round trip loss of 1%.

1.4.2 Oscillation Conditions

For pump powers above threshold, signal power inside the resonator rapidly exceeds the pump power, and the conversion of pump to signal and idler becomes very efficient. In this oscillation regime, the approximation of a non-depleted pump is not valid anymore. Instead, the signal is the most intense beam and will change only a few percent, while the change in the idler and pump powers are often much larger. To solve the coupled wave equations for a steady-state cw OPO, the assumption $\frac{\partial}{\partial z}\mathcal{E}_s = 0$ leads to $\mathcal{E}_s(z) = \mathcal{E}_s$ and two coupled differential equations:

$$\frac{\partial}{\partial z}\mathcal{E}_p(z) = i\gamma_p\,\mathcal{E}_s\mathcal{E}_i(z)\,e^{-i\Delta kz} - \frac{\alpha_p}{2}\mathcal{E}_p(z) \tag{1.44}$$

$$\frac{\partial}{\partial z}\mathcal{E}_i(z) = i\gamma_i\,\mathcal{E}_s^*\mathcal{E}_p(z)\,e^{+i\Delta kz} - \frac{\alpha_i}{2}\mathcal{E}_i(z) \quad , \tag{1.45}$$

which we can solve analogously to equations (1.20) and (1.21). We assume a set of solutions of the form $\mathcal{E}_p(z) = \hat{\mathcal{E}}_p e^{(\Psi - i\frac{\Delta k}{2})z}$ and $\mathcal{E}_i(z) = \hat{\mathcal{E}}_i e^{(\Psi + i\frac{\Delta k}{2})z}$. For Ψ we then obtain the condition:

Dieses Werk ist copyrightgeschützt und darf in keiner Form vervielfältigt werden noch an Dritte weitergegeben werden.
Es gilt nur für den persönlichen Gebrauch.

$$\left[(\Psi - i\frac{\Delta k}{2} + \frac{\alpha_p}{2})(\Psi + i\frac{\Delta k}{2} + \frac{\alpha_i}{2}) + \gamma_p\gamma_i|\mathcal{E}_s|^2\right]\hat{\mathcal{E}}_p = 0 \quad , \tag{1.46}$$

which results in the two solutions

$$\Psi_\pm = -\underbrace{\frac{1}{4}(\alpha_p + \alpha_i)}_{\alpha_*} \pm \underbrace{\sqrt{\zeta^2 - \gamma_p\gamma_i|\mathcal{E}_s|^2}}_{g_*}$$

with $\zeta = (\alpha_p - \alpha_i - 2i\Delta k)/4$. So now $\mathcal{E}_p$ and $\mathcal{E}_i$ can be written as:

$$\mathcal{E}_p(z) = \left(\hat{\mathcal{E}}_p^+ e^{+g_* z} + \hat{\mathcal{E}}_p^- e^{-g_* z}\right) e^{-\alpha_* z} e^{-i\frac{\Delta k}{2}z} \tag{1.47}$$

$$\mathcal{E}_i(z) = \left(\hat{\mathcal{E}}_i^+ e^{+g_* z} + \hat{\mathcal{E}}_i^- e^{-g_* z}\right) e^{-\alpha_* z} e^{+i\frac{\Delta k}{2}z}. \tag{1.48}$$

The amplitude coefficients $\hat{\mathcal{E}}_{p,i}^\pm$ are determined in the same way as before. With the boundary condition $\mathcal{E}_{i0} = 0$ for a singly resonant OPO one finally obtains

$$\mathcal{E}_p(z) = \mathcal{E}_{p0}\left[\cosh(g_* z) - \frac{\zeta}{g_*}\sinh(g_* z)\right] e^{-\alpha_* z} e^{-i\frac{\Delta k}{2}z} \tag{1.49}$$

$$\mathcal{E}_i(z) = \mathcal{E}_{p0}\left[i\frac{\gamma_i}{g_*}\mathcal{E}_s^* \sinh(g_* z)\right] e^{-\alpha_* z} e^{+i\frac{\Delta k}{2}z}. \tag{1.50}$$

For the case of zero absorption ($\alpha_* = \alpha_p = \alpha_i = 0$) and perfect phase matching ($\Delta k = 0$), the parameter g_* becomes purely imaginary. With the above equations for $\mathcal{E}_p$ and $\mathcal{E}_i$ simple expressions for the intensity of the waves are obtained:

$$\begin{aligned} I_p(z) \propto \left|\mathcal{E}_p(z)\right|^2 &= |\mathcal{E}_{p0}|^2 \cos^2\left(\sqrt{\gamma_p\gamma_i|\mathcal{E}_s|^2}\ z\right) \\ &\approx |\mathcal{E}_{p0}|^2\left(1 - \gamma_p\gamma_i|\mathcal{E}_s|^2 z^2\right) \end{aligned} \tag{1.51}$$

$$\begin{aligned} I_i(z) \propto \left|\mathcal{E}_i(z)\right|^2 &= \frac{\gamma_i}{\gamma_p}|\mathcal{E}_{p0}|^2 \sin^2\left(\sqrt{\gamma_p\gamma_i|\mathcal{E}_s|^2}\ z\right) \\ &\approx |\mathcal{E}_{p0}|^2\left(\gamma_i^2|\mathcal{E}_s|^2 z^2\right). \end{aligned} \tag{1.52}$$

The above equations give the idler output of a steady-state OPO, provided the signal field in the resonator is given. For small nonlinear coefficients, the sine function of distance z in equation (1.52) can be approximated as a linear function of z, resulting in a quadratic increase of idler power with crystal length. It is important to note that the circulating signal power depends on

Dieses Werk ist copyrightgeschützt und darf in keiner Form vervielfältigt werden noch an Dritte weitergegeben werden.
Es gilt nur für den persönlichen Gebrauch.

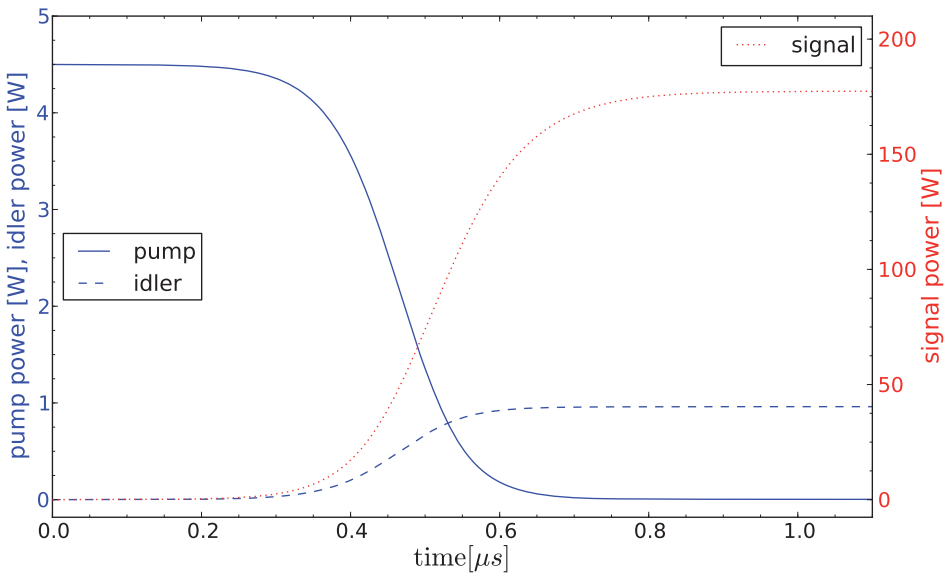

Figure 1.5: Optical powers of relevant beams in the OPO process at the output facet of the crystal during buildup of the signal field. Pump and idler wavelengths are 1064 and 5000 nm, respectively, the crystal is 5 cm long and exhibits an effective nonlinearity of d =17 pm/V. A beam radius of 100 μm as well as a cavity loss of 2% and zero absorption is assumed. At the beginning ($t < 0.3\mu$s), the residual pump power is nearly equal to the power entering the crystal. In this regime the approximation of a non-depleted pump as performed in section 1.3.2 is valid and the signal gain from equation (1.37) is independent of the signal power present at the front facet of the crystal.

the pump power, as described later. That means that the idler power does not increase linearly with the pump power as a first look on equation (1.52) might suggest.

Calculating the idler output power still requires the knowledge of the amplitude of the oscillating signal field. This can be obtained by assuming a zero pump absorption. Then the energy conservation requires

$$\frac{I_p(z) - I_{p0}}{\nu_p} = -\frac{I_s(z) - I_{s0}}{\nu_s} \quad , \tag{1.53}$$

which links the signal gain with the pump depletion. In the steady state of an OPO, the signal field reproduces after being amplified in the crystal of length L and after undergoing losses V in the resonator. This situation is described in equation (1.41). Combining this relation with equations (1.53) and (1.49), one obtains

$$|\mathcal{E}_{s0}|^2 = \frac{\gamma_s}{\gamma_p}|\mathcal{E}_{p0}|^2 \frac{1-V}{V}\left(1 - \left|\cosh(g_* L) - \frac{\zeta}{g_*}\sinh(g_* L)\right|^2 e^{-2\alpha_* L}\right) . \tag{1.54}$$

Since the cavity losses V are usually known, this relation can be used to obtain the amplitude of the oscillating signal field $\mathcal{E}_{s0}$.

Dieses Werk ist copyrightgeschützt und darf in keiner Form vervielfältigt werden noch an Dritte weitergegeben werden.
Es gilt nur für den persönlichen Gebrauch.

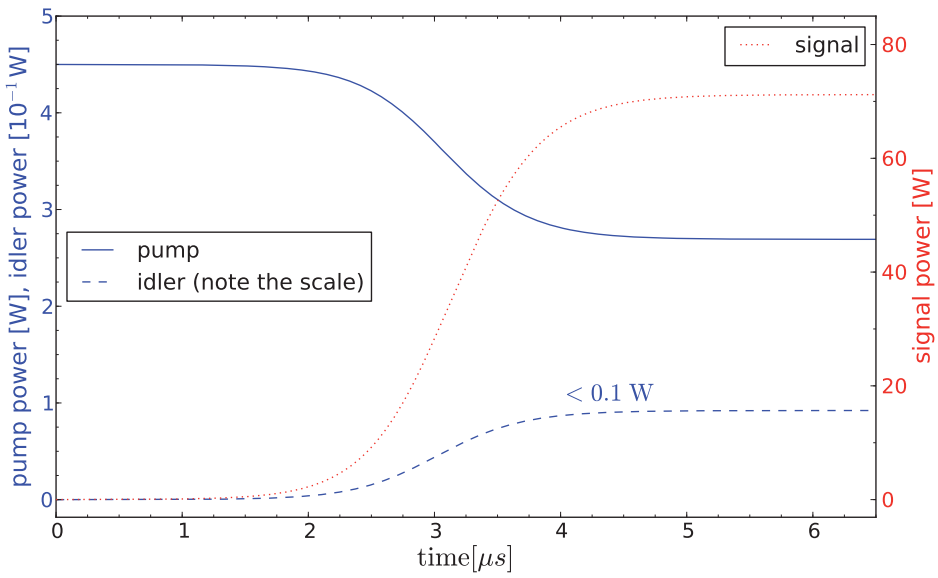

Figure 1.6: Optical powers of relevant beams in the OPO process at the output facet of the crystal during buildup of the signal field. Pump and idler wavelengths are 1064 and 5000 nm, respectively, the crystal is 5 cm long and exhibits an effective nonlinearity of d =17 pm/V. A beam radius of 100 μm as well as a cavity loss of 2% and an idler absorption of 1 cm^{-1} is assumed. At the beginning, the exiting pump power is nearly equal to the power entering the crystal. Note that the idler power is plotted with a different scale. Compared to the case with vanishing absorption (Figure 1.5), the main differences are the lower signal and idler powers, but also the increased rise time, which is visible in the different x-axis scales.

Alternatively, equations (1.16) to (1.18) can be integrated numerically to simulate the development of the OPO waves to the steady state. This way it is also possible to yield the steady-state signal and idler output powers. To perform the simulation, the crystal is split up in small segments of length <10 μm. The wave output powers of a segment calculated after equations (1.16) to (1.18) is taken as the input powers of the next segment, until the total length of the crystal is reached. After one crystal pass, the signal output power $P_s(L)$ multiplied with the transmission from the cavity $(1-V)$ is taken as the new input for the next iteration, whereas idler power $P_i(0) = 0$ and pump power $P_p(0) = P_{p0}$ are the same at the beginning of each iteration. A small starting power for the signal radiation is assumed at the beginning of the simulation and the calculation stops when the signal power increase from one iteration compared to the next is smaller than a given threshold.

The onset of oscillation is simulated this way and shown in Figures 1.5 and 1.6. Here, a small signal amplitude ($P_s = 10^{-5}$ W) is present at the front facet of the crystal at the time $t = 0$, and in both calculations the pump power equals 4.5 W. Figure 1.5 shows the simulation without any absorption in the crystal, while Figure 1.6 shows the result of a calculation including the effects of idler absorption.

Dieses Werk ist copyrightgeschützt und darf in keiner Form vervielfältigt werden noch an Dritte weitergegeben werden.
Es gilt nur für den persönlichen Gebrauch.

It can be seen that the signal power circulating in the resonator quickly builds up to orders of magnitude higher than the pump or idler powers. Absorption drastically reduces this steady-state power level. The rise time, which is defined as the time passing until the OPO reaches a steady state, increases with the absorption.

1.4.3 Steady-State Efficiency and Idler Power

The oscillation conditions of a steady-state OPO as shortly described above have also been subject to scientific analysis [19, 20, 56]. These works allow a prediction of idler output powers by knowledge of the threshold pump power only. However, they neglect absorption for the sake of the possibility of an analytically expressed result. A theoretical treatment including absorption is complicated and beyond the scope of this thesis. However, basic ideas derived from a model neglecting absorption and effects of gaussian beams can still be very useful. One important figure in these descriptions is the efficiency.

The quantum efficiency η of an optical parametric oscillator is defined as $\eta = 1 - P_p(L)/P_p(0)$ and determines the fraction of the pump power, which is actually converted to idler and signal. This number is preferably high, so a lot of idler power is available in the experiment. The efficiency η has been calculated by Kreuzer and Brunner *et al.* [56] for steady-state optical parametric oscillators in the limit of plane waves. The efficiency can be simply expressed by the squared sine of a constant Γ_B as:

$$\eta = 1 - \frac{P_p(L)}{P_p(0)} = \sin^2(\Gamma_\mathrm{B}) \quad , \tag{1.55}$$

where the constant Γ_B is dependent on the time the pump power exceeds the threshold and defined through the relation

$$\frac{P_p(0)}{P_\mathrm{th}} = \frac{\Gamma_\mathrm{B}^2}{\sin^2(\Gamma_\mathrm{B})}. \tag{1.56}$$

The resulting graph of η as a function of $P_p(0)/P_\mathrm{th}$ is plotted in Figure 1.7. The efficiency reaches its maximum of 100% at 2.5 times above the threshold. In this simple model, all of the pump power is converted into signal and idler. More sophisticated treatments including the effects of gaussian beams have also been published, but this simple model already illustrates the behavior of an OPO in steady state.

At high pump levels of more than 4.6 times over threshold, the theoretical model by Kreuzer *et al.* predicts multi-mode oscillation of the OPO [56]. In

Dieses Werk ist copyrightgeschützt und darf in keiner Form vervielfältigt werden noch an Dritte weitergegeben werden.
Es gilt nur für den persönlichen Gebrauch.

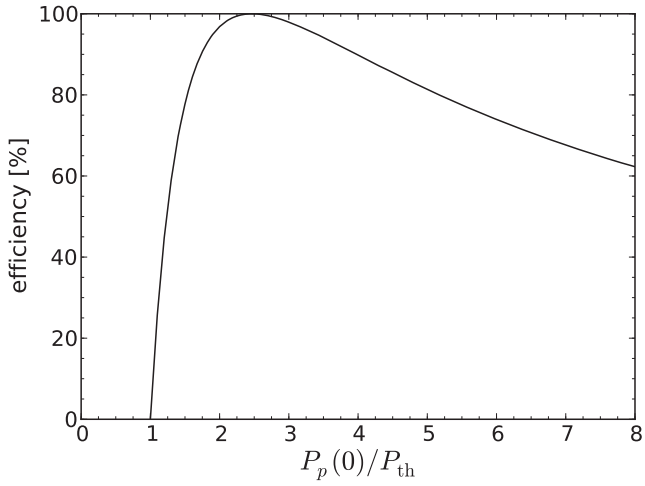

Figure 1.7: Quantum efficiency of an OPO running in steady state as a function of incident pump power over threshold in the limit of plane waves after Kreuzer *et al.* [56]. The efficiency reaches the full conversion limit at around $P_p(0)/P_{\mathrm{th}} = 2.5$. Here, all pump energy is converted into idler and signal waves.

a more recent work by Philips and Fejer, it is deduced that these instabilities sometimes occur at lower pump levels as well [83]. So the maximum pump power possible is limited either by the pump laser or by the value of roughly four times the threshold of the system.

The idler power is connected to the efficiency via the Manley-Rowe relations and can be expressed as:

$$P_i(L) = \frac{\nu_i}{\nu_p}\eta P_p(0). \tag{1.57}$$

Figure 1.8 shows two graphs for different ratios ν_i/ν_p for the two systems relevant in this thesis. It can be seen that the idler power grows monotonously with increasing pump power, but with a decreasing rate.

Some experiments need high optical powers and for these the idler output power should be maximized. For this purpose, it is necessary to design the OPO in such a way, that a threshold of $P_{p\mathrm{max}}/2.5$ is reached, with $P_{p\mathrm{max}}$ as the maximum pump power of the available pump laser. This requirement can be met for example by choosing a crystal length appropriate for the current pump laser, as the work by Sowade *et al.* proved [101]. More information about optimizing idler powers can be found in Ref. [100].

All these considerations are only valid in the limit of plane waves. For an insight into the effects of gaussian beam profiles, see the work of Bjorkholm (Ref. [11]). There, the efficiency never reaches 100% because of the imperfect overlapping of beams. Bjorkholm's prediction of the maximum efficiency is approximately 70%.

Dieses Werk ist copyrightgeschützt und darf in keiner Form vervielfältigt werden noch an Dritte weitergegeben werden.
Es gilt nur für den persönlichen Gebrauch.

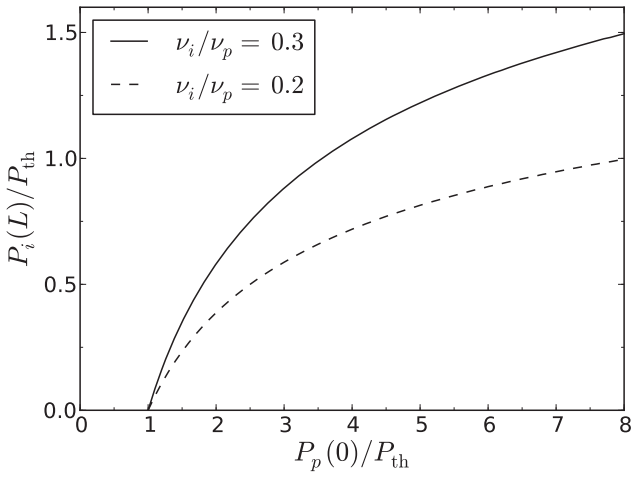

Figure 1.8: Idler power after leaving the crystal $P_i(L)$ normalized to the threshold pump power P_{th}. The two ratios of ν_i/ν_p of 0.2 and 0.3 correspond approximately to the OPOs relevant for this thesis with idler wavelengths around 5 μm and 3 μm, respectively. Note that this model does not account for absorption.

1.5 Phase Matching

The parameter $\Delta k = k_p - k_s - k_i$, also called the phase mismatch, describes the difference in the phase velocities $v_{\mathrm{ph}} = \omega/k$ of the three interacting waves in the crystal. In the coupled wave equations (1.16) to (1.18), the factor $e^{i\Delta kz}$ determines the direction of energy transfer between the interacting waves, with Δkz as the relevant phase. At a phase shift of π, the pump wave is amplified at the cost of the signal wave. This condition $\Delta kz = \pi$ defines a distance z called the coherence length L_c, up to which the signal wave is amplified.

$$L_c = \frac{\pi}{\Delta k} \tag{1.58}$$

Due to dispersion, Δk can be large in real media, because it depends on the index of refraction. The refractive index $n(\lambda)$ for $LiNbO_3$ can be seen in Figure 1.9. This is why L_c is usually small and the converted power is negligible. For example, the phase mismatch for the frequency conversion of a 1064 nm wavelength pump wave to 5 μm wavelength idler wave in a $LiNbO_3$ crystal is $\Delta k \approx +2.4 \times 10^5$ m^{-1}, which results in a coherence length of $L_c \approx 12.9$ μm. Methods of decreasing the phase mismatch are called phase matching, and are crucial to produce a notable efficiency. An important way is the so-called "quasi phase matching", which is described in the next section.

1.5.1 Quasi Phase Matching

Quasi phase matching uses a spatial modulation of the nonlinear coefficient d. By inverting the sign of the nonlinear coefficient d every coherence length L_c in the crystal, back-conversion of energy to the pump wave is prevented and macroscopic enhancement of the signal wave is made possible, as first

Dieses Werk ist copyrightgeschützt und darf in keiner Form vervielfältigt werden noch an Dritte weitergegeben werden.
Es gilt nur für den persönlichen Gebrauch.

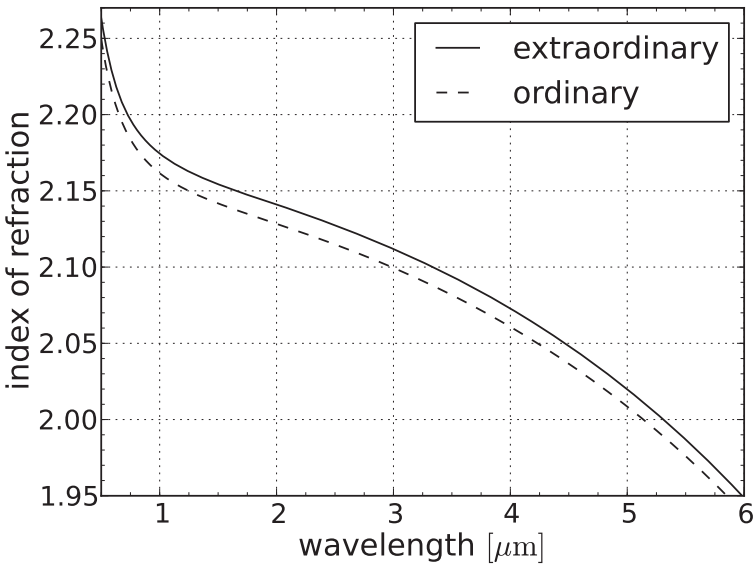

Figure 1.9: Refractive indices of MgO-doped Lithium Niobate for the ordinary and extraordinary beam, calculated with the Sellmeier equation with parameters taken from Ref. [28]. Parameters are a fit to data up to $\lambda \approx 4$ μm wavelength.

proposed by Armstrong *et al.* [2]. This modulation is a common technique in $LiNbO_3$, and crystals for this purpose are commercially available. The patterned material is called Periodically Poled Lithium Niobate (PPLN). $LiNbO_3$ is poled using high-voltage assisted growth of ferroelectric domains, where the crystallographic orientation changes with the domains every coherence length. This alternation causes the desired modulation of the nonlinear coefficient d. Figures 1.10 and 1.11 illustrate the resulting grating pattern.

Here we assume a spatial modulation as shown in Figure 1.10. The function $d(z)$ is a square wave with the period Λ and an amplitude of d_0. For easier treatment, it can be expanded in a complex Fourier series:

$$d(z) = \sum_{m=-\infty}^{m=+\infty} c_m e^{i\frac{2\pi m}{\Lambda}z} \quad , \tag{1.59}$$

with the Fourier coefficients

$$c_m = \frac{1}{\Lambda}\int_0^{\Lambda} d(z)\; e^{-i\frac{2\pi m}{\Lambda}z}\; dz \tag{1.60}$$

$$= \begin{cases} -i\frac{2}{\pi m}d_0 & \text{if } m \text{ odd,} \\ 0 & \text{if } m \text{ even} \end{cases} \quad . \tag{1.61}$$

The coefficients are getting smaller with increasing m, which is why usually only Fourier components which small values of m are dealt with. In the following, we assume $m = \pm 1$, so the nonlinear coefficient can be approximated by its Fourier components with $|m| = 1$:

$$d(z) = i\frac{2}{\pi}d_0 e^{-iK_g z} - i\frac{2}{\pi}d_0 e^{+iK_g z} + \dots \quad , \tag{1.62}$$

Dieses Werk ist copyrightgeschützt und darf in keiner Form vervielfältigt werden noch an Dritte weitergegeben werden.
Es gilt nur für den persönlichen Gebrauch.

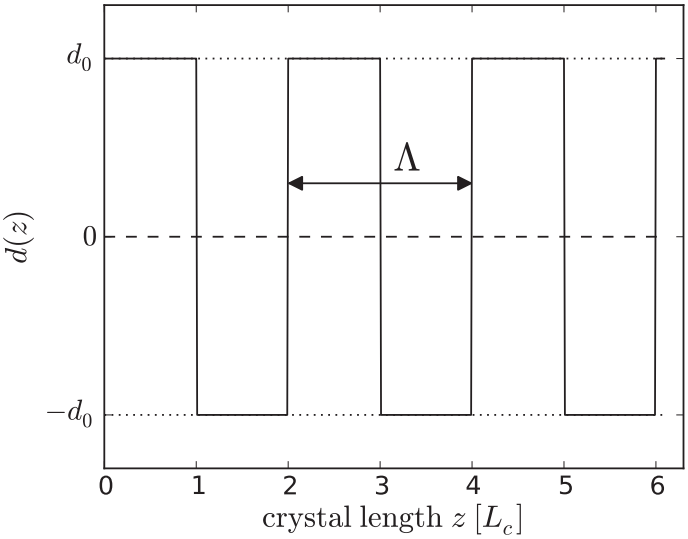

Figure 1.10: Spatial modulation of the nonlinear coefficient d as a square wave suitable for quasi phase matching. The sign of $d(z)$ changes every coherence length $L_c = \Lambda/2$ and the absolute value constantly equals d_0. Technically, the sign inversions are realized by high-voltage assisted growth of ferroelectric crystal domains with alternating orientation.

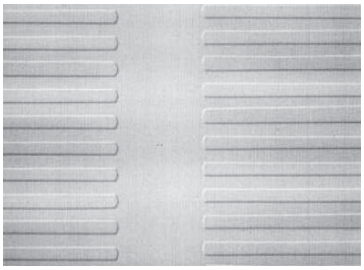

Figure 1.11: Top view of a periodically poled $LiNbO_3$ crystal with two grating structures. They are made visible by an etching process. The poling period is approximately $\Lambda = 30\ \mu$m. Beam propagation in this orientation would be in the vertical direction. The picture is taken from Ref. [96].

with the grating vector $K_\mathrm{g} = (2\pi)/\Lambda$. Inserting this result in the coupled wave equations, one obtains

$$\frac{\partial}{\partial z}\mathcal{E}_p(z) = +\gamma_p\,\mathcal{E}_s(z)\mathcal{E}_i(z)\,e^{-i\Delta kz} \quad - \frac{\alpha_p}{2}\mathcal{E}_p(z) \tag{1.63}$$

$$\frac{\partial}{\partial z}\mathcal{E}_s(z) = -\gamma_s\,\mathcal{E}_p(z)\mathcal{E}_i^*(z)\,e^{+i\Delta kz} \quad - \frac{\alpha_s}{2}\mathcal{E}_s(z) \tag{1.64}$$

$$\frac{\partial}{\partial z}\mathcal{E}_i(z) = -\gamma_i\,\mathcal{E}_p(z)\mathcal{E}_s^*(z)\,e^{+i\Delta kz} \quad , - \frac{\alpha_i}{2}\mathcal{E}_i(z) \tag{1.65}$$

where the transformations $\gamma_l = (2\pi\nu_l d_\mathrm{eff})/(n_l c)$ with an effective nonlinear coefficient $d_\mathrm{eff} = \frac{2}{\pi}d_0$ and $\Delta k = k_p - k_s - k_i - K_\mathrm{g}$ have been made. In the first equation, the Fourier component with $m = -1$ is neglected and in the other two equations the component with $m = +1$. Other terms just increase the phase mismatch for the given parametric process in this work, where Δk without quasi phase matching is always positive. Note that the above differential equations have different prefactors. However, they have the same solutions as equations (1.16) to (1.18) which have been discussed in the previous sections. The prefactors just exhibit a different phase shift in the amplitudes, which does not have any effect on the observable powers. A mathematical argument is that the parameters Γ and Ψ with the same ansatz

Dieses Werk ist copyrightgeschützt und darf in keiner Form vervielfältigt werden noch an Dritte weitergegeben werden.
Es gilt nur für den persönlichen Gebrauch.

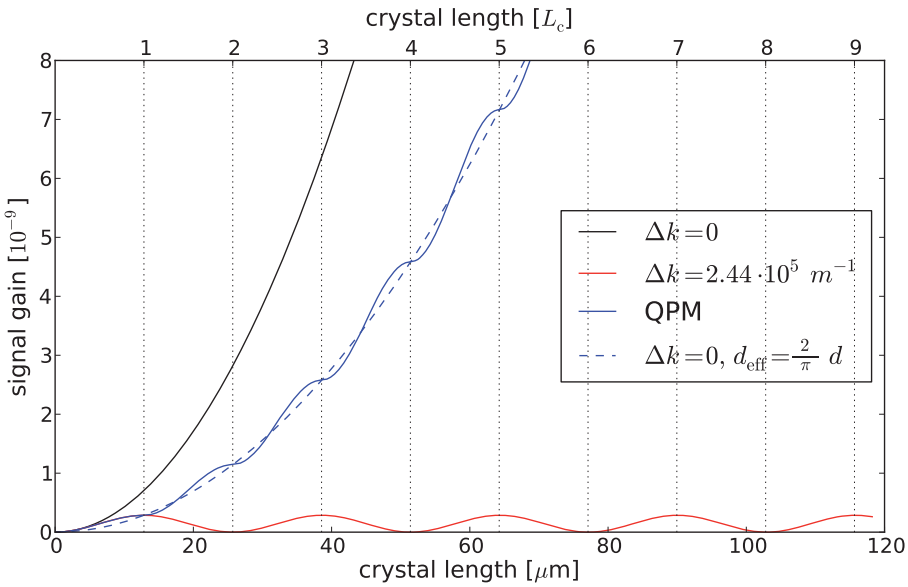

Figure 1.12: Phase matching using the periodic poling technique. The black line indicates the gain in a $LiNbO_3$ crystal for perfect phase matching conditions, which grows quadratic with distance. Dispersion results in a phase mismatch Δk, which prevents macroscopic enhancement of signal radiation (red line). Inverting the sign of the nonlinear coefficient d after every multiple of the coherence length L_c ($L_c = 12.8\mu$m in this case) results in an effective quadratic gain increase over length (blue line). This increase can be approximated with a perfect phase matching model with an effective nonlinear coefficient $d_{\mathrm{eff}} = \frac{2}{\pi} d$ (blue dashed line).

as described in the corresponding section still have the same characteristic equations as (1.22) and (1.46).

With the grating vector K_{g} as another addend in the phase mismatch, phase matching can be reached by choosing the right poling period Λ, and the phase matching condition is altered to:

$$\Delta k = k_p - k_s - k_i - \frac{2\pi}{\Lambda} = 0 \quad . \tag{1.66}$$

Figure 1.12 shows the effect of quasi phase matching. Plotted is the signal gain over the crystal length for a 1064 nm pump wavelength, 5000 nm idler wavelength and the same other parameters used in the previous figures. For the hypothetical case of perfect phase matching, the gain increases quadratically with the distance in the medium (black line). However, the phase mismatch is actually large, which is why conversion is ineffective and the gain oscillates on a microscopic scale with the period $2L_c$ (red line). Inverting the sign of the nonlinear coefficient every distance L_c, the gain is simulated in the blue line. The dashed blue line shows the effective signal gain which results when taking only the largest Fourier components into account as demonstrated above.

Dieses Werk ist copyrightgeschützt und darf in keiner Form vervielfältigt werden noch an Dritte weitergegeben werden.
Es gilt nur für den persönlichen Gebrauch.

Though the effective nonlinear coefficient is reduced by a factor $2/\pi$ when using quasi-phase matching, the principle usually allows phase matching with higher nonlinear coefficients in the same material. For example, for $LiNbO_3$ in a common noncritical phase matching setup, $d_{\text{eff}} = d_{31}$ (see equation (1.1) for the d tensor of Lithium Niobate). Using quasi-phase matching one is able to access the coefficient $d_{33} \approx 6d_{31}$. So the effective nonlinear coefficient is $d_{\text{eff}} = 2/\pi \cdot d_{33} \approx 12/\pi \cdot d_{31}$, which makes quasi phase matching approximately $(12/\pi)^2 \approx$15 times more efficient than conventional noncritical phase matching in this case.

Also note that by inserting other Fourier components in the coupled wave equations as above, other modes of quasi phase matching can be explained. Take for example conversion where the phase mismatch without quasi phase matching is negative. By choosing the right components and poling period, the phase mismatch can be made zero by adding the grating vector instead of subtracting: $\Delta k = k_p - k_s - k_i + 2\pi/\Lambda$. This changes the prefactors in the coupled wave equations, which again does not have any effect on the conversion solutions.

Table 1.1: Sellmeier coefficients for the extraordinary refractive index n_e of 5% MgO-doped congruent $LiNbO_3$ as given in Ref. [28]

Coefficient	value
a_1	5.756
$a_2 \times 10^{-3}$	98.3
a_3	0.2020
a_4	189.32
a_5	12.52
$a_6 \times 10^{-3}$	13.2
$b_1 \times 10^{-6}$	2.860
$b_2 \times 10^{-9}$	47.00
$b_3 \times 10^{-9}$	61.13
$b_4 \times 10^{-6}$	151.6

The index of refraction in $LiNbO_3$ is not only dependent on the wavelength, but also on the temperature of the crystal. The following empirically found relation called **Sellmeier-equation** describes the wavelength- and temperature-dependence of the extraordinary refractive index n_e in 5% MgO-doped congruent $LiNbO_3$ used in this work [28]:

$$n_e^2 = a_1 + b_1 f + \frac{a_2 + b_2 f}{\lambda^2 - (a_3 + b_3 f)^2} + \frac{a_4 + b_4 f}{\lambda^2 - a_5^2} - a_6 \lambda^2 \qquad (1.67)$$

Dieses Werk ist copyrightgeschützt und darf in keiner Form vervielfältigt werden noch an Dritte weitergegeben werden.
Es gilt nur für den persönlichen Gebrauch.

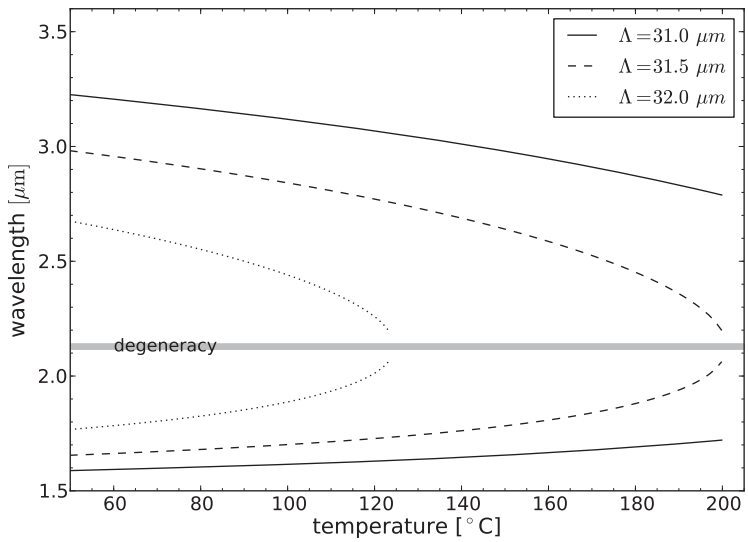

Figure 1.13: Calculated temperature tuning curves for three different poling periods Λ of the periodically poled $LiNbO_3$ crystal. The lines correspond to solutions of equation (1.66) with the refractive indices calculated from the Sellmeier equation for $LiNbO_3$ as given in the text. The pump wavelength is $\lambda_p = 1.064\,\mu$m. The branches above the point of degeneracy $\lambda = 2\lambda_p$ are called idler, the ones below it are called signal.

where $f = (T - 24.5°\mathrm{C}) \cdot (T + 570.82°\mathrm{C})$ is a temperature dependent factor and λ is the wavelength and has to be given in units of μm. Table 1.1 lists the unitless coefficients a_1 to a_6 and b_1 to b_4. In fact, the thermal expansion of the crystal also changes the poling period, which has to be taken into account:

$$\Lambda(T) = \Lambda_{19°\,\mathrm{C}}[1 + \alpha(T - 19°\,\mathrm{C}) + \beta(T - 19°\,\mathrm{C})^2] \tag{1.68}$$

with $\alpha_{\mathrm{LiNbO_3}} = 1.53 \times 10^{-5}\,\mathrm{K}^{-1}$ and $\beta_{\mathrm{LiNbO_3}} = 5.3 \times 10^{-9}\,\mathrm{K}^{-2}$ (Ref. [81]). Now for a given poling period of the crystal, the phase matching conditions are optimal for different wavelengths when the temperature is varied. Figure 1.13 shows a typical tuning behavior over temperature for different poling periods in $LiNbO_3$.

1.5.2 Parametric Bandwidth

The parametric gain as defined in the sections above is a symmetric function of ΔkL (see Figure 1.1) with a peak at $\Delta kL = 0$. If the parametric gain from Figure 1.1 is plotted as a function of idler wavelength[1] instead of the dimensionless parameter ΔkL, the result looks similar, but has varying widths for different idler wavelengths due to the different refractive index. One defines the parametric bandwidth $\Delta\nu_i$ of the idler emission at a fixed pump wavelength and crystal parameters, as the full width at half maximum (FWHM) of the corresponding gain curve. Figure 1.14 shows two of these plots for different idler wavelengths. Note that the gain curve is not symmet-

[1]The length of the crystal is set constant, and the parameter Δk is then calculated using the Sellmeier equation (1.67) for different λ_i.

Dieses Werk ist copyrightgeschützt und darf in keiner Form vervielfältigt werden noch an Dritte weitergegeben werden.
Es gilt nur für den persönlichen Gebrauch.

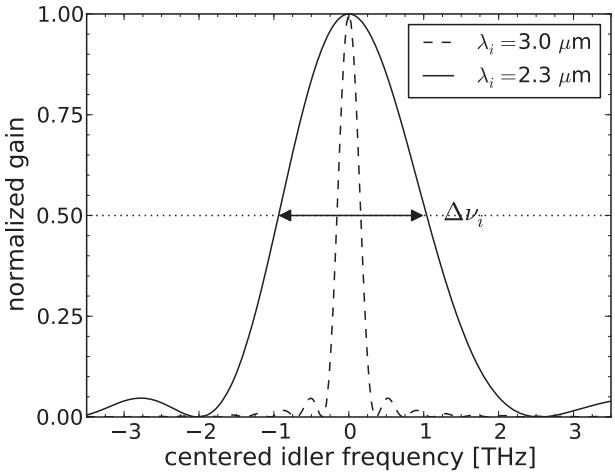

Figure 1.14: Normalized gain curve for two idler wavelengths when using a 5 cm long PPLN crystal and a pump wavelength of 1064 nm. Because of the different dispersion values for $n(\lambda_i)$, actual gain curves depend on the wavelength and are not symmetric in the idler frequency. Close to the degeneracy of the OPO process ($\lambda_i \approx 2.13$ μm for this pump wavelength), the bandwidth increases drastically. In this case the bandwidth is $\Delta\nu_i \approx 2$ THz for an idler wavelength $\lambda_i = 2.3$ μm, and $\Delta\nu_i \approx 0.5$ THz at $\lambda_i = 3$ μm

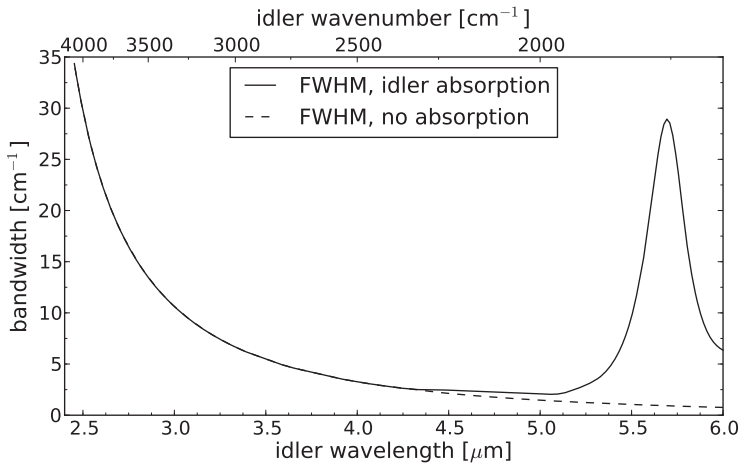

Figure 1.15: Calculation of the bandwidth of the parametric process of the generated idler wave as a function of idler wavelength. A 5 cm long PPLN crystal and a pump wavelength of 1064 nm have been assumed. The increasing absorption coefficient has a non-negligible impact for longer wavelengths.

ric, because the refractive index is a strictly monotonic decreasing function of wavelength in the relevant range.

$\Delta\nu_i$ has a great effect on the stability of an OPO, since mode-hops are favored in a broad gain profile, where many cavity resonances experiences a similar gain. Thus a small parametric bandwidth is desirable, because that would enable gain on just a single monochromatic wavelength, and reduce the chance of mode-hops.

Figure 1.15 shows the relevant wavelength dependence of the bandwidth. A steep increase toward the OPO degeneration point – where the idler and signal frequencies are equal – can be seen. Thus the stability in this region is worse than in the "classic" 3-micron wavelength regime of an OPO pumped at 1064 nm. The bandwidth decreases with the idler wavelength, but due to the absorption coefficient, the bandwidth increases with a peak at 5.7 μm wavelength.

Dieses Werk ist copyrightgeschützt und darf in keiner Form vervielfältigt werden noch an Dritte weitergegeben werden.
Es gilt nur für den persönlichen Gebrauch.

1.6 Summary of OPO Fundamentals

The following summary is not comprehensive, but instead tries to point out the most relevant facts shown in this chapter in a few sentences. Statements are based on the assumption of plane waves and zero absorption.

Nonlinear Susceptibility: The nonlinear optical susceptibility $\chi^{(2)}$ in non-centrosymmetric media gives rise to **interactions** of electromagnetic waves with different frequencies, especially the **energy transfer**.

Optical Parametric Amplification: When two waves of different frequencies travel through the same nonlinear media, the one with higher frequency (called **pump** wave) gets depleted, while the other one (called **signal** wave) gets amplified. A third wave (called **idler** wave) is generated due to energy conservation. The efficiency rises with higher input powers of all three waves and the idler power is growing **quadratically** with interaction length.

Optical Parametric Oscillation: Providing **feedback** of the amplified signal wave into the nonlinear medium enables optical parametric **oscillation**, if the gain exceeds the loss of the feedback. The pump power resulting in a parametric gain compensating the feedback losses marks the **threshold** of oscillation. Typical thresholds are of the order of 1 W.

Phase Matching: **Dispersion** in the nonlinear medium causes the three interacting waves to undergo a distance-depending **phase shift**. Energy transfer as described above (OPA) is only possible up to a distance called **coherence length** L_c after which the conversion is reversed. L_c is usually small and of the order of 10^{-5} m. **Quasi-phase matching** uses media with a spatial modulation of $\chi^{(2)}$ to overcome this problem.

Dieses Werk ist copyrightgeschützt und darf in keiner Form vervielfältigt werden noch an Dritte weitergegeben werden.
Es gilt nur für den persönlichen Gebrauch.

Dieses Werk ist copyrightgeschützt und darf in keiner Form vervielfältigt werden noch an Dritte weitergegeben werden.
Es gilt nur für den persönlichen Gebrauch.

2

Setup and Characterization of Optical Parametric Oscillators

"Engineering - this is where the semi-skilled workers realize the work of better minds."

Sheldon Cooper, in the TV series "The Big Bang Theory"

In the scope of this work, two continuous-wave OPOs have been set up for high-resolution spectroscopy in two different frequency regimes. Both of them use the quasi-phase matching technique presented in section 1.5.1 with PPLN as nonlinear crystal. In the following sections technical considerations important for the setup of an OPO are introduced and characteristics of the systems built in this work are presented.

2.1 Experimental Setup of OPOs

As described in chapter 1, an OPO consists of three main units: A pump laser delivering enough power to overcome oscillation threshold, a nonlinear medium to enable frequency mixing, and finally an optical resonator around this medium to provide optical feedback necessary for the oscillation.

Concerning the setup of optical parametric oscillators, a common distinction is the degree of feedback the optical resonator delivers into the nonlinear medium. In the simplest case only one of the idler or signal waves is fed back into the system. An OPO working like that is called *singly-resonant*, regardless of which wave provides the feedback. This type has been treated theoretically in chapter 1. When both of these fields are enhanced in one

Dieses Werk ist copyrightgeschützt und darf in keiner Form vervielfältigt werden noch an Dritte weitergegeben werden.
Es gilt nur für den persönlichen Gebrauch.

or more resonators, the OPO is referred to as *doubly-resonant*. This setup scheme has the advantage of a decreased pump threshold by a factor $2/(1-r_i)$ assuming plane waves compared to the singly-resonant scheme [104], where r_i is the reflectivity of the mirrors for the idler wave. Because of its better frequency stability and enhanced continuous tuning capabilities, the singly resonant OPO is usually preferred in spectroscopic applications, in spite of the increased threshold [104]. This is why in this work, a singly-resonant setup has been chosen. Many experimental details have been implemented as suggested in earlier works dealing with continuous-wave OPOs in the wavelength region around 3 microns (e.g. Refs. [16, 41, 73, 102, 113]).

In the following sections, details about the three crucial parts – pump laser (section 2.1.1), crystal (section 2.1.2) and resonator (section 2.1.3) — necessary to set up a working system like the ones built here are discussed. Section 2.1.4 deals with the assembly to a working system and principal guidelines of operation.

2.1.1 Pump Laser

For the requirements of high-resolution spectroscopy, a stable single-frequency laser with a small linewidth is inevitable. Furthermore, in this work the continuous tuning of idler frequency is performed by tuning the pump laser frequency, which places another specification on this crucial part.

A commercial cw Nd:YAG laser system from Innolight GmbH[1] operating at a wavelength of $\lambda_p = 1.064\ \mu$m was selected as pump source. Relevant

[1]InnoLight – Innovative Laser und Systemtechnik GmbH, Garbsener Landstraße 10, 30419 Hannover, Germany. *http://www.innolight.de*.

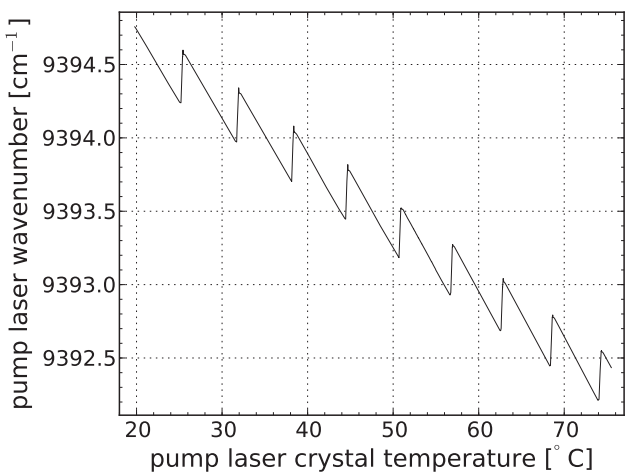

Figure 2.1: Frequency of the pump laser measured with a wavemeter as a function of the temperature of the pump laser crystal. The temperature is determined using a Pt100 platinum resistor. With increasing temperature, the frequency decreases with a tuning coefficient of -3 GHz/K. After 15 GHz (0.5 cm^{-1}) of continuous tuning, mode-hops of roughly 8 GHz occur. On average, the tuning coefficient is about -1.5 GHz/K. The overall tuning range is about 75 GHz (2.5 cm^{-1}). This tuning curve is highly reproducible, and no hysteresis effects could be measured.

Dieses Werk ist copyrightgeschützt und darf in keiner Form vervielfältigt werden noch an Dritte weitergegeben werden.
Es gilt nur für den persönlichen Gebrauch.

specifications are listed in Table 2.1. A small linewidth of $\Delta\nu = 10$ kHz combined with high output power of $P_p = 10$ W makes it suitable as optical pump. It is tuneable over more than 80 GHz by varying the Nd:YAG crystal temperature, with mode-hop free ranges of more than 15 GHz. The tuning curve is printed in Figure 2.1. The tuning behavior of the pump frequency directly translates into idler frequency tuning, when the signal frequency ν_s is kept fixed in the resonator.

Table 2.1: Relevant specifications of the continuous-wave, single frequency OPO pump laser, as given by the manufacturer Innolight GmbH.

Parameter	Value	Unit
emission wavelength	1064	nm
output power	>8	W
spectral linewidth[a]	<5	kHz
frequency drift[b]	< 1	MHz/min
beam quality factor[c] M^2	<1.2	-
polarization extinction ratio[d]	>100	-
thermal tuning range	>65	GHz
mode-hop-free tuning range	>15	GHz
thermal tuning bandwidth[e]	>3	GHz/s
piezomech. tuning range	±100	MHz
piezomech. tuning bandwidth[f]	>100	kHz

[a] On a timescale of 100 ms.
[b] Allan variance.
[c] single-frequency output, TEM_{00} mode, beam roundness < 1.1.
[d] defined as the intensity ratio. The laser has a horizontal polarization output.
[e] thermal tuning coefficient is $\Delta\nu/\Delta T < -3$ GHz/K.
[f] piezomechanical tuning coefficient is $\Delta\nu/\Delta U > 1$ MHz/V @ 1064 nm.

2.1.2 Nonlinear Crystals and Crystal Oven

In this work, Lithium Niobate has been used as nonlinear medium. Two crystals purchased from HC photonics[2] have been employed, both of which are congruent Lithium Niobate crystals doped with 5% magnesium oxide. The doping has proven to reduce optically induced refractive index inhomo-

[2] HC Photonics Corporation, F4, No. 2, Technology Rd. V, Hsinchu Science Park, Hsinchu 300, Taiwan. *http://www.hcphotonics.com.*

Dieses Werk ist copyrightgeschützt und darf in keiner Form vervielfältigt werden noch an Dritte weitergegeben werden.
Es gilt nur für den persönlichen Gebrauch.

geneities which hinder the desired nonlinear interaction (see Refs. [3, 21]).[3] However, to prevent problems with such modulations in the index of refraction, the crystals have to be kept at temperatures exceeding 50° C, when traversed by beams with high optical intensity.

The crystals employed are cut in a way that their facets are perpendicular to optical axis (and the grating vector $2\pi/\Lambda$) in order to prevent distortion and offset effects for the beams traveling through them. However, since the facets are plane-parallel surfaces, undesired etalon effects can occur, introducing a second resonator due to the partly reflecting surfaces. These can severely complicate the frequency stability conditions and are avoided by an anti-reflection coating. Besides reducing etalon effects, the coating reduces losses in the resonator, since the signal beam has to pass each crystal facet twice in one cavity round trip.

For easy achievement of phase matching, the periodic poling technique as described in section 1.5.1 has been applied. Seven distinct poling periods are present in each of the two crystals. Table 2.2 lists relevant specifications of the crystals employed in this work.

The phase matching properties of the crystal do not only depend on the poling period, but also to a large extent on the temperature of the crystal as has been shown in section 1.5.1. For controlling the temperature of the crystal in the range between 50 and 200 °C, it has been placed in an oven which consists of a copper block including heating cartridges, and a top cover which fits the crystal, so it is being enclosed from top and bottom. A Pt1000 platinum sensor has been pressed against the side of the oven near the crystal, as a temperature input for a temperature stabilization. Such a temperature controller has been set up for high temperature stability using common analog control techniques with a proportional and an integral controlling part. Connection schematics of the controller are shown in appendix B. The controller has an estimated absolute accuracy of $\pm 5\,\mathrm{K}$, but much higher precision and stability. This will be estimated from measurements in section 2.2.4.

2.1.3 Signal Cavity

The OPOs built in this work are singly-resonant for the signal beam, and the optical resonator for that wavelength has to be set up. The mirrors of the resonator have to be highly reflective for the near-infrared radiation with wavelengths $\lambda_s = 1.3 - 1.8\,\mu\mathrm{m}$, because the pump threshold according to

[3] This optically induced refractive index changes are often referred to as "optical damage", though usually this effect is reversible.

Dieses Werk ist copyrightgeschützt und darf in keiner Form vervielfältigt werden noch an Dritte weitergegeben werden.
Es gilt nur für den persönlichen Gebrauch.

Table 2.2: Relevant specifications of the nonlinear crystals of periodically poled $LiNbO_3$, doped with 5% MgO, as given by HC photonics corp. Crystal "1" is employed in OPO system 1, and crystal "2" is employed in OPO system 2.

Parameter	Crystal "1"	Crystal "2"	unit
length	50	49	mm
height	0.5	0.5	mm
width	8.2	10	mm
	28.5 (4.0)	24.40 (5.4)	μm
	29.0 (3.8)	24.73 (5.3)	μm
	29.5 (3.6)	25.13 (5.2)	μm
poling periods[a]	30.0 (3.4)	25.40 (5.1)	μm
	30.5 (3.2)	25.73 (5.0)	μm
	31.0 (2.9)	26.13 (4.9)	μm
	31.5 (2.6)	26.40 (4.8)	μm
reflectivity r_p for pump[b]	< 2	< 1	%
reflectivity r_s for signal[c]	< 1	< 1	%
reflectivity r_i for idler[d]	n.a.	< 10	%

[a]Values in parentheses are the approximate idler wavelengths (at $T \approx 120\,°C$) for the corresponding period with a pump at $\lambda_p = 1064\,nm$. Crystals have been marked with red dots by the manufacturer on the sides of the short poling period to clarify the orientation.

[b]Estimation from the coating report for $\lambda_p = 1064\,nm$. The manufacturer's specification is $r_p < 1.5\%$ for crystal "1" and $r_p < 1.0\%$ for crystal "2", both at $\lambda_p = 1030\,nm$.

[c]Wavelengths $\lambda_s = 1.45 - 1.65\,\mu m$ (crystal "1"), $\lambda_s = 1.25 - 1.4\,\mu m$ (crystal "2")

[d]For crystal "1" no values have been specified by the manufacturer due to lack of measurement tools, but an anti-reflection coating calculated for $2.9 - 4.0\,\mu m$ has been applied. Values for crystal "2" apply for $\lambda_i = 4.4 - 5.4\,\mu m$.

equation (1.43) is proportional to the losses in the resonator. At the same time, the mirrors have to be highly transparent for the pump wavelength $\lambda_p = 1.064\,\mu m$ and the idler wavelengths $\lambda_i = 2.5 - 5.4\,\mu m$ for a truly singly-resonant operation.

These requirements can only be met by dielectric mirrors which are specifically coated for the given wavelengths. For the systems relevant in this work, two different sets of mirrors have been purchased from the company layertec[4], each with a different coating. One set for use in combination with crystal "1" with signal wavelengths $\lambda_s = 1.45 - 1.85\,\mu m$ (corresponding idler wavelengths $\lambda_i = 2.5 - 4.0\,\mu m$), whose transparency curves can be seen in Figure 2.2. The second set of mirrors has been coated for use with crystal "2" and signal wavelengths $\lambda_s = 1.2 - 1.4\,\mu m$ (corresponding idler wavelengths

[4]layertec GmbH, Ernst-Abbe-Weg 1, D-99441 Mellingen. *http://www.layertec.de*

Dieses Werk ist copyrightgeschützt und darf in keiner Form vervielfältigt werden noch an Dritte weitergegeben werden.
Es gilt nur für den persönlichen Gebrauch.

Table 2.3: Specified reflectivity of the front surface of the OPO resonator mirrors. The value for the rear side is given in parentheses. Coating A is employed in OPO system 1, coating B in OPO system 2.

Reflectivity	Coating A[a]	Coating B[b]
r_p (pump)	$<$ 5(1)%	$<$ 5(1)%
r_s (signal)	$>$ 99.9(-)%	$>$ 99.9(-)%
r_i (idler)	$<$ 10(2)%	$<$ 5(1)%

[a]With this mirror set, the wavelength ranges are defined as follows: pump $\lambda_p = 1.064\,\mu$m, signal $\lambda_s = 1.43 - 1.87\,\mu$m, and idler $\lambda_i = 2.45 - 4.00\,\mu$m. The batch No. for this coating is R0407007.

[b]With this mirror set, the wavelength ranges are defined as follows: pump $\lambda_p = 1.030\,\mu$m, signal $\lambda_s = 1.2 - 1.4\,\mu$m, and idler $\lambda_i = 4.0 - 5.5\,\mu$m. Though the pump wavelength is given as 1030 nm, no significant change is expected compared to 1064 nm according to the coating report. The batch No. for this coating is R0608076.

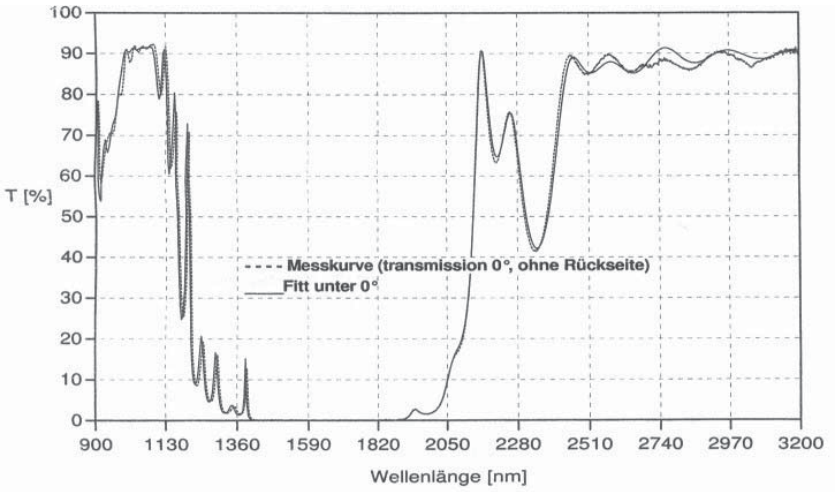

Figure 2.2: OPO cavity mirror transmission graph over wavelength. The coating has been purchased for high transmission at the pump wavelength $\lambda_p = 1.064\,\mu$m and at idler wavelengths $\lambda_i = 2.5 - 4\,\mu$m, and for high reflectivity at signal wavelengths $\lambda_s = 1.4 - 1.9\,\mu$m.

$\lambda_i = 4.4 - 9.0\,\mu$m). The coating specifications are summarized in Table 2.3 as given by the manufacturer.

The resonator for an OPO should provide feedback in the signal frequency with losses as low as possible, because the threshold is proportional to the loss according to equation (1.43). In an OPO with a linear resonator, the signal beam has to pass a surface of the nonlinear crystal four times before it can reproduce itself. In a ring resonator, this number of passes is reduced to two. Although in a ring configuration, the number of reflections on a mirror surface in one round trip is one or two times higher than with the linear one, losses on these reflections on a HR-coated surface are usually much smaller than reflection losses on transmission through the AR-coated crystal facet. To set up a low-loss cavity enabling a low oscillation threshold, the ring configuration is chosen in this work.

Dieses Werk ist copyrightgeschützt und darf in keiner Form vervielfältigt werden noch an Dritte weitergegeben werden.
Es gilt nur für den persönlichen Gebrauch.

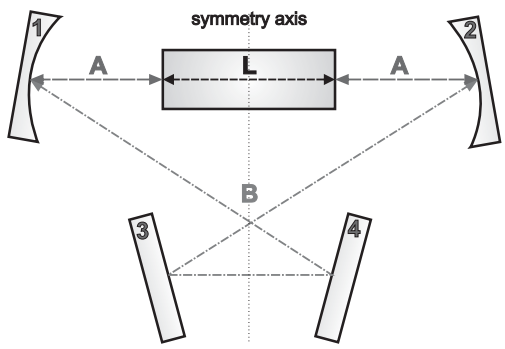

Figure 2.3: The OPO cavity consists of a symmetric arrangement of two concave mirrors (1,2) with focal length f and two plane (3,4) mirrors which are highly reflective for the signal radiation around 1.5 μm wavelength. It is also referred to as "bow-tie" ring cavity, where the beam reproduces after the fourth reflection. The PPLN crystal of length L is centered between the two curved mirrors. In the following, the distance between one crystal facet and the curved mirror is labeled A and the distance between the two curved mirrors is designated with B.

For stability reasons, the OPO resonator needs focusing optical elements. This fact can be readily seen from the ABCD-formalism of gaussian optics as introduced in Ref. [54]. A stable setup can be simulated using this formalism and assuming a ring resonator of type "bow-tie" as shown schematically in Figure 2.3. This type of cavity is a standard design as seen in other cw OPO systems and has been reported in Ref. [12] for the first time. It is widely used in similar systems (Refs. [82,115]). The labeling of the cavity geometry parameters can be also read from Figure 2.3. Because the reflecting surfaces of the curved mirrors are spherical, the angle of incidence on these should be kept as small as possible to reduce astigmatism of the signal beam in such bow-tie setups.

The beam areas of the pump and signal beam inside the nonlinear medium have great effect on the threshold and oscillation conditions of an OPO. Equation (1.43) shows a proportional dependence of the beam area on the threshold, which is why focusing has to be optimized carefully. A theoretical model by Guha (Ref. [37]) predicts the optimum value for the size of the foci of pump and signal beams in the limit of gaussian waves for a given crystal geometry. For that it is convenient to define a parameter ξ called the focusing parameter. It is defined as $\xi = L/b = \lambda L/(2\pi w_0^2)$, with L being the crystal length, and b the confocal parameter of the relevant beam, $b = 2\pi w_0^2/\lambda$. Here is λ the wavelength and w_0 the waist[5] of the beam. Guha *et al.* predict optimal conversion, when the values of ξ_p for the pump and ξ_s for the signal beam are nearly equal and in the range between 1 and 7. At high ξ values the beams are more divergent, and the limited aperture of the crystal[6] hinders the beams to propagate freely into and out of the crystal and complicates the

[5]In this work, the radius w of a gaussian beam is used as the distance to the center, where the intensity has dropped to $1/e^2$ of the center value. The waist w_0 is the minimum value of that radius for a freely propagating beam.

[6]The crystal's aperture is 500 μm in our case, compare Table 2.2 (height of crystals).

Dieses Werk ist copyrightgeschützt und darf in keiner Form vervielfältigt werden noch an Dritte weitergegeben werden.
Es gilt nur für den persönlichen Gebrauch.

alignment. This is illustrated in Figure 2.5, which will be explained in more detail in the following. Thus, in the present OPOs the focusing parameters have been chosen to be around 1.5, which translates into the beam waists $w_{0,p} \approx 80\,\mu\text{m}$ and $w_{0,s} \approx 95\,\mu\text{m}$ for the pump and signal, respectively.

The focus of the pump wave can be adjusted quite easily using common lenses. However, this is not true for the signal wave, which builds up in the OPO resonator. Its beam profile development along the resonator and crystal only depends on the resonator geometry. Assuming a perfect gaussian beam for the signal wave, the ABCD-matrix formalism as reviewed in Ref. [54] has been used to calculate the signal beam waist in the center of the crystal in a resonator with geometric properties and labels as seen in Figure 2.3. The matrices relevant for the beam propagation in the cavity are:

$$M_1 = \begin{pmatrix} 1 & L/2n \\ 0 & 1 \end{pmatrix}, \qquad M_2 = \begin{pmatrix} 1 & A \\ 0 & 1 \end{pmatrix}$$
$$M_3 = \begin{pmatrix} 1 & 0 \\ -1/f & 1 \end{pmatrix}, \qquad M_4 = \begin{pmatrix} 1 & B/2 \\ 0 & 1 \end{pmatrix} \quad .$$

The matrix for one complete cavity round trip M can be expressed by the multiplication of these, so that the result is

$$M = M_1 \cdot M_2 \cdot M_3 \cdot M_4 \cdot M_4 \cdot M_3 \cdot M_2 \cdot M_1 \equiv \begin{pmatrix} M_A & M_B \\ M_C & M_D \end{pmatrix} . \tag{2.1}$$

Given a complex gaussian beam parameter q_0 in the center of the crystal, the optical system described by the transfer matrix M changes it to q_0', which is determined by the ABCD-law as

$$q_0' = \frac{M_A \cdot q_0 + M_B}{M_C \cdot q_0 + M_D} \quad . \tag{2.2}$$

Assuming a stable cavity, the gaussian beam parameter q_0 in the center of the crystal has to reproduce after traversing the optical system represented by the matrix M, so that $q_0' = q_0$. This, together with the assumption that the waist is positioned at the center of the crystal leads to a purely imaginary parameter q_0 at this place, yields the relations $M_A = M_D$ and

$$q_0 = -i\sqrt{-M_B/M_C} \equiv -i\frac{\pi}{\lambda w_0^2} \quad , \tag{2.3}$$

which connect the matrix coefficients of M with the waist w_0 for a given wavelength.

Figure 2.4 shows the result of such a calculation for a signal wavelength of $\lambda_s = 1.5\,\mu\text{m}$ with varying cavity distances A and B. The radius of curvature

Dieses Werk ist copyrightgeschützt und darf in keiner Form vervielfältigt werden noch an Dritte weitergegeben werden.
Es gilt nur für den persönlichen Gebrauch.

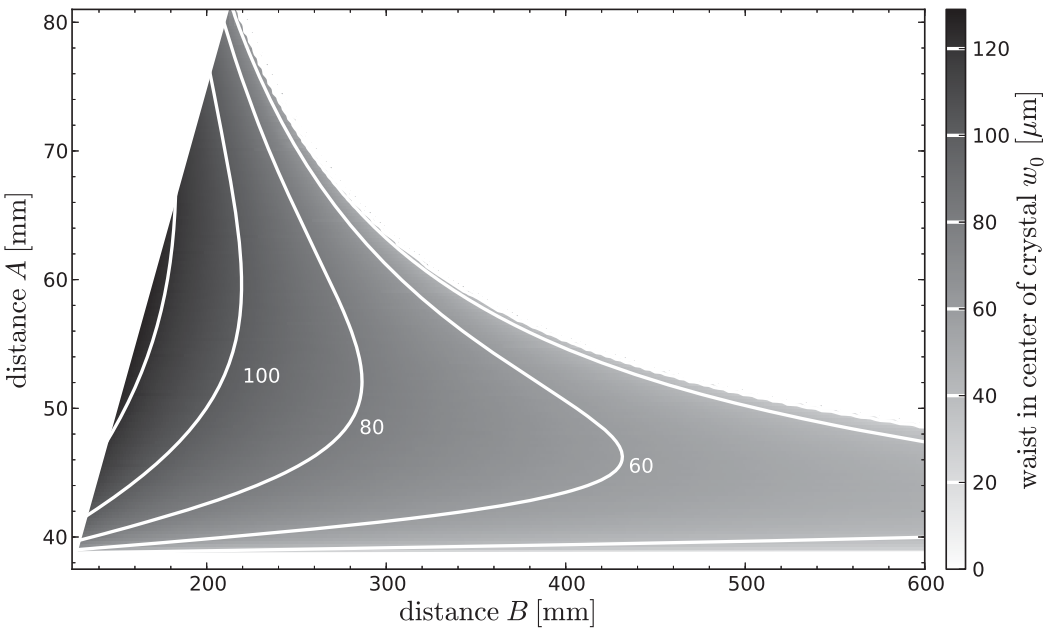

Figure 2.4: Gaussian beam waist w_0 of the signal radiation with λ_s =1.5 μm wavelength in a ring cavity with labels A and B as depicted in Figure 2.3. This calculation is based on a fixed crystal length of $L = 5$ cm with a refractive index of 2.2 and two curved mirrors with focal length $f = 5$ cm. White regions in the plot are unstable or geometrically impossible ($B < 2A+L$) cavity configurations. For other wavelengths λ, the waists have to be multiplied with a factor $\sqrt{\lambda/\lambda_s}$.

of the concave mirrors (mirror 1 and 2 from Figure 2.3) is presumed as $r = 100\,\mathrm{mm}$ and the length of the crystal is 50 mm with a refractive index of 2.2. The graph shows that a desired signal waist of $w_{0,s} \approx 95\,\mu\mathrm{m}$ in the middle of the crystal is reached with the approximate cavity parameters $A = 55\,\mathrm{mm}$ and $B = 235\,\mathrm{mm}$.

Figure 2.5 shows the calculated beam radius w_s of the signal beam as it travels through a typical bow-tie cavity configuration as pictured in Figure 2.3. In that plot, a signal beam waist of $80\,\mu$m has been assumed to be stable in the resonator. The secondary beam waist between the plane mirrors is roughly $w_{0,s} = 200\,\mu\mathrm{m}$, with the assumed position of the spherical mirrors ($A = 55\,\mathrm{mm}$) . The plot also shows the hypothetical free propagation of the signal for the case when the crystal is absent in the resonator (dotted curve). There is an offset of roughly 15 mm of this waist position to the center of the (absent) crystal. This illustrates the effect of the crystal on the propagation on the gaussian beam, which has to be taken into account when aligning the beam waist of the pump beam as described in the following section.

Dieses Werk ist copyrightgeschützt und darf in keiner Form vervielfältigt werden noch an Dritte weitergegeben werden.
Es gilt nur für den persönlichen Gebrauch.

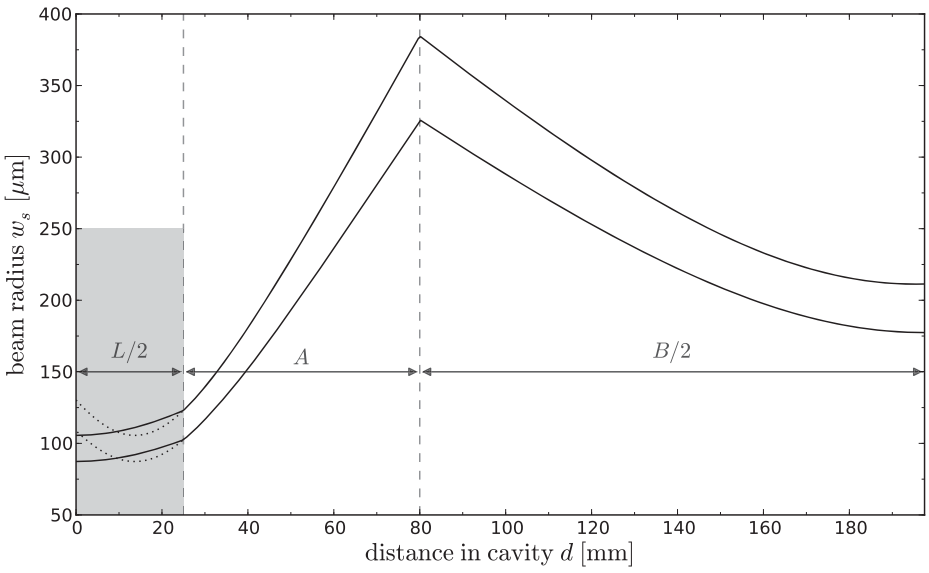

Figure 2.5: Signal beam radii w_s calculated over one half-length of one OPO cavity configuration for two wavelengths 1.3 μm (lower curve, corresponding to limit of OPO system 2) and 1.9 μm (upper curve, corresponding to limit of OPO system 1). The crystal of refractive index 2.2 has a total length of $L = 5$ cm and a height of 500 μm. It is denoted as the gray shaded area. Cavity dimensions of $A = 55$ mm, $B = 235$ mm and the focal length of the concave mirrors $f = 5$ cm result in a waist in the center of the crystal $w_{0,s} \approx 100$ μm. The dotted lines describe the free-space propagation of the beams without refraction at the crystal surface which results in a waist displacement of ≈ 12 mm with respect to the crystal center. This number is of help for the alignment of the pump laser as described in section 2.1.4.

2.1.4 System Setup

All three main elements of the OPO have been described in detail in the preceding sections. In order for the OPO to work, the assembly of these parts requires also some attention. The setup is now described exemplarily for the OPO operating around 3 micrometer idler wavelength, which will be referred to as "OPO system 1" from now on. The system differs only in a few details from the second OPO running around 5 micrometer idler wavelengths ("OPO system 2"), which are addressed in a later section.

OPO system 1 for idler wavelengths around 3 microns

OPO system 1 employs the combination of crystal 1 and cavity mirrors with coating A. A schematic setup is shown in Figure 2.6. After the pump beam leaves the laser, it is guided through a Faraday isolator serving as an optical diode. It has been purchased from EOT[7] and suppresses reflections of the

[7]Electro-Optics Technology, Inc., 5835 Shugart Lane, Traverse City, MI 49684, USA *http://www.eotech.com*

Dieses Werk ist copyrightgeschützt und darf in keiner Form vervielfältigt werden noch an Dritte weitergegeben werden.
Es gilt nur für den persönlichen Gebrauch.

pump beam traveling backwards into the laser by a factor of $> 30\,\mathrm{dB}$ whilst transmitting more than 92% of the beam intensity in the forward direction. Laser radiation being reflected back into the pump, for example from the crystal front facet, has a severe destabilizing effect on the pump intensity and therefore has to be avoided.

Besides ensuring that the pump laser is running stable, a way has to be found to enable tuning of the pump intensity traveling through the nonlinear crystal without changing the operating conditions of the pump laser itself. Though the pump laser intensity can be set using different pump currents of the MOPA, the alignment of its optical beam slightly changes as well as the beam profile and size. As a consequence, the MOPA pump laser is always operated at the maximum intensity setting to ensure stable conditions in the OPO. For the tuning of the pump power, there is a combination of a wave retarder with a polarizing beam splitter cube as the second optical element in the assembly, which have both been purchased from Bernhard Halle Nachfl. GmbH[8]. The linear polarization plane can be set by rotating the half-wave retarding plate. After that, the polarizing beam splitter cube reflects the part of the beam polarized in the s-plane and transmits the part that is polarized in the p-plane. So the intensity transmitted through the cube can be varied between 0 and 100% just by rotating the half-wave plate.

Finally, as the last element before entering the OPO resonator, the pump beam passes an anti-reflection coated plane-convex lens with a focal length of $f = 150\,\mathrm{mm}$, focusing the pump wave into the crystal. In the alignment process, the waist size and position is checked with a commercial Thorlabs[9] beam profiler type BP104-IR behind the first OPO mirror (designated with "1" in Figure 2.3). For this purpose, the crystal mount and the other mirrors are temporarily removed from the optical table. The focal length of the lens is chosen so the waist is $w_{0,p} \approx 80\,\mu\mathrm{m}$, for the reasons decribed in the preceding section. Finally, the position of the lens is varied to place the beam waist roughly 12 mm before the spot where the center of the crystal is going to be placed after this alignment process. This short distance compensates for the effect of refraction at the crystal front facet as is shown in Figure 2.5 for the signal beam as dotted line, and ensures that the pump beam waist is at its center, when the crystal is inserted between the curved mirrors. All mentioned elements have an anti-reflection coating for the near-infrared around 1064 nm wavelength to reduce losses and backward reflections of the pump laser to less than 1% each.

[8] Bernhard Halle Nachfl. GmbH, Hubertusstraße 10, D-12163 Berlin, Germany. *http://www.b-halle.de*

[9] Thorlabs GmbH, Hans-Boeckler-Straße 6, 85221 Dachau, Germany. *http://www.thorlabs.de*

Dieses Werk ist copyrightgeschützt und darf in keiner Form vervielfältigt werden noch an Dritte weitergegeben werden.
Es gilt nur für den persönlichen Gebrauch.

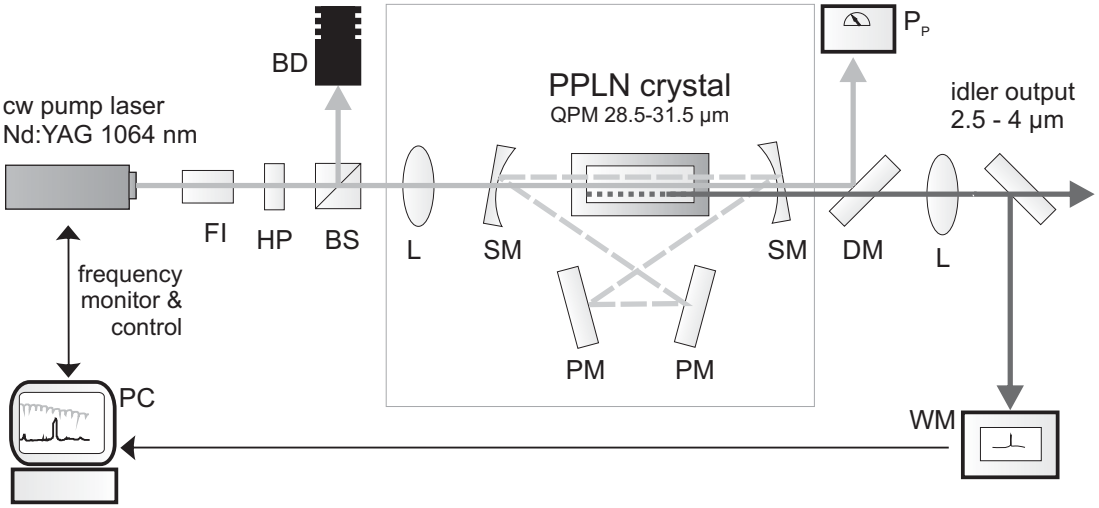

Figure 2.6: Schematic Setup of the OPO system for idler wavelengths around 3 micrometer. A continuous-wave Nd:YAG laser serves as pump source at 1.064 μm wavelength. It is focused using a lens (L) into the PPLN crystal. The signal radiation is kept resonant in a bow-tie cavity consisting of two plane mirrors (PM) and two spherically concave mirrors (SM). A dichroic mirror (DM) extracts the residual pump power to a power meter (P). A beamsplitter extracts a fraction of the idler power to produce a frequency readout of a wavemeter (WM).

The OPO cavity design has been described in theory in the preceding section and a photograph of the resonator can be seen in Figure 2.7 for the steady-state oscillation. All relevant waves in the OPO process are infrared, but there are small fractions of visible light generated as well as visible in Figure 2.7. Phase-matching of these frequencies is not intended and the power generated in the second harmonic of the pump laser (green, 532 nmm wavelength), the sum-frequency of signal and pump wave (red to orange, around 600 nm wavelength) and other possible frequency combinations is estimated to be on the sub-mW scale. However, the green light offers a good means to align the OPO resonator. The onset of oscillation is then accompanied by the generation of red to orange light. Also visible in Figure 2.7 are the different poling periods of the crystal.

For this OPO system, the mirror set with coating "A" and the PPLN crystal "1" have been employed. As can be seen in Figure 2.7, no extra intra-cavity elements for signal frequency selection purposes have been used. Commercial OPO systems[10] as well as some other home-built OPO systems in academics use an etalon to increase the frequency stability and reduce mode-hops [41, 73, 102, 113]. However, etalons have the drawback of adding

[10] Argos SF series, Lockheed Martin Aculight, 22121 20th Avenue, SE Bothell, WA 98021, USA. *http://aculight.com*

Dieses Werk ist copyrightgeschützt und darf in keiner Form vervielfältigt werden noch an Dritte weitergegeben werden.
Es gilt nur für den persönlichen Gebrauch.

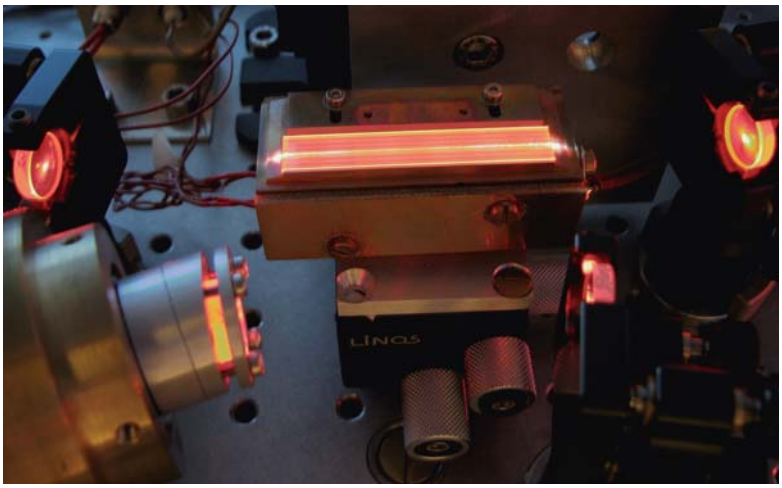

Figure 2.7: Photograph of the cavity of OPO system 1 for 3 micrometer idler wavelength, when oscillation occurs. Besides the infrared radiation, visible red light is generated in the crystal as sum frequency of signal and pump wave. The crystal poling periods are also visible.

losses into the resonator and therefore increase the oscillation threshold of the OPO. In this work, the approach of Vainio *et al.* [110] without any intracavity elements besides the crystal is followed. It is sufficient to produce frequency-stable output, thus an etalon has been omitted.

The cavity is kept fixed during measurements and the idler frequency is tuned by varying the pump laser frequency using the laser crystal temperature set point, which is controllable using an analog voltage in the range of $\pm 10\,\mathrm{V}$, which translates to an average frequency change of $\pm 15\,\mathrm{GHz}$ ($\pm\,0.5\,\mathrm{cm}^{-1}$, compare Table 2.1). The signal is resonant in the fixed cavity and does not change its frequency over the pump scan.

To improve the temperature stability of the crystal and protect the optical resonator path length from air currents during any measurement, the whole crystal-cavity system is enclosed in a plexiglass box harboring only small windows for the pump, idler beam, and all cables for the temperature control of the crystal oven.

The OPO output consists of three collinear beams of different frequencies: The residual, but still highly intense pump, the signal leaking out of the cavity, and the desired idler radiation. The signal power outside the resonator is typically on the scale of a few mW, and does not disturb most experiments. To separate the pump and idler frequencies, a low-pass filter in form of a common Nd:YAG laser line mirror is placed in the beam path, reflecting 99.9% of the pump intensity into a beam dump or a power meter (sensor model PM-30 and meter model FieldMax II-TO from Coherent[11]). Behind that last mirror, the idler radiation is ready for use in an experiment.

Depending on the experimental requirements on the frequency accuracy, different efforts have to be made for the calibration process. Just by using the

[11] Coherent Deutschland GmbH, Dieselstraße 5b, 64807 Dieburg, Germany. *http://www.coherent.de.*

Dieses Werk ist copyrightgeschützt und darf in keiner Form vervielfältigt werden noch an Dritte weitergegeben werden.
Es gilt nur für den persönlichen Gebrauch.

information of the poling period and the temperature of the crystal, one can estimate the idler frequency to an accuracy of roughly 100 cm^{-1}, depending on the exact temperature and poling period in use. As a very useful tool to measure the idler frequency, a wavemeter (Bristol Instruments[12], type 621A-IR) is employed as shown in Figure 2.6. For this purpose, a BaF_2 window serves as a beam splitter to couple about 5% of the idler power into this wavemeter. It has a specified absolute accuracy of better than 0.2 ppm at a wavelength of $\lambda = 1\,\mu$m and a repeatability over an integration time of 5 minutes of better than 0.06 ppm at the same wavelength. In practice, however, the wavemeter readout was shown to be alignment dependent, and maximum deviations were $\pm 2 \times 10^{-2}$ cm^{-1} at roughly 3000 cm^{-1} in the worst case. Typically, the accuracy reached was below $\pm 3 \times 10^{-3}$ cm^{-1}($\pm$ 90 MHz). Final frequency calibration was done depending on the experiment using the spectrum of a calibration gas and fringes of a reference interferometer as being described in the upcoming chapters. Frequency accuracies of roughly 5×10^{-4} cm^{-1} (15 MHz) have been reached this way.

OPO system 2 for idler wavelengths around 5 microns

Conventionally, PPLN-based continuous-wave optical parametric oscillators only work in the range of the idler wavelength up to $\lambda_i \leq 4.7\,\mu$m [114, 116]. This is due to the steeply rising absorption coefficient α (see section 1.3.1) in the commercially most important available nonlinear medium with possible quasi-phase matching, $LiNbO_3$. A measurement of this absorption by Myers *et al.* can be seen in Figure 2.8 [74]. In chapter 1, the negative effects of absorption in the idler wavelength on the optical parametric oscillation are discussed in detail. The idler output power diminishes as well as the oscillation threshold pump power increases drastically with increasing wavelength. Many pulsed OPOs with idler wavelengths in the region longer than 5 μm have been demonstrated using PPLN material (see for example Refs. [93, 124, 128]), however they lack the small instantaneous bandwidth needed for high-resolution spectroscopy.

Two continuous-wave OPOs have been demonstrated in the region around 5 μm wavelength with a small linewidth (Refs. [52, 108]), which both lacked the ability for a continuous tuning of the idler frequency, which is of fundamental importance for the intended applications. Accepting the limited expected output power on the order of several milli-Watts, an OPO based on PPLN has been set up in the scope of a diploma thesis by Klemann [53]

[12]Bristol Instruments, Inc., Suite 101, 7647 Main Street Fishers, Victor, New York 14564-8909, USA. *http://bristol-inst.com*

Dieses Werk ist copyrightgeschützt und darf in keiner Form vervielfältigt werden noch an Dritte weitergegeben werden.
Es gilt nur für den persönlichen Gebrauch.

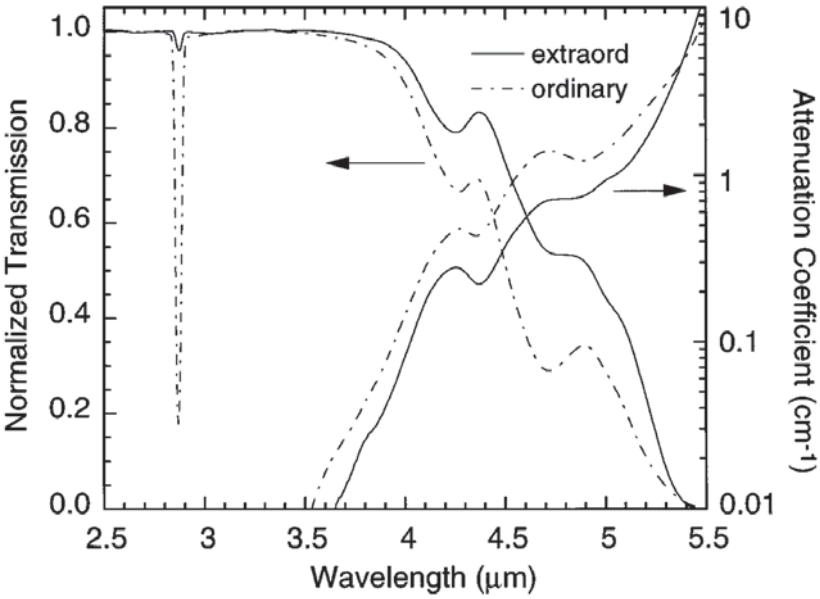

Figure 2.8: Normalized transmission T of a 9 mm thick sample of congruent $LiNbO_3$ and the absorption coefficient α where $T = exp(-\alpha L)$ as functions of wavelength. In the absorption coefficient plot, the peak at $2.9\,\mu$m is omitted for the sake of clarity. Graph taken from Ref. [74].

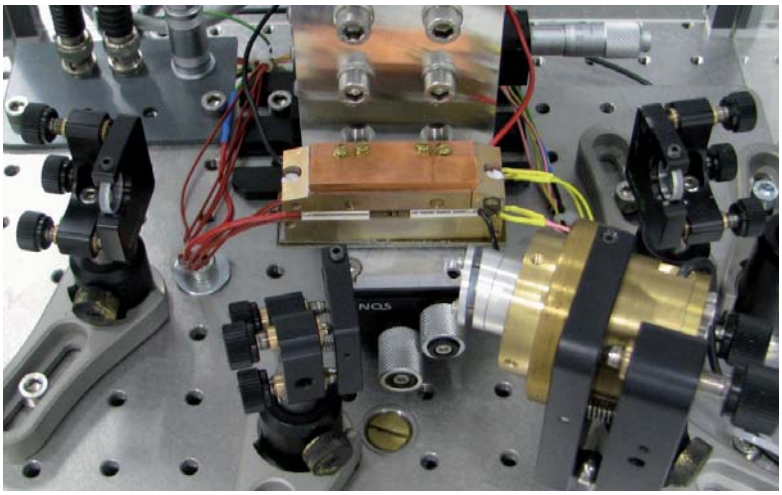

Figure 2.9: Photograph of the OPO cavity for 5 micrometer wavelength. In the upper center, the crystal is lying on the copper oven, covered by another smaller copper block. Four dielectrically coated mirrors are aligned to form a bow-tie shaped cavity.

using the same continuous idler frequency tuning scheme as described in the preceding section.

The basic setup of this OPO system is the same as described above for the OPO designed for 3 micrometer idler wavelength. However, OPO system 2 features the crystal 1 and cavity mirrors with coating B. Figure 2.9 shows a picture taken of the cavity of OPO system 2 and a schematic setup can be seen in Figure 2.10.

Besides the obvious differences in the employed mirror set with coating "B" and the PPLN crystal "2", there is one other discrepancy compared to the setup above. Here, the idler frequency cannot be measured directly using a beam splitter, because the idler output power is too small for being detected by the wavemeter, which needs at least 1 mW of optical input power for a frequency measurement at these long wavelengths. However, the idler frequency can be measured indirectly by determination of the signal frequency

Dieses Werk ist copyrightgeschützt und darf in keiner Form vervielfältigt werden noch an Dritte weitergegeben werden.
Es gilt nur für den persönlichen Gebrauch.

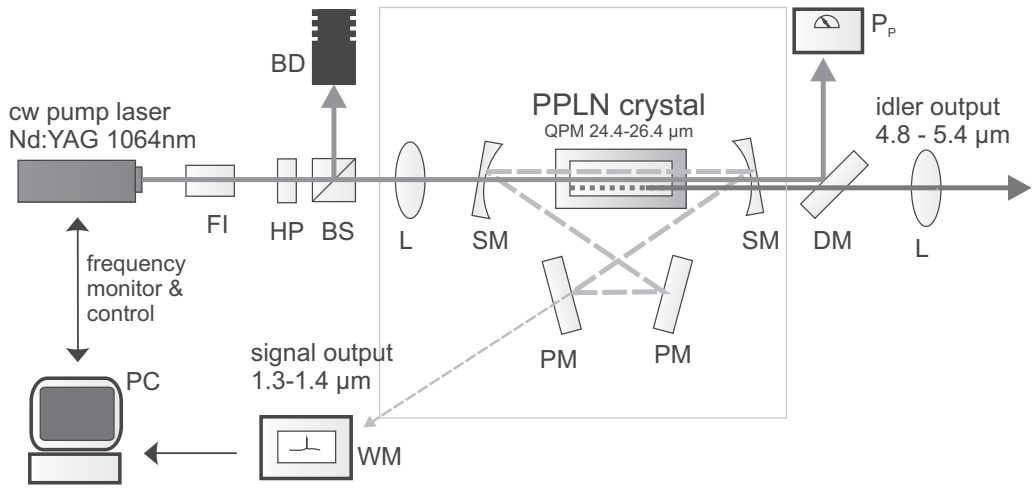

Figure 2.10: Schematic setup of the OPO for idler wavelengths around 5 micrometer. Denominations as follows: FI – Faraday Isolator, HP – half-wave plate, BS – polarizing beam splitter, BD – beam dump, L – spherical lens, SM – concave mirror, PM – plane mirror, DM – dichroic mirror, WM – wavemeter, P_P – powermeter for pump.

ν_s using the wavemeter and recording the temperature of the pump laser. This setup can be seen schematically in Figure 2.10. A look-up table linking the temperature of the scanning pump laser with its frequency ν_p has been recorded once using the wavemeter. It is used to derive the idler frequency ν_i by taking simply the difference of these two: $\nu_i = \nu_p - \nu_s$. This method ensures a frequency accuracy of approximately 100 MHz, which is limited by the accuracy of the wavemeter. Because the frequency display depends on the alignment of the idler beam into the wavemeter, this method of calibration does not necessarily result in the desired final accuracy. A calibration gas is used for eliminating this error as described above. The frequency accuracy reached with this method is on the order of $5\times10^{-4}\,\mathrm{cm}^{-1}$ (15 MHz).

To separate pump and idler beam in this setup, a dichroic mirror as used in OPO system 1 has been employed. However, since fused silica substrates are not transparent for wavelengths longer than $4\,\mu$m, a laser line mirror based on a CaF_2 substrate is applied to this setup.

2.2 OPO Performances

For both OPO systems built here, the requirements especially on the frequency accuracy and linewidth are strict considering their use in high-resolution spectroscopy. In the following, their general characteristics are described, especially in the framework of a spectroscopical application.

Dieses Werk ist copyrightgeschützt und darf in keiner Form vervielfältigt werden noch an Dritte weitergegeben werden.
Es gilt nur für den persönlichen Gebrauch.

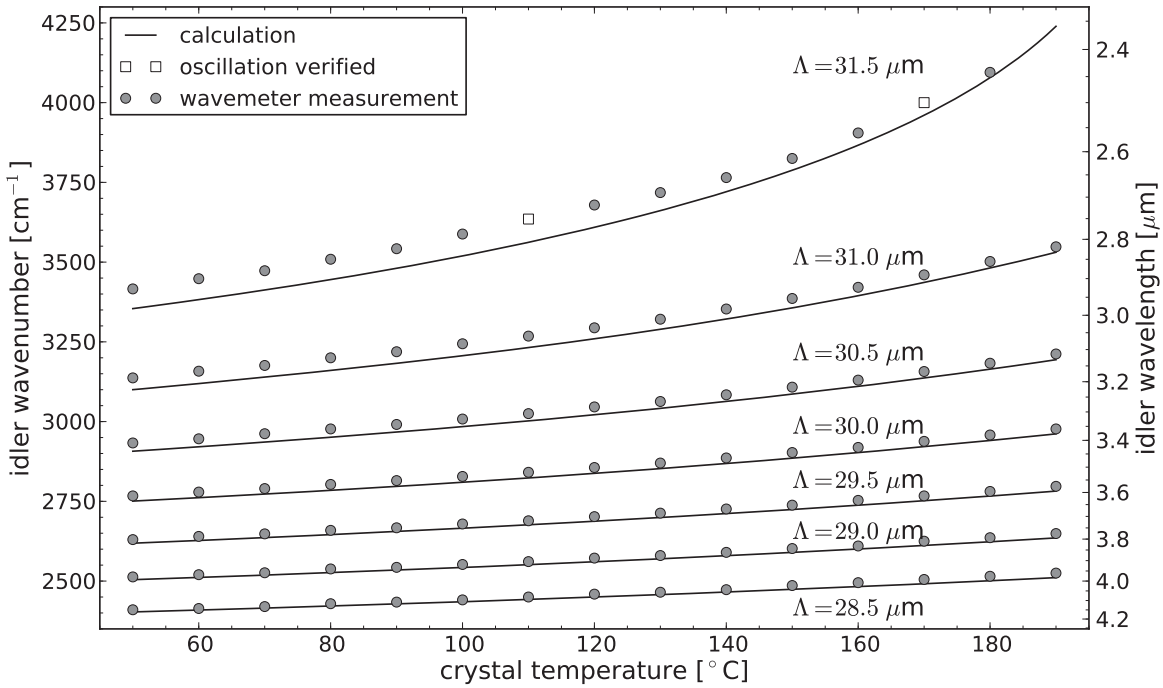

Figure 2.11: Frequency coverage of OPO system 1. Each point designates a frequency measurement on a given poling period at the corresponding crystal temperature using a high-resolution wavemeter. Data marked with white squares have been assigned an interpolated frequency, because a direct measurement with the wavemeter was not possible. Solid lines correspond to the calculated values based on the Sellmeier equation (1.67) from Ref. [28]. Absolute temperature accuracy is estimated to be better than ±5 K.

2.2.1 Idler Coverage and Tuning

Figure 2.11 shows the idler coverage for OPO system 1 with idler wavelengths around 3 micrometer and Figure 2.12 shows the analog graph for the system 2 with idler wavelengths around 5 micrometer. Every point corresponds to a highly accurate frequency measurement done using the wavemeter. However, the absolute accuracy in the temperature measurement of the crystal is estimated to be merely better than ±5 K, so a horizontal shift of the plotted data is possible. The solid lines in the plots correspond to a simulation of the temperature tuning for the corresponding poling period Λ based on the Sellmeier equation (1.67) from Ref. [28].

In Figure 2.11, a frequency coverage spanning the whole range between 2400 and 4000 cm^{-1} is demonstrated. There are two temperatures for the $\Lambda = 31.5\,\mu$m poling period, where no idler frequency could be measured, but oscillation was observed. The oscillation was proven by the presence

Dieses Werk ist copyrightgeschützt und darf in keiner Form vervielfältigt werden noch an Dritte weitergegeben werden.
Es gilt nur für den persönlichen Gebrauch.

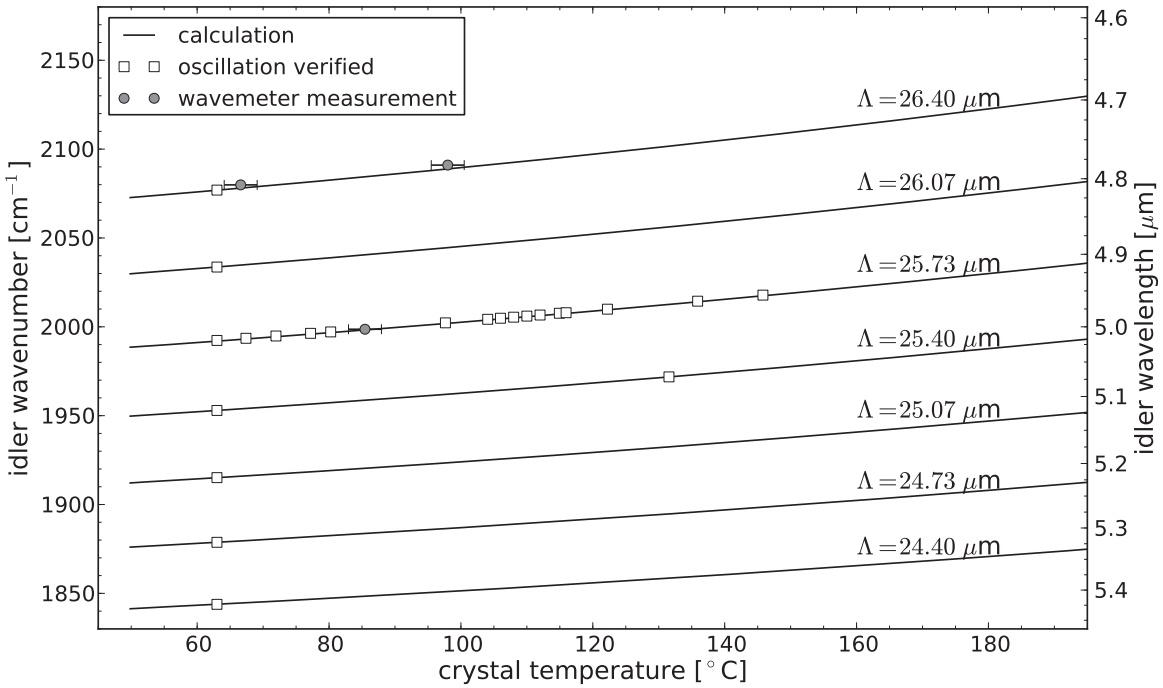

Figure 2.12: Frequency coverage of OPO system 2. Squares designate measurements of temperatures of the crystal, for which idler radiation was detected. Points with horizontal error bars designate frequencies directly measured with a wavemeter, which was not possible in general due to the low power. Data partly taken from Ref. [53].

of red light emerging from the crystal as "parasitic" effect of sum-frequency generation between oscillating signal and the pump wave, which is not phase-matched but produces enough power to be visible. At these frequencies, the idler radiation was absorbed by residual water vapor in the air on the way between the crystal end facet and the wavemeter, which adds up to a total absorption path of approximately 1.5 m.

Figure 2.12 shows the frequency coverage of the OPO with idler wavelengths around 5 μm. Since the idler output power in this case is small and reaches the sensitivity limit of the wavemeter, a direct frequency measurement – as performed for the other OPO system 1 – has only been done for three frequencies, shown as red dots in the plot. All other temperature / poling period combinations, where an oscillation was observed, are plotted as white squares.

In some parts of the spectrum, however, the oscillation threshold could not be reached with our given pump laser, although the phase matching requirements should have been met. This effect is attributed to signal absorption by water vapor in the OPO resonator. Figure 2.13 shows a simulation of signal loss induced by water absorption in the OPO cavity using molecular transitions from the HITRAN04 database [92]. Every water transition

Dieses Werk ist copyrightgeschützt und darf in keiner Form vervielfältigt werden noch an Dritte weitergegeben werden.
Es gilt nur für den persönlichen Gebrauch.

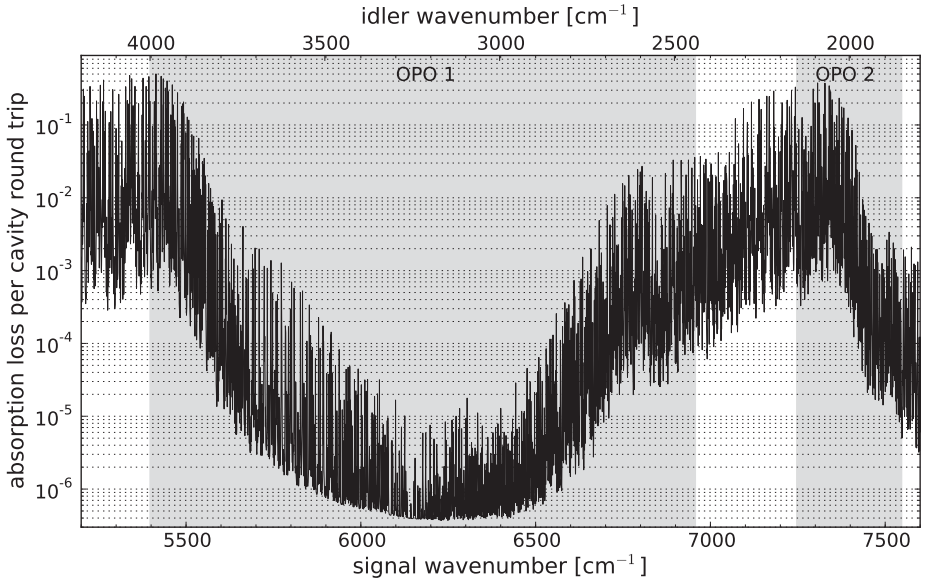

Figure 2.13: Cavity round-trip loss of signal radiation due to absorption of water vapor in laboratory air (40 % relative humidity at room temperature, path length 30 cm), simulated using the HITRAN04 database [92]. The upper frequency scale gives the corresponding idler wavenumber with a pump wavelength of 1064 nm. The grey shaded areas are the signal frequency regions of the two built OPO systems. For details see text.

in the relevant frequency range has been convolved with a Lorentzian profile with a width resulting from its air broadening coefficient (in the range from 10^{-2} to 10^{-3} cm^{-1}atm^{-1}). The simulation is based on standard atmospheric pressure and a relative humidity of 40%[13]. Many single lines are visible in the plot. However, due to pressure broadening and overlapping of lines, a non-negligible absorption continuum is formed. Both at signal frequencies around 5500 cm^{-1} and around 7350 cm^{-1} (idler wavenumbers around 3900 and around 2100 cm^{-1}), the minimum absorption loss per cavity round trip rises to a level of 10^{-3} and higher. Therefore water absorption contributes significantly to the loss per cavity round trip and is dominating the loss in these ranges. The contribution of the mirrors to the cavity round trip loss is below 10^{-3} as specified by the manufacturer.

So it is possible that in some parts of the frequency range of OPO system 2, no oscillation can be observed due to this residual absorption inside the cavity, even though the phase matching of the crystal is suitable. This effect can be described by including the frequency-dependent absorption loss in the formula for the threshold (1.43).

[13] The value of 40% relative humidity corresponds to a number density of water molecules of $n \approx 2.4 \times 10^{17}$ cm^{-3} at room temperature, which means that about 1% of air molecules are water.

Dieses Werk ist copyrightgeschützt und darf in keiner Form vervielfältigt werden noch an Dritte weitergegeben werden.
Es gilt nur für den persönlichen Gebrauch.

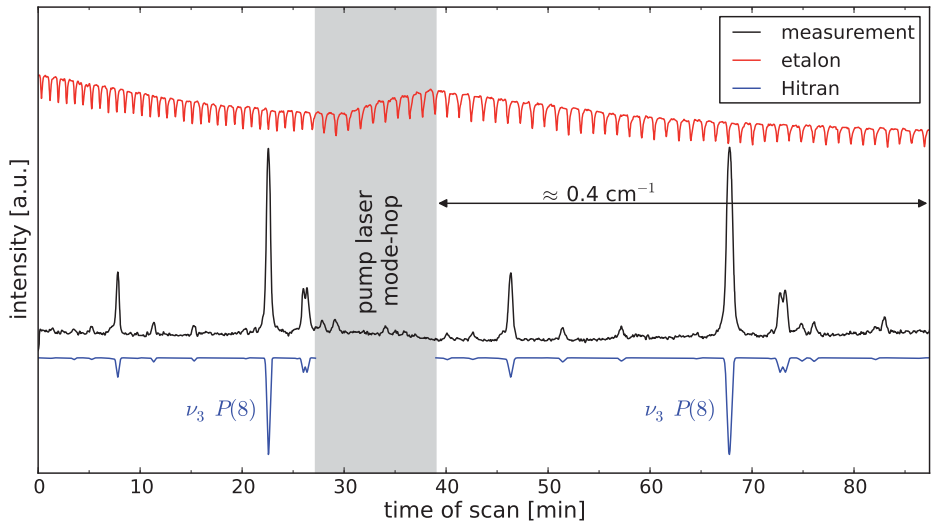

Figure 2.14: Slow frequency scan of OPO system 2 with recorded spectrum of the reference gas OCS and etalon fringes around 2005.9 cm^{-1}. The signal frequency is kept fixed at a value determined by the OPO cavity resonance closest to the maximum of the gain profile. The pump laser frequency was tuned as described in section 2.1.1, resulting in an idler frequency sweep. The scanning speed was decreased during the pump laser mode-hop (gray region), being visible as larger etalon fringe spacings.

As can be seen from the figures 2.11 and 2.12, coarse tuning of the frequency is done by choosing the poling period and temperature. However, continuous tuning is very important for most applications in high-resolution spectroscopy. In principle, the pump laser frequency change directly translates to the idler frequency, when the signal frequency is constant.

Figure 2.14 shows a typical frequency scan of OPO system 2 with a recorded spectrum of a reference gas and a reference etalon, where the pump laser crystal temperature has been decreased monotonously. It can be seen that the idler frequency is tuned continuously without any hops over more than 0.4 cm^{-1}. However, after the first 29 minutes of the scan, the pump laser frequency undergoes one of the precisely reproducible mode-hops as shown in Figure 2.1, while the signal frequency remains stable in the OPO cavity. No signal cavity mode-hop occurred for more than the displayed 80 minutes of the scan.

2.2.2 Threshold

The threshold pump power needed to enable oscillation is another important characteristic for both OPO systems 1 and 2. Ideally, it is well below the maximum power available for a perfect coverage. Especially the OPO with idler wavelengths around 5 μm exhibits greatly varying thresholds depending on the idler frequency the phase matching has been set to. Even some regions have been found, where the threshold rises above the maximum available

Dieses Werk ist copyrightgeschützt und darf in keiner Form vervielfältigt werden noch an Dritte weitergegeben werden.
Es gilt nur für den persönlichen Gebrauch.

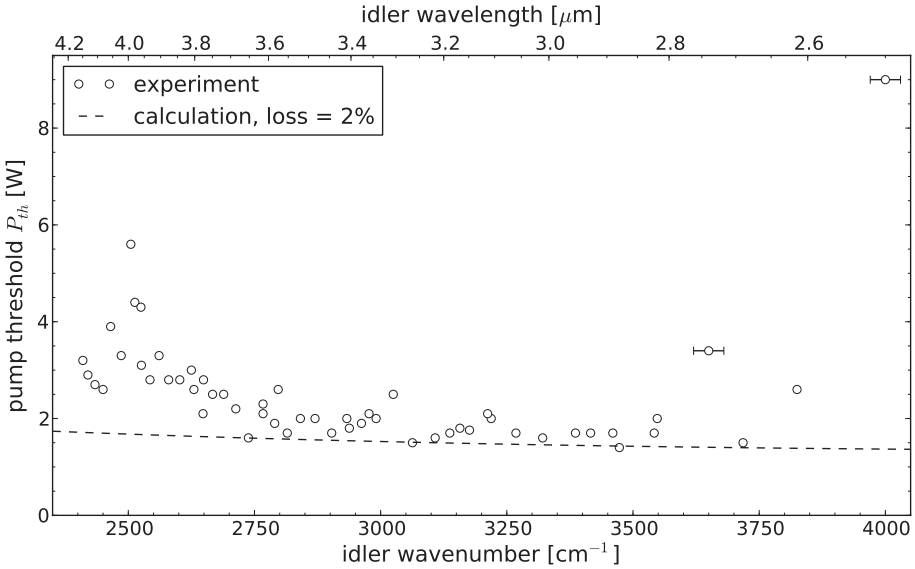

Figure 2.15: Threshold pump power of the OPO with idler wavelengths around 3 μm. For values with the horizontal error bars, no idler frequency measurement was possible and an interpolation from Figure 2.11 has been done. The calculated line corresponds to equation (1.43), which neglects absorption and assumes plane waves. A beam radius of 100 μm has been used for the calculation.

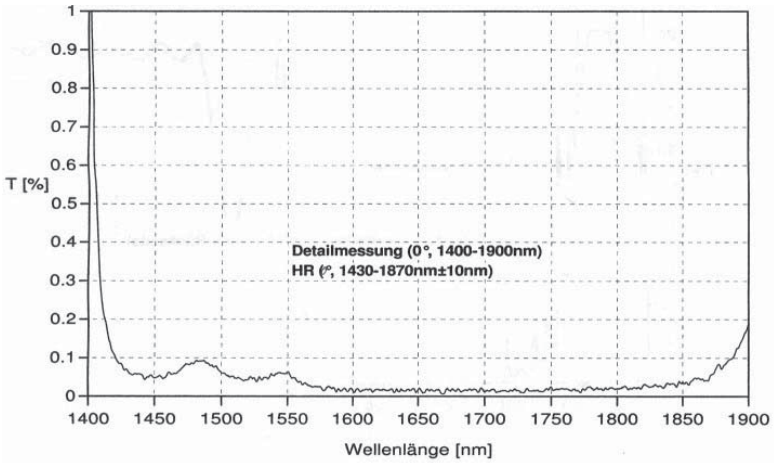

Figure 2.16: Zoom-in of the transmission graph of the OPO cavity mirrors from Figure 2.2. Because the signal beam has an angle of incidence of approximately 15 °, the whole plot shifts slighty (roughly 25 nm according to the manufacturer) towards shorter wavelengths.

pump power of 9 W measured behind the cavity as depicted in Figure 2.10. Furthermore, a low threshold simplifies the setup process because oscillation is more readily achieved with a non-perfect resonator alignment.

Figure 2.15 shows the measured threshold over the entire coverage of OPO system 1. It shows good agreement with a calculated value of the threshold assuming a 2% loss and plane waves as was done in the derivation of the employed formula (1.43). However, the consistency is good in the center of the frequency range and worse at the limit towards shorter and also towards longer idler wavenumbers.

Dieses Werk ist copyrightgeschützt und darf in keiner Form vervielfältigt werden noch an Dritte weitergegeben werden.
Es gilt nur für den persönlichen Gebrauch.

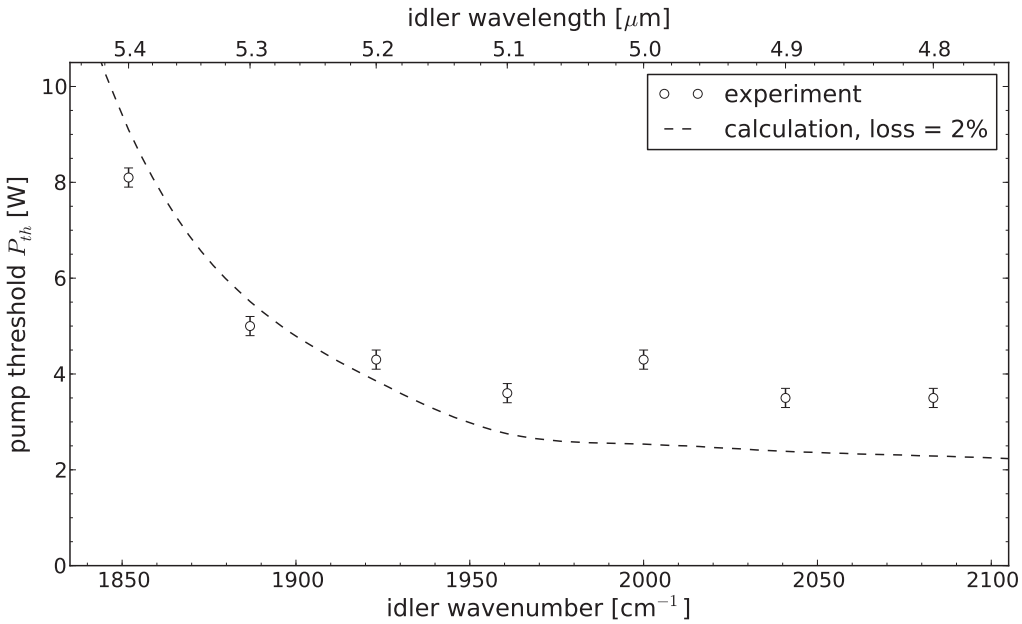

Figure 2.17: Threshold of the home-built OPO system in the mid-infrared around 5 μm wavelength. Measurement taken from Ref. [53]. The theoretical curve is based on a calculation featuring the solution of the coupled wave equations (1.16) to (1.18) with idler absorption in the limit of plane waves. Data for the absorption coefficient are taken from Myers *et al.* [74]. See text for more details.

There are two main factors inducing a frequency dependence of the cavity loss, which is proportional to the threshold: signal absorption by water vapor and the limitations of the dielectric mirror coatings, which are plotted in Figures 2.13 and 2.16, respectively. The general increase is explainable at both sides of the spectrum with the mirror reflectivity curve. For the high-frequency side of the plot the threshold variations are larger, which is an indication for the influence of the signal absorption by water, which can vary a lot over several wavenumbers.

Figure 2.17 shows the corresponding plot of the threshold for the OPO with idler wavelengths around 5 μm. An almost quantitative agreement of the calculated threshold with the measurements can be seen. The model underestimates the threshold in the shorter wavelength region and overestimates it in the longer wavelength region.

Due to the fact that the mirrors are specified to be highly reflective over the whole range, only the signal loss induced by water absorption contributes to the frequency dependent loss, which is indeed higher in the low wavelength region.

2.2.3 Idler Power

For many spectroscopic applications in the mid-infrared, an optical power of a few mW is sufficient. For example, lead-salt tunable diode lasers have been

Dieses Werk ist copyrightgeschützt und darf in keiner Form vervielfältigt werden noch an Dritte weitergegeben werden.
Es gilt nur für den persönlichen Gebrauch.

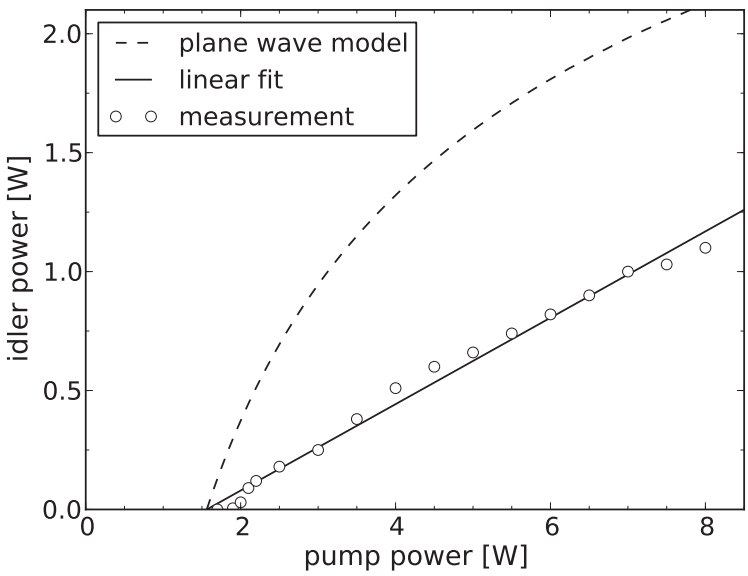

Figure 2.18: Idler Power as a function of Pump Power for the OPO system 1 running on the Λ=30.5 μm poling period at T=150 °C producing an idler wavelength of roughly 3.22 μm. The plane wave model from section 1.4.3, equation (1.57) overestimates the idler power approximately by a factor of two. A linear increasing function reproduces the measurements quite well.

used for many years in simple absorption spectroscopy with an output power of typically one mW or less (See for example Refs. [33, 75, 76]). However, a high power is always desirable to facilitate an easy alignment or to be able to employ cheaper detectors which are less sensitive. Some applications like photo-acoustic spectroscopy of trace gases even need high power for high sensitivity detection (e.g., Ref. [116]).

Generated idler power in an OPO is strongly dependent on the pump power incident on the crystal and the oscillation threshold. Figure 2.18 shows a typical increase of idler power versus pump power. Above threshold, this relation is nearly linear. However, one has to keep in mind that a singly-resonant OPO produces multimode output when it is pumped approximately four times over threshold (Ref. [56]). Recent theoretical models predict such instabilities even for lower powers (Ref. [83]) depending on the wavelength. Suppression of these multi-mode instabilities could be achieved by introducing frequency-dependent losses in the resonator, for example with an etalon or a grating mirror.

As both OPO systems 1 and 2 operate at different regimes in terms of the idler absorption, there is a large discrepancy between the measured idler power in both systems. To get an idea of the accessible idler powers, OPO system 1 has been driven with a constant pump power of 5 W and the idler output power has been recorded using a powermeter. The result is plotted in Figure 2.19. The decreasing powers towards 2400 cm^{-1} can be explained with the decreasing transmission of the laser line mirror based on a SiO_2 substrate separating the pump from the transmitted idler wave. The dip at higher wavenumbers around 3600 cm^{-1} is attributed to idler absorption in laboratory air. Overall, idler powers of 500 mW are readily achieved over a

Dieses Werk ist copyrightgeschützt und darf in keiner Form vervielfältigt werden noch an Dritte weitergegeben werden.
Es gilt nur für den persönlichen Gebrauch.

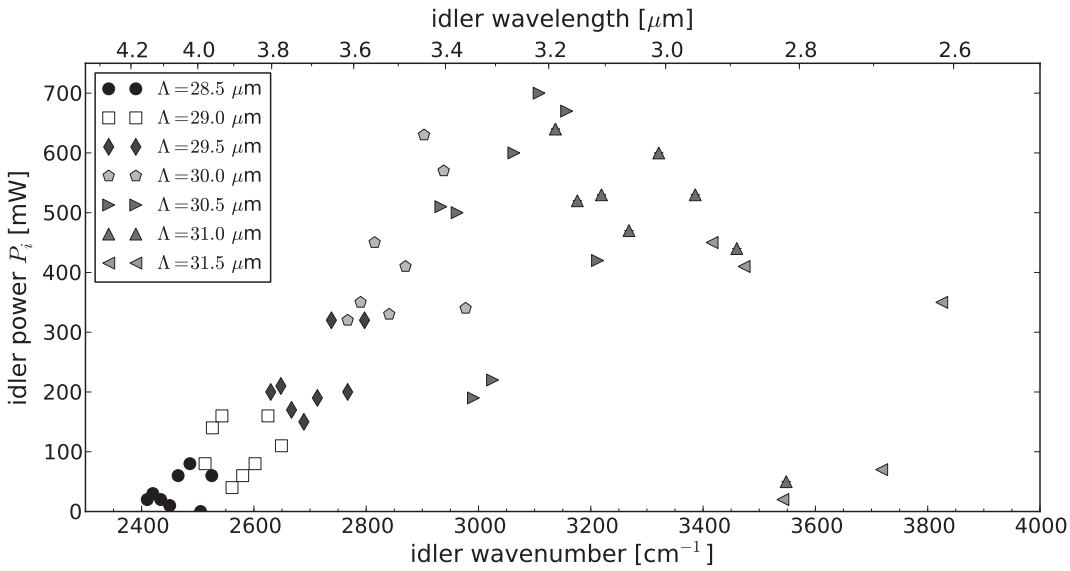

Figure 2.19: Idler Power as function of idler wavenumber for OPO system 1 for a constant incident pump power of 5 W and different poling periods Λ of the crystal. The drop at lower wavenumbers is due to the decreasing transmission of the wavelength-separating mirror. The drop at higher wavenumbers can be attributed to absorption of generated idler by water vapor in laboratory air.

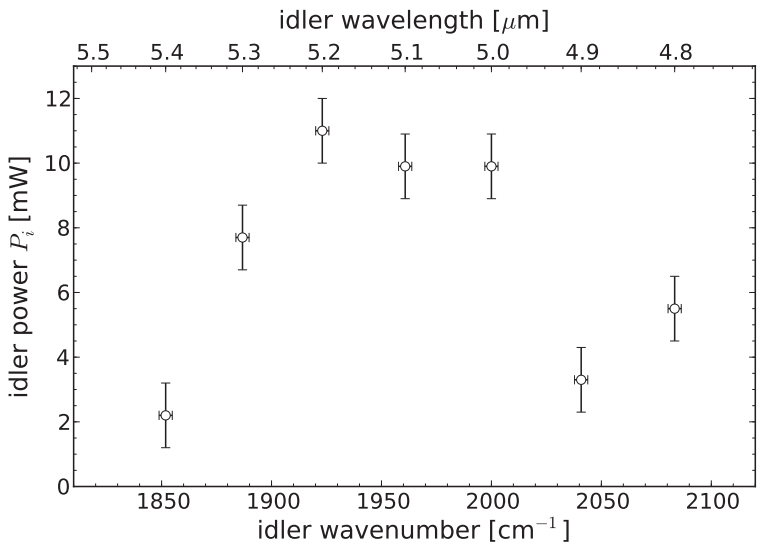

Figure 2.20: Idler Power over idler wavenumber for OPO system 2 for a constant incident pump power of 7.5 W. Data have been taken from Ref. [53].

wide frequency range, which can still be increased to more than 1000 mW when one accepts multimode behavior. While there are many continuous-wave OPOs delivering more idler power, they are usually optimized for high idler powers by using shorter crystals [101] or output coupling mirrors for the signal radiation in the OPO cavity [42], which increases the oscillation threshold rapidly.

Figure 2.20 shows the measured idler power for the OPO system 2. Due to the much lower intensity, the sensitivity of the power meter used in the

Dieses Werk ist copyrightgeschützt und darf in keiner Form vervielfältigt werden noch an Dritte weitergegeben werden.
Es gilt nur für den persönlichen Gebrauch.

measurement for OPO system 1 was insufficient, and another meter has been used (Laserprobe Inc., see also [53]). Data from Figure 2.20 have been scaled, to correct for the effect of absorption of the used dichroic mirror for separating pump and idler waves. One measurement has been done for both dichroic mirrors to determine the scaling factor of eleven [53].

2.2.4 Linewidth and Frequency Stability

When performing high-resolution spectroscopy, the linewidth of the employed radiation source is of great importance. There are spectroscopic techniques placing extreme requirements on this property, like sub-Doppler experiments. Unfortunately, the determination of a frequency linewidth is highly demanding. Usually, heterodyne methods are used to compare the linewidth and frequency stability of the target source with that of a very stable known laser [88, 89]. One other, less demanding setup to estimate the linewidth is the use of a high-finesse optical resonator. For example, Li *et al.* used a high-speed frequency sweep over a cavity fringe to produce a ringing effect to determine the finesse of an optical resonator [60]. In the fringe shape, the laser linewidth is of course another parameter. As a very simple result, one can say that the laser linewidth cannot be larger than the fringe itself.

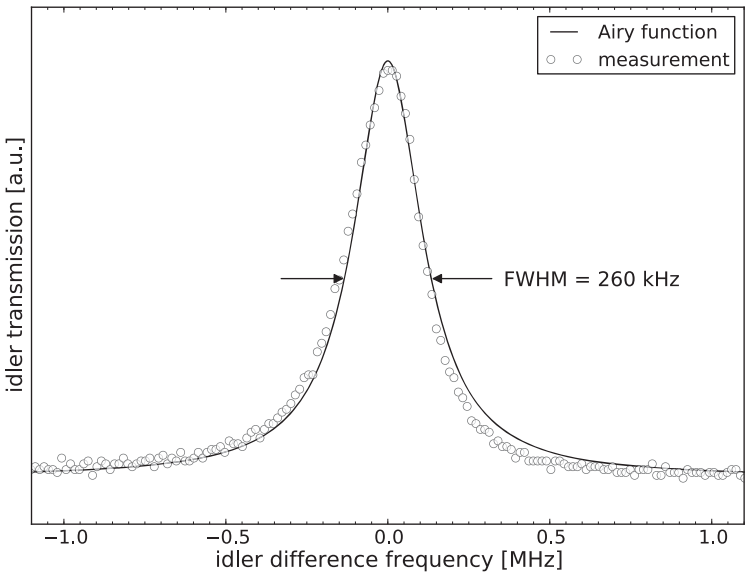

Figure 2.21: Fringe of a high finesse cavity, measured with a rapid frequency sweep of the OPO idler wave at 2079 cm^{-1} (white dots) and an Airy function fitted to the data (solid line). The frequency axis has been calibrated using the frequency difference between two neighboring fringes. Data taken from Ref. [53].

For an estimate of the OPO idler linewidth on small timescales for OPO system 2, a linear high-finesse cavity was set up with dielectric mirrors coated for high reflectivity around 2000 cm^{-1}. The transmitted idler intensity was recorded using a fast responsive, sensitive photovoltaic InSb detector, while the idler frequency was swept rapidly by fast pump frequency tuning. For this, a 100 Hz frequency modulation was transferred to the pump laser piezo

Dieses Werk ist copyrightgeschützt und darf in keiner Form vervielfältigt werden noch an Dritte weitergegeben werden.
Es gilt nur für den persönlichen Gebrauch.

element. Figure 2.21 shows the rapidly scanned fringe. It can be seen that the full width at half maximum is less than 300 kHz, which corresponds to the estimated OPO idler linewidth on the small timescale of 0.02 ms.

Due to the lack of highly reflective mirrors in the 3 micron-wavelength region, no such measurement could be performed for OPO system 1. However, because OPO system 1 and system 2 use the same pump laser and a very similar signal cavity setup, the idler linewidth of system 1 can be inferred from the above measurements to be of the same order of magnitude.

On larger timescales of seconds, the idler frequency varied in frequency intervals of roughly 10^{-3} cm^{-1}. Given that the frequency precision of the pump is orders of magnitude higher, these variations have to be caused by a signal frequency variation $\Delta\nu_s$, which is defined by the optical path length of the resonator. The following expression holds approximately with the refractive index n_s at the signal frequency ν_s, the optical path length of the resonator L and the length of the crystal l: $\Delta\nu_s/\nu_s = \Delta L/L \approx l\Delta n_s/L$. Here, the thermal expansion of geometric cavity and crystal lengths can be neglected. With Sellmeier coefficients for $n_s(T)$ taken from Ref. [28], a temperature variation of 1 mK results in a frequency variation $\Delta\nu_s/\nu_s$ of roughly 5×10^{-8}, which translates into a signal and idler uncertainty of 5×10^{-4} cm^{-1}over the time the temperature changes. From this the temperature stability of the oven can be estimated to be better than 10 mK. These slow frequency drifts can be compensated in the experiment with a proper calibration of the scans using a temperature-stable reference interferometer.

Another important aspect of the OPO for the application in high-resolution spectroscopy is the long-term frequency stability. Because the parametric gain $\Delta\nu_i$ is much higher than the OPO cavity free spectral range FSR[14], mode-hops can already occur for small variations in the cavity path length or the parametric gain profile, which are both influenced by the OPO crystal temperature. A stabilized temperature is therefore a prerequisite for an applicable instrument. Especially when changing the temperature setpoint, some time of 5 to 10 minutes is necessary for the temperature controller to stabilize the crystal at its final temperature.

Figure 2.14 shows a scan of the OPO idler frequency. Over more than the displayed 80 minutes, no signal mode-hop occurred, which is sufficient for the desired application. However, in some parts of the spectrum, the full continuous tuning range of the pump laser could not always be reached and signal mode-hops occurred after some tens of minutes. In those cases, the

[14]For idler radiation at $\lambda_i = 3\,\mu$m being pumped at $\lambda_p = 1.064\,\mu$m, the bandwidth is $\Delta\nu_i \approx 300$ GHz, while the typical fringe spacing of the cavity called free spectral range is FSR ≈ 600 MHz.

Dieses Werk ist copyrightgeschützt und darf in keiner Form vervielfältigt werden noch an Dritte weitergegeben werden.
Es gilt nur für den persönlichen Gebrauch.

temperature and the pump laser frequency need to be readjusted slightly to shift the gain profile maximum onto a cavity fringe.

2.2.5 Beam Profile

Important for guiding and focusing of an optical beam is its beam profile. Optics calculations using gaussian optics are quite common in experimental work and easy to perform (see, e.g., Refs. [54,66] for more information). The basic assumption for such calculations is that the relevant beam exhibits a near-gaussian beam shape. To check this assumption for the idler output of the OPO, a commercial beam profiler (see section 2.1.4) has been employed to check for the beam shape.

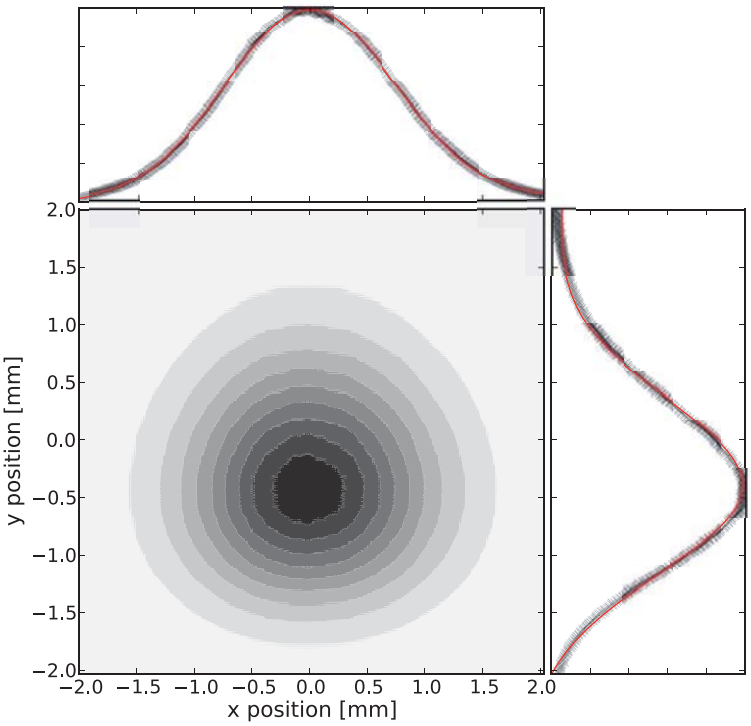

Figure 2.22: *Top and right*: Beam profiles in x- and y-direction of the signal radiation leaking out of the last mirror of the bow-tie cavity measured with a commercial beam-profiler. A least-squares fit of a gaussian-shaped function is shown in red. *bottom left*: Contour plot calculated from the x- and y-axis scans.

Unfortunately, the beam profiler is not sensitive at idler wavelengths, but merely in the near infrared with wavelengths up to $\lambda = 1.8\,\mu$m. However, the idler beam shape can be inferred from the beam shapes of the signal and pump beam. Since the pump laser has a gaussian profile specified by the manufacturer, the signal beam profile has been verified. Signal radiation leaking out of the OPO cavity is used to measure the profile. The beam has been filtered with a Nd:YAG laser line mirror to cancel out the residual 1064 nm wavelength pump in the transmitted wave, before it enters the beam profiler. The measurement has been checked for any additional pump power possibly still contained in the beam by misaligning the cavity. At first, a

Dieses Werk ist copyrightgeschützt und darf in keiner Form vervielfältigt werden noch an Dritte weitergegeben werden.
Es gilt nur für den persönlichen Gebrauch.

movement of the profile could be detected when one mirror has been shifted, but after a small misalignment, the oscillation stops suddenly and the profile vanishes completely in the noise. So the measured profile is only caused by signal radiation.

The upper and the right part of Figure 2.22 show the measured profile in x- and y-direction orthogonally to the beam propagation. In the lower left part, a two-dimensional convolution of the profiles can be seen. Deviations to a least-squares fit of a gaussian function to the data are very small and so the assumption of a gaussian shape for all beams relevant here is reasonable.

2.3 Outlook

The OPO systems described above have proven to be very useful in the laboratory, as described in the upcoming chapters. However, there still remain a lot of potential enhancements or extensions for future projects. For a recent review on continuous-wave OPOs also dealing with their future prospects see Ref. [17]. Three main areas for enhancement can be identified from the spectroscopist's point of view:

1. Frequency coverage
2. Frequency stability and/or tuning
3. Pump threshold

The use of a more suitable nonlinear crystal for the mid-infrared region would support the solution of challenge number 1. Orientation-patterned GaAs is the main candidate for future nonlinear optics applications because of its wide transparency range of $\lambda = 1 - 17\,\mu$m and large nonlinear susceptibility (Refs. [27, 120]). Unfortunately, it is still very expensive to produce using epitaxial methods and not commercially available yet.

Another way to extend the frequency coverage of coherent radiation is to make use of the high signal power circulating in the OPO resonator and use it as pump source for a secondary nonlinear process. For example, cascaded continuous-wave OPOs have been demonstrated [52] with a threshold of more than 150 W which is overcome by the signal radiation in the resonator. A simpler approach would be intra-cavity difference frequency generation of signal and idler beams in the OPO-system 1 described above. Mixing signal wavelengths of, e.g., $1.8\,\mu$m and idler wavelengths of $2.6\,\mu$m results in a difference frequency with a wavelength of $6\,\mu$m, as shown in Figure 2.23. Phase matching can be easily achieved using commercially available periodically poled Lithium Niobate. Such a process does not have a threshold at

Dieses Werk ist copyrightgeschützt und darf in keiner Form vervielfältigt werden noch an Dritte weitergegeben werden.
Es gilt nur für den persönlichen Gebrauch.

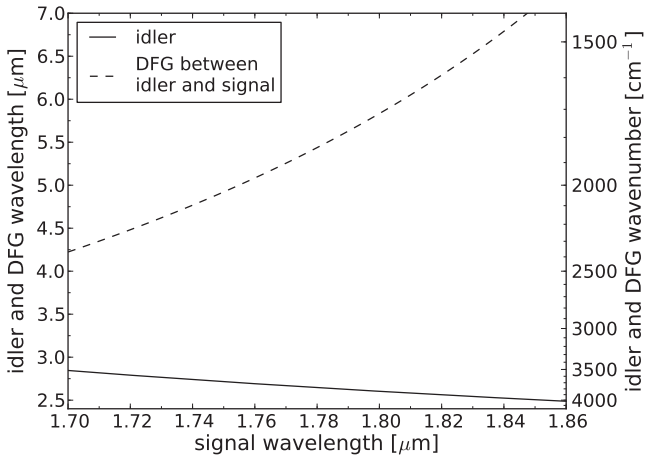

Figure 2.23: Signal wavelength dependence of the idler wavelength and the difference frequency of idler and signal in an OPO pumped at 1.064 μm. Solid line: Idler wavelength. Dashed line: Wavelength of the difference-frequency mixing output of signal and idler waves.

all and should deliver power similar to that of OPO system 2, even though the material is highly absorbing. This would suffice for many spectroscopic applications.

For improvements in challenge number 2, the stability and tuning, an optical grating replacing one cavity mirror has been shown to help gaining control over mode-hops and access large regions of the OPO bandwidth with a single temperature and poling period of the crystal [111, 112]. Unfortunately, the threshold of such a system drastically increases to more than 10 W because the lower reflectivity of the grating compared to a dielectric mirror, so that a further reduction of the threshold is desirable for the use with common pump lasers, resulting in challenge number 3.

A reduction of the threshold is desirable especially for OPO system 2, where idler absorption is high or for the case of a grating based approach as described above. One option is to introduce a gain medium inside the OPO resonator to compensate losses the signal wave experiences. These systems are called hybridly-pumped OPOs and have been demonstrated in Ref. [18]. They feature a glass doped with a gain medium which is pumped incoherently with a low-cost diode laser. To sum up, OPOs as infrared radiation sources become more and more important and even have potential for further improvements.

Dieses Werk ist copyrightgeschützt und darf in keiner Form vervielfältigt werden noch an Dritte weitergegeben werden.
Es gilt nur für den persönlichen Gebrauch.

Dieses Werk ist copyrightgeschützt und darf in keiner Form vervielfältigt werden noch an Dritte weitergegeben werden.
Es gilt nur für den persönlichen Gebrauch.

3

Action Spectroscopy of CH_2D^+ using Laser Induced Reactions

"Ionen reduzieren die statische Aufladung der Haare beim Kämmen. Daher werden für die Bürsten von Termix ionisierte Borsten verwendet. Die Haare werden glänzender und sind besser frisierbar."
Advertising slogan for hairbrush "ceramic" by Termix.

This chapter presents the measurements on the cation CH_2D^+ performed in the scope of this work*. Frequencies of rovibrational transitions have been measured with high accuracy and used to predict pure rotational transitions of the molecule which are of astrophysical relevance.

3.1 Introduction

Molecular ions are regarded as important constituents of dense molecular clouds in the interstellar medium (ISM). Because of their ability to react with neutrals without a potential barrier, they are key players in several chemical network models. So besides their pure chemical interest, the understanding

*This chapter is based on the following publications:

- Rotational transitions of CH_2D^+ determined by high-resolution IR spectroscopy. S. Gärtner, J. Krieg, A. Klemann, O. Asvany, S. Schlemmer, *Astronomy & Astrophysics* **516** L3 (2010)
- High-Resolution Spectroscopy of CH_2D^+ in a cold 22-Pole Trap. S. Gärtner, J. Krieg, A. Klemann, O. Asvany, H. S. P. Müller, S. Schlemmer, *in preparation*

Dieses Werk ist copyrightgeschützt und darf in keiner Form vervielfältigt werden noch an Dritte weitergegeben werden.
Es gilt nur für den persönlichen Gebrauch.

of these species is also important in topics related to astrochemistry (see, e.g. Ref. [99]).

Molecular ions are important with regard to regarding fractionation of rare isotopes, especially deuterium. In some regions of the universe, the deuterium content in molecules exceeds the expectation derived from pure statistics and the solar or cosmic D/H-ratio by several orders of magnitude.

One reason for this enhancement is the lower zero-point energy of a molecule containing deuterium instead of hydrogen, which becomes important in cold interstellar environments. Take for example the reaction of CH_3^+ with an HD molecule:

$$CH_3^+ + HD \rightleftharpoons CH_2D^+ + H_2 \quad . \tag{3.1}$$

The above reaction is exothermic and therefore at low temperatures, the balance will be shifted significantly towards CH_2D^+. However, determining and understanding the difference between the cosmic D/H ratio and the CH_2D^+/CH_3^+ ratio remains a challenging part of astrochemistry.

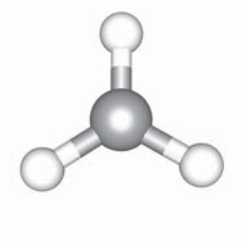

Figure 3.1: Graphical Ball and Stick representation of the $CH_3{}^+$ molecular ion. It is planar and highly symmetric, thus it possesses no permanent electric dipole moment and is not accessible by radioastronomic detection schemes. The deuterated isotopologs CH_2D^+ and CD_2H^+ have the same structure, but different symmetry and exhibit also different electric dipole moments. The bond lengths are $r_{CH} = 1.0914$ Å [23, 49].

One reason for the difficulty is that the ion CH_3^+ is not observable by standard radioastronomical means because it lacks a permanent dipole moment. Thus it exhibits no pure rotational spectrum. The isotopologs CH_2D^+ and CHD_2^+ have the same structure as their parent ion — a planar triangular shape with the carbon at the center — but separate center of mass and center of charge and thus exhibit also a pure rotational spectrum necessary for their detection. Especially the monodeuterated species CH_2D^+ is a promising candidate for detection in space because of its higher abundance.

In order to unambiguously detect an ion, one has to know the rest frequencies of rotational transitions on a high accuracy level only reached in experimental spectroscopy studies. Spectroscopy of ions is classically performed by simple absorption spectroscopy of a discharged precursor gas. However, due to the rich chemistry in those discharges, the analysis is often challenging, given that many different species can be responsible for the observed absorption pattern. A rotational temperature of $T \approx 300$ K inherent to these plasmas complicates the spectrum even more, because more transitions are visible.

Dieses Werk ist copyrightgeschützt und darf in keiner Form vervielfältigt werden noch an Dritte weitergegeben werden.
Es gilt nur für den persönlichen Gebrauch.

There are two works by the Oka group (Refs. [49, 91]), who used this technique for measuring two vibrational bands of CH_2D^+ in the infrared. Derived molecular parameters facilitated the prediction of pure rotational transitions. After the laboratory measurements, CH_2D^+ has been tentatively detected in space via two lines [61], but they matched only the predicted transitions of the older publication from the Oka group and not the new, refined one. Thus there is still no acknowledged report of interstellar CH_2D^+, and more accurate predictions would help to clarify this issue.

Spectroscopy on cold ions ($T \approx 20$ K) stored in an ion trap – like performed here – offer some advantages. An ion spectrum recorded this way has potentially higher accuracy because the Doppler line broadening is much smaller at the cryogenic trap temperature. Furthermore, the trapped ions can be mass-selected, avoiding the confusion with different species. In this work, a combination of a high-resolution mid-infrared radiation source with a cryogenic ion trap has been used to measure the rovibrational transitions of CH_2D^+ very accurately and to improve the prediction of pure rotational transitions.

3.2 Laser Induced Reactions of CH_2D^+

The method of laser induced reactions (LIR) has become an established tool to perform high-resolution spectroscopy on small numbers of trapped, cool ions (see References [4,6,7,97,98]), and its principle will be briefly introduced. Because the reaction rates of the forward and backward direction of reaction

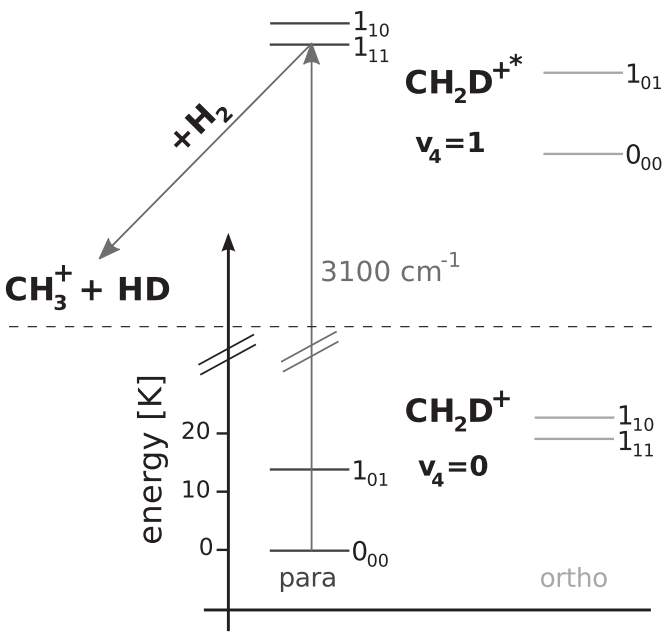

Figure 3.2: Energy level sketch for CH_2D^+ and scheme for the laser induced reaction (3.1). The cold CH_2D^+ ions in the trap (20 K) cannot react to CH_3^+ because of the high energy difference of 400 K. Rovibrational excitation of CH_2D^+ with the OPO at wavenumbers around 3100 cm^{-1} (corresponding to energies of around 4400 K) provides the ions with enough internal energy for the reaction to occur. Shown here is an excitation into the ν_4 fundamental vibration. The CH_2D^+ molecule exists in two nuclear spin configurations, named ortho and para.

Dieses Werk ist copyrightgeschützt und darf in keiner Form vervielfältigt werden noch an Dritte weitergegeben werden.
Es gilt nur für den persönlichen Gebrauch.

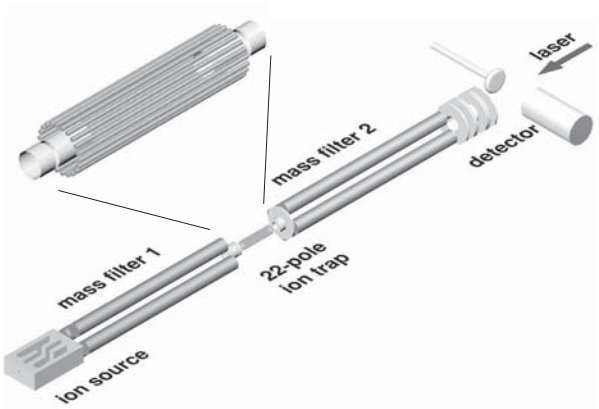

Figure 3.3: Schematic Setup of the 22-pole ion trap LIRTRAP. Ions produced by electron impact ionization on the left side are mass-selected in a quadrupole filter. Roughly 1000 ions are trapped in the 22-pole (middle), and sympathetically cooled with He buffer gas and react with neutral molecules present in the trap volume. The reaction products are then mass-filtered in a second quadrupole and counted on a Daly-type detector (right). Laser radiation can be coupled to the trapped ions and influence the reaction outcome. Graphic taken from Ref. [5].

(3.1) depend on the internal energy of the reactants, the products of an endothermic reaction can be used as a probe for the excitation of stored ions.

Here, the backward direction of reaction (3.1) was used. Figure 3.2 outlines the principle of LIR for this ion. The endothermicity of the reaction is nearly 400 K, so the reaction basically stops for the low temperatures in the ion trap of around 20 K. Only if the frequency of incident radiation coincides with a transition frequency of the parent ion CH_2D^+, the internal energy of the CH_2D^+ ions enables the reaction with ambient H_2 towards CH_3^+. Therefore the number of CH_3^+ ions in the trap is an indicator for the absorbed infrared photons, and by counting them in dependence of the laser frequency, the spectrum of CH_2D^+ is recorded.

3.3 Experimental Setup

The measurements were conducted using a combination of a 22-pole ion trap and the home-built continuous-wave OPO.

3.3.1 22-pole ion trap

A schematic setup of the 22-pole trapping apparatus can be seen in Figure 3.3. CH_2D^+ ions are produced by electron impact on CH_3D neutral gas (Cambridge Isotope Laboratories, Inc.: Methane (D1, 98%)). At the beginning of each measurement cycle, a pulse of produced CH_2D^+ ions is guided through a quadrupole mass filter and injected into the trapping volume, ensuring that only species with a certain molecular weight are present in the trap.

Dieses Werk ist copyrightgeschützt und darf in keiner Form vervielfältigt werden noch an Dritte weitergegeben werden.
Es gilt nur für den persönlichen Gebrauch.

The trap consists of 22 cylindrically aligned steel electrodes forming an RF-field. The whole system is mounted on a closed cycle helium cryostat, cooling the trap and the inlet of the buffer gas down to approximately 14 K. The incoming ions are cooled sympathetically by an intense pulse of cold helium and are then stored for typical 500 ms. During this period, the ions are exposed to the reactive H_2 gas. LIR-spectroscopy can then be performed by guiding a laser beam through the trap, which is transparent along the cylindrical symmetry axis.

The CH_3^+ ions are then extracted from the trap and mass filtered in a second quadrupole mass spectrometer. They are counted in a Daly detector (Ref. [24]) as a function of the irradiated frequency to produce a spectrum of CH_2D^+.

3.3.2 CW OPO

The setup of the OPO is basically described in chapter 2. One important addition is the use of a multipass-cell of Herriott-type to record transmission through a calibration gas simultaneously to the LIR spectrum. A schematic setup can be seen in Figure 3.4.

Idler tuning is accomplished by choosing the right poling period in the crystal, stabilizing the crystal temperature to a given setpoint and finally tuning the pump laser. The idler frequency follows the pump frequency, since the difference frequency of these two always equals the signal frequency, which is kept fixed in the OPO cavity.

3.3.3 Calibration procedure

The setup incorporates a high-resolution wavemeter, capable of a frequency accuracy better than 10^{-3} cm^{-1}. This frequency readout is recorded for every CH_2D^+ measurement cycle. However, since the frequency display depends on the alignment and is not as accurate as the experiment potentially is, each scan was calibrated with a well-known transition of a calibration gas.

The frequency deviation of the wavemeter is assumed to be constant for a given alignment of the OPO, so the scans are calibrated by shifting the recorded frequency channel so that measured reference lines agree with their known frequency. Deviations of the order of 10^{-4} cm^{-1} are visible this way and are corrected in the process.

To increase the sensitivity in the recorded calibration spectrum, a Herriott-type absorption cell (Ref. [43]) with a total absorption path of 50 m has been aligned. It has been filled with calibration gases at low pressure to prevent pressure broadening of lines.

Dieses Werk ist copyrightgeschützt und darf in keiner Form vervielfältigt werden noch an Dritte weitergegeben werden.
Es gilt nur für den persönlichen Gebrauch.

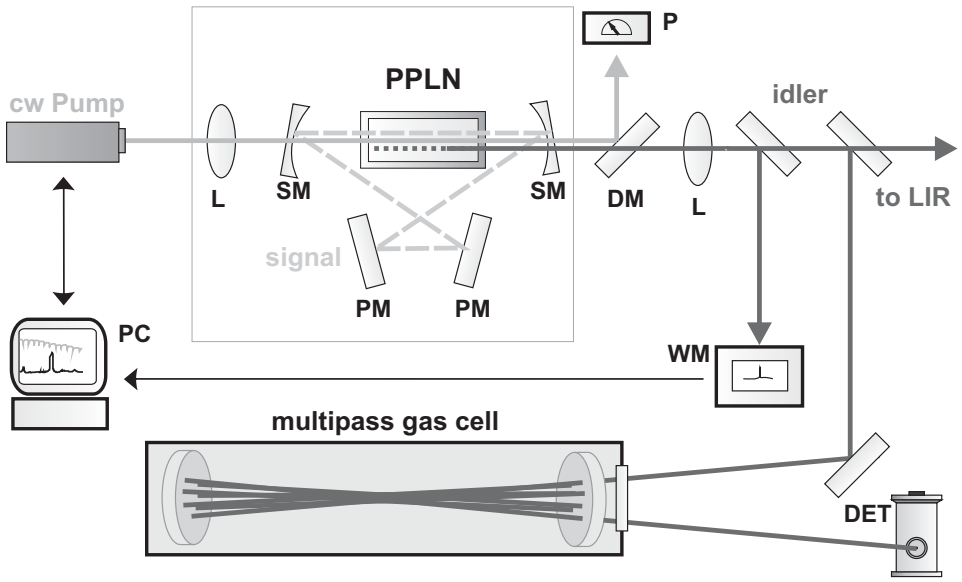

Figure 3.4: Schematic Setup of the OPO used to measure CH_2D^+. The difference to the standard setup is the application of a 50 multi-pass cell of Herriott-type for sensitively recording a calibration gas simultaneously to the LIR spectrum.

In order to achieve the highest possible frequency accuracy, only calibration lines with an uncertainty of less than 4 MHz (1.3×10^{-4} cm^{-1}) have been used for the experiment. Transitions of OCS, for example, have been measured with high accuracy using heterodyne techniques (see e.g. [94]). Based on such measurements, calculated linelists can be downloaded from NIST [1]. Due to the mentioned accuracy requirements, only the NIST OCS lines between 3066 and 3120 cm^{-1} have been used here. Most of these lines are given with an accuracy far below the 4 MHz mentioned above. Additionally, some weaker lines of OCS documented in [36] have been used, after correcting for an offset value to the more accurate NIST lines.

Outside the above mentioned range, water lines in the vicinity of CH_2D^+ lines have also been used for calibration. The positions of those lines have been determined by Fourier-transform spectroscopy [106], also with an accuracy better than 4 MHz. For the stronger water absorptions, the amount of H_2O in the laboratory air was sufficient, while for the weaker lines the absorption cell has been filled with air at low pressure.

3.4 Measurement and Analysis

An example scan of the CH_2D^+ absorption signal is shown in Figure 3.5. It shows the counts of the reaction product CH_3^+, as well as the reference

[1] data taken from *http://webbook.nist.gov/chemistry*

Dieses Werk ist copyrightgeschützt und darf in keiner Form vervielfältigt werden noch an Dritte weitergegeben werden.
Es gilt nur für den persönlichen Gebrauch.

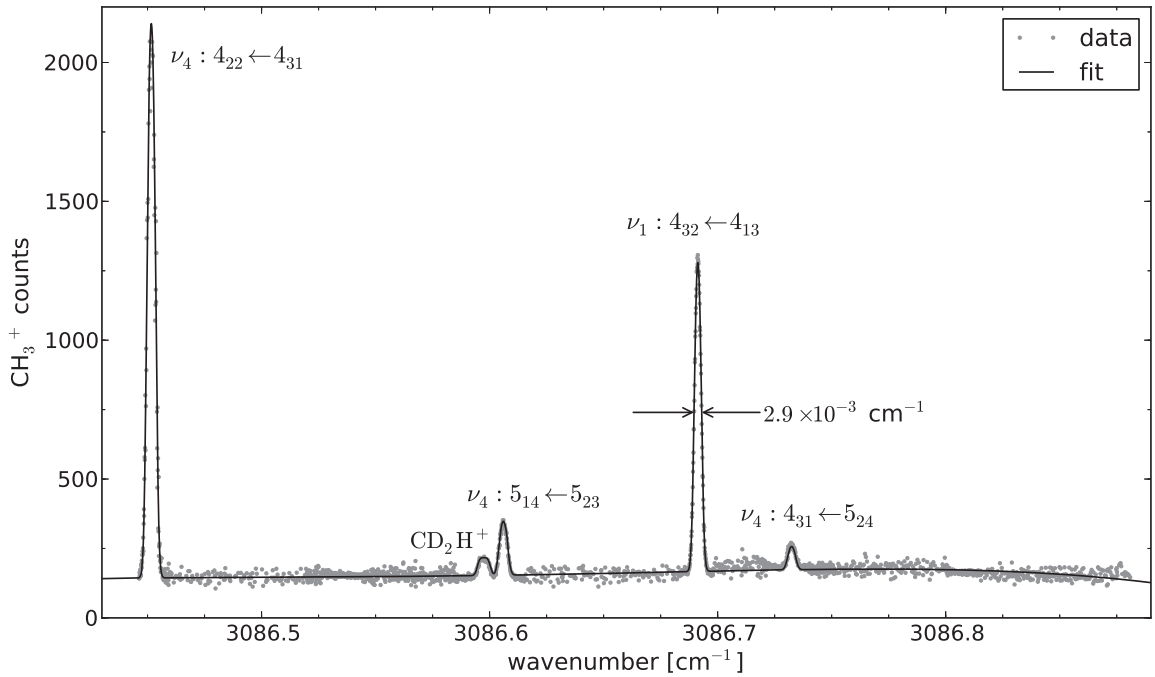

Figure 3.5: Typical frequency scan of CH_2D^+ measured with the combination of the ion trap LIRTRAP and the OPO system 1. The number of CH_3^+ ions in the trap increases when the CH_2D^+ ions are rovibrationally excited by the idler radiation from the OPO. The full width at half maximum of the lines is less than 90 MHz (3×10^{-3} cm^{-1}).

spectrum of the OCS gas in the cell. There are three reference lines in the range of this scan. The positions of the two weaker ones on the left were taken from [36] after correcting the frequency channel for the offset to the NIST lines. The saturated OCS transition on the right can be found in NIST directly.

In total, 111 rovibrational transitions have been measured and assigned to the CH_2D^+ molecule, of which 40 belong to the ν_1 vibrational band and 71 to the ν_4 band. They are listed in Tables A.1 and A.2 in appendix A with their individual uncertainties estimated from the calibration process.

Table 3.1: Comparison of ground-state combination differences ν_{cd} of CH_2D^+. Each line represents one Ground-State combination difference derived from measurements done here. Listed here are only those found doubly or triply and they should equal in their errorbars.

Virtual ground-state transition	ν_{cd} [cm^{-1}]	Excited state v	$J'_{K'_a K'_c}$
1_{01} - 2_{21}	37.45751 (14)	ν_4	1_{10}
	37.45750 (12)	ν_4	2_{12}

continued on next page

Dieses Werk ist copyrightgeschützt und darf in keiner Form vervielfältigt werden noch an Dritte weitergegeben werden.
Es gilt nur für den persönlichen Gebrauch.

Table 3.1 – continued from previous page

Virtual ground-state transition	ν_{cd} [cm^{-1}]	Excited state v	$J'_{K'_aK'_c}$
0_{00} - 2_{20}	47.52118 (12)	ν_4	1_{11}
	47.52154 (28)	ν_1	1_{01}
2_{02} - 2_{20}	20.40349 (14)	ν_4	1_{11}
	20.40348 (15)	ν_4	2_{11}
2_{11} - 3_{13}	17.36548 (14)	ν_4	2_{02}
	17.36527 (17)	ν_4	2_{20}
	17.36518 (17)	ν_1	3_{30}
2_{11} - 3_{31}	62.63370 (14)	ν_4	2_{02}
	62.63323 (34)	ν_1	3_{30}
3_{13} - 3_{31}	45.26822 (14)	ν_4	2_{02}
	45.26798 (14)	ν_4	3_{22}
	45.26805 (31)	ν_1	3_{30}
2_{20} - 3_{22}	27.10040 (22)	ν_4	2_{11}
	27.10020 (25)	ν_4	3_{13}
2_{21} - 3_{03}	5.62379 (12)	ν_4	2_{12}
	5.62384 (18)	ν_4	3_{12}
	5.62389 (15)	ν_1	3_{22}
3_{12} - 4_{14}	18.25812 (14)	ν_4	3_{03}
	18.25790 (21)	ν_4	3_{21}
3_{31} - 4_{13}	7.53750 (14)	ν_4	3_{22}
	7.53746 (14)	ν_4	4_{04}
3_{21} - 4_{23}	33.15172 (16)	ν_4	3_{30}
	33.15160 (13)	ν_4	4_{14}
4_{04} - 4_{22}	35.01870 (14)	ν_4	4_{13}
	35.01790 (51)	ν_1	4_{23}
4_{22} - 5_{24}	36.36814 (22)	ν_4	4_{31}
	36.36849 (103)	ν_4	5_{15}

To check the claimed frequency accuracy, combination differences in the ground state of CH_2D^+ have been calculated from the rovibrational transitions measured here. One ground state combination difference (GSCD) is the difference between two transition frequencies with a common upper rovibrational level. Some GSCDs can be calculated using the measured transitions with more than one common upper level. In such cases, the multiply calculated values should be equal. Table 3.1 shows the GSCDs, which were found at least two times independently in this work. These pairs of two or three values for the same GSCD exhibit an excellent agreement. Similarly, the 71 measured transitions for ν_4 in Table A.2 deliver ten pairs of combination differences in the upper ν_4 vibrational state with similar agreement, while the

Dieses Werk ist copyrightgeschützt und darf in keiner Form vervielfältigt werden noch an Dritte weitergegeben werden.
Es gilt nur für den persönlichen Gebrauch.

limited number of measured transitions in ν_1 does not give any combination difference pairs.

To predict transitions of the CH_2D^+ molecule, an effective Hamilton operator has been determined. The A-reduced Hamilton operator $\hat{H}^{(A)}$ proposed by Watson (Ref. [123]) was applied considering centrifugal distortion effects up to the sixth order:

$$\hat{H}^{(A)} = \hat{H}_r + \hat{H}_q + \hat{H}_s \tag{3.2}$$

with the operator for the undistorted rigid asymmetric top $\hat{H}_r$:

$$\hbar^2 \hat{H}_r = B_x \hat{J}_x^2 + B_y \hat{J}_y^2 + B_z \hat{J}_z^2 \quad . \tag{3.3}$$

Here, B_l $(l = x, y, z)$ are the rotational constants, and $\hat{J}_l$ the angular momentum operators of the component l. The terms that account for the centrifugal distortion are found in the other parts, namely $\hat{H}_q$ including the quartic distortion terms and $\hat{H}_s$ including the sextic terms:

$$\begin{aligned}
\hat{H}_q = &- \Delta_J \hat{J}^4 - \Delta_{JK} \hat{J}^2 \hat{J}_z^2 - \Delta_K \hat{J}_z^4 \qquad (3.4)\\
&- 2\delta_J \hat{J}^2 (\hat{J}_x^2 - \hat{J}_y^2) - \delta_K [\hat{J}_z^2 (\hat{J}_x^2 - \hat{J}_y^2) + (\hat{J}_x^2 - \hat{J}_y^2) \hat{J}_z^2] \\
\hat{H}_s = &+ \Phi_J \hat{J}^6 + \Phi_{JK} \hat{J}^4 \hat{J}_z^2 + \Phi_{KJ} \hat{J}^2 \hat{J}_z^4 + \Phi_K \hat{J}_z^6 \qquad (3.5)\\
&+ 2\phi_J \hat{J}^4 (\hat{J}_x^2 - \hat{J}_y^2) \\
&+ \phi_{JK} \hat{J}^2 [\hat{J}_z^2 (\hat{J}_x^2 - \hat{J}_y^2) + (\hat{J}_x^2 - \hat{J}_y^2) \hat{J}_z^2] \\
&+ \phi_K [\hat{J}_z^4 (\hat{J}_x^2 - \hat{J}_y^2) + (\hat{J}_x^2 - \hat{J}_y^2) \hat{J}_z^4] \quad .
\end{aligned}$$

Here, $\hat{J}$ is the operator of the total angular momentum, $\Delta_J, \Delta_{JK}, \Delta_K, \delta_J, \delta_K$ are the quartic distortion coefficients, and $\Phi_J, \Phi_{JK}, \Phi_{KJ}, \Phi_K, \phi_J, \phi_{JK}, \phi_K$ are the sextic distortion coefficients. The above treatment is done separately for different vibrational states, according to the Born-Oppenheimer approximation.

Equations (3.2) to (3.5) describe the energy levels of each rotational state in a given vibrational state. There are restrictions concerning a pair of states between those a dipole transition can occur, which are called selection rules. The selection rules consist of $\Delta J = 0, \pm 1$ for all kinds of transitions. Additional selection rules are $\Delta K_a = 0, \pm 2, \ldots,$ $\Delta K_c = \pm 1, \pm 3, \ldots$ for a-type transitions (transition dipole moment along the a-axis like for the ν_1 band of CH_2D^+), and $\Delta K_a = \pm 1, \pm 3, \ldots,$ $\Delta K_c = \pm 1, \pm 3, \ldots$ for b-type transitions (transition dipole moment along the b-axis like for the ν_4 band of CH_2D^+). Rovibrational transition frequencies are then determined by the energy difference between the involved states.

The programs PGOPHER and SPFIT (Refs. [84, 125]) have both been used to fit the described Hamiltonian to the observations. The fit was performed

Dieses Werk ist copyrightgeschützt und darf in keiner Form vervielfältigt werden noch an Dritte weitergegeben werden.
Es gilt nur für den persönlichen Gebrauch.

using the 111 observed transition frequencies as well as by using merely the 61 ground state combination differences extractable from the data. All fits show consistent results, as long as some sextic distortion constants are included. Figure 3.6 shows the residuals of the PGOPHER fit. The fit yields an average absolute error of 1.9×10^{-4} cm^{-1}. Table 3.2 summarizes molecular parameters of all involved vibrational states.

Table 3.2: Molecular parameters of CH_2D^+ in the ground and excited vibrational states $v_1 = 1$ and $v_4 = 1$ given in cm^{-1}. 34 parameters have been used to reproduce 111 transitions. The unweighted average error is $< 3 \times 10^{-4}$ cm^{-1}. Fit residuals can be seen in Figure 3.6

Parameter		Ground State	$v_4 = 1$	$v_1 = 1$
ΔE			3105.840613(55)	3004.764610(94)
A		9.368522(28)	9.270318(37)	9.210897(58)
B		5.771332(15)	5.732480(17)	5.757223(54)
C		3.525279(18)	3.502908(13)	3.494159(51)
Δ_J	$\times 10^3$	0.12050(35)	0.12205(40)	0.1193(12)
Δ_{JK}	$\times 10^3$	0.3609(19)	0.3429(39)	0.3568(44)
Δ_K	$\times 10^3$	0.2615(27)	0.2996(20)	0.261(12)
δ_J	$\times 10^3$	0.04680(29)	0.04631(18)	0.0490(14)
δ_K	$\times 10^3$	0.4191(42)	0.4017(14)	0.442(17)
Φ_J	$\times 10^6$			
Φ_{JK}	$\times 10^6$		0.138(97)	1.49(75)
Φ_{KJ}	$\times 10^6$	−0.28(13)		−5.0(23)
Φ_K	$\times 10^6$			4.2(15)
ϕ_J	$\times 10^6$			0.070(27)
ϕ_{JK}	$\times 10^6$	0.60(15)		
ϕ_K	$\times 10^6$			4.8(17)

3.5 Conclusion and Outlook

The results on the CH_2D^+ rovibrational spectrum give precise information about the molecule's ground state, helping in the detection of pure rotational transitions in space and in the laboratory. Key to these valuable predictions is a high frequency accuracy of a few MHz. This work shows that this accuracy is readily achieved with the OPO system.

The presented measurement method therefore allows very precise predictions of pure rotational transitions. In 2010, Amano found four rotational transitions of CH_2D^+ in a discharge cell (Ref. [1]). Table 3.3 lists predic-

Dieses Werk ist copyrightgeschützt und darf in keiner Form vervielfältigt werden noch an Dritte weitergegeben werden.
Es gilt nur für den persönlichen Gebrauch.

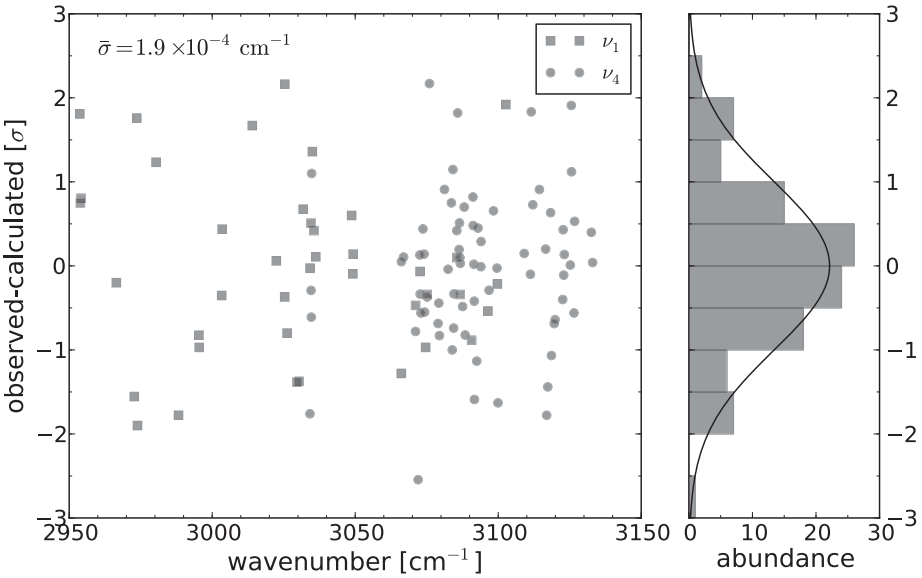

Figure 3.6: (left) Residuals of the fit for CH_2D^+as a function of frequency in units of the individual frequency uncertainty σ. **(right)** Histogram of the residuals. As an estimate for absolute errors, the averaged value of σ is $\bar{\sigma} = 1.9 \times 10^{-4}$ cm^{-1}. The histogram also harbors a plot of the standard normal distribution with $\sigma = 1$ (solid black line).

tions of rotational transitions based on molecular parameters derived from this work and compares them with frequencies which have been measured directly by Amano. For comparison, predictions based on the work by Rösslein *et al.* (Ref. [91]) and Jagod *et al.* (Ref. [49]) are shown for these lines as well.

The calculated frequencies from the pioneering measurements of Rösslein *et al.* fit the observed frequencies best. However, the given uncertainties are of the order of 10 MHz, which can be too large when trying to unambiguously assign lines in a messy spectrum. The follow-up work from Jagod *et al.* from the same group basically enlarged the data set of CH_2D^+ lines. Therefore one would expect an increase in the prediction accuracy because of the better determined molecular parameters. Quite contrary to this expectation, Table 3.3 shows that the predictions deviate significantly to the measured lines. The reason for this behavior can only be speculated for. In fact, however, measured transitions from Jagod *et al.* have a significant shift to the frequencies determined in this work, which still lies within the experimental uncertainty given by Jagod *et al.*, but may be a hint to a systematic calibration problem. A small and variable frequency error may have caused the decline in precision. Predictions made with this work show a reasonable agreement. Two lines are within the uncertainty and two being within two times the uncertainty.

Together with the rotational transitions measured by Amano, the spectroscopic picture of CH_2D^+ is rather circumstantial, which means that lines

Dieses Werk ist copyrightgeschützt und darf in keiner Form vervielfältigt werden noch an Dritte weitergegeben werden.
Es gilt nur für den persönlichen Gebrauch.

Table 3.3: Predicted and observed pure rotational transitions of CH_2D^+ in MHz.

Transition	Predicted			Measured
	Ref. [91] (1991)	Ref. [49] (1992)	This work	Ref. [1] (2010)
2_{12} - 1_{11}	490 012.3(98)	489 998.0(44)	490 011.0(9)	490 012.247(30)
2_{11} - 1_{10}	624 492.6(125)	624 472.2(73)	624 490.9(9)	624 492.648(20)
3_{13} - 2_{12}	722 354.7(144)	722 333.7(66)	722 355.5(9)	722 354.622(25)
3_{22} - 2_{21}	835 465.3(167)	835 445.1(83)	835 464.2(10)	835 464.376(50)

can be predicted now with very good accuracy for low J values. A prediction of transition frequencies made from a fit of all available experimental data can be found in the Cologne Database for Molecular Spectroscopy CDMS (http://www.astro.uni-koeln.de/cdms/, Ref. [72]). For better predictions of higher frequencies, further high-accuracy measurements especially of high-J transitions are necessary.

One possibility of further precision enhancement of the presented experiment is the frequency stabilization of the OPO idler wave to a frequency comb. Using this technique, measurements in the infrared can finally give information with uncertainties on the kHz-level (see, for example Refs. [48, 55, 59, 121]). For this, a sub-Doppler measuring scheme would be desirable to establish, where the idler beam traverses the ion trap in forward and backward direction, reducing the measured linewidth to the natural linewidth, which is much smaller. Such measurements in the infrared could finally reach accuracy on the kHz-level like those in the microwave regime.

Dieses Werk ist copyrightgeschützt und darf in keiner Form vervielfältigt werden noch an Dritte weitergegeben werden.
Es gilt nur für den persönlichen Gebrauch.

4

Rovibrational Spectroscopy of the Silicon-Carbon Cluster Si_2C_3

"I do not like it, and I am sorry I ever had anything to do with it."
Erwin Schrödinger, speaking of quantum mechanics.

The continuous-wave optical parametric oscillator emitting idler radiation around 5 μm wavelength described in chapter 2 has been combined with a supersonic jet spectrometer. High-resolution spectra of the silicon-carbon cluster Si_2C_3 have been measured and molecular parameters of the ν_3 fundamental vibration have been derived most precisely. Furthermore, a new vibrational band has been detected*.

4.1 Introduction

Silicon is known as a very non-volatile element. In fact, most of the silicon on earth is bound in the solid state, and silicon containing molecules have a

*This chapter is based on the following publications:

- A continuous-wave optical parametric oscillator around 5 μm wavelength for high-resolution spectroscopy. J. Krieg, A. Klemann, I. Gottbehüt, S. Thorwirth, T. F. Giesen, S. Schlemmer, *Review of Scientific Instruments* **82** 063195 (2011)
- High-resolution OPO spectroscopy of Si_2C_3 at 5 μm: Observation of hot band transitions associated with ν_3. S. Thorwirth, J. Krieg, V. Lutter, I. Keppeler, S. Schlemmer, M. E. Harding, J. Vázquez, T. F. Giesen, *Journal of Chemical Physics*, in press (2011)

Dieses Werk ist copyrightgeschützt und darf in keiner Form vervielfältigt werden noch an Dritte weitergegeben werden.
Es gilt nur für den persönlichen Gebrauch.

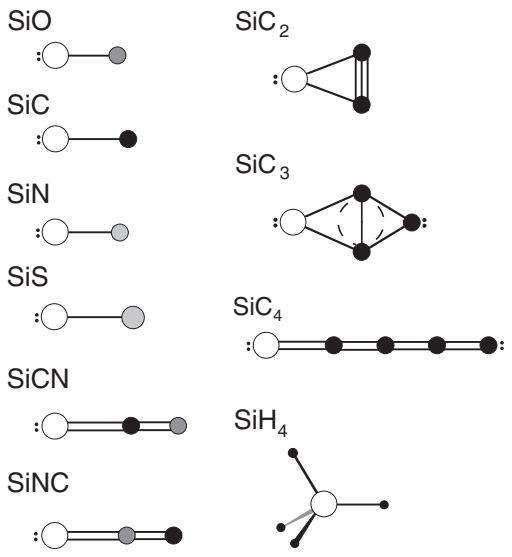

Figure 4.1: Silicon containing molecules detected in space. All these species have been detected by their pure rotational spectrum using radioastronomical techniques, except for silane SiH_4, whose rovibrational infrared spectrum has been recorded. Large open circles denote silicon atoms, large filled circles carbon atoms, large shaded circles hetero atoms (N, O or S), and small filled circles hydrogen atoms. Silicon-carbon clusters Si_nC_m are an important subclass of these molecules. Figure taken from Reference [64].

negligible abundance in the terrestrial atmosphere. This situation is different in space: Of the approximately 160 molecules detected in space up to now, almost 10% of them contain silicon. Especially in late-type stars and in star forming regions, these molecules are known to contribute to the astrochemical complexity (see, e.g. Ref. [64]). Figure 4.1 gives a summary of inter- and circumstellar silicon molecules detected so far.[1]

One important class of these molecules are the silicon-carbon clusters of type Si_nC_m $(n, m = 1, 2, 3, \ldots)$. This becomes evident in the list of detected molecules, where SiC_m, $m = 1, 2, 3, 4$ have all been observed. Strikingly, up to now only mono-silicon clusters have been observed. This fact is due to the presence of a permanent electric dipole moment in these species, which simplifies the detection significantly. In case of an absent dipole moment, no pure rotational spectrum is present. Rotation-vibrational transitions in the mid-infrared are the way to observe those species like SiH_4, whose ν_4 vibration has been detected in absorption in the circumstellar envelope of the late-type star IRC+10216.

Disilicon-carbon clusters Si_2C_m $(m = 3, 4, \ldots)$ in their isomer of lowest energy are linear, centro-symmetric and therefore non-polar, so they lack a pure rotational spectrum which could be detected by conventional radioastronomic means. Van Orden *et al.* were the first to measure a rotationally resolved spectrum of a disilicon-cluster. They reported on the ν_3 fundamental stretching vibration of Si_2C_3 [117]. This molecule still remains the only non-polar silicon-carbon cluster detected yet (for a graphical representation of its structure see Figure 4.2).

[1]Other silicon molecules which have been only tentatively detected are SiH (Ref. [95]) and SiH_2 (Ref. [109]). See also the website of the Cologne Database for Molecular Spectroscopy *http://www.astro.uni-koeln.de/cdms* for an up-to-date overview.

Dieses Werk ist copyrightgeschützt und darf in keiner Form vervielfältigt werden noch an Dritte weitergegeben werden.
Es gilt nur für den persönlichen Gebrauch.

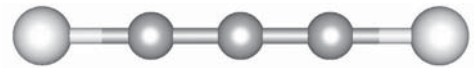

Figure 4.2: Graphical ball and stick representation of the Si_2C_3 molecule. On a linear carbon chain backbone, two silicon atoms terminate the chain in both directions. The calculated bond distances are r_{SiC} =1.6829 Å and r_{CC} =1.2895 Å at the CCSD(T)/cc-pwCVQZ level of theory [105].

Van Orden *et al.* found indication of a second band of lines in their spectrum. Due to the poor signal-to-noise ratio they did not manage to analyze it, but it was thought to originate from a hot band involving a bending vibration low in energy. They argued that the clusters had a fairly low vibrational temperature, because they were produced in a supersonic jet expansion, and only the lowest vibrational states should be populated. An infrared study of this hot band of Si_2C_3 would yield useful information about the involved bending mode.

In an effort to gain information about the vibrational ground state as well as the lowest vibrational bending mode of the nonpolar linear cluster Si_2C_3 the antisymmetric stretching fundamental band ν_3 as well as the $\nu_3 + \nu_7 - \nu_7$ hot band of that molecule has been measured at high resolution. For this purpose, an infrared jet spectrometer has been set up and characterized in performing this analysis.

4.2 Spectrometer for transient molecules

The spectrometer basically consists of a supersonic jet expansion, where transient molecules are produced via laser ablation, a continuous-wave OPO with a broad frequency coverage, and a sensitive detection scheme.

4.2.1 CW OPO and Frequency Calibration

For this experiment, the OPO system 2 was employed as radiation source. It emits idler radiation around 5 μm wavelength and is described in chapter 2. All measurements have been conducted using the poling period of 25.4 μm. Coarse frequency tuning was performed by varying the crystal temperature and continuous frequency tuning of the idler radiation necessary for experimental scans was finally achieved through pump laser tuning.

The wavemeter setup for this OPO explained in section 2 gave a first frequency information during the measurements and the frequency readout was recorded together with the data. This information greatly supported the assignment of reference gas transitions. To achieve a better frequency

Dieses Werk ist copyrightgeschützt und darf in keiner Form vervielfältigt werden noch an Dritte weitergegeben werden.
Es gilt nur für den persönlichen Gebrauch.

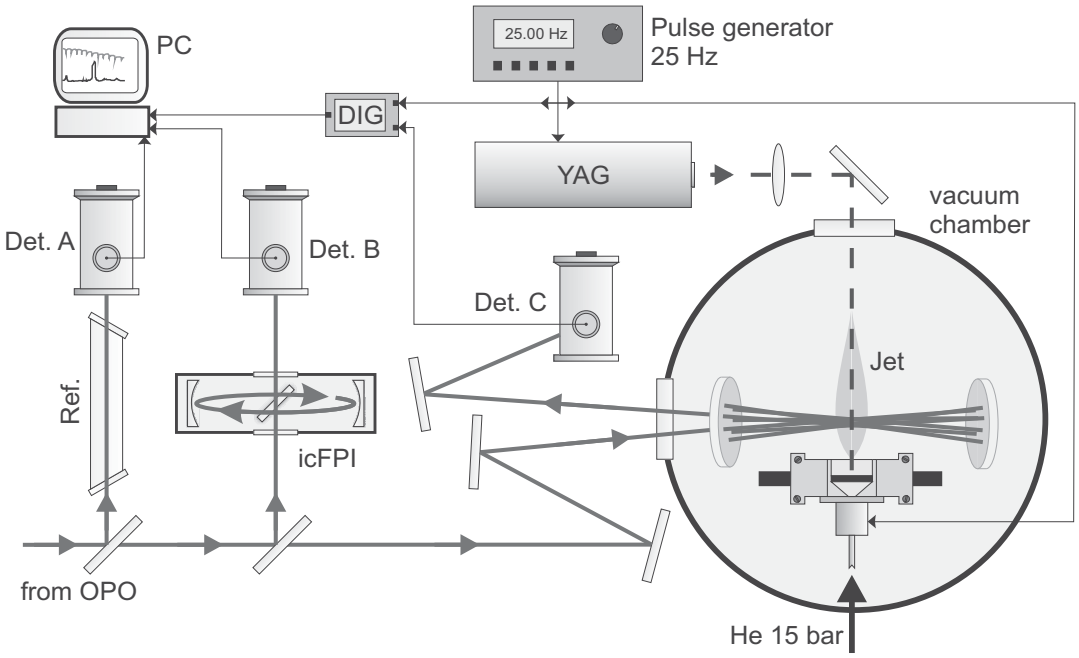

Figure 4.3: Schematic setup of the jet spectrometer. Parts of the OPO beam are guided through a reference gas cell (Ref) and a reference interferometer (icFPI) for calibration purposes. The beam passing the jet through a multipass reflection cell is detected and its signal digitized using an USB Oscilloscope (DIG). The jet is produced by ablating solid samples with a high-energy laser and a flow of helium at high pressure.

accuracy, the frequency channels of scans were finally calibrated using the simultaneously recorded spectra of a reference gas (Allene, C_3H_4) and a reference Fabry-Pérot interferometer. For this purpose, sensitive liquid nitrogen-cooled, photovoltaic InSb detectors were implemented (*Det. A* and *Det. B* in Figure 4.3).

Reference interferometers are widely used for calibration in frequency scans. Their fringes are assumed to be equidistant in frequency in the process of calibration. Therefore it is very important that fringes do not change their frequency position during the time of a scan. Commonly used solid germanium etalons are quite sensitive to temperature changes in this respect. An estimation for this temperature sensitivity of the resonance frequency ν of a solid germanium etalon can be made as follows: $\Delta\nu/\nu \approx \Delta n/n = \Delta n/\Delta T \cdot \Delta T/n \approx 1 \times 10^{-6}$ with the refractive index of germanium $n = 4$, the temperature dependence of this coefficient $\Delta n/\Delta T = 4 \times 10^{-4}$ [47]. Here, the length expansion of germanium can be neglected, because the linear expansion coefficient is roughly two orders of magnitude smaller than the change in the index of refraction. A small temperature variation of $\Delta T = 10^{-2}$ K results in a drift of the resonance frequency of the Ge etalon of 2×10^{-3}cm^{-1} at a frequency of 2000cm^{-1}. When using such an etalon, one has to make sure that its temperature is very stable during measurement, which can take an hour or more in our case.

Dieses Werk ist copyrightgeschützt und darf in keiner Form vervielfältigt werden noch an Dritte weitergegeben werden.
Es gilt nur für den persönlichen Gebrauch.

The internally coupled Fabry-Pérot Interferometer (icFPI) used in the experiment is designed to be insensitive to temperature changes and as such avoids the problems depicted. The setup and properties of our icFPI are described in Ref. [87]. The icFPI is evacuated and therefore has negligible coefficients for $\Delta n/\Delta T$, and the thermal expansion of the spacings between the interferometer mirrors is also compensated in the construction. This makes the icFPI an ideal tool for calibrating spectra.

Allene, C_3H_4, has been used as a reference gas. It exhibits a strong and dense spectrum around $5\,\mu$m, making it well suited for the calibration purposes described here. Allene line positions in the $2000\,\mathrm{cm}^{-1}$ region are known very accurately from Fourier-Transform Infrared measurements [9].

Final frequency calibration of the recorded Si_2C_3 spectrum was executed by making etalon fringes equidistant in the data using linear interpolation of frequency between fringes. After that, the complete frequency channel of the scan was altered using a linear function, so that the observed reference gas spectrum coincided with the known frequency positions from the literature. In overlapping scans, positions of observed target molecule transitions were also taken into account. In the present study, the fitting of the desired linear functions was done manually. The accuracy reached here is of the order of $5 \cdot 10^{-4}$ cm^{-1} (≈ 15 MHz).

4.2.2 Production of Species

Carbon-silicon clusters were produced using laser ablation followed by supersonic jet expansion similar to the approach described earlier [57, 75]. The experimental setup is drawn schematically in Figure 4.3. Radiation of a Q-switched Nd:YAG laser (Continuum Lasers, model INLITE III-30) with a repetition rate of 25 Hz is frequency multiplied. The third harmonic frequency at 355 nm wavelength is then focused onto the solid silicon carbide target rod. With approximately 1 ms long pulses of helium flow at backing pressures of approximately 15 bar, the ablated material is guided through a 7 mm long reaction channel, prior to expansion into a vacuum chamber, where the pressure is kept below 0.05 mbar by a roots blower. As a result of adiabatic cooling, rotational temperatures of approximately 20 K are typically found in the jet.

4.2.3 Detection Technique

To increase the sensitivity, the probing infrared beam traverses the jet more than 40, typically 60 times in a multipass-setup of Herriott-type [43], before it is focused on a sensitive InSb infrared detector.

Dieses Werk ist copyrightgeschützt und darf in keiner Form vervielfältigt werden noch an Dritte weitergegeben werden.
Es gilt nur für den persönlichen Gebrauch.

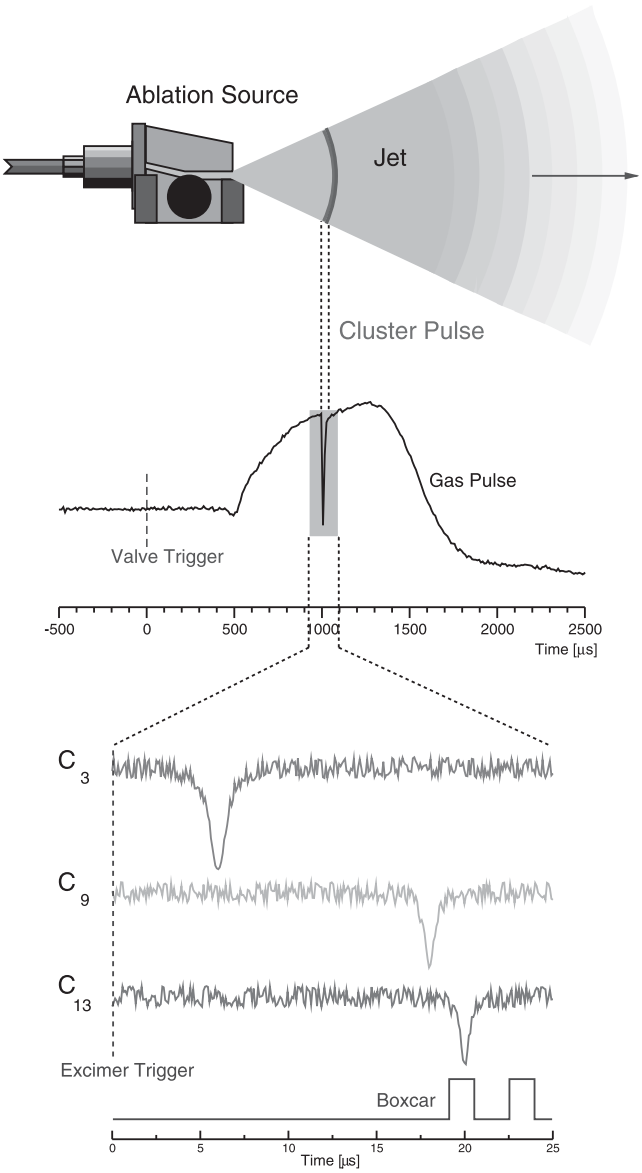

Figure 4.4: Schematic of the timing in the measurement procedure using the supersonic jet expansion.
During the helium buffer gas pulse, which is produced using a solenoid valve and lasts about 1 ms, a high-energy laser pulse ablates material from a solid precursor target (in our case a silicon-carbide rod). Clusters of different size form while the ablated material is being flushed by the buffer gas through an approximately 7 mm long reaction channel. The time of flight of present molecules depends on their mass. This allows to separate different species in the detection mechanism by choosing the time slot of boxcar integration according to their time of flight. In the present example, the boxcar setting is optimized for the C_{13} cluster. Usually, the result of a second boxcar integration shortly after the cluster pulse is subtracted for baseline correction.
The spectrometer built in this work records the full sampled jet signal, typically the first 50 μs after the laser pulse fired, instead of just recording the result of boxcar integration. This allows post-processing of data and therefore simultaneous detection of differently sized molecules. Figure taken from Reference [75].

Due to the low jet repetition rate of 30 Hz and the short cluster pulse duration of about 10 μs, the duty cycle of the spectrometer is about 0.03%. Usually, boxcar integrators are adopted to measure only during on-times of the cluster pulse. For background correction, a second boxcar integration shortly after on-time is subtracted. This is a sensitive detection technique, but has the disadvantage that the acquired signal strongly depends on the boxcar settings, namely the boxcar widths and delays, as illustrated in Figure 4.4. That means the exact timing of the cluster pulse has to be known beforehand, otherwise a frequency scan with a given boxcar setting leads to non-optimal results.

To overcome this drawback, in this work an oscilloscope (USB oscilloscope PicoScope 4000 series, Pico technology, UK) digitizing the complete jet ab-

Dieses Werk ist copyrightgeschützt und darf in keiner Form vervielfältigt werden noch an Dritte weitergegeben werden.
Es gilt nur für den persönlichen Gebrauch.

sorption signal is applied. Triggered by the ablation laser, the oscilloscope records typically 50 μs with a sampling rate of ≥ 10 MS/s to a hard disk. Due to the different time of flights of different clusters, the absorption signal of different species produced in the jet expansion can be separated in time (see Figure 4.4). A major advantage over boxcar integrators commonly used in these experiments is the possibility of post-processing of data because the entire time-resolved detector signal is recorded. That means that in contrast to the old Cologne setup, the boxcar integrators are software-emulated and their gates can be optimized after the measurement for the best signal-to-noise ratio. Another advantage is that different species present in the jet can be analyzed separately using data from just one single frequency scan.

4.3 Measurement and Analysis: Si_2C_3

In this work, the ν_3 fundamental band of Si_2C_3 has been measured by recording a total of 74 individual scans in the frequency interval between 1964 and 1972 cm^{-1}. Each scan was performed by varying the frequency in small steps of around 5 MHz, after having recorded 15 shots of the jet signal, so a single scan of 15 GHz lasts for 30 minutes at a repetition rate of 25 Hz. Selected regions have been measured more than once to increase the signal-to-noise ratio.

The scans were reduced in the following way: Each of them was calibrated as described in section 4.2.1 using the interferometer for the relative frequency calibration and allene ($H_2C{=}C{=}CH_2$) as reference gas for absolute frequency calibration. After that, an averaging algorithm has been applied to the partly overlapping spectra. This algorithm divides the relevant frequency range in bins with a width of 5×10^{-4} cm^{-1} and averages all data in one bin to one single data point. Because of varying jet conditions and idler power transmitted through the multipass cell, line intensities are only correct within approximately 30%, which is why spectra are normalized in intensity and weighted with their individual noise level beforehand. The resulting spectrum of Si_2C_3 obtained here is shown in Figure 4.5. A simulated spectrum is also shown. It has been obtained using the program PGOPHER [125] as discussed in the following.

4.3.1 The ν_3 fundamental band

50 lines of the measurements described above have been assigned to the ν_3 fundamental band of Si_2C_3 in the wavenumber range between 1964.6 cm^{-1} and 1971.1 cm^{-1}, covering rovibrational transitions P(50) to R(50). The

Dieses Werk ist copyrightgeschützt und darf in keiner Form vervielfältigt werden noch an Dritte weitergegeben werden.
Es gilt nur für den persönlichen Gebrauch.

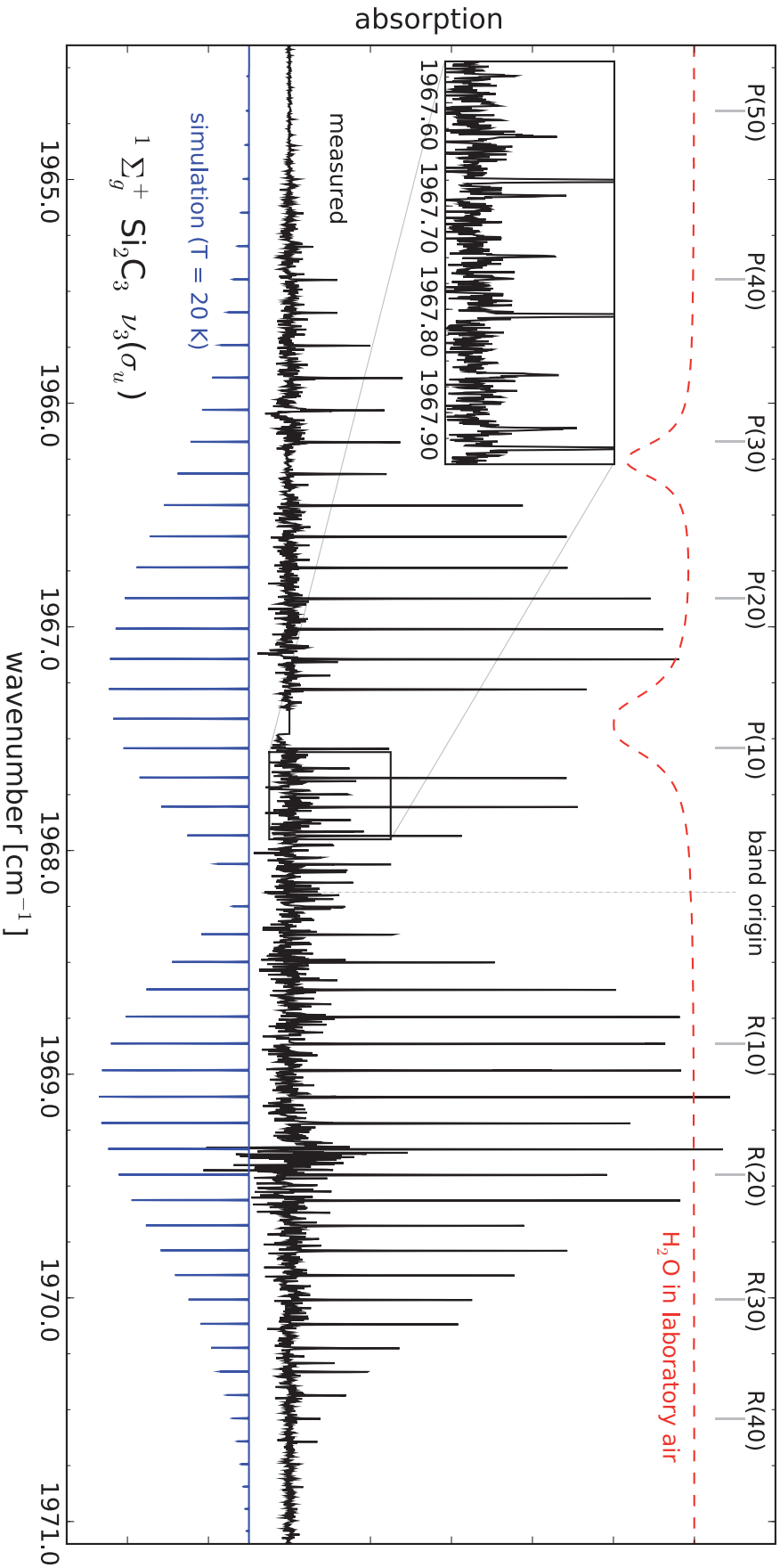

Figure 4.5: Spectrum of the ν_3 stretching vibration of Si_2C_3. Lines have a spacing of four times the rotational constant, because transitions with odd numbered values of the ground state rotational quantum number J'' are missing due to spin statistics. Transmission of infrared radiation through laboratory air is sketched in the dashed line using a HITRAN simulation. The inset shows a second rotational band originating from a hot band transition involving a vibrational bending mode (see section 4.3.2).

Dieses Werk ist copyrightgeschützt und darf in keiner Form vervielfältigt werden noch an Dritte weitergegeben werden.
Es gilt nur für den persönlichen Gebrauch.

P(12) transition could not be measured due to interference with a strong atmospheric water line. Table 4.2 lists all measured frequency positions and their deviations to the predicted frequencies from a least-squares fit.

The rovibrational energy levels of Si_2C_3 have been determined using a standard model for linear molecules (see for example Ref. [10]). The allowed rotational energy levels E of the molecule depends on the rotational quantum number J and is usually expressed as

$$\frac{E(J)}{h} = \nu_0 + B\,J(J+1) - D\,[J(J+1)]^2 + H\,[J(J+1)]^3 + \dots \tag{4.1}$$

with the rotational constant B, and the centrifugal distortion coefficients $D, H, L, \dots$ for each involved vibrational state. ν_0 is the band center for the relevant vibrational transition. The dependence of the rotational constant B_v of the vibrational excitation with quantum numbers v_i, on the rotation-vibration coupling constants α_i and the degeneracy of the mode d_i is:

$$B_v = B_e - \sum_i \alpha_i (v_i + d_i/2) + \dots \tag{4.2}$$

Selection rules for rovibrational transitions for a band of σ-symmetry (like the antisymmetric stretching vibration ν_3) are $\Delta J = \pm 1$. Transitions with $\Delta J = -1$ form the so-called P-branch of the spectrum, those with $\Delta J = +1$ the R-branch. Neglecting centrifugal distortion, vibration-rotation coupling and nuclear spin effects, the spectrum consists of two branches of equidistant lines with a spacing of $2B$, separated by a $4B$ distance at the band origin.

Owing to a $D_{\infty h}$ symmetry and statistics of identical nuclei with spin zero, there are no rotational levels with odd values of J in the ground state of Si_2C_3. Hence the spectrum of this molecule consists of two branches with approximately equidistant lines with a spacing of roughly four times the rotational constant B. The band center can be determined by the characteristic separation of the P- and R-branch of $6B$.

Molecular parameters based on a least-squares fit to this standard linear molecule model using the SPFIT program [84] are shown in Table 4.1. Values by Van Orden *et al.* are also shown for comparison as well as *ab initio* values by Botschwina [13] obtained at the coupled-cluster level of theory. The precision in the rotational constants B_0, B_3 was enhanced by a factor of five. For this fit, the experimental uncertainty of the frequency positions was set to 5×10^{-4} cm^{-1}, which results in a weighted rms value of 0.54 and is therefore conservatively approximated. Both B values are slightly smaller than reported by Van Orden, but still in the range of their estimated errors.

Dieses Werk ist copyrightgeschützt und darf in keiner Form vervielfältigt werden noch an Dritte weitergegeben werden.
Es gilt nur für den persönlichen Gebrauch.

Table 4.1: Molecular parameters for the ν_3 fundamental band of Si_2C_3 in units of cm^{-1}. The average deviation of the observed to the calculated frequencies is 2.6×10^{-4} cm^{-1}, the experimental uncertainty of the positions in the fit was conservatively set to 5×10^{-4} cm^{-1}, resulting in a weighted rms value of 0.54.

	This work			
Parameter	Experiment	*ab initio*[a]	Orden *et al.* [117]	*ab initio* [13]
B_0	0.0315678(12)	0.0316079	0.0315751(60)	0.0315652
$D_0 \times 10^9$	< 0.8[b]	–	1.0[c]	–
ν_3	1968.18865(14)	1979	1968.18831(18)	2020[d]
B_3	0.0314305(13)	0.0314261	0.0314374(57)	0.0314294[e]
$D_3 \times 10^9$	< 0.8[b]	–	1.0[c]	–

[a]See Ref. [105] for more information.

[b]Introduction of D did not significantly improve the fit. This value has been kept fixed at zero. As an estimation for an upper limit, the 1σ value of a common D parameter for ground and excited state (when released in the fitting procedure), is given.

[c]The authors gave this value as an estimate, believed to be correct within one order of magnitude.

[d]Harmonic value ω.

[e]Calculated from vibration-rotation coupling constants given in the reference.

Table 4.2: Line positions of the ν_3 fundamental band of Si_2C_3 in cm^{-1}. The value in parentheses is calculated. No measurement was possible here due to idler absorption caused by an atmospheric water line. The deviations from the predictions based on a least-squares fit are also given in the columns "obs.-calc.". See Table 4.1 for a list of these best fit molecular parameters.

J	R(J)	obs.-calc. $\times10^{-3}$	P(J)	obs.-calc. $\times10^{-3}$
0	1968.2521	0.6	–	
2	1968.3762	−0.2	1968.0621	0.0
4	1968.5002	−0.0	1967.9346	0.2
6	1968.6229	−0.0	1967.8057	−0.0
8	1968.7445	−0.0	1967.6757	−0.2
10	1968.8644	−0.6	1967.5455	0.6
12	1968.9839	−0.5	(1967.4129)	–
14	1969.1029	0.2	1967.2802	0.5
16	1969.2202	0.3	1967.1452	−0.3
18	1969.3361	0.1	1967.0103	0.1
20	1969.4508	−0.2	1966.8737	−0.0
22	1969.5649	−0.0	1966.7361	−0.1
24	1969.6778	0.1	1966.5972	−0.4

continued on next page

Dieses Werk ist copyrightgeschützt und darf in keiner Form vervielfältigt werden noch an Dritte weitergegeben werden.
Es gilt nur für den persönlichen Gebrauch.

Table 4.2 – continued from previous page
(Si_2C_3 line positions)

J	R(J)	obs.-calc. $\times 10^{-3}$	P(J)	obs.-calc. $\times 10^{-3}$
26	1969.7896	0.2	1966.4576	−0.2
28	1969.8998	−0.2	1966.3168	−0.2
30	1970.0094	−0.1	1966.1747	−0.3
32	1970.1182	0.3	1966.0321	0.2
34	1970.2254	0.3	1965.8877	−0.1
36	1970.3313	−0.0	1965.7427	0.2
38	1970.4366	0.2	1965.5959	−0.3
40	1970.5405	0.2	1965.4487	0.1
42	1970.6429	−0.3	1965.3004	0.3
44	1970.7448	−0.1	1965.1501	−0.3
46	1970.8452	−0.3	1964.9996	0.1
48	1970.9453	0.3	1964.8481	0.5
50	1971.0432	−0.2	1964.6944	−0.2

4.3.2 The $\nu_3 + \nu_7 - \nu_7$ hot band

As could already be seen from the inset in Figure 4.5, there is a weaker band of transitions visible. Figure 4.6 features this band in more detail. The ν_3 fundamental band is shown in the upper part, while zoom-ins of the P- and R-branches of the new band are shown in the middle and lower parts of the figure. For visibility reasons, the strong lines of the ν_3 fundamental were blanked out.

In total, 44 rotation-vibration transitions of this new band were recorded and are listed in Table 4.3. The analysis of this band is however not straightforward, because only the strongest transitions in the P- and $R-$branch could be detected. Since the intensity of lines drops significantly between the branches, no band origin with the expected Q-branch of a hot band of π symmetry could be recognized. However, the spacing between adjacent lines is nearly constant with about half the spacing observed in the ν_3 fundamental band. This is a strong indication of the relationship of the band to the Si_2C_3 molecule. There are two possibilities for the origin of the band: it could originate from the ν_3 vibration of a isotopic species of Si_2C_3, or a hot band transition $(\nu_3 + \nu_i) - \nu_i$ of vibrationally excited Si_2C_3 with i being the index of a bending vibration of low energy. Finally, the observed band has been assigned to the $(\nu_3 + \nu_7) - \nu_7$ hot band of Si_2C_3 for reasons explained in the following.

Dieses Werk ist copyrightgeschützt und darf in keiner Form vervielfältigt werden noch an Dritte weitergegeben werden.
Es gilt nur für den persönlichen Gebrauch.

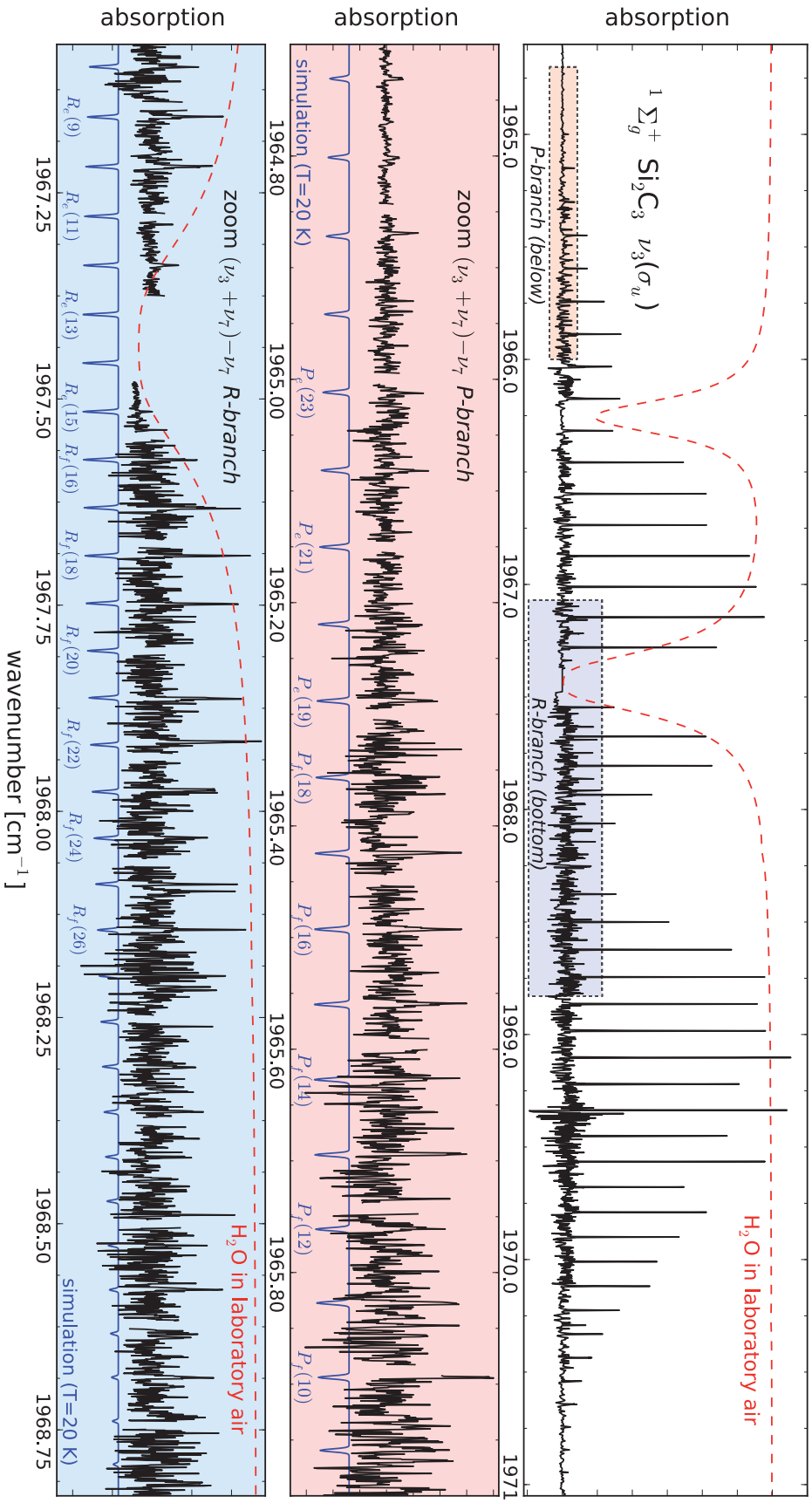

Figure 4.6: P and R branch of the $\nu_3+\nu_7-\nu_7$ hot band of Si_2C_3. Lines have a spacing of approximately two times the rotational constant, because of additional vibrational angular momentum from the involved bending motion. Transmission of infrared radiation through laboratory air is sketched in the dashed line using a HITRAN simulation. Transitions belonging to the ν_3 fundamental band have been blanked out for better visibility.

Dieses Werk ist copyrightgeschützt und darf in keiner Form vervielfältigt werden noch an Dritte weitergegeben werden.
Es gilt nur für den persönlichen Gebrauch.

The stable isotopes of the two elements carbon and silicon that Si_2C_3 is made of, are (with the natural abundance in parentheses): ^{12}C (98.9%), ^{13}C (1.1%), ^{28}Si (92.2%), ^{29}Si (4.7%) and ^{30}Si (3.1%). Assuming a statistical distribution of all possible isotopes in the molecule, the three most abundant isotopologues are: SiCCCSi (82.2%), ^{29}SiCCCSi (8.4%) and ^{30}SiCCCSi (5.6%). The most abundant isotopologues are therefore not centro-symmetric, thus the spacing between neighboring lines of a σ-band should be $2B$ as observed in the spectrum. However, if the observed band belonged to one of those species, the intensity of its lines should be 5% or less of that of the fundamental band[2], but are measured to be roughly 10%.

The strongest argument against the assumption of an isotopic nature of the band is the fact that there should be two distinct, at least partially resolved bands (Si_2C_3 mono-substituted with ^{29}Si and ^{30}Si) with an intensity ratio of roughly 3:2 visible instead of only a single one. Since the rotational constants should be quite different, an accidental overlap of those is not possible over the entire range measured. These bands, as shown already in a previous investigation [85], both exhibit a very small isotopic shift (< 0.5 cm^{-1}) relative to the parent species and would have been observed in the recorded frequency range. The isotopic shift of any ^{13}C species is known to be much larger [85], while the abundances are getting too small with other isotopic species (1.8% for Si^{13}CCCSi, which is not observable with the given sensitivity of the spectrometer). Therefore, an isotopic origin of the band can be ruled out and the only possibility is a hot band involving a bending mode.

For the π-transition of a hot band involving a bending mode, a different set of energy levels compared to equation (4.1) is expected, because the additional angular momentum caused by the degenerate bending mode has to be taken into account. The quantum number for this momentum is called l. See for example Refs. [10, 35] for an introduction into this topic. To sum up briefly, the energy levels E of a linear polyatomic molecule in such a degenerate vibrational bending mode split up. This effect is called l-type doubling and the size of the splitting is in good approximation proportional to $J(J+1)$. For each level E with $l = 1$, there are now two levels $E_\pm$, which can be expressed as

[2]Due to symmetry reasons, there are two possibilities to exchange an silicon isotope (one for each end of the chain), which gives a factor of roughly 10% in the abundance of ^{29}SiCCCSi compared to the parent SiCCCSi. However, since there are all rotational states allowed in a non-centrosymmetric molecule, the partition function is two times larger than in the case of the parent isotopologue Si_2C_3, where only states with even J are present in the ground state. Thus, the intensity of the isotopically induced transitions is roughly 5% or less.

Dieses Werk ist copyrightgeschützt und darf in keiner Form vervielfältigt werden noch an Dritte weitergegeben werden.
Es gilt nur für den persönlichen Gebrauch.

$$\frac{E_{\pm}(J)}{h} = \nu_0 + B[J(J+1) - l^2] - D[J(J+1) - l^2]^2 + H[J(J+1) - l^2]^3 + \ldots$$
$$\pm \frac{1}{2}\left(q[J(J+1) - l^2] + q_D[J(J+1) - l^2]^2 + \ldots\right) \quad . \tag{4.3}$$

Here, $B, D, H, \ldots$ are the rotation constant and the centrifugal distortion coefficients as defined in (4.1). The coefficients q ($q_D, q_H, q_L, \ldots$) describe the l-type doubling (and the centrifugal distortion of the l-type doubling). The lower levels are of e-parity (minus in the above equation), while the upper levels have f-parity (plus in the above equation). Due to spin statistics in a linear molecule of $D_{\infty h}$ symmetry, the e-parity levels are only present for odd values of J and the f-parity levels for even values of J in the bending vibrational state. So there is a spacing between the lines which is $2B$ in a first-order approximation, but alternating[3] at a closer look. This alternation gets larger with increasing values of J. Selection rules in such a band are $\Delta J = 0, \pm 1$, with a weak Q-branch of $\Delta J = 0$ and a P- and R-branch like in a σ-band.

Assuming that the observed vibrational band is a hot band $(\nu_3 + \nu_i) - \nu_i$, with i being the vibrational index of a low-lying vibrational bending mode, one expects nearly equidistant lines with spacings of approximately $2B$. Such hot bands have been observed previously for a number of pure carbon clusters produced under similar conditions (see, e.g., Refs. [57,76,118], and references therein). Due to the weak intensity of the band, no low-J- and no Q-branch transitions (see Table 4.3) could be observed, which is why the location of the band center could not be determined without further assumptions based on data from high-level quantum-chemical calculations.

Experience from similar analyses of hot bands in supersonic jets indicates that only bending modes low in energy are populated on a relevant scale (Refs. [57, 76, 118]). Thus in this case the transition originating from the ν_7 mode is most plausible, since the calculated energies of the two lowest modes (on the CCSD(T) level) are 77 cm^{-1} for the ν_7 mode and 187 cm^{-1} for ν_5 (Ref. [105]). Taking this vibrational assignment as premise, the band origin of the rotational assignment is still uncertain.

Test assignments and trial fits of the band were performed by shifting the possible band origin by $2B$. This way, a band origin was found with the observed B constant deviating only 1.7×10^{-5} cm^{-1} (0.05%) from the predicted rotational constant. Changing the assignment of $J \pm 1$ results in a change of the rotational constant B of $\pm 1.4 \times 10^{-4}$ cm^{-1}(0.5%), which is

[3]This alternation of the frequency spacing is referred to as "staggering" of lines.

Dieses Werk ist copyrightgeschützt und darf in keiner Form vervielfältigt werden noch an Dritte weitergegeben werden.
Es gilt nur für den persönlichen Gebrauch.

larger than the estimated uncertainty in the high-level quantum-chemical calculations and cannot be explained with any other reasonable combination of the rotational and rotation-vibration interaction constants.

The l-type doubling constant q is another important diagnostic for the analysis. However, the calculated values for q are quite small and the present dataset unfortunately is not accurate enough to yield results on that. Using only three parameters (B_7, B_{3+7} and the band center), the rms value of the fit is $5.4 \times 10^{-4}\,\mathrm{cm}^{-1}$ and hence roughly half the estimated uncertainty of transition frequencies of $1 \times 10^{-3}\,\mathrm{cm}^{-1}$. If q_7 is fixed to the calculated value of $q_7 = 0.78\,\mathrm{MHz}$ in the fit, the rms increases to $9.1 \times 10^{-4}\,\mathrm{cm}^{-1}$, while releasing the parameter leads to an rms of $4.9 \times 10^{-4}\,\mathrm{cm}^{-1}$, yielding an unphysical value of $q_7 = -0.36(22)\,\mathrm{MHz}$. The possibility of q_7 being influenced by a perturbation can also be excluded by considering the calculated anharmonic force field. Thus we can conclude that q_7 is smaller than what is expected from quantum-chemical calculations.

Table 4.3: Measured transition frequencies of the $\nu_3 + \nu_7 - \nu_7$ hot band of Si_2C_3 in cm^{-1}. Best fit residuals are also given (see Table 4.4 for the fit parameters). Values in parentheses are calculated and could not be measured due to low signal-to-noise ratio or interfering water absorption.

J	$R(J)$	obs.-calc. ($\times 10^3$)	$P(J)$	obs.-calc. ($\times 10^3$)
3e	1966.7907	0.3	(1966.3489)	–
4f	1966.8526	0.2	(1966.2847)	–
5e	1966.9139	−0.2	(1966.2203)	–
6f	1966.9751	−0.4	(1966.1555)	–
7e	1967.0368	0.2	1966.0903	−0.1
8f	1967.0974	0.0	(1966.0252)	–
9e	1967.1578	−0.1	(1965.9596)	–
10f	1967.2181	−0.1	1965.8938	0.2
11e	(1967.2782)	–	1965.8275	0.0
12f	1967.3378	−0.1	1965.7607	−0.3
13e	(1967.3973)	–	1965.6939	−0.4
14f	(1967.4564)	–	1965.6266	−0.7
15e	1967.5155	0.2	1965.5593	−0.7
16f	1967.5738	−0.1	1965.4926	0.2
17e	1967.6325	0.3	1965.4242	−0.4
18f	1967.6902	0.0	1965.3567	0.3
19e	1967.7486	0.7	1965.2879	−0.1
20f	(1967.8054)	–	1965.2206	1.3
21e	1967.8635	0.9	(1965.1505)	–

continued on next page

Dieses Werk ist copyrightgeschützt und darf in keiner Form vervielfältigt werden noch an Dritte weitergegeben werden.
Es gilt nur für den persönlichen Gebrauch.

Table 4.3 – continued from previous page
(Si_2C_3 $\nu_3 + \nu_7 - \nu_7$ hot band frequencies)

J	$R(J)$	obs.-calc. ($\times 10^3$)	$P(J)$	obs.-calc. ($\times 10^3$)
22f	(1967.9195)	–	1965.0818	0.7
23e	(1967.9761)	–	1965.0123	0.7
24f	1968.0321	−0.3	(1964.9419)	–
25e	1968.0884	−0.1	1964.8693	−2.4
26f	1968.1435	−0.7	1964.8017	0.4
27e	1968.1999	0.2	1964.7307	0.1
28f	(1968.2549)	–	1964.6596	−0.1
29e	1968.3104	0.6	1964.5885	0.1
30f	1968.3641	−0.4	1964.5170	0.1
31e	(1968.4189)	–	1964.4457	0.5
32f	(1968.4730)	–	(1964.3733)	–
33e	(1968.5268)	–	(1964.3010)	–
34f	1968.5798	−0.5	(1964.2284)	–
35e	(1968.6335)	–	(1964.1555)	–
36f	1968.6864	−0.6	(1964.0823)	–

Table 4.4: Molecular parameters for the $\nu_3 + \nu_7 - \nu_7$ hot band of Si_2C_3 based on a least-squares fit. 5 parameters have been used to reproduce the frequencies of 44 transitions. All values are given in units of cm^{-1}.

Parameter	This work Experiment	*ab initio*[a]	*ab initio* [13]
ν_7	x[b]	77	79[c]
B_7	0.0316795(22)	0.0316589	0.0316523[d]
q_7 $\times 10^6$	9.1(43)	26.0	25.4
$\nu_3 + \nu_7$	$x + 1966.53981(15)$[b]	–	–
B_{3+7}	0.0315391(21)	0.0315175	0.0315165[d]
$q_{3+7} \times 10^6$	9.4(43)	–	–

[a] See Ref. [105] for more details.
[b] The experiment allows only for the determination of the difference $(\nu_3 + \nu_7) - \nu_7$.
[c] Harmonic value ω.
[d] Calculated from vibration-rotation coupling constants given in the reference.

4.4 Conclusion and Outlook

Using the carbon-silicon cluster Si_2C_3 as a target molecule, a powerful combination of a cw long-wavelength OPO based on PPLN with an instrument for

Dieses Werk ist copyrightgeschützt und darf in keiner Form vervielfältigt werden noch an Dritte weitergegeben werden.
Es gilt nur für den persönlichen Gebrauch.

application in sensitive high-resolution spectroscopy of transient molecules was demonstrated. The frequency range of the OPO between 1850 and 2130cm^{-1} provides superb wavelength coverage in a very important spectral region in the MIR, where many linear cumulenic structures with a carbon chain backbone of type C_m (m=3,4,...) exhibit strong features in this range. Thus the built instrument is potentially capable of detecting other similar clusters like, e.g. Si_2C_5.

The frequency accuracy achieved with the present setup is of the order of a few MHz. Further improvement of the frequency accuracy may be obtained by stabilizing the OPO signal frequency to a reference interferometer. A stabilized mode-locked laser or frequency comb can yield even greater accuracy on the kHz-level [48].

Further improvement in sensitivity of the spectrometer may be achieved by using cavity enhanced spectroscopy instead of the multipass reflection cell. High-reflectivity mirrors may be used to achieve up to several 100 effective passes. Additionally, the infrared probing beam in a standing wave cavity is constrained to a much smaller volume of the jet than in a multipass cell, which would enable further enhancing the absorption signal by optimizing the position of the jet relative to the beam.

Dieses Werk ist copyrightgeschützt und darf in keiner Form vervielfältigt werden noch an Dritte weitergegeben werden.
Es gilt nur für den persönlichen Gebrauch.

Dieses Werk ist copyrightgeschützt und darf in keiner Form vervielfältigt werden noch an Dritte weitergegeben werden.
Es gilt nur für den persönlichen Gebrauch.

5

High-Resolution Spectroscopy of Small Carbon Clusters

"There are things we know that we know. [...] There are things that we now know we don't know. But there are also [...] things we don't know we don't know"

Donald Rumsfeld, former defense secretary of the USA

Using the OPO system 1 described in chapter 2, the vibrational combination band $(10^01)\leftarrow(00^00)$ as well as the hot band $(11^11)\leftarrow(01^10)$ of C_3 have been detected and analyzed for the first time[1]. The measurements help to refine theoretical models for the potential of the C_3 molecule.

In addition, the antisymmetric stretching mode ν_5 of the linear cluster C_7 has been remeasured in unprecedented accuracy by using a quantum cascade laser system. An improvement in sensitivity compared to earlier measurements enabled the detection of a second band of lines, which has been tentatively assigned to the $\nu_5 + \nu_{11} - \nu_{11}$ hot band. Analysis of these bands results in the currently best parameter set available for this molecule.*

[1]The vibrational states of C_3 are designated with $(v_1 v_2^l v_3)$, where v_i is the vibrational quantum number in the i-th vibrational mode and $l\hbar$ the vibrational angular momentum.

*This chapter contains yet unpublished results on C_3. The part about C_7 is based on the following publication:

- The ν_5 antisymmetric stretching mode of linear C_7 revisited in high resolution. J. Krieg, V. Lutter, F.-X. Hardy, S. Schlemmer, T. F. Giesen, *Journal of Chemical Physics* **132** 224306 (2010)

Dieses Werk ist copyrightgeschützt und darf in keiner Form vervielfältigt werden noch an Dritte weitergegeben werden.
Es gilt nur für den persönlichen Gebrauch.

5.1 Introduction

Pure carbon clusters, C_n, $n = 2, 3, 4 \ldots$, are of fundamental interest for their role in combustion processes, benchmark systems for quantum chemistry, and also play an important role in the chemical processes of carbon-rich environments in space. Chemical network models of regions such as the envelopes of late type stars, e.g. IRC+10216, show pathways to carbonaceous species which undergo carbon enrichment and hydrogen depletion (see e.g. Ref. [67]). Understanding the formation process of pure carbon clusters and their detection in space are thus key to test and verify these models. So far, only C_2, C_3, and C_5 have been detected in diffuse clouds, circumstellar shells of carbon stars, and in the interstellar medium via rovibronic or electronic spectroscopy (see Refs. [22, 32, 62, 69, 71]). A systematic search for larger carbon clusters lacks experimental data in the mid- and far-infrared.

Of clusters known to exist, antisymmetric stretching vibrations of C_3 to C_{10} and C_{13} in the mid-IR region have been recorded by means of laboratory spectroscopy with resolved rotational structure, which is a prerequisite for an unambiguous detection in space (e.g. Refs. [31, 33, 46, 63, 69, 70, 75, 76, 119]). In the following, experiments are described which have been conducted to enlarge the available dataset of highly accurate rovibrational data of the two clusters C_3 and C_7. Valuable information could be gained for the ground and the lowest vibrational bending modes of both molecules.

5.2 Experiments on linear C_3

The C_3 molecule has been subject to research for more than five decades. Electronic bands have been observed in emission spectra of comets as early as 1882 [45], but could not be assigned to any species at that time. In 1951, the spectra were reproduced in the laboratory and assigned to linear triatomic carbon C_3 for the first time by Douglas [25]. A graphical representation of the structure is shown in Figure 5.1. The astrophysical importance of C_3 has been demonstrated through several interstellar detections [32, 79], and a recent paper proved the existence of C_3 in star forming regions using the Herschel satellite [71].

Up to now, it seems to be the only pure carbon cluster known as "floppy", which means that the bending vibration has a very shallow, anharmonic po-

Figure 5.1: Graphical ball and stick representation of the linear carbon cluster C_3. The calculated equilibrium bond length is $r_e = 1.2945$ Å on a CCSD(T)/cc-pVQZ level of theory (Ref. [68]).

Dieses Werk ist copyrightgeschützt und darf in keiner Form vervielfältigt werden noch an Dritte weitergegeben werden.
Es gilt nur für den persönlichen Gebrauch.

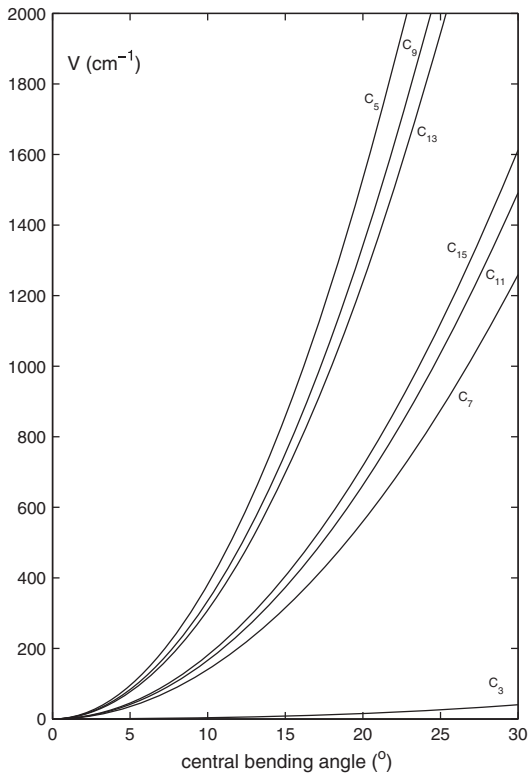

Figure 5.2: Plot of the calculated potential of linear carbon chains C_{2n+1}, (n=1-7) for bending around the central carbon atom on a CCSD(T)/cc-pVQZ level of theory. The graph has been taken from Ref. [15]. Bond lengths and other angles are kept fixed to the equilibrium values. In contrast to other carbon clusters, C_3 exhibits a highly anharmonic and shallow bending potential.

tential. This shallow potential allows a large amplitude motion and complicates theoretical treatment of internal dynamics. Figure 5.2 shows a calculated potential for the bending motion around the central atom while the rest of the molecule has been assumed rigid as taken from Ref. [15]. For this reason, C_3 has been subject to several theoretical treatments describing the potential with different approaches [50, 122].

The first detection of C_3 in its electronic ground state with resolved rotational structure has been performed using laser diode spectroscopy in 1988 by Matsumura *et al.* [63]. C_3 was produced via photolysis using diacetylene and allene as precursor molecules and probed in its ν_3 fundamental vibration around 2040 cm^{-1}. Soon after, the same group published measurements of hot bands and combination bands in the neighboring frequency regime [51]. Many further vibrational levels have already been detected using laser-induced-fluorescence spectroscopy [8, 90], many of which are infrared-inactive when the transition starts from the ground state. Especially, the ν_1 fundamental frequency of the symmetric stretching mode has been determined using this sort of measurements. In 1967, Merer found the value $\nu_1 = 1224.5\,\mathrm{cm}^{-1}$ [65].

The region of the combination bands involving the symmetric stretching mode has been unexplored yet except for C_3 trapped in inert-gas matrices. There, a value for the (10^01) energy of $\nu_{1+3} = 3245.2\,\mathrm{cm}^{-1}$ in solid argon [80] and $\nu_{1+3} = 3255.6\,\mathrm{cm}^{-1}$ in solid neon [34] has been reported. In

Dieses Werk ist copyrightgeschützt und darf in keiner Form vervielfältigt werden noch an Dritte weitergegeben werden.
Es gilt nur für den persönlichen Gebrauch.

the experiment described in the following, the supersonic jet spectrometer featuring OPO system 1 has been used to perform high-resolution rovibrational spectroscopy of gas phase C_3 in the frequency range of the vibrational combination band (10^01).

5.2.1 Experimental Setup

The basic experimental setup of the spectrometer as well as the data acquisition scheme has been described in chapter 4. As precursor in the form of a solid target for ablation, a commercial graphite rod is exposed to high-energy pulses from a Q-switched Nd:YAG laser running on its third harmonic frequency. The schematic setup is shown in Figure 4.3. Besides the graphite rod, only the radiation source differs: the OPO system for idler wavelengths around 3 μm, aligned for the crystal poling period of $\Lambda = 31.0\,\mu$m, has been used. Ammonia, NH_3, has been chosen as a reference gas.However, the intensities of the ammonia absorption lines are quite small in the required range, which is why a multi-pass cell of Herriott-type similar to the one presented in chapter 3 has been aligned in order to increase the absorption path length to 20 m.

A typical frequency scan was performed by tuning the pump frequency continuously over a small frequency range of around 15 GHz (0.5 cm^{-1}) with a scanning speed of 5 to 10 MHz/s. The idler frequency has been recorded every 15 ablation cycles during scans using the wavemeter readout. The repetition rate of the ablation and therefore the measurement rate was 25 Hz.

5.2.2 Measurements and Results: C_3

A total of 57 rovibrational transitions has been measured in the frequency range covering more than 45 cm^{-1} between 3233.8 cm^{-1} and 3280.6 cm^{-1}. Twenty-three of them have been assigned to the $(10^01)\leftarrow(00^00)$ combination band of C_3, and 34 to the associated $(11^11)\leftarrow(01^10)$ hot band. They are listed in Tables 5.1 and 5.2, respectively. When the assignment of the transitions was unambiguous, gaps in the mentioned range have been allowed to reduce the already long measurement time. Special attention has been paid to the high-J transitions which give information on the distortion parameters of the molecule.

Frequency calibration has been performed using the same approach as described in section 3.3.3, where the recorded frequency readout from the wavemeter has been offset, so that frequencies of recorded reference gas transitions match the catalog values. However, due to the rather sparse spectra of suitable reference gases and the limited continuous tuning range of the

Dieses Werk ist copyrightgeschützt und darf in keiner Form vervielfältigt werden noch an Dritte weitergegeben werden.
Es gilt nur für den persönlichen Gebrauch.

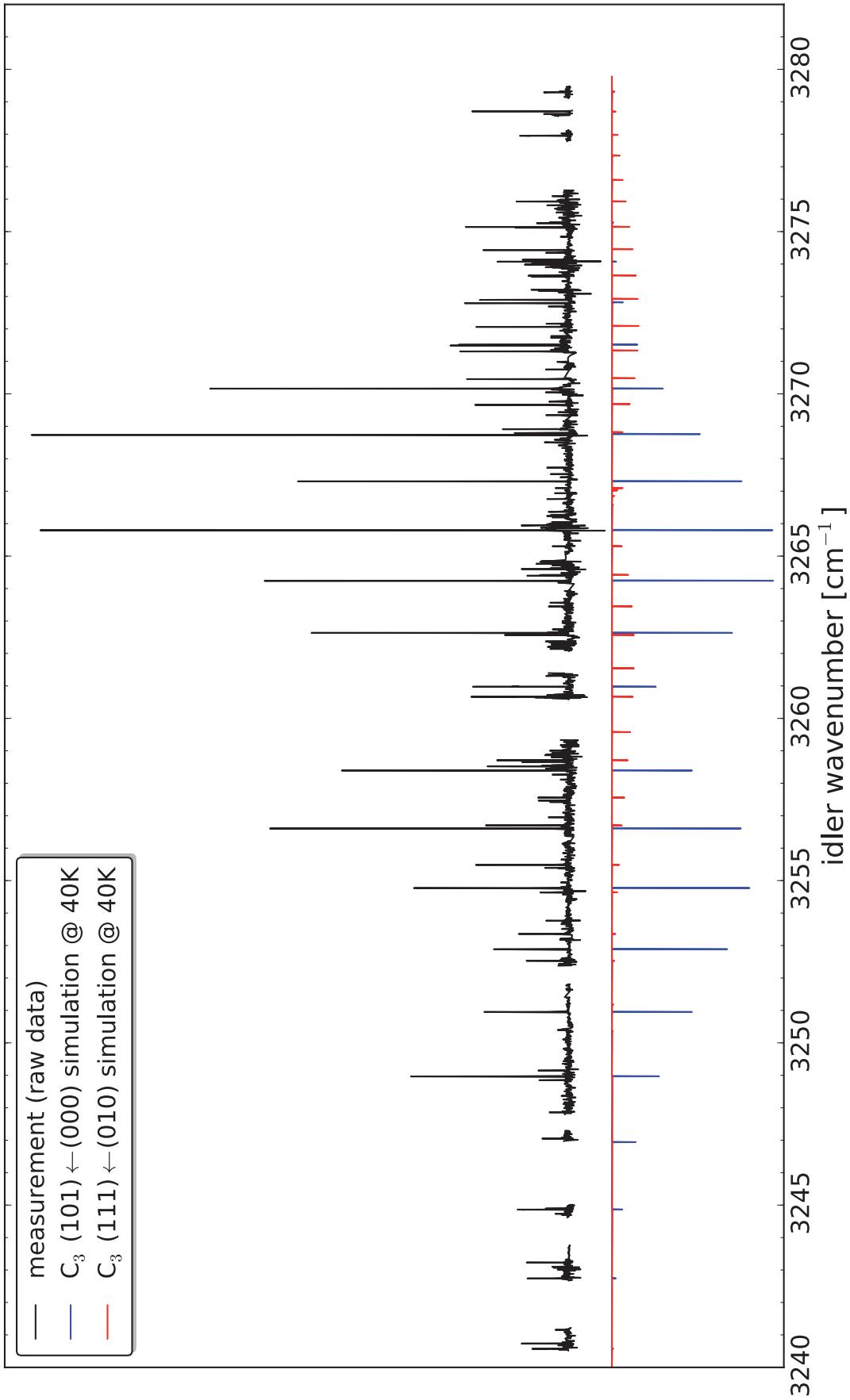

Figure 5.3: Overview spectrum of the $(10^01)\leftarrow(00^00)$ and $(11^11)\leftarrow(01^10)$ combination bands of the linear carbon cluster C_3. Pointing downwards is a simulation of both bands at a rotational temperature of 40 K.

Dieses Werk ist copyrightgeschützt und darf in keiner Form vervielfältigt werden noch an Dritte weitergegeben werden.
Es gilt nur für den persönlichen Gebrauch.

OPO idler frequency, a calibration in the mentioned way was not possible for every scan. Transitions have been given with an increased uncertainty, when no water vapor or ammonia absorption line could be included in the respective frequency range of the scan. The uncertainty of lines calibrated this way has been determined empirically by conservatively estimating the wavemeter offsets experienced from data presented here and in chapter 4.

The $(10^01)\leftarrow(00^00)$ combination band

Table 5.1 lists all measured transitions which have been assigned to the $(10^01)\leftarrow(00^00)$ combination band of C_3. The $6B$ spacing between $P(2)$ and $R(0)$ transitions is a characteristic feature of a σ-vibrational band of a molecule featuring Bose-Einstein spin statistics. This finding makes the presented assignment unambiguous. A least-squares fit has been performed using the PGOPHER program on the theoretical basis which has been introduced in equations (4.1) in section 4.3.1. The result is shown in Table 5.3.

Table 5.1: List of the 23 observed transition frequencies of the (101)←(000) combination band of C_3 in cm^{-1}. The uncertainty in the last digit is given in parentheses. Values marked with an asterisk (*) are calculated using the fit parameters. Best fit residuals are also given (see Table 5.3 for the best fit parameters). The unweighted average error of the fit is 3.7×10^{-4} cm^{-1}.

J	$P(J)$	obs.-calc. ($\times10^3$)	$R(J)$	obs.-calc. ($\times10^3$)
0	–		3260.9744(6)	−0.5
2	3258.3915(5)	0.2	3262.6340(20)	0.3
4	3256.6061(5)	0.2	3264.2415(5)	−0.0
6	3254.7701(5)	−0.2	3265.7983(5)	0.1
8	3252.8857(5)	0.3	3267.3032(20)	−0.4
10	3250.9513(5)	−0.2	3268.7595(20)	1.4
12	3248.9690(20)	−0.3	3270.1620(5)	−0.1
14	3246.9396*	–	3271.5163(5)	0.1
16	3244.8634(5)	0.0	3272.8208(5)	−0.3
18	3242.7418(5)	−0.1	3274.0776(5)	0.1
20	3240.5760(20)	−0.1	3275.2854*	–
22	3238.3673(7)	0.5	3276.4446*	–
24	3236.1143(5)	−0.3	3277.5528*	–
26	3233.8189(5)	0.1	3278.6059(5)	−0.0

The band center has been determined to be 3260.1264(2) cm^{-1}, which presents the most accurate measurement of this vibrational energy up to now. This information gives also input to a better understanding of the

Dieses Werk ist copyrightgeschützt und darf in keiner Form vervielfältigt werden noch an Dritte weitergegeben werden.
Es gilt nur für den persönlichen Gebrauch.

potential of C_3. In a very simple treatment, the vibrational energy levels G of a linear molecule can be expressed using the notation of Ref. [10] (see also Ref. [26]) as:

$$G(v_1, v_2, \ldots) = \sum_r \omega_r(v_r + \frac{d_r}{2}) + \sum_{r \leq s} x_{rs}(v_r + \frac{d_r}{2})(v_s + \frac{d_s}{2}) + \sum_{r \leq s} g_{rs} l_r l_s \ldots \quad (5.1)$$

with the harmonic frequencies ω and the anharmonicity constants x_{rs}. The indices r and s represent the vibrational modes of the molecule. v is the corresponding vibrational quantum number, d the degeneracy of that mode and $l\hbar$ the vibrational angular momentum. In the present case of a binary combination band of two vibrational modes 1 and 3 with the frequencies $\nu_1 = G(1,0,0) - G(0,0,0)$ and $\nu_3 = G(0,0,1) - G(0,0,0)$, its frequency $\nu_{1+3} = G(1,0,1) - G(0,0,0)$ simplifies using the above equation to

$$\nu_{1+3} = \nu_1 + \nu_3 + x_{13} \quad , \quad (5.2)$$

neglecting higher-order terms in the anharmonic potential. Since both of the fundamental frequencies $\nu_1 = 1226.6(10)\,\mathrm{cm}^{-1}$ and $\nu_3 = 2040.0198(8)\,\mathrm{cm}^{-1}$ are known[2] [63, 78], the anharmonicity constant x_{13} can be estimated from the presented measurements of $\nu_{1+3} = 3260.1264(2)\,\mathrm{cm}^{-1}$ as $x_{13} = -6.5(10)\,\mathrm{cm}^{-1}$. The uncertainty is comparably large because the ν_1 vibrational mode is the symmetric stretching vibration and therefore not infrared active. ν_1 has been determined from stimulated emission pumping spectra in the UV and visible, where the absolute frequency accuracy is not as high as in the infrared.

The rotational constant and the centrifugal distortion in the (10^01) state agrees well with the calculated values from Špirko *et al.* [122], but the deviation in the band center is roughly $15\,\mathrm{cm}^{-1}$ (corresponding to about 0.5%), indicating that the theoretical models for the potential still can be improved. The measurements are not accurate enough to compete with those done on the $(01^10)\leftarrow(00^00)$ band by Gendriesch *et al.* [29], which have been performed in the sub-mm regime with uncertainties on the kHz-level. However, the molecular parameters obtained for the ground state (00^00) just by fitting the new measurements on C_3 agree reasonably well with those given by Gendriesch *et al.*

The $(11^11)\leftarrow(01^10)$ hot band

Thirty-four transitions in the above mentioned frequency regime were assigned to the $(11^11)\leftarrow(01^10)$ hot band, as listed in Table 5.2. As already

[2]Note that Merer found a different value for the symmetric stretch energy, namely $\nu_1 = 1224.5\,\mathrm{cm}^{-1}$ [65].

Dieses Werk ist copyrightgeschützt und darf in keiner Form vervielfältigt werden noch an Dritte weitergegeben werden.
Es gilt nur für den persönlichen Gebrauch.

shown in section 4.3.2, a hot band transition starting from a degenerate bending mode is of π symmetry and exhibits an almost regular spectrum. The spacing between lines is approximately $2B$ and so-called staggering is present. Staggering is briefly explained in section 4.3.2, and means that the spacing between neighboring lines alternates as a result of Bose-Einstein nuclear spin statistics. A weak Q-branch is characteristic of these bands at the band origin. Figure 5.4 features the observed Q-branch of the $(11^11)\leftarrow(01^10)$ hot band together with the $R(8)$ transition of the $(10^01)\leftarrow(00^00)$ combination band. The hot band is roughly 15 to 20% less intense than the combination band.

Table 5.2: List of the 34 observed transition frequencies of the $(11^11)\leftarrow(01^10)$ hot band of C_3 in cm^{-1}. The uncertainty in the last digits is given in parentheses. Best fit residuals are also given (see Table 5.3 for the fit parameters). Values marked with an asterisk ($*$) are calculated using the fit parameters. The rms value of the fit is 1.3×10^{-3} cm^{-1}.

J	$P(J)$	o.-c. $\times 10^3$	$Q(J)$	o.-c. $\times 10^3$	$R(J)$	o.-c. $\times 10^3$
1e			3267.0962(20)	0.4	3268.8181(20)	1.2
2f	3265.3039(5)	0.7	3267.0249(20)	0.5	3269.6834(5)	−0.2
3e	3264.4199(5)	−1.1	3267.0807(20)	0.4	3270.4783(20)	−2.7
4f	3263.4510(5)	0.6	3266.8499(20)	−1.2	3271.3342(5)	0.5
5e	3262.5698(20)	0.3	3267.0536(20)	1.4	3272.0907(5)	0.2
6f	3261.5412*	–	3266.5786(20)	−0.8	3272.9241(5)	−0.8
7e	3260.6648(8)	−0.4			3273.6445(5)	−0.7
8f	3259.5763*	–			3274.4576(5)	0.5
9e	3258.7078(5)	−0.6			3275.1458(5)	1.0
10f	3257.5567(5)	0.1			3275.9302(10)	−0.5
11e	3256.7012(5)	1.7			3276.5897*	–
12f	3255.4817(9)	−1.5			3277.3465*	–
13e	3254.6373(5)	−1.3			3277.9794(5)	1.0
14f	3253.3574(5)	0.2			3278.7060(5)	−0.0
15e	3252.5309(20)	4.6			3279.3192(5)	0.8
16f	3251.1804(5)	0.1			3280.0118*	–
17e	3250.3635*	–			3280.6030(20)	−2.9
18f	3248.9538(20)	−0.9			3281.2675*	–

The band center was found to lie at 3267.0988(5) cm^{-1}, but since the vibrational energy of the lower state (01^10) is known very accurately from measurements in the far-infrared region, one can determine the energy of the upper level (11^11) precisely to $\nu_{1+2+3} = 3330.5154(5)\,cm^{-1}$. This measurement can be used to refine the potential of C_3 in the future. Here, a first estimation will be given as in the preceding section: Using equation (5.1)

Dieses Werk ist copyrightgeschützt und darf in keiner Form vervielfältigt werden noch an Dritte weitergegeben werden.
Es gilt nur für den persönlichen Gebrauch.

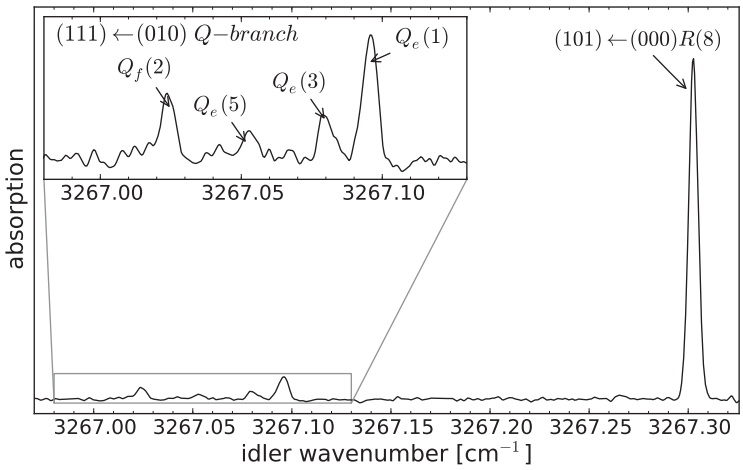

Figure 5.4: Q-branch of the $(11^11)\leftarrow(01^10)$ hot band of C_3 together with the $R(8)$ transition of the combination band.

and by again neglecting higher order terms, one obtains for the frequency ν_{1+2+3} of the combination band (11^11):

$$\begin{aligned}\nu_{1+2+3} &= \nu_1 + \nu_2 + \nu_3 + x_{12} + x_{23} + x_{13} \\ &= \nu_{1+3} + \nu_2 + x_{12} + x_{23}\end{aligned} \tag{5.3}$$

so that with the known frequencies $\nu_{1+3}, \nu_{1+2+3}, \nu_2$ (see Table 5.3) one obtains a very accurate value for the sum $x_{12} + x_{23} = +6.9724(6)\,\mathrm{cm}^{-1}$. Using data from Ref. [51], the value of $x_{23} = -38.930(4)\,\mathrm{cm}^{-1}$ can be eliminated, and one obtains an estimation of x_{12}, on which the presented measurement has significant influence, as $x_{12} = +45.902(4)\,\mathrm{cm}^{-1}$.

This large and positive value of x_{12} shows that the symmetric stretching motion has a stabilizing effect on the bending vibration and even overcompensates the anharmonic effects of the bending mode which tends to significantly redshift any hot band as in the case of the $(01^11)\leftarrow(01^10)$ hot band observed by Kawaguchi *et al.* [51].

As in the case of the $(10^01)\leftarrow(00^00)$ combination band, the calculated rotational constants from Ref. [122] agree reasonably well with the values from a least-squares fit. Although the distortion constants were found to be comparably large, the results obtained from the fit appear reasonable. The average deviation of observed lines from the calculated frequencies produced by the fit is $1.3 \times 10^{-3}\,\mathrm{cm}^{-1}$ and hence a factor of roughly four larger than for the combination band, although the frequency calibration procedure should yield the same accuracy. This is an indication for a more complicated behavior of the hot band which can hardly be described with a standard hamiltonian for linear molecules.

Dieses Werk ist copyrightgeschützt und darf in keiner Form vervielfältigt werden noch an Dritte weitergegeben werden.
Es gilt nur für den persönlichen Gebrauch.

Table 5.3: Molecular parameters of all vibrational states of C_3 in its $\tilde{X}^1\Sigma_g^+$ electronic ground state involved in the measurements presented here. Uncertainties in the last digit are given in parentheses. Values are given in cm^{-1}.

vibrational state	Parameter	This work[a]	Ref. [29]	theory [122]
(00^00)	ν	0.0	0.0	0.0
	B	0.4306090(140)	0.4305726(47)	0.4305
	D $\times 10^6$	1.668(77)	1.478(13)	1.27
	H $\times 10^9$	0.560(170)	0.136(61)	-
	L $\times 10^{12}$	−0.35(11)	-	-
(01^10)	ν	63.4165889[b]	63.4165889(54)	62.2
	B	0.4424670(450)	0.4424043(36)	0.4420
	D $\times 10^6$	2.750(330)	2.346(13)	1.95
	H $\times 10^9$	1.340(730)	0.257(12)	-
	q $\times 10^3$	5.7000(420)	5.6935(25)	-
	q_D $\times 10^6$	−1.090(160)	−0.879(30)	-
	q_H $\times 10^{12}$	-	40.(26)	-
(10^01)	ν	3260.12638(16)	-	3275.6
	B	0.424267(15)	-	0.4240
	D $\times 10^6$	1.489(94)	-	0.93
	H $\times 10^9$	0.93(22)	-	-
	L $\times 10^{12}$	−0.74(15)	-	-
(11^11)	ν	3330.51539(46)[b]	-	3346.7
	B	0.435499(41)	-	0.4352
	D $\times 10^6$	2.70(31)	-	1.68
	H $\times 10^9$	1.92(70)	-	-
	q $\times 10^3$	5.180(39)	-	-
	q_D $\times 10^6$	0.77(13)	-	-

[a] The parameters in the (00^00) and (01^10) levels have been given with the precision of those from Ref. [29] for the sake of comparability.

[b] The $\nu_{(01^10)}$ frequency has been kept fixed to that of Ref. [29], because this measurement can only give information about the frequency difference $\nu_{(11^11)} - \nu_{(01^10)}$.

5.2.3 Conclusion and Outlook

The $(10^01)\leftarrow(00^00)$ and $(11^11)\leftarrow(01^10)$ vibrational bands of gas phase C_3 in its electronic ground state have been measured at high spectral resolution and with high accuracy for the first time. Rotational and centrifugal distortion constants have been determined for these states, which are in reasonable agreement with theoretical models. The relative accuracy $\Delta\nu/\nu$ of the measured transition frequencies is of the order of 1.7×10^{-7} (absolute ac-

Dieses Werk ist copyrightgeschützt und darf in keiner Form vervielfältigt werden noch an Dritte weitergegeben werden.
Es gilt nur für den persönlichen Gebrauch.

curacy $5\times10^{-4}\,\mathrm{cm}^{-1}$ or 15 MHz) and even slightly better than the precision of far-infrared measurements with $\Delta\nu/\nu = 2.5\times10^{-7}$ (Ref. [29]). Broadband coverage of the OPO resulted in a large number of observed transitions, which yields well determined molecular parameters. All in all, the conducted experiment results in a further enlargement of the available dataset for the C_3 molecule in the electronic and vibrational ground state. In the future, a global fit of all available rovibrational measurements performed on C_3 including data measured here will provide a excellent basis for the understanding of the molecule.

The obtained band origins give valuable information on the potential of C_3, which is of fundamental interest for quantum chemistry and the evaluation of the internal dynamics of the C_3 molecule. A very simple approach to the potential has been applied to extract the anharmonicity parameters x_{13} and x_{12}, neglecting higher order terms. Especially in the case of C_3, these terms have to be included for a more accurate model. However, the treatment demonstrates the applicability of the obtained data for modeling the C_3 potential.

Searches for other infrared-active vibrational bands of C_3 are worth conducting to further increase the dataset of highly accurate vibrational energy levels. As shown in this study, the combination of the jet spectrometer with the OPO is an ideal tool for such broadband experiments. For example the bands $(12^01)\leftarrow(00^00)$ or other hot bands $(1\ 2x\ 1)\leftarrow(0\ 2x\ 0)$, with $x = 2, 4, \ldots$, should be detectable in nearby frequency regimes. Adding computer control of the crystal temperature and pump power will enable automated searches and unbiased line surveys in large spectral regions of the carbon jet.

Dieses Werk ist copyrightgeschützt und darf in keiner Form vervielfältigt werden noch an Dritte weitergegeben werden.
Es gilt nur für den persönlichen Gebrauch.

5.3 Experiments on linear C_7

C_7 is a linear cluster of $D_{\infty h}$ symmetry and possesses a $^1\Sigma_g^+$ electronic ground state. A graphical representation of its structure is shown in Figure 5.5. In the gas phase, it has been first detected at high resolution by Heath *et al.* in 1990 (Ref. [39]), when the ν_4 fundamental band has been resolved with infrared laser diode spectroscopy around 2138 cm^{-1}. Soon after, the same group published their analysis of the hot band transition involving the ν_{11} bending mode [38]. The derived rotational constants for the ground state and the ν_{11} bending state were very different from each other. A shallow bending potential was deduced from that and even a theory of alternating rigidity in carbon clusters with cluster size was set up. The analysis of the second strongest fundamental band (ν_5) of this cluster by the same group seemed to confirm the results about the floppiness of C_7, because they found large and negative centrifugal distortion constants. However, all these findings were in contrast to high-level quantum-chemical calculations done by Botschwina [14], which predicted the C_7 bending potential to be rather rigid.

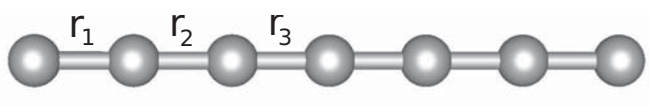

Figure 5.5: Graphical ball and stick representation of the linear carbon cluster C_7. The calculated equilibrium bond lengths at the CCSD(T)/cc-pVQZ level of theory (Ref. [14]) are from the outside to the inside: $r_1 = 1.2894$ Å, $r_2 = 1.2863$ Å, $r_3 = 1.2720$ Å.

This contradiction between experiment and theory was solved in 2008, when the understanding of the properties of the linear carbon cluster C_7 improved thanks to new high resolution laboratory data from Ref. [76]. Measurements on the ν_4 fundamental band at 2138 cm^{-1} and associated hot bands showed only small variations in the rotational constants which proved the molecule to be rather rigid, in agreement with the *ab initio* calculations by Botschwina [14].

In the experiment presented here, carbon cluster spectroscopy has been performed using a commercial narrow linewidth quantum cascade laser system to obtain very accurate molecular data of the ν_5 fundamental band of C_7 for further clarification of the molecular properties. It is the first time a quantum cascade laser has been applied in a supersonic jet spectrometer for this kind of experiment.

Besides the ν_5 fundamental, a new vibrational band has been detected. It has been tentatively assigned to the hot band $\nu_5 + \nu_{11} - \nu_{11}$. A global fit of these transition frequencies together with data from the ν_4 fundamental

Dieses Werk ist copyrightgeschützt und darf in keiner Form vervielfältigt werden noch an Dritte weitergegeben werden.
Es gilt nur für den persönlichen Gebrauch.

band (including the associated hot bands) measured by Neubauer-Guenther *et al.* [76] was performed and gives final proof for the rigidity of C_7. The parameters obtained for the vibrational ground state and the ν_{11} vibrational state therefore present the up-to-date reference for this molecule.

5.3.1 Spectrometer Setup

The spectrometer used in this experiment — although physically a different one from the one built for the measurements in the above sections — has the same schematic setup as shown in Figure 4.3. Its basic working principle is also briefly described in the preceding sections (see section 4.2) and in Ref. [75]. It comprises an ablation source where the molecules of interest are formed, and a detection scheme featuring a novel infrared laser. The following significant improvements to the experimental setup were made to enhance the performance of the existing spectrometer from Ref. [76] in terms of sensitivity and frequency accuracy:

- Instead of a tunable lead-salt diode laser, a high power mode-hop free tunable, continuous-wave external cavity quantum cascade laser (EC-QCL) system purchased from *Daylight Solutions*[3]) was used as IR radiation source. The system basically comprises a quantum cascade laser which is locked to an external cavity. The technique and applications of EC-QCLs has been described elsewhere, e.g. in Refs. [103, 126, 127]. The system provides an optical output power of more than 30 mW and a complete spectral coverage of the range from 1875 to 1935 cm^{-1}. The laser linewidth is specified to be less than 45 MHz. The small long term thermal frequency drift behavior allows slow mode-hop free scans at high resolution over more than 40 GHz.

- To improve calibration accuracy, the solid germanium etalon employed usually in spectrometers of this kind was replaced by a home-built internally coupled Fabry-Perot interferometer (icFPI, Ref. [87]) with a free spectral range of 300 MHz. This device has been designed for high thermal stability. Because a frequency scan over 30 GHz takes up to one hour, thermal stability is important for reaching high calibration accuracy. The reasons for the improved frequency stability and the necessity of it are discussed in section 4.2.1. An increase of the frequency accuracy by a factor of two to five compared to earlier measurements with the same spectrometer and a solid germanium etalon of 450 MHz free spectral range has been observed.

[3] *http://www.daylightsolutions.com*

Dieses Werk ist copyrightgeschützt und darf in keiner Form vervielfältigt werden noch an Dritte weitergegeben werden.
Es gilt nur für den persönlichen Gebrauch.

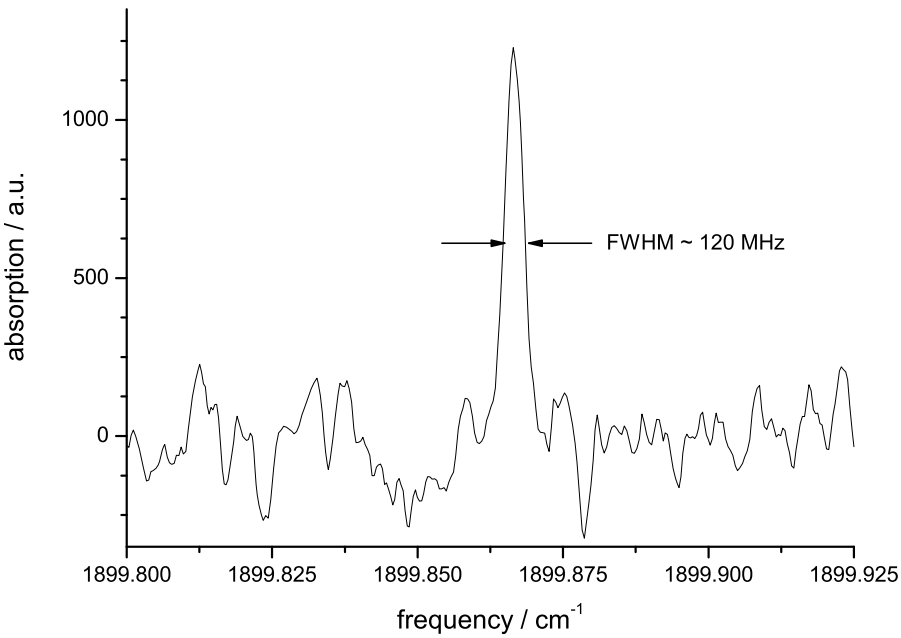

Figure 5.6: $R(24)$ transition of the ν_5 band of C_7 with a linewidth (FWHM) of 120 MHz measured with a single scan.

- The previously applied excimer laser has been superseded by a Q-switched Nd:YAG laser operating at its third harmonic frequency at 355 nm. Since cluster production and hence the strength of the absorption signal depends on the output power of the ablating laser, energy variations in time should be as small as possible to measure line intensities and -profiles correctly. Furthermore, long-term power stability is of concern for stable jet conditions. Compared to the excimer laser used earlier, the Nd:YAG laser guarantees very stable measuring conditions over many hours, which is crucial for extended frequency scans and for stable line intensity conditions.

5.3.2 Measurements and Results: C_7

Fifty rovibrational transitions in the spectral range between 1895 and 1901.5 cm^{-1} have been recorded and assigned to the transitions from $P(48)$ to $R(50)$ of the ν_5 fundamental band of C_7. Observed frequencies are listed in Table 5.4. Similarly to Si_2C_3 and C_3, the cluster C_7 is a centrosymmetric molecule of point group symmetry $D_{\infty h}$ and has a Σ_g^+ electronic ground state. Due to Bose-Einstein spin statistics of carbon ^{12}C nuclei, there are no energy levels with even-numbered rotational quantum numbers J in the ground state, as explained in section 4.3.1.

The experimental spectrum is shown in the upper part of Figure 5.8, and a calculated spectrum based on a least-squares fit of molecular parameters is plotted below. The measurement comprises 32 separate frequency scans ranging from 0.2 to 1.2 cm^{-1}. Overlapping spectra have been averaged with a binning of 5×10^{-4} cm^{-1}. Regions of weak lines have been scanned several

Dieses Werk ist copyrightgeschützt und darf in keiner Form vervielfältigt werden noch an Dritte weitergegeben werden.
Es gilt nur für den persönlichen Gebrauch.

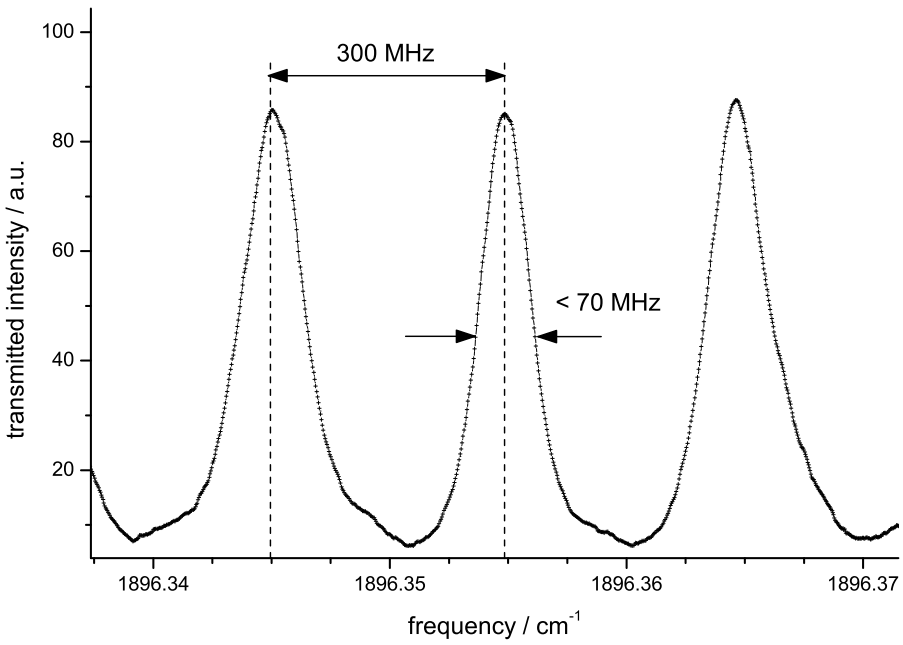

Figure 5.7: Etalon fringes of an internally coupled Fabry-Pérot Interferometer. The derived finesse $F^\star \approx 4.3$ is close to the expected theoretical value of $F^\star \approx 6$ (see Ref. [87]).

times. Spectra have been co-added for better signal-to-noise ratios. As an example for a single scan spectrum the $R(24)$ transition is depicted in Figure 5.6. The line intensity distribution of P- and R-branch transitions is best reproduced by a Boltzmann distribution at a rotational temperature of 25 K.

The observed linewidths of about 120 MHz FWHM (full width at half maximum) are caused by Doppler broadening due to the velocity component of the molecular jet along the line of sight. Linewidths of 120 MHz correspond to a molecular velocity dispersion of roughly ± 300 m/s along the line of sight, which is plausible for a slightly divergent jet when probed perpendicularly. It agrees very well with linewidths of Si_2C_3 (section 4) observed with the similar spectrometer described in the sections above. Since the etalon fringes of the calibration icFPI have a width of roughly 70 MHz (FWHM), the linewidth of the laser is significantly smaller, which can be seen in Figure 5.7. The theoretical finesse of 6 (see Ref. [87]), corresponds to fringes of about 50 MHz width, and thus the laser linewidth is certainly less than 70 MHz.

The achieved sensitivity of the spectrometer is better than $\Delta I/I = 1 \times 10^{-4}$, when averaging each spectral point over 30 shots of the pulsed molecular beam. Though a comparison is difficult due to different setups used to record the two bands, the intensity of the ν_5 band is estimated to be 5 to 10 times weaker than the ν_4 band.

The ν_5 fundamental band

In order to increase the accuracy of the determined ground state parameters, a global fit of the 50 observed ν_5 band transition frequencies together with 45 lines of the ν_4 fundamental band, taken from Ref. [76], was performed.

Dieses Werk ist copyrightgeschützt und darf in keiner Form vervielfältigt werden noch an Dritte weitergegeben werden.
Es gilt nur für den persönlichen Gebrauch.

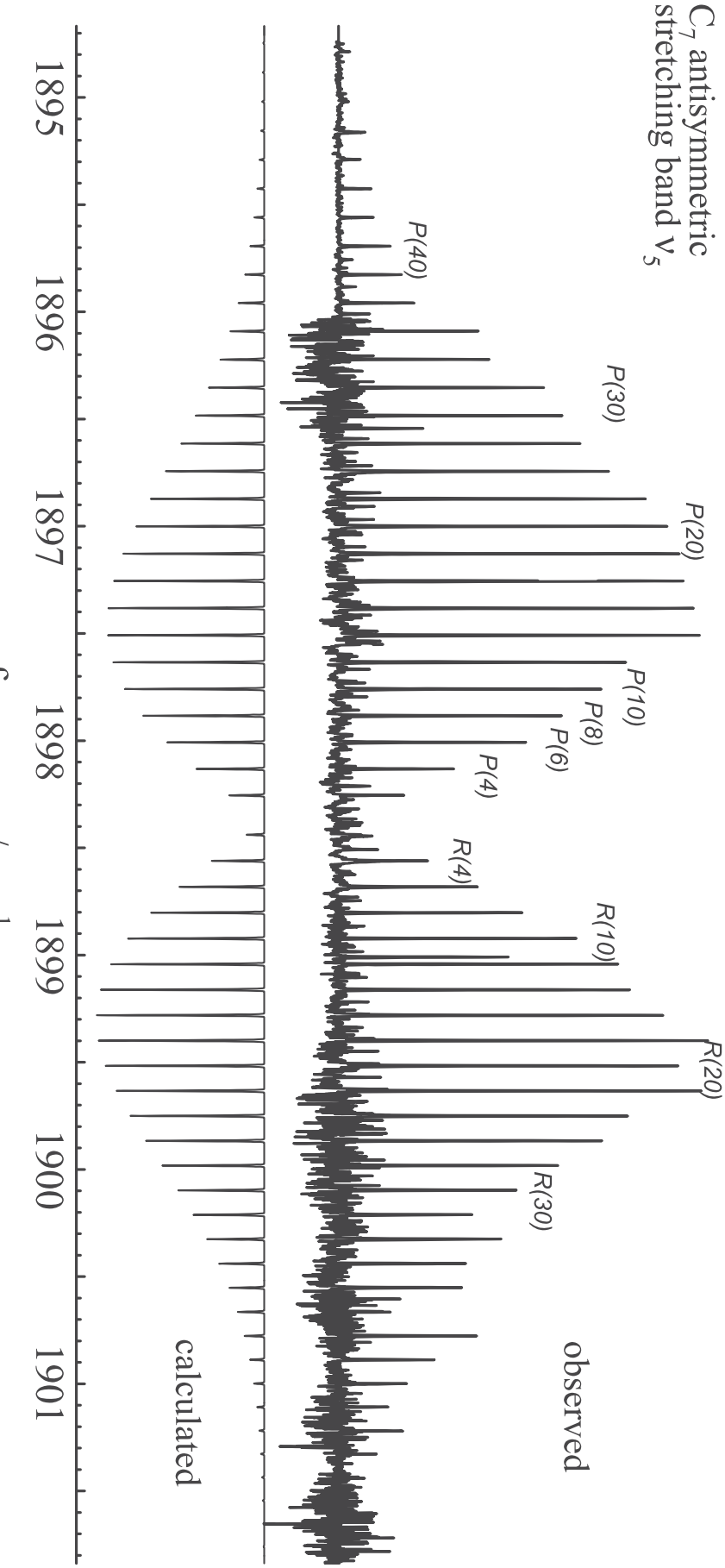

Figure 5.8: The ν_5 fundamental band of linear C_7 at 1898.4cm^{-1} and the simulated spectrum with a rotational temperature of T=25 K using the program PGOPHER (Ref. [125]). Transitions with odd numbered rotational quantum numbers J'' in the ground state are missing due to Bose-Einstein spin statistics.

Dieses Werk ist copyrightgeschützt und darf in keiner Form vervielfältigt werden noch an Dritte weitergegeben werden.
Es gilt nur für den persönlichen Gebrauch.

The experimental accuracy of the ν_5-band transitions are a factor of two smaller than those of the ν_4-band. The program PGOPHER was used for fitting an effective Hamiltonian to reproduce the experimental spectrum [125]. Equation (4.1) from section 4.3.1 gives the standard energy levels which are fitted to the observations. More information about the characteristics of a band of σ-symmetry as present here can also be found in the mentioned section. The rms of all fitted transitions was less than 35 MHz (1.2×10^{-3} cm^{-1}), and 20 MHz (0.7×10^{-3} cm^{-1}) when only the new measurements of ν_5 band transitions were taken into account.

Table 5.4: Measured transition frequencies of the ν_5 fundamental of C_7 in cm^{-1}. Best fit residuals are also given.

J	$R(J)$	obs.-calc. ($\times 10^{-3}$)	$P(J)$	obs.-calc. ($\times 10^{-3}$)
0	1898.4406	1.9	–	
2	1898.5608	0.2	1898.2547	−0.3
4	1898.6813	−0.6	1898.1314	−0.5
6	1898.8027	0.0	1898.0077	−0.5
8	1898.9228	−0.1	1897.8838	−0.2
10	1899.0424	−0.3	1897.7597	0.4
12	1899.1612	−0.7	1897.6341	0.0
14	1899.2805	−0.1	1897.5083	−0.0
16	1899.3990	0.2	1897.3819	−0.1
18	1899.5164	−0.1	1897.2548	−0.5
20	1899.6337	0.1	1897.1280	0.1
22	1899.7509	0.7	1897.0001	0.0
24	1899.8666	0.3	1896.8722	0.5
26	1899.9820	0.1	1896.7430	0.2
28	1900.0965	−0.4	1896.6137	0.3
30	1900.2114	−0.0	1896.4842	0.7
32	1900.3248	−0.6	1896.3537	0.6
34	1900.4390	0.1	1896.2217	−0.4
36	1900.5512	−0.7	1896.0902	−0.4
38	1900.6642	−0.1	1895.9575	−1.1
40	1900.7766	0.4	1895.8266	0.6
42	1900.8878	0.2	1895.6937	0.7
44	1900.9996	1.1	1895.5597	0.3
46	1901.1083	−0.6	1895.4257	0.4
48	1901.2198	1.1	1895.2893	−1.4
50	1901.3275	−0.5	–	

Dieses Werk ist copyrightgeschützt und darf in keiner Form vervielfältigt werden noch an Dritte weitergegeben werden.
Es gilt nur für den persönlichen Gebrauch.

Table 5.5: Molecular parameters in cm^{-1} for ground state, and vibrationally excited ν_4 and ν_5 states of C_7. α values from experimental data have been calculated from $B_i = B_0 - \alpha_i$. Line positions of the ν_4 band were taken from Ref. [76]. The rms for the global fit was 7.2×10^{-4} cm^{-1}.

Parameter	global fit (This Work)	Neubauer-Guenther *et al.* (Ref. [76])	Heath *et al.* (Ref. [40])	*Ab initio* (Ref. [14])
B_0	0.0306221(12)	0.0306244(28)	0.030613(14)	0.03063[a]
$D_0 \times 10^8$	< 0.1 [b]		−2.33(85)	0.0337[c]
$H_0 \times 10^{12}$			−5.4(15)	
ν_4	2138.31454(22)	2138.31442(20)	2138.3152(5)	2203.8
$\alpha_4 \times 10^4$	1.157(16)	1.153(39)	1.17(20)	1.137
B_4	0.0305064(11)	0.0305091(27)	0.030496(14)	0.03052[a]
$D_4 \times 10^8$	< 0.1 [b]		−2.51(91)	
$H_4 \times 10^{12}$			-5.9(17)	
ν_5	1898.37761(11)		1898.3758(8)	1933.3
$\alpha_5 \times 10^4$	0.653(16)		0.57(21)	0.6727
B_5	0.0305568(11)		0.030556(15)	0.03057[a]
$D_5 \times 10^8$	0.152(43)		−1.6(11)	
$H_5 \times 10^{12}$			−4.4(31)	

[a] Calculated from B_e and α_i values as given in the reference.
[b] Including the given parameter does not improve the fit significantly. The 1σ deviation is given as an upper limit.
[c] *ab initio* value for D_e as given in Ref. [14].

The ν_5 band origin has been determined unambiguously and with high accuracy as $\nu_5 = 1898.37761(11)$ cm^{-1}. This value is in good agreement with a band center position of 1898.3758(8) cm^{-1} published by Heath *et al.*, although it is slightly above the 1σ error limit [40]. It is worth mentioning that Heath *et al.* had not been able to record the ν_5 band origin due to lack of appropriate diode lasers. Table 5.5 summarizes the molecular parameters obtained in this work, the parameters from Ref. [40] and the results from *ab initio* calculations by Botschwina [14].

In contrast to the analysis by Heath *et al.*, no centrifugal distortion constants were necessary to include in the fitting procedure except for D_5. The large and negative values of these parameters from Ref. [40] have been taken by the authors as another indication for the floppiness of C_7. This could not be reproduced.

Hotband transitions

In addition to the 50 transitions of the ν_5 fundamental band, 29 lines from at least one other band of C_7 have been detected. The upper part of Figure

Dieses Werk ist copyrightgeschützt und darf in keiner Form vervielfältigt werden noch an Dritte weitergegeben werden.
Es gilt nur für den persönlichen Gebrauch.

Table 5.6: Measured transitions of the $\nu_5 + \nu_{11} - \nu_{11}$ hot band of C_7 in cm^{-1}. Best fit residuals are also given. Values in parentheses are calculated upon best fit parameters, when unambiguous identification was not possible, e.g. due to blending with strong fundamental lines.

J	$R(J)$	obs.-calc. ($\times 10^{-3}$)	$P(J)$	obs.-calc. ($\times 10^{-3}$)
10	1898.5078	−0.3	(1897.2213)	–
11	1898.5674	0.5	1897.1584	−1.3
12	(1898.6279)	–	1897.0956	−0.4
13	(1898.6863)	–	1897.0331	−1.2
14	1898.7465	−0.7	1896.9689	−1.3
15	(1898.8052)	–	1896.9081	−0.4
16	1898.8670	0.9	1896.8441	0.1
17	(1898.9237)	–	1896.7861	3.9
18	1898.9842	−0.3	1896.7181	0.8
19	(1899.0416)	–	1896.6558	0.3
20	1899.1045	2.0	1896.5914	1.2
21	(1899.1591)	–	1896.5280	−0.2
22	1899.2191	−0.8	(1896.4625)	–
23	1899.2752	−1.0	(1896.4005)	–
24	1899.3379	1.0	(1896.3344)	–
25	(1899.3927)	–	(1896.2723)	–
26	1899.4506	−2.8	(1896.2058)	–
27	1899.5067	−2.1	(1896.1436)	–
28	1899.5705	1.0	(1896.0768)	–
29	1899.6251	0.7	(1896.0145)	–
30	1899.6855	0.5	1895.9475	0.3
31	(1899.7395)	–	1895.8833	−1.6
32	(1899.8001)	–	1895.8163	−0.9
33	(1899.8542)	–	1895.7570	2.2

5.10 shows details of the recorded spectrum. For better visibility of these weak transitions, fundamental band transitions have been blanked out. The observed lines of the new band are listed in Table 5.6. The spacing of adjacent lines is roughly two times the rotational constant B with a small alternation, which is a strong argument for the relation of the band to the C_7 molecule. The alternation – the so-called "staggering" – is an indication for hot band transition of a bending mode with vibrational angular momentum $l = 1$. The nature of such a hot band is introduced briefly in section 4.3.2. Figure 5.9 features an energy term scheme of C_7 for further clarification.

Dieses Werk ist copyrightgeschützt und darf in keiner Form vervielfältigt werden noch an Dritte weitergegeben werden.
Es gilt nur für den persönlichen Gebrauch.

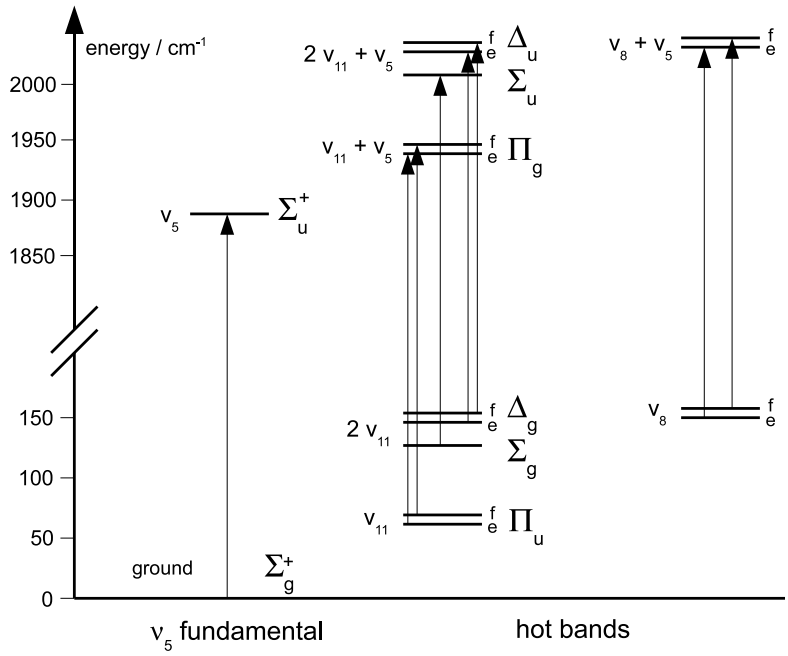

Figure 5.9: Schematic energy level diagram for vibrational states of C_7. The two lowest ν_8 and ν_{11} bending energies are calculated to be 70 and 156cm^{-1} (Ref. [14]). For states in which the bending mode is excited, vibrational angular momentum has to be taken into account. l-type interaction splits $l > 0$ states into two components with e and f symmetry. A similar scheme for the ν_4 vibration of linear C_7 is given in Ref. [76].

The signal-to-noise ratio of these hot band transitions is small. In spite of averaging over many scans, these bands are not clearly visible over the whole recorded spectral range, which makes a secure assignment of lines hardly feasible. In particular, the band origin is not clearly determined. Two assumptions have been made in order to obtain a tentative assignment. First, the two groups of observed transitions are part of the same vibrational band and constitute parts of the P and R-branch. Second, this band is originating from the ν_{11} vibrational state. Both the ν_8 and ν_{11} vibrations are energetically low lying bending modes which could give rise to the observed hot band. However, in the cool jet, the lowest bending mode should be the most populated state besides from the ground state and thus the corresponding hot band should be the strongest in intensity. So the most plausible assignment of the hot band is the $\nu_5 + \nu_{11} - \nu_{11}$ transition.

With these assumptions, a conclusive assignment can be found in the following way. The molecular parameters for the bending mode ν_{11} are known with good accuracy from the hot band analysis of $\nu_4 + \nu_{11} - \nu_{11}$ by Neubauer-Guenther *et al.* Using these parameters, the hot band $\nu_5 + \nu_{11} - \nu_{11}$ has been assigned as shown in Fig. 5.10, so that residuals of a least-squares fit are the smallest.

Finally the data from Ref. [76] have been used for a global fit of the ν_{11} vibrational state. Results are given in Table 5.7. The average residual is 1.1×10^{-3} cm^{-1}, which is plausible for weak lines with less signal-to-noise ratio.

Furthermore, there is a way to estimate the energy of a bending vibrational mode from the measurement of the l-type doubling constant q. For an $l = 1$ state like ν_{11}, the doubling constant q can be expressed according to Refs. [77, 107] as:

Dieses Werk ist copyrightgeschützt und darf in keiner Form vervielfältigt werden noch an Dritte weitergegeben werden.
Es gilt nur für den persönlichen Gebrauch.

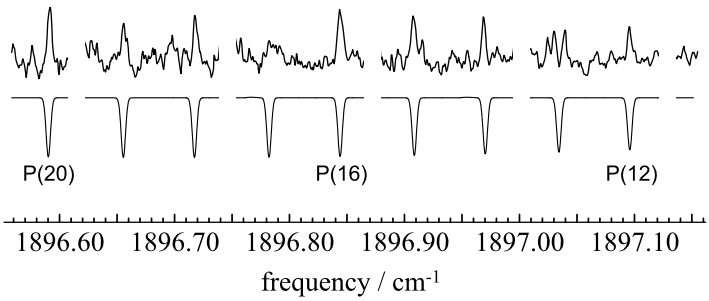

Figure 5.10: Hotband transitions of C_7 at 1897 cm^{-1}. The strong ν_5 fundamental band transitions have been blanked out for better visibility of the weak hot band transitions. The lower trace shows a calculated spectrum of the $\nu_5 + \nu_{11} - \nu_{11}$ hot band.

Table 5.7: Parameters for the $\nu_4 + \nu_{11} - \nu_{11}$ and $\nu_5 + \nu_{11} - \nu_{11}$ hot bands in cm^{-1}. Line positions of the $\nu_4+\nu_{11}-\nu_{11}$ hot band were taken from Ref. [76]. The average on the residuals was 0.0011 cm^{-1} and did not differ very much in the two bands.
^{a} calculated from B_e and α_i values as given in the reference.

Parameter	global fit (This Work)	Neubauer-Guenther *et al.* (Ref. [76])	*Ab initio* (Ref. [14])
B_{11}	0.0306744(37)	0.0306759(38)	0.03078^a
$q_{11} \times 10^5$	4.54(74)	3.71(76)	2.68
$\nu_4 + \nu_{11} - \nu_{11}$	2137.73850(24)	2137.73856(16)	–
B_{4+11}	0.0305607(40)	0.0305522(41)	0.03061^a
$q_{4+11} \times 10^8$	4.62(78)	–	
$\nu_5 + \nu_{11} - \nu_{11}$	1897.84053(40)	–	–
B_{5+11}	0.0306151(37)	–	0.03068^a
$q_{5+11} \times 10^5$	4.56(74)	–	–

$$q = 2\frac{B_e^2}{\omega_b}\left(1 + 4\sum_i \xi_{bi}^2 \frac{\omega_b^2}{\omega_i^2 - \omega_b^2}\right) \quad , \tag{5.4}$$

where ξ_{bi} are certain Coriolis parameters dependent on the masses, dimensions and harmonic force constants of the molecule. ω_i stands for any vibrational frequency different from the bending mode ω_b and the sum is over all non-degenerate vibrations. B_e is the equilibrium rotational constant. With the abbreviation

$$f_q = 2\left(1 + 4\sum_i \xi_{bi}^2 \frac{\omega_b^2}{\omega_i^2 - \omega_b^2}\right), \tag{5.5}$$

the above expression simplifies to $\omega_b = f_q \frac{B_e^2}{q}$. Unfortunately, the constant f_q is not known for the C_7 molecule. For similar analyses of the cluster C_5 and C_9 (Refs. [69], [118]), the value of $f_q = 2.15(5)$ obtained by Holland *et al.* (Ref. [44]) for the molecule C_3S_2, has been used. The equilibrium rotational constant B_e is also unknown, but the *ab initio* calculations by Botschwina

Dieses Werk ist copyrightgeschützt und darf in keiner Form vervielfältigt werden noch an Dritte weitergegeben werden.
Es gilt nur für den persönlichen Gebrauch.

have proven to agree excellent with all measured vibrational levels, so the value of $B_e = 0.03058\,\mathrm{cm}^{-1}$ is assumed to be correct within fractions of a percent as well. This approximation yields a value of $\omega_{11} = 44.3(73)\,\mathrm{cm}^{-1}$ compared to $\omega_{11} = 54.2(111)\,\mathrm{cm}^{-1}$ with the q value from Ref. [76] and the *ab initio* value of $\omega_{11} = 70\,\mathrm{cm}^{-1}$ [14].

5.3.3 Conclusion and Outlook

Compared to Ref. [40], the molecular parameters derived here are a factor of five to ten more accurate. This is attributed to the improved calibration procedure involving the internally coupled Fabry-Pérot reference interferometer and the better signal-to-noise ratio. The set of molecular parameters required to reproduce the measured lines within error bars has been reduced to the band origins and the rotational constants for the two relevant excited states and for the ground vibrational state.

In contrast, the analysis presented in Ref. [40] leads to large and negative distortion constants for both the ground state and the excited state, which was attributed to an unknown perturbation. However, the 1σ error from the presented fit gives an estimation of the upper limits of D_4, which are two orders of magnitude smaller compared to Ref. [40]. The simple Kratzer relation $D = 4B_e^3/\omega_e^2$ points to rather small centrifugal distortion constants of $D \approx 3 \times 10^{-11}\,\mathrm{cm}^{-1}$, which is in good agreement with the experimental results. Distortion constants of higher order were not significant in the fit. Therefore, it can be concluded that both the ground state and the ν_5 excited state are not perturbed and that C_7 is surely a rigid molecule.

The analysis is consistent with high-level *ab initio* calculations reported by Botschwina (Ref. [14]). Table 5.5 lists these values as well, revealing a deviation of the calculated rotational constants of less than 0.05% from the experimental results. There are no calculated values for the distortion constants in the vibrational ground state and excited states. However, the value of D_e in the equilibrium state is given, which is one order of magnitude smaller than the measured value and thus below the detection limit.

The band intensity of the ν_5 band transition is estimated to be 5 to 10 times weaker than ν_4 band intensity, though a comparison is difficult because the two measurements were performed with different setups. Heath *et al.* reported a factor of 5 to 7 times, while calculations by Kurtz and Adamowicz (Ref. [58]) predict a factor of 4.4 on a MP2/6-31G* level of theory, which both complies with the presented estimation. The sensitivity of the spectrometer is on a level which allowed hot band transitions involving the ν_5 band to be detected for the first time. These are typically 10 to 20 times weaker than fundamental transitions.

Dieses Werk ist copyrightgeschützt und darf in keiner Form vervielfältigt werden noch an Dritte weitergegeben werden.
Es gilt nur für den persönlichen Gebrauch.

The presented tentative assignment of lines to the $\nu_5 + \nu_{11} - \nu_{11}$ hot band is based on the analysis of Neubauer-Guenther *et al.* and the extended data set of the $\nu_4 + \nu_{11} - \nu_{11}$ band. The frequency accuracy for these latter lines is about 50% less than for the fundamental transitions, which can be explained by the poor signal-to-noise level. The q parameter obtained here allows to get a better estimate of the band center of the bending mode ν_{11} based on experimental observations.

The new value for the ω_{11} frequency does not agree with the value calculated by Botschwina ($\omega_{11} = 70\,\mathrm{cm}^{-1}$). The deviation is significant, but one has to consider that deriving band origins from l-type doubling constants gets more difficult for larger carbon chains. A better signal-to-noise ratio could secure the presented assignment and analysis of the observed hot band.

The results on C_7 with the improved Cologne Carbon Cluster Experiment show a high performance of the new setup. The frequency accuracy is obviously on a high level compared to similar setups and of the order of $10^{-4}\,\mathrm{cm}^{-1}$. The EC-QCL system is well suited for high resolution measurements offering high output power, small linewidth and large tuning range. These new radiation sources promise extension of precise measurements to other carbon clusters as well and mark an alternative to the use of optical parametric oscillators. This is true especially in the long-wavelength regime, where no suitable nonlinear material is commercially available yet.

Dieses Werk ist copyrightgeschützt und darf in keiner Form vervielfältigt werden noch an Dritte weitergegeben werden.
Es gilt nur für den persönlichen Gebrauch.

Dieses Werk ist copyrightgeschützt und darf in keiner Form vervielfältigt werden noch an Dritte weitergegeben werden.
Es gilt nur für den persönlichen Gebrauch.

A

Rovibrational transitions of CH_2D^+

"There was a point to this story, but it has temporarily escaped the chronicler's mind."

Douglas Adams, "So Long and Thanks for all the Fish"

Table A.1: Frequencies of the 40 observed rovibrational transitions of the ν_1 band of CH_2D^+. Errors of transitions measured by Jagod *et al.* [49] are given by the authors to 300×10^{-5} cm^{-1}. The parameter Δ_{exp} is the deviation between the measured frequency from this work and from Ref. [49]. All values are given in units of cm^{-1}.

$J'_{K'_a K'_c} \leftarrow J_{K_a K_c}$	ν_{obs}		o. − c. $\times 10^5$	Ref. [49]	$\Delta_{\mathrm{exp}} \times 10^5$
$2_{02} \leftarrow 3_{21}$	2953.70810	(12)	22	–	–
$4_{40} \leftarrow 5_{41}$	2953.90830	(20)	15	–	–
$4_{41} \leftarrow 5_{42}$	2954.15290	(20)	16	–	–
$1_{01} \leftarrow 2_{20}$	2966.49431	(20)	−4	–	–
$3_{13} \leftarrow 4_{14}$	2972.75642	(20)	−31	2972.754	242
$2_{20} \leftarrow 3_{21}$	2973.63617	(10)	18	2973.633	317
$2_{11} \leftarrow 3_{12}$	2973.87663	(10)	−19	2973.877	−37
$2_{12} \leftarrow 3_{13}$	2980.37367	(12)	15	2980.372	167
$1_{11} \leftarrow 2_{12}$	2988.23021	(40)	−71	2988.235	−479
$4_{23} \leftarrow 4_{22}$	2995.37400	(12)	−10	–	–
$0_{00} \leftarrow 1_{01}$	2995.46840	(10)	−10	–	–
$2_{21} \leftarrow 2_{20}$	3003.32125	(40)	−14	3003.321	25
$3_{30} \leftarrow 3_{31}$	3003.48600	(30)	13	3003.485	100
$1_{01} \leftarrow 0_{00}$	3014.01585	(20)	33	–	–
$2_{02} \leftarrow 1_{01}$	3022.41837	(50)	3	3022.416	237
$2_{11} \leftarrow 1_{10}$	3025.35013	(10)	−4	3025.347	313

continued on next page

Dieses Werk ist copyrightgeschützt und darf in keiner Form vervielfältigt werden noch an Dritte weitergegeben werden.
Es gilt nur für den persönlichen Gebrauch.

Table A.1 – continued from previous page (CH_2D^+ transitions in ν_1-band)

$J'_{K'_aK'_c} \leftarrow J_{K_aK_c}$	ν_{obs}		o. − c. $\times 10^5$	Ref. [49]	$\Delta_{\text{exp}} \times 10^5$
$4_{13} \leftarrow 4_{14}$	3025.39420	(80)	173	–	–
$3_{22} \leftarrow 3_{03}$	3026.19814	(9)	−7	–	–
$3_{03} \leftarrow 2_{02}$	3029.63517	(12)	−17	3029.635	17
$4_{23} \leftarrow 4_{04}$	3030.39190	(50)	−69	–	–
$3_{22} \leftarrow 2_{21}$	3031.82203	(12)	8	–	–
$5_{33} \leftarrow 5_{14}$	3034.21902	(30)	−1	–	–
$3_{21} \leftarrow 2_{20}$	3034.55695	(12)	6	3034.556	95
$3_{12} \leftarrow 2_{11}$	3035.02110	(10)	14	3035.014	710
$4_{14} \leftarrow 3_{13}$	3035.57560	(10)	4	3035.574	160
$4_{04} \leftarrow 3_{03}$	3036.21680	(12)	1	3036.218	−120
$3_{30} \leftarrow 3_{13}$	3048.75405	(9)	5	–	–
$6_{16} \leftarrow 5_{15}$	3049.19294	(20)	−2	3049.188	494
$6_{06} \leftarrow 5_{05}$	3049.28108	(20)	3	3049.280	108
$3_{30} \leftarrow 2_{11}$	3066.11923	(15)	−19	–	–
$4_{22} \leftarrow 3_{03}$	3071.12714	(10)	−5	–	–
$3_{31} \leftarrow 2_{12}$	3072.65881	(12)	−1	–	–
$4_{31} \leftarrow 3_{12}$	3074.63715	(10)	−10	–	–
$8_{36} \leftarrow 7_{35}$	3075.13560	(50)	−17	3075.130	560
$5_{32} \leftarrow 4_{13}$	3085.53365	(10)	1	–	–
$4_{32} \leftarrow 3_{13}$	3086.69140	(10)	−3	–	–
$5_{23} \leftarrow 4_{04}$	3090.70740	(100)	−89	–	–
$4_{41} \leftarrow 3_{22}$	3096.42787	(8)	−4	–	–
$5_{41} \leftarrow 4_{22}$	3099.71230	(20)	−4	–	–
$5_{33} \leftarrow 4_{14}$	3102.67485	(15)	29	–	–

Table A.2: Frequencies of the 71 observed rovibrational transitions of the ν_4 band of CH_2D^+ Errors of transitions measured by Jagod *et al.* [49] are given by the authors to 300×10^{-5} cm^{-1}. The parameter Δ_{exp} is the deviation between the measured frequency from this work and from Ref. [49]. All values are given in units of cm^{-1}.

$J'_{K'_aK'_c} \leftarrow J_{K_aK_c}$	ν_{obs}		o. − c. $\times 10^5$	Ref. [49]	$\Delta_{\text{exp}} \times 10^5$
$2_{02} \leftarrow 3_{31}$	3034.17340	(10)	−18	–	–
$3_{31} \leftarrow 4_{40}$	3034.56725	(12)	−4	3034.565	225
$5_{23} \leftarrow 6_{34}$	3034.65230	(20)	−12	3034.649	330
$3_{30} \leftarrow 4_{41}$	3034.77728	(12)	13	3034.775	228
$4_{04} \leftarrow 5_{15}$	3066.14115	(10)	1	3066.140	115
$2_{11} \leftarrow 3_{22}$	3066.91140	(20)	2	3066.911	40
$1_{11} \leftarrow 2_{20}$	3071.09211	(10)	−8	–	–
$5_{33} \leftarrow 5_{42}$	3072.00010	(20)	−51	3071.997	310
$4_{32} \leftarrow 4_{41}$	3072.62389	(10)	1	3072.619	489

continued on next page

Dieses Werk ist copyrightgeschützt und darf in keiner Form vervielfältigt werden noch an Dritte weitergegeben werden.
Es gilt nur für den persönlichen Gebrauch.

Table A.2 – continued from previous page (CH_2D^+ transitions in ν_4-band)

$J'_{K'_aK'_c} \leftarrow J_{K_aK_c}$	ν_{obs}	o. − c. $\times 10^5$	Ref. [49]	$\Delta_{exp} \times 10^5$
$5_{15} \leftarrow 5_{24}$	3072.71760 (100)	−34	3072.716	160
$3_{03} \leftarrow 4_{14}$	3072.98875 (10)	−6	3072.988	75
$3_{22} \leftarrow 4_{13}$	3073.68560 (10)	4	3073.684	160
$1_{10} \leftarrow 2_{21}$	3074.08749 (10)	1	3074.083	449
$3_{13} \leftarrow 4_{04}$	3074.27680 (10)	−6	3074.273	380
$5_{05} \leftarrow 5_{14}$	3075.17829 (10)	−4	3075.176	229
$5_{24} \leftarrow 5_{33}$	3075.96194 (10)	22	3075.958	394
$4_{14} \leftarrow 4_{23}$	3078.95675 (7)	−5	3078.951	575
$4_{23} \leftarrow 4_{32}$	3079.24519 (7)	−3	3079.243	219
$2_{02} \leftarrow 3_{13}$	3079.44162 (10)	−8	3079.438	362
$3_{22} \leftarrow 3_{31}$	3081.22310 (10)	9	3081.222	110
$2_{12} \leftarrow 3_{03}$	3082.47516 (10)	−0	3082.473	216
$4_{04} \leftarrow 4_{13}$	3083.63054 (10)	8	3083.629	154
$3_{31} \leftarrow 4_{22}$	3083.93400 (50)	−50	–	–
$3_{13} \leftarrow 3_{22}$	3084.16766 (15)	17	3084.166	166
$3_{21} \leftarrow 3_{30}$	3084.42506 (10)	−7	3084.424	106
$4_{41} \leftarrow 5_{32}$	3084.53631 (51)	−17	–	–
$2_{21} \leftarrow 3_{12}$	3085.52922 (10)	4	3085.526	322
$1_{01} \leftarrow 2_{12}$	3085.83733 (10)	18	3085.834	333
$6_{24} \leftarrow 6_{33}$	3086.32560 (200)	39	–	–
$4_{22} \leftarrow 4_{31}$	3086.45169 (9)	5	3086.449	269
$5_{14} \leftarrow 5_{23}$	3086.60622 (10)	1	3086.596	1022
$4_{31} \leftarrow 5_{24}$	3086.73256 (10)	0	–	–
$5_{23} \leftarrow 5_{32}$	3087.55431 (12)	−5	3087.554	31
$2_{12} \leftarrow 2_{21}$	3088.09895 (7)	5	3088.096	295
$4_{40} \leftarrow 5_{33}$	3088.45050 (40)	−33	–	–
$4_{04} \leftarrow 3_{31}$	3091.16800 (10)	8	–	–
$3_{03} \leftarrow 3_{12}$	3091.24687 (10)	5	3091.245	187
$1_{11} \leftarrow 2_{02}$	3091.49560 (10)	0	–	–
$5_{05} \leftarrow 4_{32}$	3091.63090 (10)	−4	–	–
$4_{13} \leftarrow 4_{22}$	3091.68410 (10)	−16	3091.689	−490
$3_{30} \leftarrow 4_{23}$	3092.48393 (12)	−14	–	–
$0_{00} \leftarrow 1_{11}$	3092.94730 (10)	5	3092.944	330
$3_{12} \leftarrow 3_{21}$	3093.96000 (10)	−0	3093.959	100
$2_{11} \leftarrow 2_{20}$	3094.01180 (10)	3	3094.013	−120
$2_{02} \leftarrow 2_{11}$	3096.80710 (10)	−3	3096.805	210
$3_{21} \leftarrow 4_{14}$	3098.33395 (20)	13	–	–
$2_{20} \leftarrow 3_{13}$	3099.57345 (15)	−0	–	–
$1_{01} \leftarrow 1_{10}$	3099.93800 (10)	−16	3099.938	0
$5_{15} \leftarrow 4_{22}$	3109.08609 (25)	4	–	–

continued on next page

Dieses Werk ist copyrightgeschützt und darf in keiner Form vervielfältigt werden noch an Dritte weitergegeben werden.
Es gilt nur für den persönlichen Gebrauch.

Table A.2 – continued from previous page (CH_2D^+ transitions in ν_4-band)

$J'_{K'_aK'_c} \leftarrow J_{K_aK_c}$	ν_{obs}		o. − c. $\times 10^5$	Ref. [49]	$\Delta_{exp} \times 10^5$
$3_{13} \leftarrow 2_{20}$	3111.26786	(20)	−2	–	–
$1_{10} \leftarrow 1_{01}$	3111.54500	(09)	17	3111.543	200
$4_{14} \leftarrow 3_{21}$	3112.10835	(11)	8	–	–
$2_{11} \leftarrow 2_{02}$	3114.41528	(11)	10	3114.407	828
$3_{21} \leftarrow 3_{12}$	3116.59185	(7)	10	3116.590	185
$2_{20} \leftarrow 2_{11}$	3116.93872	(9)	−16	3116.937	172
$4_{23} \leftarrow 3_{30}$	3117.33931	(10)	−14	–	–
$4_{22} \leftarrow 4_{13}$	3118.32043	(6)	4	3118.318	243
$1_{11} \leftarrow 0_{00}$	3118.61329	(6)	−6	3118.611	229
$3_{12} \leftarrow 3_{03}$	3119.58926	(15)	−10	3119.589	26
$2_{02} \leftarrow 1_{11}$	3119.88180	(15)	−10	3119.888	−620
$5_{24} \leftarrow 4_{31}$	3122.54580	(10)	−4	–	–
$5_{23} \leftarrow 5_{14}$	3122.70310	(10)	4	3122.701	210
$2_{21} \leftarrow 2_{12}$	3122.90150	(10)	−1	3122.900	150
$4_{31} \leftarrow 4_{22}$	3123.10070	(20)	3	3123.098	270
$3_{12} \leftarrow 2_{21}$	3125.21310	(10)	0	–	–
$2_{12} \leftarrow 1_{01}$	3125.55645	(10)	19	3125.556	45
$3_{30} \leftarrow 3_{21}$	3125.63565	(10)	11	–	–
$3_{22} \leftarrow 3_{13}$	3126.49108	(10)	−6	3126.492	−92
$4_{13} \leftarrow 4_{04}$	3126.70280	(10)	5	–	–
$5_{41} \leftarrow 5_{32}$	3132.54970	(10)	4	3132.553	−330
$5_{33} \leftarrow 5_{24}$	3132.99855	(10)	0	3132.998	55

Dieses Werk ist copyrightgeschützt und darf in keiner Form vervielfältigt werden noch an Dritte weitergegeben werden.
Es gilt nur für den persönlichen Gebrauch.

B

Temperature Controller Electronics

"Many were increasingly of the opinion that they'd all made a big mistake in coming down from the trees in the first place. And some said that even the trees had been a bad move, and that no one should ever have left the oceans."

Douglas Adams, "The Hitchhikers Guide To The Galaxy"

Two crystal ovens for OPO systems 1 and 2 have been employed in this work, both of which are equipped with an analog control electronics to stabilize their temperature. A Pt1000 platinum resistor is used as a temperature sensor. Heating cartridges have been purchased from HS Heizelemente GmbH and implanted in the copper crystal oven. Figure B.1 shows the schematics of the output stage of the controller. Figure B.2 features the scheme of the electronics generating the correction signal.

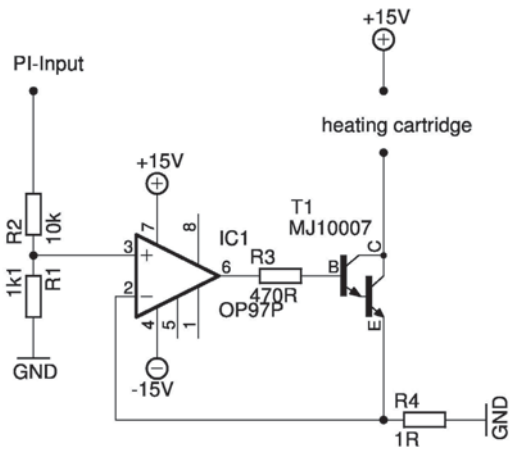

Figure B.1: Connection scheme of the output stage of the temperature controller. An input voltage from the proportional-integral amplifier from Figure B.2 is connected to the upper left junction. The signal is used on an operational amplifier to operate a power Darlington transistor as a current regulator.

Dieses Werk ist copyrightgeschützt und darf in keiner Form vervielfältigt werden noch an Dritte weitergegeben werden.
Es gilt nur für den persönlichen Gebrauch.

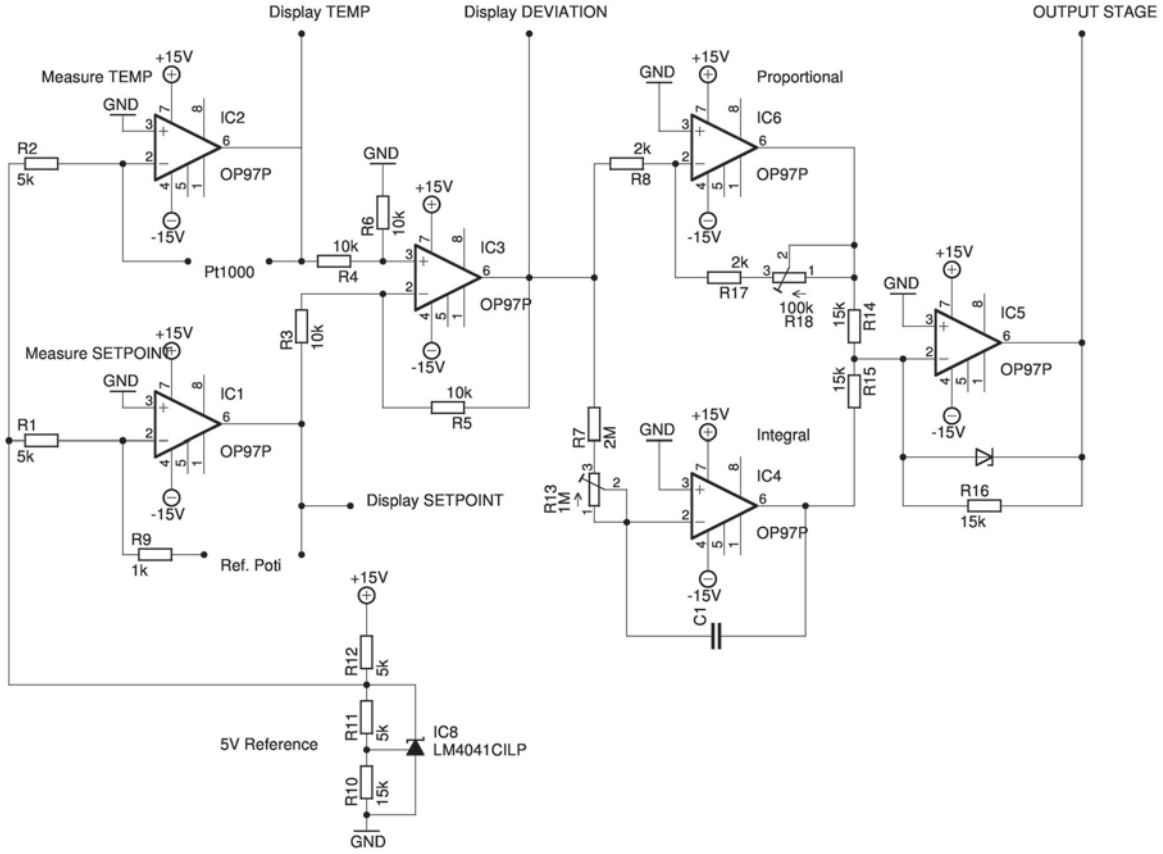

Figure B.2: Connection scheme of temperature controller electronics. A stable reference voltage is generated using a shunt regulator LM4041. This voltage induces a current through the Pt1000 thermo-resistor and the setpoint resistor. The deviation between the two resistances is then amplified in IC6 for the proportional part and integrated in IC4 for an integral part. The electronics output is lead to a power amplifier in form of an output stage (Figure B.1), which drives the heating resistor (heating cartridges from Heinz Stegmeier GmbH) in the oven.

Dieses Werk ist copyrightgeschützt und darf in keiner Form vervielfältigt werden noch an Dritte weitergegeben werden.
Es gilt nur für den persönlichen Gebrauch.

Bibliography

[1] T. Amano, *Submillimeter-wave spectrum of CH_2D^+*, Astronomy & Astrophysics **516** (2010), L4.

[2] J. A. Armstrong, N. Bloembergen, J. Ducuing, and P. S. Pershan, *Interactions between light waves in a nonlinear dielectric*, Physical Review **127** (1962), 1918–1939.

[3] A. Ashkin, G. D. Boyd, J. M. Dziedzic, R. G. Smith, A. A. Ballman, J. J. Levinstein, and K. Nassau, *Optically-induced refractive index inhomogeneities in $LiNbO_3$ and $LiTaO_3$*, Applied Physics Letters **9** (1966), 72–74.

[4] O. Asvany, T. Giesen, B. Redlich, and S. Schlemmer, *Experimental determination of the ν_5 cis-bending vibrational frequency in ground state ($X^2\Pi_u$) $C_2H_2^+$ using laser induced reactions*, Physical Review Letters **94** (2005), 073001.

[5] O. Asvany, E. Hugo, F. Müller, F. Kühnemann, S. Schiller, J. Tennyson, and S. Schlemmer, *Overtone spectroscopy of hd and dh using laser induced reactions*, Journal of Chemical Physics **127** (2007), 154317.

[6] O. Asvany, P. Kumar P, B. Redlich, I. Hegemann, S. Schlemmer, and D. Marx, *Understanding the Infrared Spectrum of Bare CH_5^+*, Science **309** (2005), 1219–1222.

[7] O. Asvany, O. Ricken, H. S. P. Müller, M. C. Wiedner, T. F. Giesen, and S. Schlemmer, *High-Resolution Rotational Spectroscopy in a cold Ion Trap: H_2D^+ and D_2H^+*, Physical Review Letters **100** (2008), 233004.

Dieses Werk ist copyrightgeschützt und darf in keiner Form vervielfältigt werden noch an Dritte weitergegeben werden.
Es gilt nur für den persönlichen Gebrauch.

[8] J. Baker, S. K. Bramble, and P. A. Hamilton, *A hot band LIF study of the $A^1\Pi_u$ - $X^1\Sigma_g^+$ transition in C_3*, Chemical Physics Letters **213** (1993), 297–302.

[9] H. Beckers, *private communication*, 2010.

[10] P. E. Bernath, *Spectra of atoms and molecules*, second ed., Oxford University Press, New York, 2005.

[11] J. E. Bjorkholm, *Some effects of spatially nonuniform pumping in pulsed optical parametric oscillators*, IEEE Journal of Quantum Electronics **7** (1971), 109–118.

[12] W. R. Bosenberg, A. Drobshoff, J. I. Alexander, L. E. Myers, and R. L. Byer, *93% pump depletion, 3.5-w continuous-wave, singly resonant optical parametric oscillator*, Optics Letters **21** (1996), 1336–1338.

[13] P. Botschwina, *An Accurate Equilibrium Structure and CCSD (T) Spectroscopic Constants for Linear C_3Si_2*, Journal of Molecular Spectroscopy **198** (1999), 192.

[14] _____, *A coupled cluster study of linear C_7: no evidence of floppiness*, Chemical Physics Letters **354** (2002), 148.

[15] P. Botschwina and R. Oswald, *On the vibrations of linear C_{11}: A coupled cluster study*, Chemical Physics **325** (2006), 485 – 491.

[16] I. Breunig, *Optisch parametrische Oszillatoren für die Erzeugung monochromatischen Lichtes im mittleren und fernen Infrarot*, Ph.D. thesis, Rheinische Friedrich-Wilhelms-Universität Bonn, 2009.

[17] I. Breunig, D. Haertle, and K. Buse, *Continuous-wave optical parametric oscillators: recent developments and prospects*, Applied Physics B: Lasers and Optics **In Press** (2011), –.

[18] I. Breunig, J. Kiessling, B. Knabe, R. Sowade, and K. Buse, *Hybridly-pumped continuous-wave optical parametric oscillator*, Optics Express **16** (2008), 5662–5666.

[19] W. Brunner, R. Fischer, and H. Paul, *Der einfach-resonante optische parametrische Oszillator*, Annalen der Physik **30** (1973), 299–308.

[20] W. Brunner and H. Paul, *Progress in optics*, vol. XV, North-Holland Publishing Company, Amsterdam, 1977.

Dieses Werk ist copyrightgeschützt und darf in keiner Form vervielfältigt werden noch an Dritte weitergegeben werden.
Es gilt nur für den persönlichen Gebrauch.

[21] D. A. Bryan, R. Gerson, and H. E. Tomaschke, *Increased optical damage resistance in Lithium Niobate*, Applied Physics Letters **44** (1984), 847–849.

[22] D. Crampton, A. P. Cowley, and R. M. Humphreys, *Spectroscopic Observations of CRL 2688*, Astrophysical Journal **198** (1975), L135.

[23] M. W. Crofton, M. F. Jagod, B. D. Rehfuss, W. A. Kreiner, and T. Oka, *Infrared spectroscopy of carbo-ions. III. ν_3 band of methyl cation CH_3^+*, Journal of Chemical Physics **88** (1988), 666–678.

[24] N. R. Daly, *Scintillation Type Mass Spectrometer Ion Detector*, Review of Scientific Instruments **31** (1960), 264–267.

[25] A. E. Douglas, *Laboratory Studies of the λ 4050 Group of Cometary Spectra.*, Astrophysical Journal **114** (1951), 466–468.

[26] J. L. Duncan, *The determination of vibrational anharmonicity in molecules from spectroscopic observations*, Spectrochimica Acta, Part A **47** (1991), 1–27.

[27] L. A. Eyres, P. J. Tourreau, T. J. Pinguet, C. B. Ebert, J. S. Harris, M. M. Fejer, L. Becouarn, B. Gerard, and E. Lallier, *All-epitaxial fabrication of thick, orientation-patterned GaAs films for nonlinear optical frequency conversion*, Applied Physics Letters **79** (2001), 904.

[28] O. Gayer, Z. Sacks, E. Galun, and A. Arie, *Temperature and wavelength dependent refractive index equations for MgO-doped congruent and stoichiometric $LiNbO_3$*, Applied Physics B: Lasers and Optics **91** (2008), 343–348.

[29] R. Gendriesch, K. Pehl, T. Giesen, G. Winnewisser, and F. Lewen, *Terahertz spectroscopy of linear triatomic CCC: High precision laboratory measurement and analysis of the ro-vibrational bending transitions*, Zeitschrift für Naturforschung A: Journal of Physical Sciences **58** (2003), 129–138.

[30] G. M. Gibson, M. H. Dunn, and M. J. Padgett, *Application of a continuously tunable, cw optical parametric oscillator for high-resolution spectroscopy*, Optics Letters **23** (1998), 40–42.

[31] T. F. Giesen, U. Berndt, K. M. T. Yamada, G. Fuchs, R. Schieder, G. Winnewisser, R. A. Provencal, F. N. Keutsch, A. van Orden, and R. J. Saykally, *Detection of the Linear Carbon Cluster C_{10}: Rotationally Resolved Diode-Laser Spectroscopy*, ChemPhysChem **4** (2001), 242.

Dieses Werk ist copyrightgeschützt und darf in keiner Form vervielfältigt werden noch an Dritte weitergegeben werden.
Es gilt nur für den persönlichen Gebrauch.

[32] T. F. Giesen, A. van Orden, J. D. Cruzan, R. A. Provencal, R. J. Saykally, R. Gendriesch, F. Lewen, and G. Winnewisser, *Interstellar detection of CCC and high-precision laboratory measurements near 2 THz*, Astrophysical Journal **551** (2001), L181.

[33] T. F. Giesen, A. van Orden, H. J. Hwang, R. S. Fellers, R. A. Provencal, and R. J. Saykally, *Infrared laser spectroscopy of the linear C_{13} carbon cluster*, Science **265** (1994), 756.

[34] E. Gonzalez, C. M. L. Rittby, and W. R. M. Graham, *Isotopic Study of New Fundamentals and Combination Bands of Linear C_5, C_7, and C_9 in Solid Ar*, Journal of Physical Chemistry A **115** (2011), 2533–2539.

[35] W. Gordy and R. L. Cook, *Microwave molecular spectra*, second ed., John Wiley & Sons, Inc., New York, 1984.

[36] G. Guelachvili and K. N. Rao, *Handbook of infrared standards ii*, Academic Press, Inc., San Diego, 1993.

[37] S. Guha, F. J. Wu, and J. Falk, *Effects of Focusing on Parametric Oscillation*, IEEE Journal of Quantum Electronics **18** (1982), 907–912.

[38] J. R. Heath and R. J. Saykally, *Infrared laser absorption spectroscopy of the ν_4 (σ_u) fundamental and associated ν_{11} (π_u) hot band of C_7 - Evidence for alternating rigidity in linear carbon clusters*, Journal of Chemical Physics **94** (1991), 1724–1729.

[39] J. R. Heath, R. A. Sheeks, A. L. Cooksy, and R. J. Saykally, *The C_7 Cluster: Structure and Infrared Frequencies*, Science **249** (1990), 895–897.

[40] J. R. Heath, A. van Orden, E. Kuo, and R. J. Saykally, *The ν_5 band of C_7*, Chemical Physics Letters **182** (1991), 17–20.

[41] A. Hecker, *Entwicklung optisch parametrischer Oszillatoren zur hochauflösenden Spektroskopie und Analyse des van-der-Waals-Komplexes $(N_2O)_2$*, Ph.D. thesis, Ruhr-Universität Bochum, 2003.

[42] A. Henderson and R. Stafford, *Intra-cavity power effects in singly resonant cw OPOs*, Applied Physics B: Lasers and Optics **85** (2006), 181–184.

[43] D. Herriott, H. Kogelnik, and R. Kompfner, *Off-axis paths in spherical mirror interferometers*, Applied Optics **3** (1964), 523–526.

Dieses Werk ist copyrightgeschützt und darf in keiner Form vervielfältigt werden noch an Dritte weitergegeben werden.
Es gilt nur für den persönlichen Gebrauch.

[44] F. Holland, M. Winnewisser, C. Jarman, H. W. Kroto, and K. M. T. Yamada, *The ν_3 band system of SCCCS: High-resolution Fourier transform and diode laser measurements*, Journal of Molecular Spectroscopy **130** (1988), 344 – 370.

[45] W. Huggins, *On the Photographic Spectrum of Comet (Wells) I, 1882*, Proceedings of the Royal Society of London **34** (1882), 148.

[46] H. J. Hwang, A. van Orden, K. Tanaka, E. W. Kuo, J. R. Heath, and R. J. Saykally, *Infrared laser spectroscopy of jet-cooled carbon clusters: Structure of triplet C_6*, Molecular Physics **79** (1993), 769.

[47] H. W. Icenogle, B. C. Platt, and W. L. Wolfe, *Refractive indexes and temperature coefficients of germanium and silicon*, Applied Optics **15** (1976), no. 10, 2348–2351.

[48] H. Inaba, T. Ikegami, F. L. Hong, A. Onae, Y. Koga, T. R. Schibli, K. Minoshima, H. Matsumoto, S. Yamadori, O. Tohyama, and S. I. Yamaguchi, *Phase locking of a continuous-wave optical parametric oscillator to an optical frequency comb for optical frequency synthesis*, IEEE Journal of Quantum Electronics **40** (2004), 929–936.

[49] M.-F. Jagod, M. Rösslein, C. M. Gabrys, and T. Oka, *Infrared Spectroscopy of Carbo-ions: The ν_1 and ν_4 Bands of CH_2D^+, and the ν_1 Band of CHD_2^+*, Journal of Molecular Spectroscopy **153** (1992), 666–679.

[50] P. Jensen, *A new morse oscillator-rigid bender internal dynamics (MORBID) Hamiltonian for triatomic molecules*, Journal of Molecular Spectroscopy **128** (1988), 478–501.

[51] K. Kawaguchi, K. Matsumura, H. Kanamori, and E. Hirota, *Diode laser spectroscopy of C_3: The $\nu_2+\nu_3-\nu_2$, $2\nu_2+\nu_3-2\nu_2$, and $2\nu_2+\nu_3$ bands*, Journal of Chemical Physics **91** (1989), 1953–1957.

[52] J. Kiessling, R. Sowade, I. Breunig, K. Buse, and V. Dierolf, *Cascaded optical parametric oscillations generating tunable terahertz waves in periodically poled lithium niobate crystals*, Optics Express **17** (2009), 87–91.

[53] A. Klemann, *Aufbau und Charakterisierung eines OPO Systems für die Spektroskopie bei 5 μm*, Diploma Thesis, Universität zu Köln, 2010.

Dieses Werk ist copyrightgeschützt und darf in keiner Form vervielfältigt werden noch an Dritte weitergegeben werden.
Es gilt nur für den persönlichen Gebrauch.

[54] H. Kogelnik and T. Li, *Laser beams and resonators*, Applied Optics **5** (1966), 1550–1567.

[55] E. V. Kovalchuk, T. Schuldt, and A. Peters, *Combination of a continuous-wave optical parametric oscillator and a femtosecond frequency comb for optical frequency metrology*, Optics Letters **30** (2005), 3141–3143.

[56] L. B. Kreuzer, *Single and multi-mode oscillation of the singly resonant optical parametric oscillator*, Proceedings of the Joint Conference on Lasers and Opto-Electronics, 1969, pp. 52–63.

[57] J. Krieg, V. Lutter, F.-X. Hardy, S. Schlemmer, and T. F. Giesen, *The ν_5 antisymmetric stretching mode of linear C_7 revisited in high resolution*, Journal of Chemical Physics **132** (2010), 224306.

[58] J. Kurtz and L. Adamowicz, *Theoretical vibrations of carbon chains C3, C4, C5, C6, C7, C8, and C9*, Astrophysical Journal **370** (1991), 784–790.

[59] N. Leindecker, A. Marandi, R. L. Byer, and K. L. Vodopyanov, *Broadband degenerate OPO for mid-infrared frequency comb generation*, Optics Express **19** (2011), 6296–6302.

[60] Z. Li, R.G.T. Bennett, and G.E. Stedman, *Swept-frequency induced optical cavity ringing*, Optics Communications **86** (1991), 51 – 57.

[61] D. C. Lis, P. F. Goldsmith, E. A. Bergin, E. Falgarone, M. Gerin, and E. Roueff, *Hydrides in Space: Past, Present, and Future*, Submillimeter Astrophysics and Technology: a Symposium Honoring Thomas G. Phillips (D. C. Lis, J. E. Vaillancourt, P. F. Goldsmith, T. A. Bell, N. Z. Scoville, & J. Zmuidzinas, ed.), Astronomical Society of the Pacific Conference Series, vol. 417, December 2009, pp. 23–24.

[62] J. P. Maier, N. M. Lakin, G. A. H. Walker, and D. A. Bohlender, *Detection of C_3 in diffuse interstellar clouds*, Astrophysical Journal **553** (2001), 267.

[63] K. Matsumura, H. Kanamori, and K. Kawaguchi, *Infrared diode laser kinetic spectroscopy of the ν_3 band of C_3*, Journal of Chemical Physics **89** (1988), 3491.

[64] M. C. McCarthy, C. A. Gottlieb, and P. Thaddeus, *Silicon molecules in space and in the laboratory*, Molecular Physics **101** (2003), 697–704.

Dieses Werk ist copyrightgeschützt und darf in keiner Form vervielfältigt werden noch an Dritte weitergegeben werden.
Es gilt nur für den persönlichen Gebrauch.

[65] A. J. Merer, *Absorption spectra of C_3 and C_3H_2 from the flash photolysis of diazopropyne*, Canadian Journal of Physics **45** (1967), 4103–4111.

[66] D. Meschede, *Optik, Licht und Laser*, Vieweg+Teubner Verlag, Wiesbaden, 2008.

[67] T. J. Millar, E. Herbst, and R. P. A. Bettens, *Large molecules in the envelope surrounding IRC+10216*, Monthly Notices of the Royal Astronomical Society **316** (2000), 195.

[68] M. Mladenovič, S. Schmatz, and P. Botschwina, *Large-scale ab initio calculations for C_3*, Journal of Chemical Physics **101** (1994), 5891–5899.

[69] N. Moazzen-Ahmadi, J. J. Thong, and A. R. W. McKellar, *Diode laser spectroscopy of gas phase C_5: The ν_3 fundamental and associated hot bands*, Journal of Chemical Physics **91** (1989), 2140.

[70] ———, *Infrared diode laser spectroscopy of the ν_3 fundamental and $\nu_3+\nu_5-\nu_5$ sequence bands of the C_4 radical in a hollow cathode discharge*, Journal of Chemical Physics **100** (1994), 4033.

[71] B. Mookerjea, T. Giesen, J. Stutzki, J. Cernicharo, J. R. Goicoechea, M. de Luca, T. A. Bell, H. Gupta, M. Gerin, C. M. Persson, P. Sonnentrucker, Z. Makai, J. Black, F. Boulanger, A. Coutens, E. Dartois, P. Encrenaz, E. Falgarone, T. Geballe, B. Godard, P. F. Goldsmith, C. Gry, P. Hennebelle, E. Herbst, P. Hily-Blant, C. Joblin, M. Kaźmierczak, R. Kołos, J. Krełowski, D. C. Lis, J. Martin-Pintado, K. M. Menten, R. Monje, J. C. Pearson, M. Perault, T. G. Phillips, R. Plume, M. Salez, S. Schlemmer, M. Schmidt, D. Teyssier, C. Vastel, S. Yu, P. Dieleman, R. Güsten, C. E. Honingh, P. Morris, P. Roelfsema, R. Schieder, A. G. G. M. Tielens, and J. Zmuidzinas, *Excitation and abundance of C_3 in star forming cores. Herschel/HIFI observations of the sight-lines to W31C and W49N*, Astronomy & Astrophysics **521** (2010), L13.

[72] H. S. P. Müller, F. Schlöder, J. Stutzki, and G. Winnewisser, *The Cologne Database for Molecular Spectroscopy, CDMS: a useful tool for astronomers and spectroscopists*, Journal of Molecular Structure **742** (2005), 215 – 227.

[73] Müller, F., *Spurengasnachweis und spektroskopie im mittleren infrarot mit einem dauerstrich-optisch-parametrischen oszillator*, Ph.D. thesis, Rheinische Friedrich-Wilhelms-Universität Bonn, 2005.

Dieses Werk ist copyrightgeschützt und darf in keiner Form vervielfältigt werden noch an Dritte weitergegeben werden.
Es gilt nur für den persönlichen Gebrauch.

[74] L. E. Myers, R. C. Eckardt, M. M. Fejer, R. L. Byer, and W. R. Bosenberg, *Multigrating quasi-phase-matched optical parametric oscillator in periodically poled $LiNbO_3$*, Optics Letters **21** (1996), 591–593.

[75] P. Neubauer-Guenther, T. F. Giesen, U. Berndt, G. Fuchs, and G. Winnewisser, *The Cologne Carbon Cluster Experiment: ro-vibrational spectroscopy on C_8 and other small carbon clusters*, Spectrochimica Acta, Part A: Molecular and Biomolecular Spectroscopy **59** (2003), 431.

[76] P. Neubauer-Guenther, K. M. T. Yamada, T. F. Giesen, and S. Schlemmer, *High resolution infrared spectra of the linear carbon cluster C_7: The ν_4 stretching fundamental band and associated hot bands*, Journal of Chemical Physics **127** (2007), 014313.

[77] Harald H. Nielsen, *The Vibration-Rotation Energies of Molecules*, Reviews of Modern Physics **23** (1951), 90.

[78] F. J. Northrup and T. J. Sears, *Stimulated-emission pumping spectroscopy study of jet-cooled C_3: pure bending levels and bend-symmetric-stretch combination levels of $\tilde{X}^1\Sigma_g^+$*, Journal of the Optical Society of America B: Optical Physics **7** (1990), 1924–1934.

[79] T. Oka, J. A. Thorburn, B. J. McCall, S. D. Friedman, L. M. Hobbs, P. Sonnentrucker, D. E. Welty, and D. G. York, *Observations of C_3 in Translucent Sight Lines*, Astrophysical Journal **582** (2003), 823.

[80] B. J. Ortman, R. H. Hauge, J. L. Margrave, and Z. H. Kafafi, *Reactions of small carbon clusters with water in cryogenic matrixes: the FTIR spectrum of hydroxyethynyl carbene*, The Journal of Physical Chemistry **94** (1990), 7973–7977.

[81] O. Paul, A. Quosig, T. Bauer, M. Nittmann, J. Bartschke, G. Anstett, and J. A. L'Huillier, *Temperature-dependent Sellmeier equation in the MIR for the extraordinary refractive index of 5% MgO doped congruent $LiNbO_3$*, Applied Physics B: Lasers and Optics **86** (2007), 111–115.

[82] S. Persijn, F. Harren, and A. vander Veen, *Quantitative gas measurements using a versatile OPO-based cavity ringdown spectrometer and the comparison withspectroscopic databases*, Applied Physics B: Lasers and Optics **100** (2010), 383–390.

[83] C. R. Phillips and M. M. Fejer, *Stability of the Singly Resonant Optical Parametric Oscillator*, Journal of the Optical Society of America B: Optical Physics **27** (2010), 2687–2699.

Dieses Werk ist copyrightgeschützt und darf in keiner Form vervielfältigt werden noch an Dritte weitergegeben werden.
Es gilt nur für den persönlichen Gebrauch.

[84] H. M. Pickett, *The fitting and prediction of vibration-rotation spectra with spin interactions*, Journal of Molecular Spectroscopy **148** (1991), 371 – 377.

[85] J. D. Presilla-Márquez and W. R. M. Graham, *Vibrational spectra of penta-atomic silicon–carbon clusters. II. Linear Si_2C_3*, Journal of Chemical Physics **100** (1994), 181.

[86] P. L. Raston, C. J. Knapp, and W. Jäger, *Rotovibrational spectroscopy of hydrogen peroxide embedded in superfluid helium nanodroplets*, Physical Chemistry Chemical Physics **In Press** (2011), –.

[87] M. Reich, R. Schieder, H. J. Clar, and G. Winnewisser, *Internally coupled Fabry-Perot interferometer for high precision wavelength control of tunable diode lasers*, Applied Optics **25** (1986), 130.

[88] J. Reid, D. T. Cassidy, and R. T. Menzies, *Linewidth measurements of tunable diode lasers using heterodyne and etalon techniques*, Applied Optics **21** (1982), 3961–3965.

[89] L. Richter, H. Mandelberg, M. Kruger, and P. McGrath, *Linewidth determination from self-heterodyne measurements with subcoherence delay times*, IEEE Journal of Quantum Electronics **22** (1986), 2070–2074.

[90] E. A. Rohlfing, *Laser-induced-fluorescence spectroscopy of jet-cooled C_3*, Journal of Chemical Physics **91** (1989), 4531.

[91] M. Rösslein, M. F. Jagod, C. M. Gabrys, and T. Oka, *Laboratory Infrared Spectra of CH_2D^+ and $HCCD^+$ and Predicted Microwave Transitions*, Astrophysical Journal **382** (1991), L51–L53.

[92] L. S. Rothman, D. Jacquemart, A. Barbe, D. C. Benner, M. Birk, L. R. Brown, M. R. Carleer, C. Chackerian, K. Chance, L. H. Coudert, V. Dana, V. M. Devi, J. M. Flaud, R. R. Gamache, A. Goldman, J. M. Hartmann, K. W. Jucks, A. G. Maki, J. Y. Mandin, S. T. Massie, J. Orphal, A. Perrin, C. P. Rinsland, M. A. H. Smith, J. Tennyson, R. N. Tolchenov, R. A. Toth, J. Vander Auwera, P. Varanasi, and G. Wagner, *The HITRAN 2004 molecular spectroscopic database*, Journal of Quantitative Spectroscopy and Radiative Transfer **96** (2005), 139–204.

[93] M. Sato, T. Hatanaka, S. Izumi, T. Taniuchi, and H. Ito, *Generation of 6.6-μm Optical Parametric Oscillation with Periodically Poled $LiNbO_3$*, Applied Optics **38** (1999), 2560–2563.

Dieses Werk ist copyrightgeschützt und darf in keiner Form vervielfältigt werden noch an Dritte weitergegeben werden.
Es gilt nur für den persönlichen Gebrauch.

[94] S. Saupe, M. H. Wappelhorst, B. Meyer, W. Urban, and A. G. Maki, *Sub-Doppler Heterodyne Frequency Measurements near 5 μm with a CO-Laser Sideband System: Improved Calibration Tables for Carbonyl Sulfide Transitions*, Journal of Molecular Spectroscopy **175** (1996), 190–197.

[95] P. Schilke, D. J. Benford, T. R. Hunter, D. C. Lis, and T. G. Phillips, *A Line Survey of Orion-KL from 607 to 725 GHz*, The Astrophysical Journal Supplement Series **132** (2001), 281.

[96] S. Schiller and J.-P. Meyn, *Von der Photonenspaltung zum kontinuierlich emittierenden Universallaser*, Physik Journal, June 2002.

[97] S. Schlemmer, T. Kuhn, E. Lescop, and D. Gerlich, *Laser excited N_2^+ in a 22-pole ion trap: experimental studies of rotational relaxation processes*, International Journal of Mass Spectrometry **185** (1999), 589–602.

[98] S. Schlemmer, E. Lescop, J. van Richthofen, and D. Gerlich, *Laser Induced Reactions in a 22-Pole Trap: $C_2H_2^+ + h\nu_3 + H_2 \rightarrow C_2H_3^+ + H$*, Journal of Chemical Physics **117** (2002), 2068–2075.

[99] D. Smith, *The ion chemistry of interstellar clouds*, Chemical Reviews **92** (1992), 1473–1485.

[100] R. Sowade, *Continuous-wave Terahertz Light from Optical Parametric Oscillators*, Ph.D. thesis, Rheinische Friedrich-Wilhelms-Universität Bonn, 2010.

[101] R. Sowade, I. Breunig, J. Kiessling, and K. Buse, *Influence of the pump threshold on the single-frequency output power of singly resonant optical parametric oscillators*, Applied Physics B: Lasers and Optics **96** (2009), 25–28.

[102] U. Strößner, *Development of optical synthesizers*, Ph.D. thesis, Universität Konstanz, 2001.

[103] D. Stupar, J. Krieg, P. Kroetz, G. Sonnabend, M. Sornig, T. F. Giesen, and R. Schieder, *Fully reflective external-cavity setup for quantum-cascade lasers as a local oscillator in mid-infrared wavelength heterodyne spectroscopy*, Applied Optics **47** (2008), 2993.

[104] R. L. Sutherland, D. G. McLean, and S. Kirkpatrick, *Handbook of nonlinear optics*, Marcel Dekker, New York, 2003.

Dieses Werk ist copyrightgeschützt und darf in keiner Form vervielfältigt werden noch an Dritte weitergegeben werden.
Es gilt nur für den persönlichen Gebrauch.

[105] S. Thorwirth, J. Krieg, V. Lutter, I. Keppeler, S. Schlemmer, M. E. Harding, J. Vázquez, and T. F. Giesen, *High-resolution OPO spectroscopy of Si_2C_3 at 5 μm: Observation of hot band transitions associated with ν_3*, Journal of Molecular Spectroscopy **In Press** (2011), –.

[106] R. A. Toth, *$2\nu_2 - \nu_2$ and $2\nu_2$ bands of $H_2^{16}O$, $H_2^{17}O$ and $H_2^{18}O$: line positions and strenghts*, Journal of the Optical Society of America B: Optical Physics **10** (1993), 1526–1544.

[107] C. H. Townes and A. L. Schawlow, *Microwave spectroscopy*, Dover Publications, 1975.

[108] G. A. Turnbull, D. McGloin, I. D. Lindsay, M. Ebrahimzadeh, and M. H. Dunn, *Extended mode-hop-free tuning by use of a dual-cavity, pump-enhanced optical parametric oscillator*, Optics Letters **25** (2001), 341.

[109] B. E. Turner, *Gaseous Refractory Elements in the Circumstellar Shell of IRC+10216*, Astrophysics and Space Science **224** (1995), 297–303.

[110] M. Vainio, J. Peltola, S. Persijn, F. J. M. Harren, and L. Halonen, *Singly resonant cw OPO with simple wavelength tuning*, Optics Express **16** (2008), 11141–11146.

[111] M. Vainio, M. Siltanen, J. Peltola, and L. Halonen, *Continuous-wave optical parametric oscillator tuned by a diffraction grating*, Optics Express **17** (2009), 7702–7707.

[112] _____, *Grating-cavity continuous-wave optical parametric oscillators for high-resolution mid-infrared spectroscopy*, Applied Optics **50** (2011), A1–A10.

[113] M. van Herpen, *Continuous-wave optical parametric oscillator for trace gas detection in life sciences*, Ph.D. thesis, Katholieke Universiteit Nijmegen, 2004.

[114] M. van Herpen, S. E. Bisson, and F. J. M. Harren, *Continuous-wave operation of a single-frequency optical parametric oscillator at 4-5 μm based on periodically poled $LiNbO_3$*, Optics Letters **28** (2003), 2497–2499.

Dieses Werk ist copyrightgeschützt und darf in keiner Form vervielfältigt werden noch an Dritte weitergegeben werden.
Es gilt nur für den persönlichen Gebrauch.

[115] M. M. J. W. van Herpen, S. Li, S. E. Bisson, S. T. Hekkert, and F. J. M. Harren, *Tuning and stability of a continuous-wave mid-infrared high-power single resonant optical parametric oscillator*, Applied Physics B: Lasers and Optics **75** (2002), 329–333.

[116] M. M. J. W. van Herpen, A. K. Y. Ngai, S. E. Bisson, J. H. P. Hackstein, E. J. Woltering, and F. J. M. Harren, *Optical parametric oscillator-based photoacoustic detection of CO_2 at 4.23 μm allows real-time monitoring of the respiration of small insects*, Applied Physics B: Lasers and Optics **82** (2006), 665–669.

[117] A. van Orden, T. F. Giesen, R. A. Provencal, H. J. Hwang, and R. J. Saykally, *Characterization of silicon-carbon clusters by infrared laser spectroscopy: The $\nu_3(\sigma_u)$ band of linear Si_2C_3*, Journal of Chemical Physics **101** (1994), 10237.

[118] A. van Orden, H. J. Hwang, E. W. Kuo, and R. J. Saykally, *Infrared laser spectroscopy of jet-cooled carbon clusters: The bending dynamics of linear C_9*, Journal of Chemical Physics **98** (1993), 6678–6678.

[119] A. van Orden, R. A. Provencal, F. N. Keutsch, and R. J. Saykally, *Infrared laser spectroscopy of jet-cooled carbon clusters: The ν_5 band of linear C_9*, Journal of Chemical Physics **105** (1996), 6111.

[120] K. L. Vodopyanov, O. Levi, P. S. Kuo, T. J. Pinguet, J. S. Harris, M. M. Fejer, B. Gerard, L. Becouarn, and E. Lallier, *Optical parametric oscillation in quasi-phase-matched GaAs*, Optics Letters **29** (2004), 1912–1914.

[121] K. L. Vodopyanov, E. Sorokin, I. T. Sorokina, and P. G. Schunemann, *Mid-IR frequency comb source spanning 4.4–5.4μm based on subharmonic GaAs optical parametric oscillator*, Optics Letters **36** (2011), 2275–2277.

[122] V. Špirko, M. Mengel, and P. Jensen, *Calculation of Rotation-Vibration Energy Levels in Ground State C_3 by a Born-Oppenheimer-Type Separation of the Vibrational Motions*, Journal of Molecular Spectroscopy **183** (1997), 129–138.

[123] J. K. G. Watson, *Vibrational spectra and structure*, ch. Aspects of Quartic and Sextic Centrifugal Effects on Rotational Energy Levels, Marcel Dekker, New York, 1977.

Dieses Werk ist copyrightgeschützt und darf in keiner Form vervielfältigt werden noch an Dritte weitergegeben werden.
Es gilt nur für den persönlichen Gebrauch.

[124] M. A. Watson, M. V. O'Connor, P. S. Lloyd, D. P. Shepherd, D. C. Hanna, C. B. E. Gawith, L. Ming, P. G. R. Smith, and O. Balachninaite, *Extended operation of synchronously pumped optical parametric oscillators to longer idler wavelengths*, Optics Letters **27** (2002), 2106–2108.

[125] C. M. Western, University of Bristol, UK, PGOPHER*, a Program for Simulating Rotational Structure, version 7.*

[126] G. Wysocki, R.F. Curl, F.K. Tittel, R. Maulini, J.M. Bulliard, and J. Faist, *Widely tunable mode-hop free external cavity quantum cascade laser for high resolution spectroscopic applications*, Applied Physics B: Lasers and Optics **81** (2005), 769.

[127] G. Wysocki, R. Lewicky, R.F. Curl, F.K. Tittel, L. Diehl, F. Capasso, M. Troccoli, G. Hofler, D. Bour, S. Corzine, R. Maulini, M. Giovannini, and J. Faist, *Widely tunable mode-hop free external cavity quantum cascade lasers for high resolution spectroscopy and chemical sensing*, Applied Physics B: Lasers and Optics **92** (2008), 305.

[128] J. Yi, H. Ishizuki, I. Shoji, T. Taira, and S. Kurimura, *Generation of 6 μm Radiation by Optical Parametric Oscillator and Difference Frequency Generation in Periodically Poled $LiNbO_3$*, Japanese Journal of Applied Physics **45** (2006), 111–115.

Dieses Werk ist copyrightgeschützt und darf in keiner Form vervielfältigt werden noch an Dritte weitergegeben werden.
Es gilt nur für den persönlichen Gebrauch.

Dieses Werk ist copyrightgeschützt und darf in keiner Form vervielfältigt werden noch an Dritte weitergegeben werden.
Es gilt nur für den persönlichen Gebrauch.

Danksagung

Ich möchte mich hiermit bei allen bedanken, die mich bei der Ausführung dieser Arbeit unterstützt haben.

Herrn Prof. Dr. Stephan Schlemmer gebührt ein großer Dank für die Betreuung dieser Arbeit und das Schaffen eines sehr guten Arbeitsklimas. Sein Engagement für seine Mitarbeiter und sein Interesse am Fortschritt der Arbeit haben mich stets motiviert. Ich habe viel gelernt. Danke!

Herrn PD Dr. Joachim Hemberger danke ich für die Übernahme der Rolle des Zweitgutachters der Arbeit. Bei Herrn Prof. Dr. Axel Klein möchte ich mich für sein Einverständnis bedanken, den Prüfungsvorsitz zu führen.

Herr Prof. Dr. Thomas Giesen hat mich während der gesamten Arbeit mit vielen guten Ideen versorgt. Seine Expertise zu Kohlenstoffketten und seine Lösungsvorschläge zu experimentellen Problemen jeder Art haben mir an vielen Stellen weitergeholfen.

Dr. Ingo Breunig danke ich für die nette Starthilfe was den OPO angeht. Ihm, Dr. Rosita Sowade und Jens Kießling danke ich für viele fachliche Diskussionen. André Klemann danke ich für seine experimentelle Hartnäckigkeit, was den OPO angeht, und den Humor im Labor und außerhalb.

Für gute Zeiten im Jet-Labor bedanke ich mich sehr bei Volker Lutter und Imke Keppeler. Dr. Sven Thorwirth verdient hier eine besondere Erwähnung. Von ihm habe ich einiges über Moleküle, aber auch über Sport, Musik, Filme, Apple und den hessischen Dialekt gelernt. *Kerle na!* Ich danke François-Xavier Hardy und Volker Lutter für das engagierte Hervorkitzeln von schwachen Linien. Frau Dr. Neubauer-Guenther hat mir sehr viel bei der Einarbeitung in Kohlenstoff-Jets und Infrarot-Spektrometern geholfen.

Danke an Sabrina Gärtner und Dr. Oskar Asvany für den effizienten Schichtbetrieb und die ansteckende Begeisterung beim Messen und Auswerten von Ionen-Spektren. Es hilft zwischendurch, wenn Kollegen einem vor Freude über das Experiment auf den Arm springen, oder das Labor mit gemeinsam gemessenen Spektren tapezieren.

Der gesamten Besetzung von Raum 317: Danke für viele Diskussionen und Anekdoten, auch an Dušan Stupar. Dr. Christian Endres danke ich für seine technische Unterstützung jeder Art.

Vielen Dank an alle Mitglieder der Spektroskopie-Gruppe. Unter anderem für alle nerdigen Diskussionen, die man sonst nirgendwo führen kann, laute

Dieses Werk ist copyrightgeschützt und darf in keiner Form vervielfältigt werden noch an Dritte weitergegeben werden.
Es gilt nur für den persönlichen Gebrauch.

Lacher, die man über den ganzen Flur hört und viel Kuchen! Die Arbeit hat nicht zuletzt dank Euch so viel Spaß gemacht!

Danke der feinmechanischen Werkstatt für viele Beratungen und die schnelle und sehr gute Anfertigung aller nötigen Werkstücke, ohne die der OPO und das neue Spektrometer nicht hätten gebaut werden können. Vielen Dank an Dr. Frank Lewen und an die elektronische Werkstatt für die Hilfe bei der Entwicklung und dem Bau der Kristall-Temperaturregelung.

Herrn Prof. Dr. Martin Weitz danke ich für sein Interesse an meiner Arbeit und interessante Diskussionen.

Der Bonn-Cologne Graduate School of Physics and Astronomy danke ich für finanzielle Unterstützung und interessante Events.

Das Korrekturlesen (m)einer Arbeit erfordert viel Geduld. Danke hierfür an Sven Thorwirth, Thomas Giesen, André Klemann, Petra Neubauer-Guenther, Volker Lutter, Imke Keppeler, Dušan Stupar, meine liebe Frau und meinen Vater.

Nicht genug kann ich meiner Familie danken. Meinen Eltern danke ich für ihre volle Unterstützung während meines Studiums. Meinen lieben Kindern danke ich für das abwechslungsreiche Programm zuhause. Es war nie langweilig. Doch allen voran danke ich Dir, Lena, für die jahrelange Unterstützung, Deinen Optimismus und das Spenden guter Laune. Zusammen schaffen wir alles!

"I never did a day's work in my life, it was all fun."
Thomas Alva Edison

Dieses Werk ist copyrightgeschützt und darf in keiner Form vervielfältigt werden noch an Dritte weitergegeben werden.
Es gilt nur für den persönlichen Gebrauch.

Erklärung

Ich versichere, dass ich die von mir vorgelegte Dissertation selbständig angefertigt, die benutzten Quellen und Hilfsmittel vollständig angegeben und die Stellen der Arbeit - einschließlich Tabellen, Karten und Abbildungen -, die anderen Werken im Wortlaut oder dem Sinn nach entnommen sind, in jedem Einzelfall als Entlehnung kenntlich gemacht habe; dass diese Dissertation noch keiner anderen Fakultät oder Universität zur Prüfung vorgelegen hat; dass sie - abgesehen von unten angegebenen Teilpublikationen - noch nicht veröffentlicht worden ist sowie, dass ich eine solche Veröffentlichung vor Abschluss des Promotionsverfahrens nicht vornehmen werde. Die Bestimmungen dieser Promotionsordnung sind mir bekannt. Die von mir vorgelegte Dissertation ist von Professor Dr. Stephan Schlemmer betreut worden.

Dieses Werk ist copyrightgeschützt und darf in keiner Form vervielfältigt werden noch an Dritte weitergegeben werden.
Es gilt nur für den persönlichen Gebrauch.

Dieses Werk ist copyrightgeschützt und darf in keiner Form vervielfältigt werden noch an Dritte weitergegeben werden.
Es gilt nur für den persönlichen Gebrauch.

Teilpublikationen

- J. Krieg, V. Lutter, F.-X. Hardy, S. Schlemmer, and T. F. Giesen. The ν_5 antisymmetric stretching mode of linear C_7 revisited in high resolution. *Journal of Chemical Physics* **132** 224306 (2010)

- J. Krieg, A. Klemann, I. Gottbehüt, S. Thorwirth, T. F. Giesen, and S. Schlemmer. A continuous-wave optical parametric oscillator around 5 μm wavelength for high-resolution spectroscopy". *Review of Scientific Instruments* **82** 063195 (2011)

- S. Thorwirth, J. Krieg, V. Lutter, I. Keppeler, S. Schlemmer, M. E. Harding, J. Vazquez, and T. F. Giesen. High-resolution OPO spectroscopy of Si_2C_3 at 5 μm: Observation of hot band transitions associated with ν_3. *Journal of Chemical Physics*, in press (2011)

- S. Gärtner, J. Krieg, A. Klemann, O. Asvany, and S. Schlemmer. Rotational transitions of CH_2D^+ determined by high-resolution IR spectroscopy. *Astronomy & Astrophysics* **516** L3 (2010)

Dieses Werk ist copyrightgeschützt und darf in keiner Form vervielfältigt werden noch an Dritte weitergegeben werden.
Es gilt nur für den persönlichen Gebrauch.

Dieses Werk ist copyrightgeschützt und darf in keiner Form vervielfältigt werden noch an Dritte weitergegeben werden.
Es gilt nur für den persönlichen Gebrauch.

Lebenslauf

Jürgen Krieg
Winterberger Str. 41
51109 Köln

Geburtstag:	27.06.1980
Geburtsort:	Köln
Staatsangehörigkeit:	deutsch
Familienstand:	verheiratet, zwei Kinder

Schulbildung

1986–1990	Gemeinschaftsgrundschule Dürscheid, Kürten
1990–1999	Gymnasium Herkenrath, Bergisch-Gladbach
06/1999	Abitur

Studium

10/2000	Studienbeginn an der Universität zu Köln Fachrichtung: Physik Diplom
04/2005	Beginn der Diplomarbeit am I. Physikalischen Institut der Universität zu Köln
04/2006	Abschluss des Diplomstudiums
05/2006	Aufnahme des Promotionsstudiums am I. Physikalischen Institut der Universität zu Köln

Zivildienst

08/1999–06/2000	Zivildienst im mobilen sozialen Dienst der Caritas

Berufstätigkeit

01/2004–12/2004	Studentische Hilfskraft am Geophysikalischen Institut der Universität zu Köln
01/2005–04/2006	Studentische Hilfskraft am I. Physikalischen Institut der Universität zu Köln
seit 05/2006	Wissenschaftlicher Mitarbeiter am I. Physikalischen Institut der Universität zu Köln

Dieses Werk ist copyrightgeschützt und darf in keiner Form vervielfältigt werden noch an Dritte weitergegeben werden.
Es gilt nur für den persönlichen Gebrauch.

Dieses Werk ist copyrightgeschützt und darf in keiner Form vervielfältigt werden noch an Dritte weitergegeben werden.
Es gilt nur für den persönlichen Gebrauch.

Dieses Werk ist copyrightgeschützt und darf in keiner Form vervielfältigt werden noch an Dritte weitergegeben werden.
Es gilt nur für den persönlichen Gebrauch.

Dieses Werk ist copyrightgeschützt und darf in keiner Form vervielfältigt werden noch an Dritte weitergegeben werden.
Es gilt nur für den persönlichen Gebrauch.